Harvesting Philosopher's Wool: A Study in the Growth, Structure and Optoelectrical Behaviour of Epitaxial ZnO

William C. T. Lee

A thesis submitted in partial fulfilment
of the requirements for the degree of
Doctor of Philosophy
in
Electrical and Electronic Engineering
at the
University of Canterbury,
Christchurch, New Zealand.

April 2008

For Mum, Dad, Rebecca, Raymond and Judy —
The ones I love the most in this world.

ABSTRACT

This thesis is about the growth of ZnO thin films for optoelectronic applications. ZnO thin films were grown using plasma assisted molecular beam epitaxy and were studied using various conventional and novel characterisation techniques.

The significance of different growth variables on growth efficiency was investigated. The growth rate of ZnO films was found to be linearly dependent on the Zn flux under O-rich growth conditions. Under Zn-rich conditions, the growth rate was dependent on both atomic and molecular oxygen flux. By characterising the oxygen plasma generated using different RF power and aperture plate designs and correlating the results with the growth rates observed, it was found that atomic oxygen was the dominant growth species under all conditions. Molecular oxygen also participated in the growth process, with its importance dependent on the aperture plate design. In addition, an increase in growth temperature was found to monotonically decrease the growth rate. A growth rate of 1.4 Å/s was achieved at a growth temperature of 650 °C by using an oxygen flow rate of 1.6 standard cubic centimetres utilising a plasma source with a 276 hole plate operating at 400 W, and a Zn flux 1.4×10^{15} atoms/cm^2·s.

Characterisation of the MBE grown thin films revealed that the qualities of ZnO thin films were dependent on the growth conditions. Experimental evidence suggested that a maximum adatom diffusion rate can be achieved under Zn-rich conditions, giving samples with the best structural quality. O-rich conditions in general led to statistical roughening which resulted in rough and irregular film surfaces. Experimental results also suggested that by increasing the atomic oxygen content and decreasing the ion content of the plasma, the excitonic emission of the ZnO thin films can possibly be improved. It was also found that the conductivity of the films can possibly be reduced by increasing the plasma ion content.

By investigating the evolution of the buffer layer surface during the early stages of growth, dislocation nucleation and surface roughening were found to be important strain relief mechanisms in MBE grown ZnO thin films that affected the

crystal quality. The usage of LT-buffer layers was found to improve substrate wetting, and was shown to significantly reduce dislocation propagation. Further strain reduction was achieved via the application of a 1 nm MgO buffer layer, and a significant reduction of carrier concentration and improvement in optical quality was subsequently observed. A carrier concentration of $<1\times10^{16}$ cm^{-3} and a near band emission full width half maximum of 2 meV was observed for the best sample.

The study of electrical characteristics using the variable magnetic field Hall effect confirmed the existence of a degenerate carrier and a bulk carrier in most MBE grown ZnO thin films. The bulk carrier mobility was measured to be ~120 - 150 cm^2/Vs for most as-grown samples, comparable to the best reported value. A typical bulk carrier concentration of $\sim1\times10^{16}$ - 1×10^{18} cm^{-3} was observed for as-grown samples. Annealing was found to increase the mobility of the bulk carrier to ~120 - 225 cm^2/Vs and decrease the bulk carrier concentration by two orders of magnitude.

Using time resolved photoluminescence, it was found that the radiative recombination in MBE grown ZnO thin films was dominated by excitonic processes, and followed a $T^{3/2}$ trend with temperature. A maximum radiative lifetime of 10 ns was observed for as-grown samples. The non-radiative lifetime in ZnO thin films was dominated by the Shockley-Read-Hall recombination processes. The modelling of the temperature dependence of the non-radiative lifetime suggested that an electron trap at ~0.065 eV and a hole trap at ~0.1 eV may be present in these samples. The application of time resolved photoluminscence also allowed the direct observation of carrier freeze-out in these ZnO films at low temperature.

ACKNOWLEDGEMENT

First and foremost I would like to thank my supervisor Assoc. Prof. Steve Durbin for the vast amount of time and effort he put in this project despite his busy schedule. This project has faced some rough times and I am very grateful that Steve gave me enormous encouragement as well as valuable insight and guidance which got me through the worst of times. I would also like to thank my co-supervisor Assoc. Prof. Roger Reeves for his significant contribution to the ideas behind this research, and his expertise in optics has been extremely handy in many of the optical measurements and data interpretations that were involved in this thesis.

Financially, this project was funded by the MacDiarmid Institute for Advanced Materials and Nanotechnology, the Marsden Fund, and the Tertiary Education Commission Doctoral Scholarship Fund. These sources of funding allowed me to do my research without worrying about costs, giving me opportunities to attend many more conferences than I would otherwise have been able to, and keeping me alive by providing me money to live on.

The scope of this research was so large that it is unfair to claim that all of the results here were solely my own work. It is the help of other research students, postdocs and technicians that allowed me to complete this study. I would especially like to thank Mr. Chito Kendrick, who taught me so many of the laboratory skills that I needed to know, and was always there to help whenever there was a problem that I couldn't solve or an issue that I couldn't handle. I would also like to thank the other two members of the MBE team: Ms. Jessica Chai and Dr. Phill Anderson, who provided valuable help throughout my studies and made the MBE lab a much more fun place to work in. The help of Dr. Robert Kinsey and Dr. Ed Walsby on various aspects of experimental work during the first two years of my thesis is deeply appreciated, and the instrumental discussion and fruitful experimental work on electrical characterisations and devices with Dr. Craig Swartz and Mr. Martin Allen I truly appreciated, not to mention their solid effort in proof reading this thesis. The lab maintenance work by Mr. Gary Turner and Ms. Helen Devereux has been extremely important and I am deeply grateful for their efforts.

I owe many of the interesting results presented in this thesis to my collaborators who I am all very grateful to. At University of Canterbury, Mr Paul Miller and Mr Martin Henseler have been the most wonderful in performing all of the PL measurements. I am very grateful to their time and effort. I am also thankful to have to opptunity to work with Mr. Sandeep Chandril (and Dr. Craig Swartz) and Prof. Tom Myers at West Virginia University for variable magnetic field Hall measurements and interpretation. I especially admire Prof. Tom Myers' deep knowledge in MBE growth and electrical characterisations which provided me with fruitful discussions. My time at University at Buffalo, SUNY was exemplary thanks to Prof. Alex Cartwright and his student Mr. Maurice Cheung who not only taught me how to measure and interpret TRPL results, but had also incredibly provided me with TRPL data for almost all the of the films of interest. I am also very grateful to Alex's other student Mr. Sung-Jin Kim for his hospitality and his valuable time for the not so fruitful experiments that we did together. Although I did not have to opptunity to work with them, Prof. Redwing and Dr. Xiaojun Weng's work on the TEM of the ZnO samples was most timely, and I am truly indebted to them. I am also thankful for the time and effort of Mr. Dongho Lee and Dr. Chu Wie for the XRD measurements. The image analysis by Prof. Rick Millane, TEM analysis by Prof. Simon Ringer and Dr. Zongwen Liu, and the NMR analysis by Prof. Paul Callaghan and Dr. Kate Washburn on the porous ZnO material are also deeply appreciated.

Last but certainly not least, I would like to thank my family and friends who have supported me throughout this thesis. I want to sincerely thank my Mum and Dad, without their guidance and love I would not be where I am today. I would also like to thank my sister Rebecca and my brother Raymond, whose love and support is the best that I can ever get. I am indebted to my dearest friends Alan and Chuck, who have helped to keep my life colourful and showed continuous support emotionaly and technically, especially Alan who has been painstakingly trying to correct my grammar on and off paper. And Judy, my wonderful girl, I cannot thank you enough for your support, the joy that you bring, and your love. Thank you.

TABLE OF CONTENTS

LIST OF FIGURES

LIST OF TABLES

Chapter 1

INTRODUCTION

Lighting is such an important part of modern life that it has become the major source of energy consumption in the world. For example, in the USA, lighting alone amounted for approximately 22% of total energy consumption in 2004, leading to an electrical energy usage of 915.4 TWh [1]; similarly, in Hong Kong, artificial lighting contributed to 20 - 30% of the total electricity usage in 2006, and is second only to air-conditioning during summer months [2]. Meanwhile, it has been recognised over the last few decades that increasing energy demand coupled with the world's shortage of fossil fuel will trigger a global energy crisis in the near future. It is expected that reducing energy consumption will play a major part in solving this energy problem. Therefore, improving lighting efficiency is indispensable for a sustainable society in the new millennium and beyond.

Currently, light generation is predominantly provided by incandescent lighting, which is very inefficient and limited by the maximum filament temperature achievable (a maximum efficiency of 17 lm/W) [3]. Fluorescent lights, which are slightly more efficient than incandescent lamps, are still limited by the efficiency of the UV to visible conversion involved (a maximum efficiency of 90 lm/W) [3]. Because of such efficiency limits, these two lighting technologies ultimately cannot be part of the long term solution. A more plausible approach is to use solid state lighting (SSL). SSL generates light by utilising the direct recombination of electrons and holes in a semiconductor, sometimes in conjunction with a phosphor. Because of this direct conversion process, there is no theoretical limit to the achievable efficiency. In fact, it is expected that solid state white light can reach an efficiency of 200 lm/W by 2020 [4], and can theoretically reach over 400 lm/W depending on the design [1]. The incorporation of SSL in everyday applications would therefore allow a large reduction in energy requirements. It is speculated that gradual replacement of incandescent and fluorescent lighting with SSL in the US would slash the lighting

energy consumption by 50% by 2020, reducing the expenditure by over $100 billion over the next 20 years [5]. Worldwide, it is expected that SSL will also reduce the energy consumption by 50%, resulting in a expenditure saving of 3 - 4 times the US figure [6].

Currently, red, orange and green SSL devices with efficiency reaching 108 lm/W [7] are already in use in many commercial applications, replacing conventional lamps, neon lights and cathode ray tubes. Achieving widespread usage of SSL requires only one missing piece, namely, the efficient generation of blue-violet light to complete the visible spectrum, allowing for the generation of true white light. Therefore, finding an economical material that can efficiently generate light in the blue to UV region is vital. One material that fulfils the criteria is zinc oxide.

1.1 History of ZnO

Zinc oxide (ZnO) is a material that is regarded as one of the best candidates for high energy, short wavelength optoelectronics applications. However, ZnO is not a novel or new material that results from complex material engineering or nature defying mechanisms. On the contrary, it is an everyday material that has been known for centuries. Even elementary chemistry students would likely be familiar with the classic textbook reaction:

$$2Zn(s) + O_2(g) \rightarrow 2ZnO(s)$$

as an example of a combustion reaction. Known historically as *pompholyx* and *lana philosophica* (philosopher's wool) [8], ZnO commonly exists in Zn ores as a white woolly form or as pure hexagonal zincite crystals (Figure 1.1). It is also known by the names flowers of zinc, *nihil album* and zinc white. ZnO has such a comprehensive range of applications that its usefulness matches that of both of its parental elements [9]. For example, ZnO is found in Chinese White which is a high grade artist pigment used in ancient times; zinc ointment which is 20% ZnO with bees wax for treating dyshidrosis, a type of skin disease; Tinosorb^{TM} for clothing products to prevent UV damage; and zinc oxide Eugenol that is used for dental fillings. ZnO is also used in cosmetic products, especially in sunscreens and sunlotions, and is also an important ingredient for manufacturing rubber, allowing a faster and more controllable cure [9].

Figure 1.1 Natural occurring zincite ore (from Weissman and Nikischer [10]).

Prior to the 1930s, scientific research on ZnO was mostly limited to studies involving the processing of Zn metal for the steel industry [11-13], catalytic action for chemical processes [14-16], and basic properties such as heat capacity, electronic structure and lattice structures [17-19]. In the 1940s, ZnO was "discovered" as a semiconductor [20] and it was only then that ZnO started to become interesting to the world of electronics and circuitry. Large scale investigation of ZnO in the 50s and 60s led to the discovery of attractive properties such as gas dependent conductivity [21], non-ohmic resistivity [22] and piezoelectricity [23], each of which contributed to new fields of electronic devices. Subsequently, ZnO became a common material for high frequency surface acoustic wave (SAW) devices [24], sensors [25] and varistors [22]. By the end of the 1980s, however, research activities on ZnO slowed as research efforts were directed to other compound semiconductors.

Interest in ZnO was reignited in the late 1990s following the demonstration of optically pumped lasing in the UV region [26, 27]. It was during the period when indium gallium nitride (InGaN), the best candidate material at the time for high efficiency blue lighting, was found to have several limitations, such as low efficiency, high fabricating costs and limited indium supplies, which are difficult to overcome. Therefore, the demonstration of efficient UV lasing in ZnO and its potential for replacing InGaN immediately sparked worldwide interest in the material.

This "rediscovery" of ZnO as an optoelectronics material has since returned ZnO to the spotlight of compound semiconductor research. ZnO is now the focus of research not only for optoelectronic devices, but also for spintronics [28], nano-size gas sensors [29], biotechnology as enzyme and protein catching nanostructures [30] and nano-transistor logic [31]. With the current amount of research effort put into this

field, it is expected that widespread commercialisation of ZnO optoelectronic devices will occur within the next 10 years.

1.2 Some Important Properties of ZnO

ZnO belongs to the group of semiconductors known as II-VI semiconductors which include HgCdTe, ZnSe and ZnTe. Like all other II-VI semiconductors ZnO can crystallise as cubic zincblende, hexagonal wurtzite or rocksalt, although ZnO is most stable and most commonly found in the wurtzite form [32]. The unit cell of wurtzite ZnO is shown in Figure 1.2. As the Zn-O bond in the wurtzite ZnO structure is asymmetrical in the [0001] direction, not all surfaces on the unit cell are equivalent. In particular, as seen in Figure 1.2 on the +c face (facing upwards) the Zn atoms in the Zn-O bond are facing towards the surface and therefore that face is known as the Zn-polar surface. Similarly, the -c face (facing downwards) has the O atoms facing towards the surface and is therefore known as the O-polar surface. As the Zn-O bond is symmetrical in all other directions, all other surfaces on the unit cell are known as non-polar. It is well known that this surface polarity has important effects on the properties of the material and implications for device fabrication [33, 34].

Table 1 shows the lattice constant of ZnO compared to other common III-V and II-VI semiconductors. It can be seen that ZnO is the odd one out compared to other II-VI compounds such as ZnS and ZnSe, with a much smaller a-axis lattice

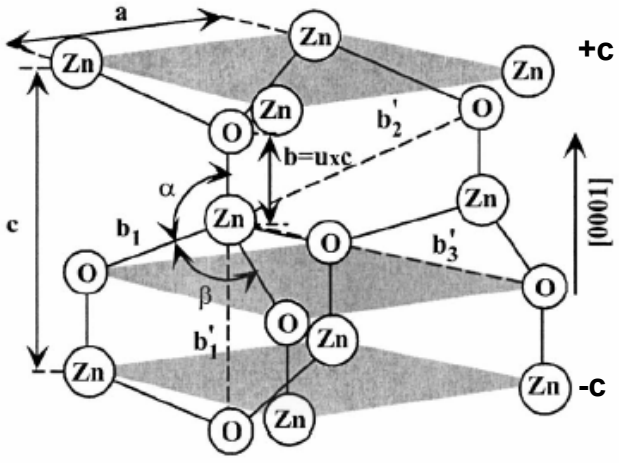

Figure 1.2 Unit cell of wurtzite ZnO (from Ozgur et al. [32]).

Table 1: Lattice constants of ZnO and selected common semiconductors (Data from Levinshtein et al. [35] and Tamargo [36]).

Material	a-axis lattice constant (Å)	c-axis lattice constant (Å)
ZnO	3.249	5.205
ZnSe	5.671 (cubic)	
ZnS	3.820	6.260
GaN	3.189	5.185
SiC	3.086	15.117
GaAs	5.653 (Zinc blende)	

constant. The lattice constant of ZnO in both directions are closest to GaN. This highlights the similarity and compatibility of the two materials.

Because of the large electronegativity differences between the zinc and oxygen atoms, the Zn-O bond is strongly polarised. The strong bond polarity places ZnO midway between pure covalent and pure ionic crystals. ZnO therefore inherits many advantageous properties of ionic crystals. For example, ZnO is a thermally stable compound with a melting point of 1975 °C, allowing ZnO devices to operate under extreme heat. Unlike many other semiconductors, ZnO is also structurally hard, mechanically robust and resistant to mechanical deformation [32], making it much easier to process mechanically. ZnO is readily dissolvable in aqueous solutions such as diluted acids, allowing wet etching which simplifies device fabrication processes. The near ionic character of ZnO also means that the human body would absorb ZnO as Zn and O ions, which are both non-toxic. This means that ZnO is completely non-toxic to humans, making it very desirable in all consumer areas, especially biotechnology applications.

The electronic structure of ZnO governs the electrical and optical properties of the material. ZnO is a direct bandgap material, with a bandgap of 3.4 eV at 300 K. This direct wide bandgap means that ZnO is an efficient UV emitter, although electrical conduction through ZnO would rely heavily on impurity induced midgap states. Due to crystal field spin-orbit interactions, the valence band maximum of ZnO is split into three bands - a Γ_9 band and two Γ_7 bands [37], more commonly known as A (heavy hole), B (light hole) and C (crystal field splitting) bands. This splitting means that three types of excitons exist in ZnO, namely, the A, B and C excitons. While for most semiconductors, including InGaN, exciton assisted recombination only dominates at low temperatures, the high binding exciton energy of ZnO (59 meV

for the A exciton) means that excitonic emission can be sustained even above room temperature. This high exciton binding energy combined with the wide direct bandgap mean that ZnO is an excellent material for high efficiency short wavelength device applications.

1.3 ZnO Deposition Techniques

Although ZnO can be easily formed via simple oxidation of Zn metal, fabrication of high quality crystals for device applications involves more complex processes. In particular, the formation of bulk single crystal ZnO requires a controlled reaction process.

There are currently three common methods for growing bulk ZnO crystals. These are vapour transport [38], melt growth [39], and hydrothermal [40]. Vapour transport was the earliest bulk single crystal ZnO growth method, with the first chemical vapour transport growth of a ZnO crystal 2 mm in diameter and 8 mm long reported in 1971 [38]. It was the primary growth method used by the first commercial supplier of ZnO substrates, Eagle-Pitcher. Vapour transport grown ZnO crystals have been commonly employed as a reference material for comparing the qualities of ZnO grown by other methods. Melt growth was inspired by the success of melt growth of silicon, which produces very high purity material at a relatively low cost. Unfortunately, applying melt growth to ZnO is very difficult as the melting point of ZnO (1975 °C) is extremely high compared to that of Si (1414 ºC). As a result, the melt growth of ZnO often suffers from mechanical problems due to extreme heating and cooling, such as cracks and defect formation [41]. Nevertheless melt growth has been successfully used by various commercial companies such as Cermet Inc. The hydrothermal process is a more recent bulk ZnO growth technique. In this method, a seed crystal is lowered into a solution containing $Zn(OH)_2$ and $Li(OH)_2$ or other similar alkaline solvents. ZnO then crystallises onto the seed crystal, forming a large single crystal which is then cleaved into substrates [40]. Currently, hydrothermally grown ZnO substrates are considered the best available ZnO material, with a background carrier concentration as low as $\sim 10^{13}$ cm^{-3} and excellent crystallinity [34]. Compared to freestanding GaN and InGaN material, bulk ZnO crystals can be fabricated much more readily with a much higher achievable quality. However, even

with the relatively simpler growth process the production cost of bulk ZnO substrates is still extremely high. In 2007, the cost of a 0.5 mm thick 1×1 cm^2 was approximately $320 USD.

The large scale fabrication of most optoelectronic devices usually involve the growth of thin epitaxial layers on a bulk substrate, which allows more complex device structures such as p-n junctions, multiple active layer structures and quantum devices to be produced. However, due to the high cost of bulk ZnO material, it is more common to grow ZnO thin films on more economical substrates such as glass, Si or sapphire. Currently there are a large number of methods for growing ZnO thin films. Sputtering was the first technique used for making ZnO thin films, mostly for SAW devices [42]. Sputtering continues to be one of the most common techniques for the growth of ZnO, due to its cheap running cost, fast deposition rate and reasonable crystal quality. However, because sputtering is a highly energetic process the resulting material is often polycrystalline with a high density of structural defects. These films are generally unsuitable for light emitting devices, where low carrier concentration, high mobility and excellent UV emission are required.

Pulsed laser deposition (PLD) is another commonly used technique, especially after the demonstration of lasing from PLD grown ZnO [43]. In PLD, the desired material is deposited onto a substrate via the laser ablation of a target that is made of the same material. The high energy laser evaporates and knocks off atoms from the target surface, creating a plume that deposits the material onto the substrate forming an epitaxial layer. Sometimes referred to as "laser molecular beam epitaxy" (LMBE) when performed under ultra high vacuum conditions, PLD is currently one of the most successful epitaxial growth technique for ZnO with reports of very high quality material rivalling that of bulk ZnO [44]. However, most of these reports use commercial ZnO bulk crystal as targets and exotic materials such as $ScAlMgO_4$ as substrates, which are both very expensive and as such the process is not cost effective. There are several reports of reasonably good ZnO material utilising high vacuum systems with an affordable target and more practical substrates [45, 46], although the resulting thin films are not significantly better than other deposition techniques.

Another method that is commonly used for epitaxial growth is metal organic chemical vapour deposition (MOCVD), where the deposition depends on the chemical reaction between two gaseous organic reactants containing the elemental components of the desired material. In particular, MOCVD is predominantly used in

the commercial fabrication of GaN/InGaN light emitting devices. Although not as popular for ZnO, there is still a reasonable number of reports on the growth of ZnO thin films by MOCVD (see for example, ref [47], [48] and [49]). However, MOCVD grown ZnO thin films suffer from a major drawback, namely, the unintentional incorporation of hydrogen from the organic reactants. As hydrogen has been proven to be a shallow donor in ZnO [50], MOCVD may not be suitable for growing low conductivity ZnO that is needed for optoelectronic applications.

One other epitaxial deposition technique that has been used for ZnO growth is molecular beam epitaxy (MBE). MBE has been successfully employed previously to make many other materials. In fact, the earliest studies on epitaxial ZnO were almost exclusively through MBE and the first lasing was demonstrated with MBE grown material [26]. Although currently MBE is not the most popular or most successful epitaxial technique for ZnO growth, the very successful application of MBE to other semiconductors such as GaAs and InGaN suggests that it should be a promising technique for effective ZnO growth. It is for this reason that in this thesis, the growth and characterisation of MBE grown ZnO is thoroughly and exclusively studied.

1.4 ZnO Characterisation Techniques

To correlate the different growth variables and growth processes to the resulting quality of the ZnO thin films, the structural, optical and electrical properties of samples grown under controlled conditions must be measured and compared. A number of conventional characterisation techniques for each of these three important properties were used in this work, and are described in this section.

One of the most powerful techniques for examining the surface of a thin film is reflection high-energy electron diffraction (RHEED). RHEED allows in-situ monitoring of the atomic structure of the surface, down to the monolayer level. Details of the principles behind RHEED can be found in the literature (see for example, Refs [51-53]). While RHEED is very useful for real time monitoring of the evolution of a thin film surface during growth, it can also be used for surface characterisation of the thin film after growth. In particular, in this work, the after growth RHEED was extensively used as a preliminary assessment of the ZnO thin

film surface, as it was not installed in the same growth chamber (necessitating UHV transfer).

Two microscopy techniques that are commonly used for nanosize surface features were used in this study — scanning electron microscopy (SEM) and atomic force microscopy (AFM). Details on the theory and operation of these two techniques can be found in many references [54-56]. The short wavelength electrons used in SEM allows the imaging of nanometre size features, and is capable of giving very sharp images of the sample surface, although it lacks quantitative height information. With care, image contrasts can be used as a rough estimate of the height of surface features. SEM is typically used when a survey of the sample surface over a relatively large area is needed.

In contrast, AFM is substantially different to conventional microscopy techniques, with the surface analysed by the interaction between an AFM tip and the surface. In particular, during an AFM scan, the AFM tip is illuminated by a laser, and is moved across the sample surface. The surface information is then obtained by detecting a change in the laser reflection originated from the vertical movement of the tip as it moves through different morphologies (see Figure 1.3). Because the tip size is in the nanometre range, AFM is capable of imaging features much finer than SEM. Further, AFM scans inherently contain quantitative height information and therefore are very useful in assessing the feature sizes on a thin film sample. AFM is typically

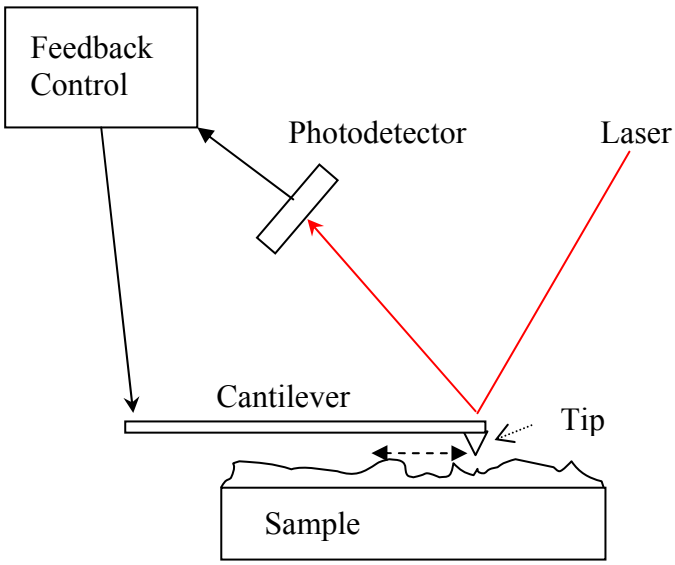

Figure 1.3 Schematic diagram of basic AFM operation.

used for detailed analysis of sample surfaces over a very small region, giving information such as step height, island density and terrace formations. An important quantity provided by AFM is the surface roughness of the sample, which is a quantitative way to analyse the surface structure and the crystal quality. As defects or dislocations in the bulk lattice manifest themselves on the sample surface as irregular features, an increased roughness implies an increase in defect density or irregularity in the bulk crystal lattice. The smoothness of the thin film surface is also very important for contact deposition and junction formation.

A common method that studies the overall structural quality is x-ray diffraction (XRD). XRD is a common technique used for identifying the composition of a material by comparing a diffraction spectrum (θ-2θ scan) with the known spectrum of pure specimens of different elements or compounds. For thin film applications, the θ-2θ scan can be used to identify different phases that are present in the bulk of the sample. Further, by altering the orientation of the x-ray beam relative to the samples, one can measure a rocking curve with a width proportional to the dislocation density of the sample. Therefore, the full width half maximum (FWHM) of the rocking curve is often used as a common figure of merit for the overall structural quality of thin film crystals. A more detailed discussion of XRD and high resolution XRD (HR-XRD) can be found in references [51, 57, 58].

The universal figures of merit for the electrical characteristics of a semiconductor thin film are the carrier concentration and the carrier mobility. Both the carrier concentration and the mobility of a thin film are commonly measured using the conventional Hall effect technique (Figure 1.4), which consist of two separate measurements. Firstly, the resistivity of the sample is determined by measuring the resistance across the sample; secondly, the carrier concentration of the sample is measured by utilising the electrons' movement due to an external magnetic field (the Hall effect) which creates a measurable voltage difference. While a relatively simple technique, built-in assumptions and geometric effects can complicate the interpretation of the results (discussed in Chapter 5). Nonetheless, room temperature Hall effect measurements are commonly used as a primary electrical characterisation technique.

The most common technique for measuring the optical properties of a semiconductor is photoluminescence (PL). In PL the sample is excited by an above

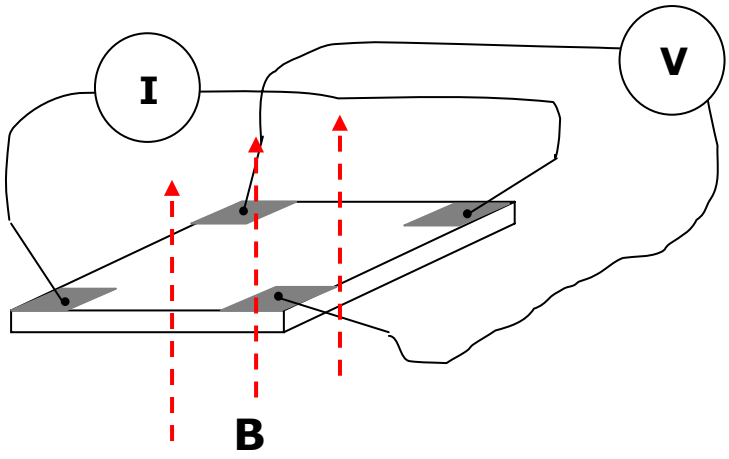

Figure 1.4 Schematic of the Hall effect measurement of a thin film sample, with contacts placed in the van der Pauw geometry.

bandgap laser and the emission from the relaxation of the excited electrons is measured. The measured emission spectrum is in general similar to the emission obtained from electrical excitation of a device structure (electroluminescence). Therefore, room temperature PL is often used to predict the performance of a sample when used as a light emitting device at room temperature. By comparing the peak position of the PL with the known spectrum of a pure specimen, one can extract specific information about the sample including density and type of structural defects, strain, and concentration and type of impurities. In addition, since the spreading of the emission peak originates from crystal imperfections that cause a variation of the local band structure, the FWHM of the bandedge PL is often used as a figure of merit for crystal quality.

1.4 Issues in ZnO

Although there are many different ZnO deposition techniques, currently material quality is quite low compared to that of InGaN epilayers. Ultimately, this is associated with a lack of understanding of the ZnO growth process, which makes material optimisation difficult. Apart from that, the understanding of the ZnO material system is also limited. Although ZnO has been studied thoroughly for the last decade, many aspects of the material are still unknown. Indeed, ZnO is such an interesting

material that as crystal quality increases more questions regarding the fundamental properties of the material arise. Mysteries such as the origins of photoluminescence peaks [34], behaviour of point defect complexes [59], and the effects of surface conduction [60] are only a few of the issues that remain poorly understood.

One of the other issues is p-type doping of ZnO. As suggested by theoretical calculations, formation of shallow acceptors in ZnO is extremely difficult [61]. Coupled with the high residual n-type carrier concentration that is usually present due to the ease of formation of shallow donors, p-type doping of ZnO has proved difficult to achieve. Nonetheless, through the enormous amount of research effort that was applied in this direction for the last few years, the fabrication of p-type ZnO, even LEDs, has been reported in a number of recent publications. Unfortunately, most of the reported p-type ZnO fabrications are somewhat unreliable, with data that could be explained by noise and offsets [62, 63], irreproducible or difficult to repeat (such as the fabrication of undoped p-type ZnO [64]), or involve very cumbersome procedures that are impractical, such as the repetitive annealing process reported by Tsukazaki et al. [65]. There is also the issue of interface hole accumulation between n-type ZnO and a conducting substrate which is often interpreted as p-type ZnO conduction [66]. From these, it can be seen that easy access of p-type ZnO is still one of the major hurdles that prevents the commercialisation of ZnO devices.

The unreliable measurements reported by many groups claiming p-type doping highlight another issue, namely, the validity of measurement techniques. While many traditional semiconductor characterisation techniques have been applied to ZnO with reliable and accurate results, it is possible that limitations of different characterisation techniques (such as Hall effect measurements) may be affected by the unique properties of ZnO, such as spontaneous polarisation and low mobility, as most semiconductor characterisation techniques were designed for bulk, narrow bandgap semiconductors with low resistivity. Therefore, the interpretation of results from conventional measurements is also an issue that surrounds ZnO materials and devices.

The aim of this thesis is to examine some of these issues in detail, with the goal of providing insights into how these issues can be solved and to allow further advancement of ZnO technology. A major part of this thesis is devoted to the MBE ZnO growth process. By correlating the process variables and measured characteristics, it is hoped that a detailed understanding of the MBE growth process can be obtained, from which a universal optimisation can be achieved. To address the

p-type doping issue, the first step is to reduce the residual carrier concentration as much as possible, and therefore, the reduction of electron concentration of the ZnO thin films without sacrificing other properties is another goal of this work. Finally, to gain a further understanding of the ZnO material system and to overcome some of the limitations of conventional measurements, ZnO thin films were also examined using novel characterisation techniques to study the material from a new angle.

1.5 Thesis Outline

In the next chapter, the basics of MBE growth of ZnO are described, with emphasis on the effect of basic parameters and basic crystal growth process on the growth efficiency. In Chapter 3, a detailed study on the effect of flux ratio, active oxygen species and growth temperature on film properties using conventional characterisation techniques is presented to develop a further understanding of the MBE growth process. This is followed by an in-depth investigation of the relationship between strain, structure and the consequent effect on the properties of the ZnO epilayers in Chapter 4, highlighting the nucleation process and the effect of buffer layers. Chapter 5 is devoted to the electrical characterisation of ZnO thin films using variable magnetic field Hall effect to illustrate the limitations of conventional measurements and the importance of degenerate layers. This is followed by an in-depth characterisation of the recombination dynamics in ZnO using time-resolved photoluminescence in Chapter 6, which examines the behaviour of carrier recombinations in ZnO epilayers. Finally, a summary of results, correlations and recommended future directions are presented in Chapter 7.

Chapter 2

MBE GROWTH OF ZNO

2.1 Literature Review: MBE and ZnO

Molecular Beam Epitaxy (MBE) is a fabrication technique for growing thin epitaxial films using atomic or molecular beams of constituent elements, which interact and bond with each other on the substrate surface via thermal kinetic processes. It is, unlike many other deposition techniques, a non-equilibrium process [51]. MBE was first reported in the literature by Cho and co-workers in 1971 [67], and since then has become an important epitaxial technique. Cho, considered by many to be the father of MBE, used knowledge from surface physics and ion propulsion technology to create this new form of epitaxial technique [68]. During that time, there were increasing needs for the preparation of submicron thickness thin film compound semiconductors, but the conventional chemical vapour deposition (CVD) techniques could not satisfy the continuously evolving industrial requirements [67]. At the same time, there had been substantial advancement in vacuum systems. These factors together fuelled the birth of the MBE technique.

Since its inception, MBE has been used to fabricate a wide range of materials and structures. It is widely used in many semiconductor systems such as GaAs [69], HgCdTe [70] and various oxides [71]. MBE was instrumental in the development of many technologies such as superlattices and modulation doping [68], blue-green laser diodes [72], quantum cascade lasers [73] as well as the discovery of the fractional quantum Hall effect [74]. The main advantage of the MBE technique is that it is a non-equilibrium process. The film growth is therefore mainly dependent on the interaction between individual adatoms with the substrate, rather than the mass diffusion and reaction of a large amount of precursors as in CVD processes. It is therefore easier to control the reaction at a finely adjusted level. As a consequence, growth rates and film composition can be carefully tuned, making it arguably the best

epitaxial technique for growing quantum wells and superlattices. Another advantage of MBE is that it is generally conducted in an ultra high vacuum (UHV) environment. This greatly reduces the amount of impurities that are incorporated into the growing films. The UHV environment also allows many different in-situ characterisation techniques such as Auger electron spectroscopy, reflection high-energy electron diffraction (RHEED), and in-situ scanning electron microscopy to be used. The possible use of these techniques makes MBE very popular for the investigation of novel materials and for studying the growth processes of well established materials at an atomic scale.

Although MBE has many advantages that can potentially make it the best epitaxial technique in existence, it does suffer from some limitations. Firstly, MBE generally yields a lower growth rate than other deposition techniques. Although this may be a limitation that can never be overcome, it can in some circumstances be advantageous as the lower growth rate allows more accurate control of the thickness. A more severe limitation of MBE is its cost. Because of the need for UHV, MBE systems are expensive to manufacture, operate and maintain. This has certainly limited the use of MBE for the research and development of novel materials and devices commercially and academically.

The first account of MBE growth of ZnO was reported by Johnson in 1996 [75], where ZnO was investigated solely as a buffer layer for GaN growth. The breakthrough for MBE ZnO came after the report of room temperature lasing of MBE grown ZnO thin films by Bagnall et al. [26], who deposited ZnO onto c-plane sapphire using MBE and observed lasing at 240 kW/cm^2 after cleaving into laser cavities. This discovery showed both the attractiveness of ZnO as a UV lasing material and the ability of MBE to fabricate high quality ZnO layers. Subsequent studies initially concentrated on the growth of ZnO on various substrates ranging from common sapphire substrates to exotic materials such as $LiNbO_3$ [76] and CaF_2 [77]. However, most of the exotic substrates have been eventually phased out as it was found that sapphire, particularly c-plane sapphire, is the most cost effective option. However, c-plane sapphire has a very large lattice mismatch to ZnO (18%), resulting in poor quality films. Therefore, many of the early efforts were dedicated to the optimisation of ZnO thin films via modification of the growth interface by using special substrate surface treatments or via employment of buffer layer systems. For example, Du et al. used Ga pre-exposure to eliminate rotation domains and greatly

reduced the dislocation density as well as eliminating the defect band emission [78]; Ohgaki et al. reported the use of a low temperature ZnO buffer to improve the electrical quality of the ZnO layer [79]; and by the use of MgO buffer layers, Chen et al. successfully grew ZnO layers with an atomically smooth surface [80].

Apart from investigations on improving the growth surface, considerable effort was also devoted to the optimisation of growth parameters. For example, Kato et al. suggested that by adjusting the Zn/O flux ratio to 1:1, the best ZnO thin films could be formed, based on surface morphology and photoluminescence (PL) [81]; investigation of the plasma condition was undertaken by Sakurai et al.[82] who reported an improvement of crystal quality with increasing applied RF power; and the optimal growth temperature was suggested to be in the region of 720 °C by Jung et al. [83]. There were also investigations on other variables such as substrate offset angles [84] and annealing [85].

Even though ZnO films of relatively high crystal quality can be achieved easily using MBE, the background carrier concentration remains high, and the mobility remains low even after a decade of research. The highest mobility reported to date for a non-annealed, MBE grown ZnO structure is 145 cm^2/Vs [86], achieved by using low growth rate buffer layers to improve the electrical properties. This mobility is still short of the ~205 cm^2/Vs reported for early bulk materials [87] and the more contemporary values of ~240 cm^2/Vs for high quality hydrothermal bulk ZnO [88]. In fact, apart from the high impurity content, bulk ZnO crystals remain far superior to MBE grown thin films even today. This lack of progress and inferior thin film quality suggests that the understanding of the MBE ZnO growth process is still limited.

Recently, reports of low carrier concentration and high resistivity materials have prompted a growing number of research groups to pursue the goal of realising p-type doping. Although Zhang et al. have postulated that p-type doping in ZnO is problematic due to the low formation energy of compensating n-type intrinsic defects such as V_O and Zn_i under typical p-type conditions [61], a large number of dopants, such as N, As, P, Ag and Li, all of which can be readily incorporated into standard MBE processes, are expected to introduce acceptors in ZnO thin films. The first investigation of p-type doping with MBE appeared in 2000, when Iwata et al. experimented with nitrogen doping by using a N_2/O_2 plasma mixture [89]. However, in that report, it was found that the addition of nitrogen resulted in an increase in

donor concentration through the creation of N-induced defects. The first p-type Hall effect measurement was reported in 2002 by Look et al. who used a nitrogen plasma to grow ZnO:N on single crystal ZnO substrates [90]. Most subsequent investigations on p-type doping of MBE films were based on N-doping, either by using a nitrogen or NO plasma, although there are ongoing investigations on other possible dopants and co-doping techniques.

Even though p-type investigation is an area of high intensity research at present, the quality of the undoped material is still poor compared to that achievable with bulk material. As a result, researchers who want to study p-type doping of ZnO by MBE are forced to use materials that are far from optimal. For example, the first report of p-type doping via Sb by Xiu et al. used base materials with high carrier concentration ($\sim 5 \times 10^{18}$ cm^{-3}) and poor PL with large FWHM [91]. Similarly, Wang et al. performed nitrogen doping on undoped ZnO thin films of poor electrical quality with mobilities ~15 cm^2/Vs [92]. The doping of poor quality material undoubtedly results in poor quality doped material, and therefore is possibly the reason why although there are many claims of p-type doping, hardly any of them are reproducible by other groups. It can be seen that the quality of the undoped material is still very important.

In summary, it is clear that despite extensive investigations on the MBE growth of ZnO over the past 10 years, the trends and predictions from these studies are not complete and there are still many aspects of MBE ZnO growth that need to be examined, both system dependent and system independent. For this thesis, the goal is to examine the effects of different components and system variables on the growth of ZnO, and in the process, gain knowledge on system independent properties of the growth processes and the ZnO material itself, in order to achieve a greater understanding of the MBE growth of ZnO that can be transferred between different systems. In the remainder of this chapter, the basic growth of ZnO using a modified Perkin-Elmer 430 MBE system at the University of Canterbury will be described, and the results will be discussed in terms of the crystal growth process and the transferability to other MBE systems.

2.2 Key Aspects of the Canterbury MBE System

2.2.1 Vacuum System

Figure 2.1 shows the ZnO MBE system at the University of Canterbury. Originally from Purdue University, this modified Perkin-Elmer 430 system was formerly used for the growth of CdTe and MnTe [93], which were grown at relatively low substrate temperatures (~300 °C), using solid source sublimation.

Figure 2.2 shows a schematic of the Perkin-Elmer 430 system, modified for ZnO growth. To grow ZnO, a substrate is first mounted with indium onto a 75 mm diameter molybdenum substrate holder, and then introduced into the system through a load-lock. Prior to transferring to the UHV growth chamber, the substrate and substrate holder are typically outgassed for 1 h at 650 ºC in a UHV transfer tube which connects the two separate growth chambers of the Canterbury MBE system. The substrate holder is then placed on an E-Science platinum heater (model ES-06-0209), capable of sustaining temperatures of up to 1000 °C in an oxygen environment, to heat the substrate to an elevated temperature at which the growth can occur. During the growth process, molecular beams of zinc and oxygen are targeted at the substrate, allowing atoms to diffuse, collide, and interact with each other along the surface of the substrate to form a ZnO epilayer. View ports are placed in various positions to

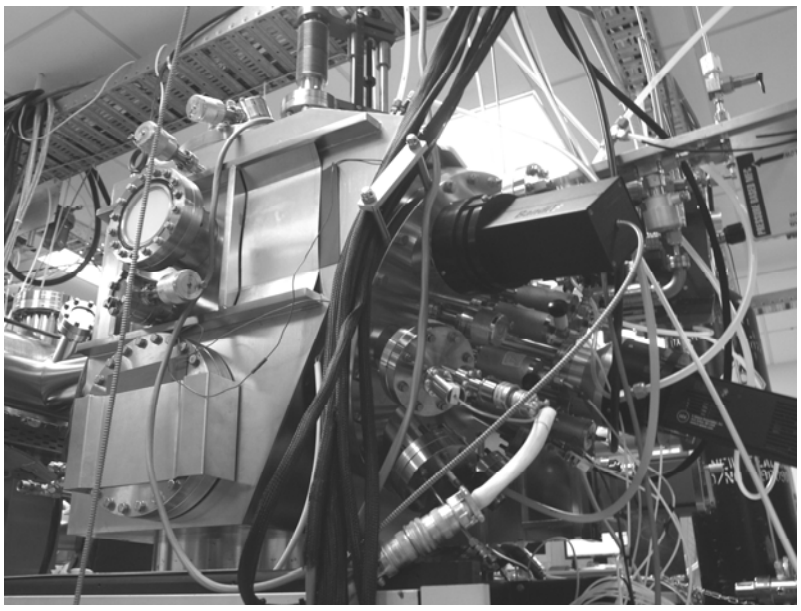

Figure 2.1 Perkin-Elmer 430 system at the University of Canterbury.

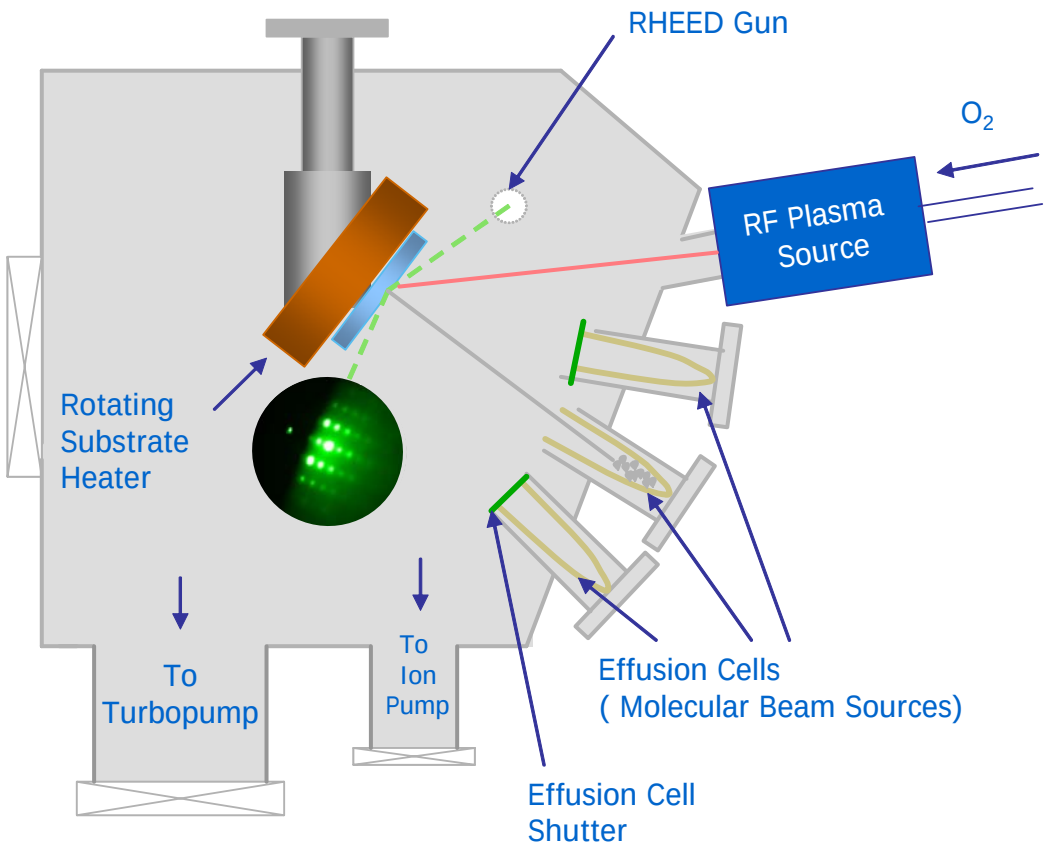

Figure 2.2 Schematic of the Perkin-Elmer 430 MBE system, modified for ZnO growth.

allow the visual monitoring of the growth process. A range of in-situ characterisation tools are also used during growth to control and study the different growth behaviours, including RHEED, laser interferometry and quadrupole mass spectrometry.

For an MBE system, a UHV environment is almost always essential. Conventionally, UHV denotes a pressure below 1×10^{-9} Torr, where the mean free path of particles in the system is comparable to or greater than the dimension of the system. MBE requires a UHV base pressure as it minimises impurities that can interrupt the growth process, and it also serves to maintain the high purity sources that are typically used. Note that the process pressure, especially for MBE systems that use gas reactants, is often much higher than UHV. However, since most of the introduced species leading to the increased pressure are desired reactants, this typically does not impact the level of impurity incorporation in the final film.

Because of this minimal impurity requirement, the choice of pumping system is therefore important, as it must be able to achieve the desired base pressure, handle any reactive gases that must be pumped, and not introduce contaminants — meaning

that generally all pumps must be oil free by design. The Perkin-Elmer 430 system uses a combination of two pumping systems. The primary system is a 500 l/s ion pump. The ion pump is an entrapment type pump where gaseous particles are ionised through collision with electrons emitted from the cathode to anode, both made from titanium plates. The ions are then evacuated either through the chemical reaction of these active ions with the titanium plates into low vapour pressure compounds or by the burial of the ions into the bulk of the titanium plates. Because of the nature of the pumping process, the ion pump can only be used in the UHV region where the gas load is low. The ion pump is mainly used for maintaining the MBE system in UHV when the system is idle, and to assist during bake out.

Since the ion pump operates best at pressures below 1×10^{-6} Torr, there is a need for another pumping system that can be used during the growth process, where the pressure can reach up to $\sim5\times10^{-5}$ Torr depending on the gas flow. A helium cooled cryogenic pump, commonly called a cryopump, was provided in the original Perkin-Elmer 430 system for this specific purpose. In a cryopump, coated metal fins are kept below 15 K via a cryogenic compressor. As particles in the chamber flow into the pump they condense onto the fins, and are thereby eliminated from the atmosphere of the MBE chamber. Because of this freezing action, cryopumps are very efficient at pumping water vapour, which is often the major contributor to the outgassing from chamber walls and components. A cryopumped system can achieve an extremely low base pressure of 1×10^{-11} Torr.

Unfortunately, while very efficient in pumping water vapour, cryopumps are not well-suited to pumping oxygen, especially if reactive species are present. In particular, after a few months of ZnO growth it was observed that the chamber pressure was constantly decreasing during the growth process. The installation of a calibrated mass flow controller to monitor the oxygen flow rate revealed that in fact the effective pumping speed of the cryopump was not constant. It was suspected that this fluctuating pumping speed was closely related to the extensive corrosion of the cooling fins that was observed upon reservicing. There was also a concern that the potential for trace production of ozone during the operation of oxygen plasma sources, as indicated by a number of anecdotal reports and measurements, could lead to the collection of explosive frozen ozone inside the cryopump. Therefore, for both reasons of safety and practicality, it was determined that it was necessary to replace

the existing cryopump with a turbomolecular pump designed for reactive oxygen, backed by an oil-free mechanical pump.

A turbomolecular pump (turbopump) is essentially a large turbine. The pumping action originates from the spinning action of the fins of the turbopump, which can reach over 10000 revolution/s for some turbopumps. Because of this rotary action, particles that enter the pump impacting on the blade are imparted with enormous momentum towards the other side of the pump, and are thereby removed from the system, reducing the system pressure. Since the gas is transferred to the other side of the pump, a separate pump known as the backing pump must be attached at the outlet to prevent build-up of the evacuated gas load. To avoid contamination, a UHV compatible, magnetically levitated turbopump, which uses magnetic fields to operate the pump without any mechanical parts that require lubricants, is needed. Similarly, an oil free diaphragm pump is used as a backing pump.

To select a turbopump for the Perkin-Elmer 430 system for ZnO growth, the pumping speed S_p required was calculated using [94]:

$$S_p = Q / P \tag{2.1}$$

where Q is the throughput of the system and P is the inlet pressure to the pump, which in this case is the base pressure required. The throughput is the amount of gas per unit time entering the chamber with a conductance C. The conductance is given by [94]

$$C = \frac{AD}{3L}\sqrt{\frac{3RT}{\pi M}} = \frac{D^3\pi}{12L}c \tag{2.2}$$

where R is the ideal gas constant, T is the gas temperature, M is the molecular mass of the gas, c is the speed of the gas particles, and A, D and L are the area, diameter and length of the connection between the chamber and the pump, respectively. Taking the ideal gas constant to be 8.31447 $JK^{-1}mol^{-1}$, the velocity of oxygen at room temperature is calculated to be 683.877 ms^{-1}. For the Perkin-Elmer system, the turbopump is connected to the chamber via a port and extension tube that can be approximated by a cylindrical tube 27.25 cm in diameter and 40.3 cm in length. This gives a conductance of 8945 l/s. With an anticipated gas load of oxygen at a flow rate

of approximately 1.0 sccm (which means Q = 0.01265 Torr-Litre/s as 1 Torr-Litre/s = 79 sccm), and a target process pressure of 1×10^{-5} Torr (i.e. P = 1×10^{-5} Torr), the effective pumping speed required can be calculated to be 1265 l/s. The effective pumping speed is related to the actual pumping speed by [94]:

$$\frac{1}{S_{eff}} = \frac{1}{S_{pump}} + \frac{1}{C} \tag{2.3}$$

giving S_{pump} = 1537 L/s. For a cost-effective solution, the closest matched turbopump, the TMU 1600M from Pfeiffer (1400 l/s), was chosen. This pump has proven to be sufficient for the growth of ZnO in the Perkin-Elmer 430 system; in actual use, a process pressure of $\sim1\times10^{-5}$ Torr for a flow rate of 1 sccm is routinely obtained.

2.2.2 Zn Sources

The most common means of providing elemental metallic flux in MBE is by using effusion cells, where inert and thermally stable crucibles (such as pyrolytic boron nitride, or pBN) are heated in the range of 200 ºC to 1200 °C, although higher temperatures are possible with specialised designs. A typical effusion cell is shown in Figure 2.3.

The performance of effusion cells can be described by the Knudsen evaporation model. The general evaporation process is governed by the Hertz-Knudsen equation [51], which describes the evaporation rate:

$$\frac{dN_e}{A_e dt} = a_v(p_{eq} - p)\sqrt{\frac{N_A}{2\pi M k_B T}} \tag{2.4}$$

where dN_e = number of atoms evaporated; A_e = evaporation area; a_v = evaporation coefficient, which accounts for atoms reflecting from the evaporation surface; M is

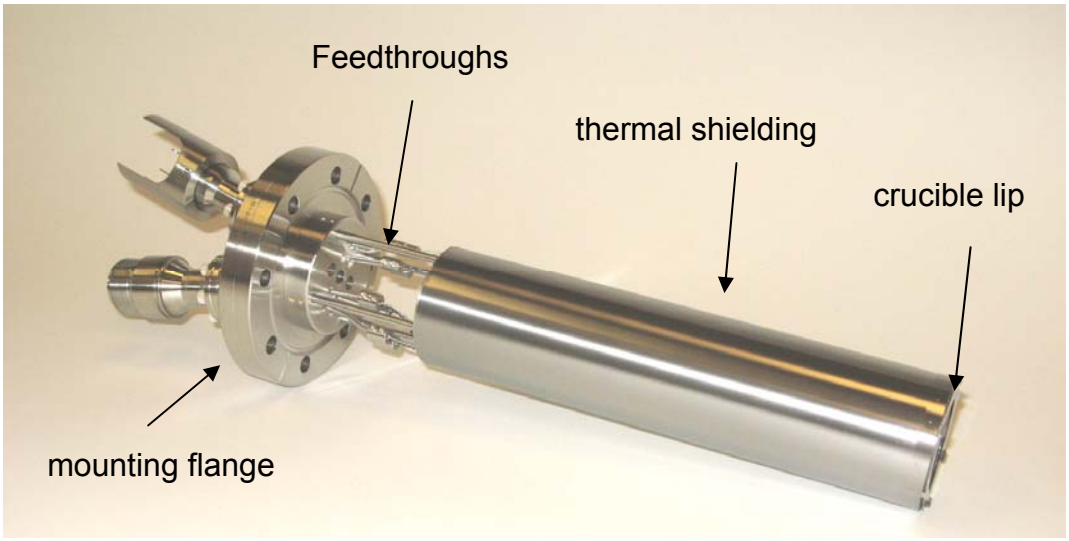

Figure 2.3 A typical effusion cell (From E-Science).

the molecular mass of the evaporant, p_{eq} = equilibrium pressure; and p = pressure exerted on the surface by surrounding atmosphere contributing to a return flux. All the other symbols have their usual meaning.

This equation was first formulated by Hertz, and was improved by Knudsen in 1915 [95] by inserting a_v to account for the observed discrepancy between experimental observations and theory. While this equation was originally derived for the evaporation from a free, unconstrained liquid surface, Langmuir showed that the equation can also be applied to evaporation or sublimation from solid surfaces [96]. Knudsen then further showed that if the evaporation was carried out in an isothermal enclosure with an orifice diameter much smaller than the mean free path of the evaporant at the equilibrium pressure, and assuming an infinitesimally thin orifice wall, then the Knudsen-Hertz equation can still be applied [97]. In that case, the orifice becomes the effective evaporation surface with a_v = 1 due to the lack of interaction between the orifice wall and the gas atoms [97], i.e.

$$\Gamma_e = \frac{dN_e}{dt} = A_e(p_{eq} - p)\sqrt{\frac{N_A}{2\pi M k_B T}} \tag{2.5}$$

where Γ_e is known as the evaporation flux and has units of molecules per second, and A_e is now the area of the orifice.

This Knudsen effusion equation theoretically describes the evaporation rate for a given material at a given temperature. It represents the total amount of atoms per second that escape from the effusion cell. If a substrate is placed at a distance r_A perpendicular to the effusion cell, then each point on the substrate would only receive a small portion of these atoms. It can be shown geometrically [51] that the flux received at a particular point away from the effusion cell is governed by the cosine law of effusion:

$$d\Gamma_\theta = \frac{\Gamma_e}{\pi} cos\,\theta \; d\omega \tag{2.6}$$

where $d\Gamma_\theta$ is the flux swept by atoms travelling on an angle between θ and $d\theta$, and ω is the solid angle which is the area of a circular spot on the sphere swept by the angle θ and $\theta + d\theta$. By combining the Knudsen equation and the cosine law, it can be shown that the impingement rate (or atomic flux per unit area) at a point directly on the axis of the orifice is given by:

$$I_A = \frac{d\Gamma}{dS} = \frac{\Gamma_e}{\pi \cdot r_A{}^2} = \frac{A_e}{\pi \cdot r_A{}^2}(p_{eq} - p)\sqrt{\frac{N_A}{2\pi M k_B T}} \tag{2.7}$$

and for a point deviated from the orifice axis by an angle θ but still on the plane perpendicular to the cell, the deviated flux I_B is given by:

$$I_B = I_A \cos^4 \theta \tag{2.8}$$

where the $\cos^4\theta$ term is the result of the difference in distance and therefore the coverage area at different angles. According to Equation 2.8, the flux across a 75 mm diameter substrate holder placed perpendicularly to the cell at a distance of 20 cm would decrease radially with increasing distance from the centre, as shown in Figure 2.4. It is clear that a small piece of substrate mounted at the centre as shown would experience an essentially uniform flux across the whole substrate with a maximum deviation of around 2% depending on the position of the substrate.

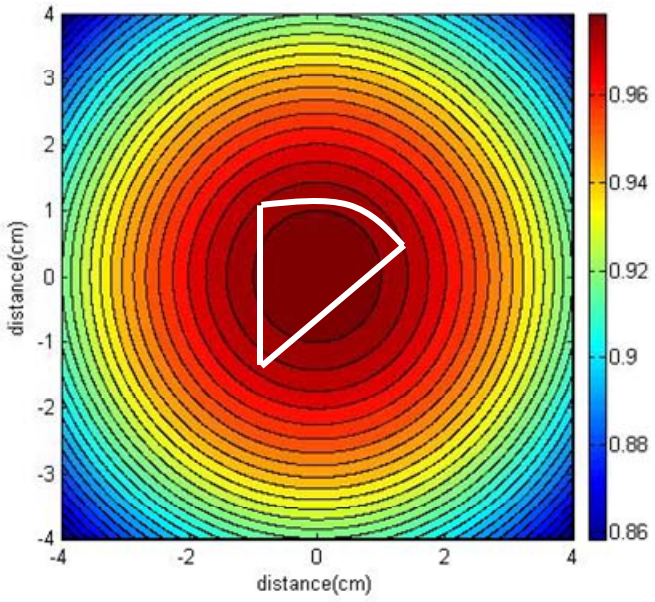

Figure 2.4 Angular distribution of Zn flux for an ideal Knudsen cell approximation of the Perkin-Elmer style 60 cc conical cell, with an orifice diameter of 4.5 cm and a distance of 20 cm perpendicular from the centre of the 75 mm substrate mounting block. A typical sized portion of a 50 mm diameter sapphire substrate is shown in white.

This distribution assumes that the cell axis is perpendicular to the substrate surface. In reality this is never the case. For example, in the Perkin-Elmer 430 system, while the perpendicular distance (along the "z-axis") between the substrate and the source flange (a flange parallel to the substrate where the effusion cells are installed) is 20 cm, the actual Zn cell is placed on the perimeter of the source flange, pointing to the substrate at an angle. This will affect the angular distribution of the Zn flux and hence the actual impingement rate on the substrate by changing the actual distance between the source and the substrate as well as the impingement angle. It can be shown that in the case of off-axis effusion cells, the cosine law still applies [51], where the impingement rate on the substrate is now given by:

$$I_{B}^{'} = I_{A} \frac{r_A}{r_B} \cos\theta \cos(\theta + \phi) \qquad (2.9)$$

with ϕ as the off-axis angle, r_A is the distance from the source to the centre of the substrate and r_B is distance from the cell to a particular point on the substrate. As Equation 2.9 is based on a 2-D geometry, applying it to a 3-D situation requires the actual values of r_A, r_B and ϕ to be calculated from the distance from the centre of the

substrate to the source flange (20 cm), and the position of the source on the flange (30º from the source flange - substrate axis and 30º from the horizontal axis) via geometric arguments (see Appendix A). Figure 2.5 shows the distribution of flux for the same area as Figure 2.4 given by an off-axis Zn source following the geometry of the Perkin-Elmer 430 system. The flux is now concentrated on the corner closest to the source, and for a substrate placed at the centre, the Zn flux deviation is now $\sim \pm 10\%$. Note that the uniformity can be improved with a greater distance from the cell, and of course, smaller angles from the centre axis.

Note that a conical effusion cell, which is a common type of effusion cell for MBE growth, is in reality far from an ideal cell. However, it is expected that with the large opening of the conical cell, the evaporation approaches a free surface evaporation without orifice interactions, and therefore can be sufficiently approximated by the ideal Knudsen model for the purpose of this thesis. The actual flux, especially the distribution, would be different from the theory due to less collimation from a large opening as well as the non-equilibrium condition of an open cell.

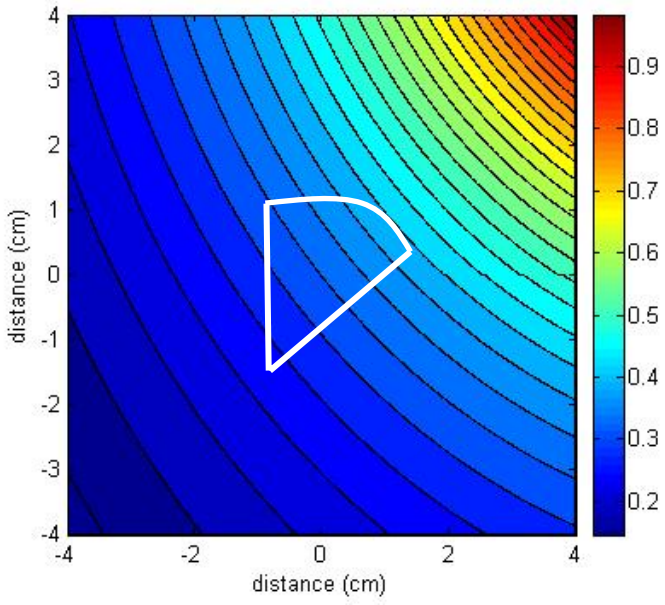

Figure 2.5 Angular distribution of an ideal cell under the same condition as in Figure 2.4 but 30º off axis and 30º off centre from the substrate. The Zn cell is assumed to be perpendicular to the point (5,5).

Figure 2.6 shows the theoretical flux as predicted by the Equation 2.7 for an off-axis cell 23.7 cm away from the substrate (see Appendix A), using an orifice

diameter of 3.75 cm, corresponding to the evaporation surface of a half full 60 cc conical crucible (Zn vapour pressures were taken from [98]). To grow ZnO with a growth rate of 1 Å/s (a typical growth rate for MBE growth), the minimum Zn flux needed to provide sufficient Zn atoms is 1.82×10^{14} atoms/cm^2·s, assuming every Zn atom that reaches the substrate reacts (i.e. a unity sticking coefficient). Therefore, the ideal Knudsen cell equation predicts that a Zn cell temperature of ~275 °C is needed. In reality, a typical cell temperature of around 300 °C - 350 ºC was required for a ~ 1 Å/s growth rate.

Even though the conical crucible had successfully been used for Ga, In, and many other metals in the other growth chamber of the same MBE system, it was found that for the growth of ZnO, a conical crucible experiences a major problem - namely, the oxidation of the Zn source. While unreported in the literature, this oxidation seems to be a common problem for ZnO growers [99]. It was observed over time that intermittently the Zn flux could decrease very rapidly after oxygen was introduced into the system. No such problem was observed with Mg loaded into an identical crucible and effusion cell. It is now believed that the high vapour pressure of Zn combined with the reactivity of oxygen plasma species have caused this problem that has not been observed in other material systems. In particular, the high vapour pressure of Zn leads to a high concentration of Zn vapour in the effusion cell, which forms ZnO particles with the oxygen present in the cell, consuming the Zn source.

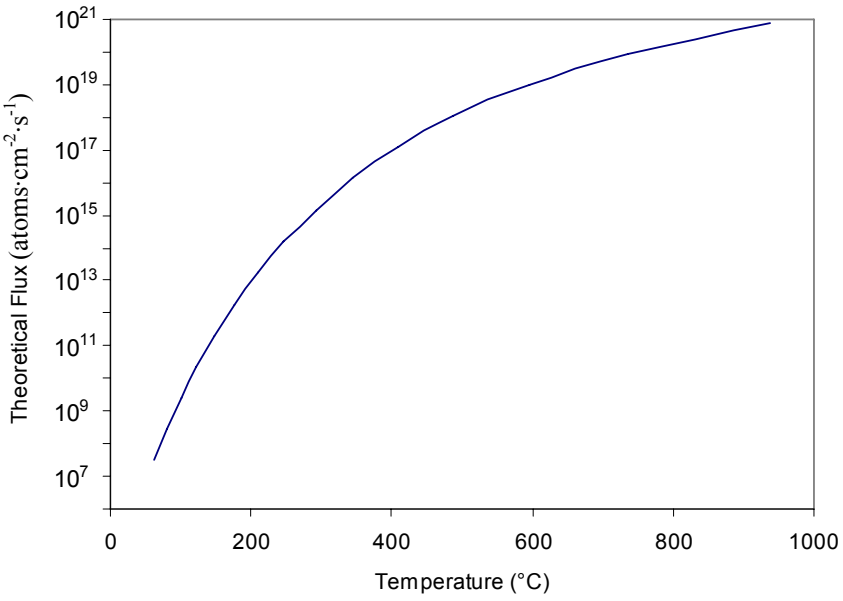

Figure 2.6 Theoretical Zn flux verses temperature as calculated from the ideal Knudsen equation for the 60 cc conical crucible.

After discussion with other research groups involved in the MBE growth of ZnO, it became apparent that the best solution was a dual heating zone design in combination with a small aperture to minimise oxygen coming into contact with the Zn surface. This dual zone cell, manufactured by e-Science, was installed in 2006. The dual zone cell uses an 80 cc cylindrical crucible, with a 5 mm thick pBN capping plate having a 1 mm diameter aperture at the centre. This results in an effusion cell that is much closer to the ideal Knudsen cell than the open-mouth conical crucible design. In fact, it can be modelled as a near-ideal cylindrical effusion cell, given that the orifice diameter is much smaller than the diameter of the cell.

Clausing [100] investigated the theoretical modelling of near-ideal cylindrical effusion cells, where atoms hitting the orifice wall were assumed to randomly reflect back into the effusion cell. According to this model, the ideal Knudsen equation would need to be multiplied by a correction factor known as the Clausing transmission factor, W_a, that is dependent on the dimension and the geometry of the orifice. Motzfeldt [101] further modified the Clausing model by taking into account the interaction between the atoms and the effusion cell wall and considering the cell as another orifice with a Clausing factor W_b, as shown in Figure 2.7. Thus, the flux of the cell can be described by,

$$\Gamma_e = \frac{A_e(p_{eq} - p)W_a}{1 + f(\alpha^{-1} + W_b^{-1} - 2)}\sqrt{\frac{N_A}{2\pi M k_B T}} \tag{2.10}$$

where $f = W_a \cdot a/b$ is the escape coefficient (a and b are the cross-sectional area of the cell and the orifice, respectively), and α is the gas condensation coefficient.

To evaluate the impingement flux from near-ideal cylindrical cell, the cosine law must also be modified, due to the interaction between the orifice wall and the atoms as they exit the orifice. In particular, the flux coming out at a particular angle θ is the sum of the flux that escaped in that direction, plus atoms that escape in that direction after being randomly reflected off the orifice wall. It was shown by Dayton [102] that:

$$d\Gamma_\theta = \frac{w_1}{4}\cos\theta \, d\omega \, d_0^2 C_o \tag{2.11}$$

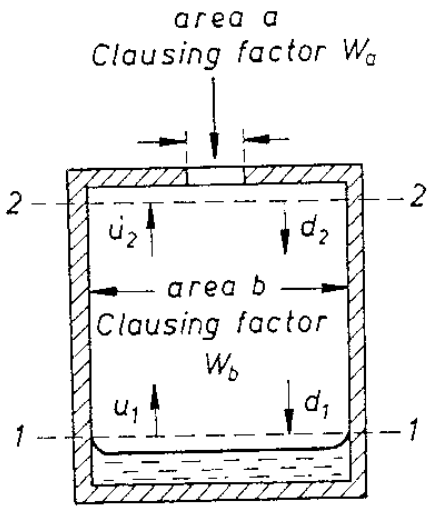

Figure 2.7 The Clausing-Motzfeldt model of a near ideal cylindrical effusion cell. Parameters u and d represent the upward pressure and downward pressure exerted on plane 1 (above the evaporation surface) and plane 2 (below the orifice) by molecules evaporating from the surface and reflections of these molecules by the cell (from Herman [51]).

where w_1 = flux per unit area that is escaping from the orifice (i.e. Γ_e/A_e), and C_0 is the correction factor dependent on the dimension of the orifice as well the escape angle (See Appendix A). The same geometric argument as the ideal case can then be applied to give

$$I_A = \frac{d\Gamma}{dS} = \frac{\Gamma_e d_0^{\,2} C_0(0)}{A_e 4 r_A}(p_{eq} - p)\sqrt{\frac{N_A}{2\pi M k_B T}} \tag{2.12}$$

and

$$I_B = I_A \cos^4\theta \frac{C_0(\theta)}{C_0(0)} \tag{2.13}$$

for a substrate perpendicular to the orifice.

Ignoring the off-axis position of a typical effusion cell momentarily, the flux distribution plot for a substrate 20 cm away for such a setup is shown in Figure 2.8, with parameters outlined in Appendix A. It can be seen that the flux variation across the substrate is around 10%, higher than the ideal case. Note that the distribution depends on the ratio between the orifice thickness and the orifice diameter

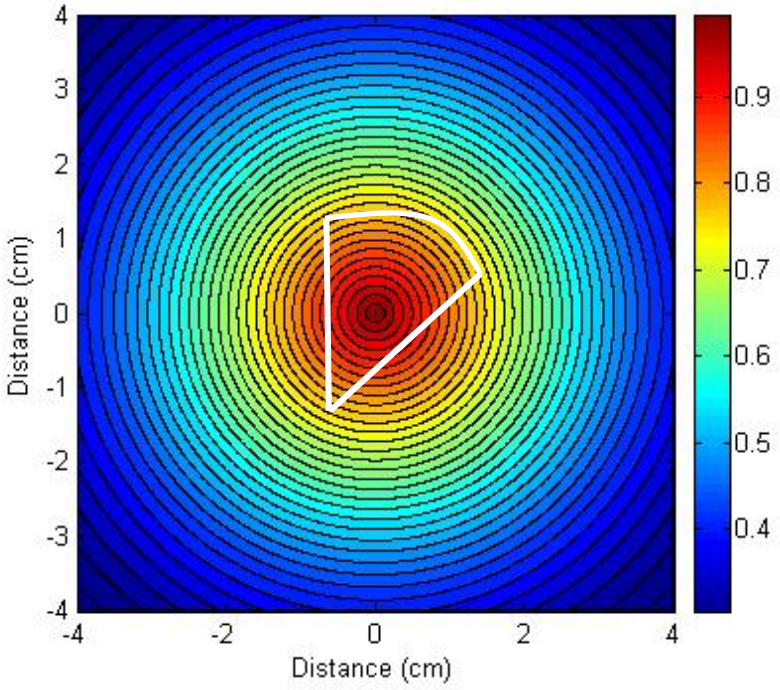

Figure 2.8 Flux distribution for dual-zone cell predicted by the near-ideal cylindrical cell model, for an orifice diameter of 1 mm, orifice thickness of 5 mm, and a substrate placed 20 cm perpendicularly from the cell orifice.

L_0/D_0. In particular, as $D_0 \rightarrow \infty$ or $L_0 \rightarrow 0$, the ratio L_0/D_0 becomes 0, and the ideal Knudsen equation applies. Therefore, it is expected that with a fixed orifice diameter, the uniformity would improve with decreasing orifice thickness. Considering that the orifice size must be small enough to remedy the oxidation problem, the plate must be made as thin as mechanical robustness allows, to ensure the best uniformity.

The flux distribution for a cylindrical cell in the Perkin-Elmer 430 setup, taking into account the off-axis geometry, is shown in Figure 2.9. Again, the uniformity of the Zn distribution further decreases to a deviation of $\sim \pm 15\%$ at the centre. This deviation is not that different from what was calculated for an off-axis ideal effusion cell in the same system geometry.

Figure 2.10 shows the theoretical flux as a function of temperature for the modified Zn cell at the centre of the substrate holder, compared to the typical conical cell. It can be seen that because the flux has been reduced by the small aperture, a much higher temperature is needed to achieve the same flux. In particular, it can be seen from the graph that the Zn needs to be heated above its melting point of 429 °C just to obtain the theoretical minimum flux of 1.82×10^{14} atoms/cm^2·s for a 1 Å/s growth rate. A typical temperature used for the new Zn cell is ~ 450 - 500 ºC.

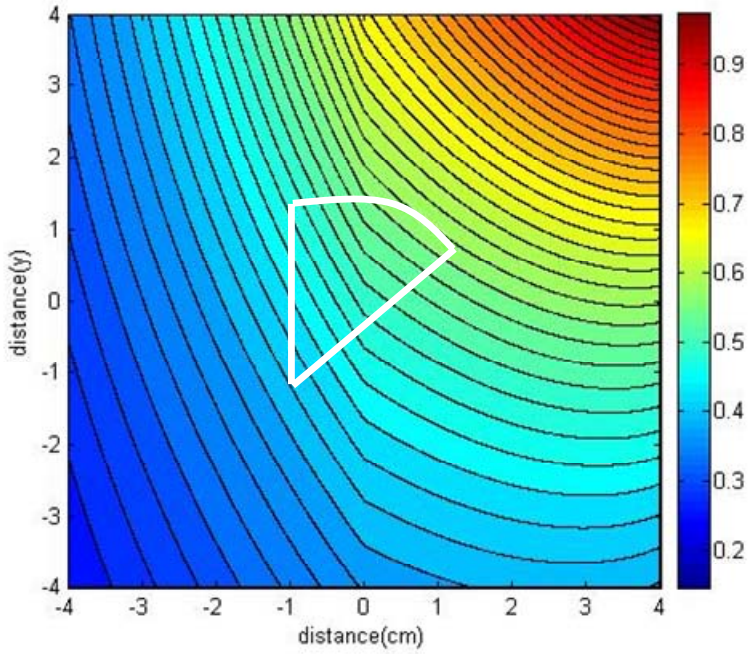

Figure 2.9 Flux distribution predicted by the modified cosine law of diffusion for a near ideal cylindrical cell placed 30° off axis and 30° off centre from the substrate.

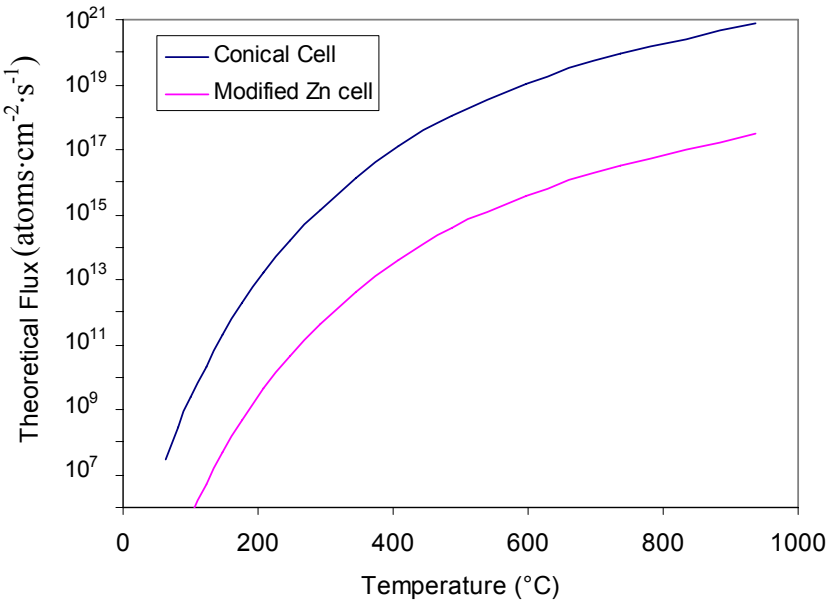

Figure 2.10 Theoretical Zn flux versus temperature for the 60 cc conical crucible (modelled by the ideal Knudsen equation), compared with the dual zone cell with 80 cc cylindrical crucible (modelled by the Clausing-Motzfeldt model).

While theoretical prediction serves as a good guideline for what to expect from a particular Zn cell, experimental determination of the actual Zn flux is essential for reproducing the same flux on a daily basis. Different variables such as thermal oscillations, Zn depletion, and Zn oxidation inevitably change the actual Zn flux even if the temperature reading from the thermocouple is constant. One method of measuring the Zn flux in-situ is by using a water-cooled quartz crystal microbalance (QCM). In this method, a piezoelectric crystal is placed in the position where the deposition normally takes place, and the Zn atoms are thereby condensed onto the crystal. The increase in the mass of the crystal composite changes the resonant frequency of the crystal, and therefore by measuring the change in resonant frequency over time, the rate of arrival of Zn atoms can be deduced.

It was shown by Lu that by taking into account the difference between the piezoelectric properties of the quartz crystal and the deposited material, the deposited thickness can be calculated by [103]:

$$t_t = \frac{\rho_q t_q f_q}{Z f_c \rho_t \pi} tan^{-1}\{ Z\, tan\left[\frac{\pi(f_q - f_c)}{f_q}\right]\} \qquad (2.14)$$

where ρ_q and ρ_t are the density of quartz and the deposited material respectively, fq and f_c are the before and after resonance frequencies, respectively, and Z is the tooling factor which is dependent on the density and the shear wave velocity of the material. From this, the atomic flux over a time s can be calculated by assigning $N_q = f_q t_q$:

$$\Gamma_t = \frac{\rho_q N_q N_A}{s Z f_c m_t \pi} tan^{-1}\{ Z\, tan\left[\frac{\pi \Delta f}{f_q}\right]\} \qquad (2.15)$$

where Δf is the frequency difference measured from the crystal reading, m_t is the mass of the thin film and N_q is known as the crystal constant, equal to 166800 cm·s^{-1} for quartz crystals.

Equation 2.15 suggests that for a particular flux, a constant Δf with time will be observed for a given effusion cell temperature. Unfortunately, the crystal monitor readings for Zn at a particular temperature are rarely constant, even within a single trial. There are a number of factors that cause this variation in crystal reading such as

shutter transients, crystal heating, or simply noise originating from small fluctuations in the Zn flux. Therefore, as a common practice, the Zn flux is determined by taking the average of a number of Δf readings measured at 5 s intervals after the Zn is at the desired temperature (typically 1 h) for a sufficient time period for the flux to stabilise.

However, the number of readings taken in the averaging process is usually at the discretion of the operator. This, of course, is not very satisfying statistically, and since the QCM is essential for confirming the day to day reproducibility for different experiments, it is worthwhile to investigate how to interpret these readings to map out the true experimental flux from the effusion cell. To investigate the statistical behaviour of Δf, the experimental data from 107 experiments were used. For each experiment, a number of Δf values were taken. To compare between experiments, these Δf readings were normalised to the median value of each particular experiment (giving a median value of 1), and the normalised reading at each time interval was then averaged over all of the experiments.

Figure 2.11 shows these mean normalised crystal readings as a function of time for the dual zone Zn cell, with each red error bar representing the region within 1 standard deviation of the mean. It can be seen that the measured value increases rapidly for the first 10 s and then starts to saturate and become almost constant after

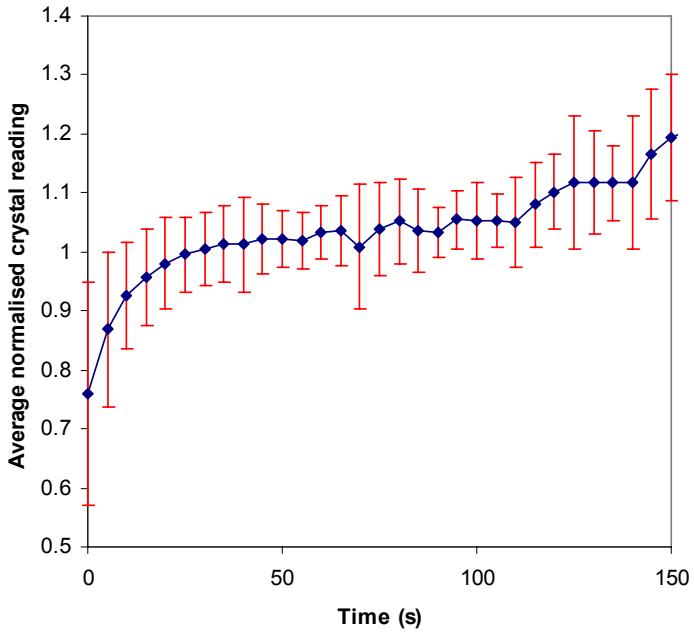

Figure 2.11 The crystal readings over time normalised with the median for each experiment and averaged over 107 Zn flux readings. It can be seen that the data from the first 25 s and after 90 s are not a representative measure of the flux.

25 - 30 s. This constant frequency change is sustained until after about 20 readings, corresponding to approximately 100 s, above which the measured Δf increases in a superlinear fashion. As the Zn cell temperature was stabilised prior to the experiment, it is clear that these apparent variations in the measurement originated from the behaviour of the crystal rather than a real variation in the Zn flux. In particular, as the measurement commences with the lowering of the QCM followed immediately by the opening of the QCM shutter, the initial climb in the measured frequency change is possibly related to the transient effect of the crystal vibration, shutter opening and other initial effects. The superlinear increase of Δf after 100 s can be readily explained by the heating of the crystal. It is well known that the oscillation frequency of quartz crystals is affected by the temperature [104, 105]. In particular, for typical AT-cut quartz crystals used in QCM, it was found that the Δf is related to the temperature in a cubic relation [106, 107], with an increase of frequency with temperature expected for temperatures greater than ~ 90 ºC [107]. As the Zn cell is usually above 350 °C, it is very plausible that radiative heating causes the crystal to heat up over a long period of time, resulting in the superlinear increase in the observed frequency change. From these, it can be seen that meaningful data can only be extracted from the QCM measurement between the 25 and 90 s time frame.

The experimentally measured flux for a range of temperatures, analysed using the rule deduced from Figure 2.11, is plotted for the two cell designs in Figure 2.12 and Figure 2.13, respectively. Note that the flux has been calibrated with the thickness measurements to account for the difference between the position of the crystal monitor and the substrate. It can be seen that the theoretical curves and the data share essentially the same shape for both cell designs. Even though there is an offset, this matching shape means that the Zn flux estimation from theoretical predictions will be perfectly reliable as long as an experimental measurement is used as a starting point. For the conical cell, it can be seen that the measured fluxes are always less than the predicted flux. This can be attributed to the large orifice of the cell which gives a more diffused molecular beam, resulting in a smaller flux received by each point on the substrate. For the modified dual zone cell, the difference between the experimental and the calculated flux is reduced, suggesting that the capped cylindrical crucible can be described very nicely by the near-ideal model. In particular, the relatively small

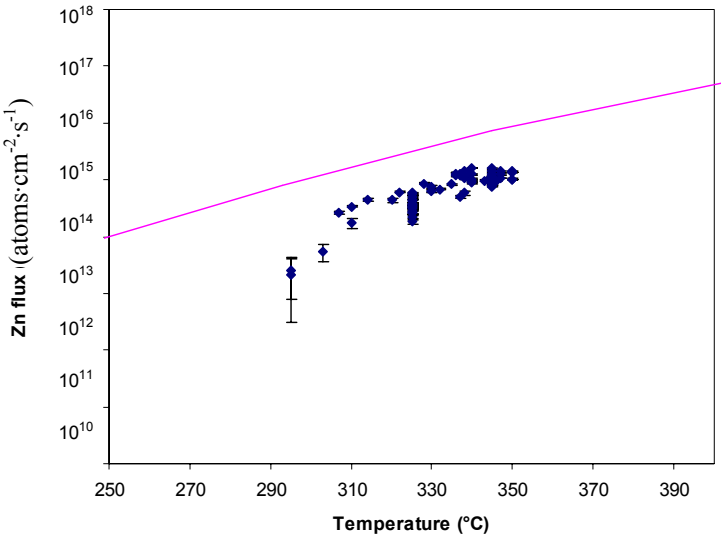

Figure 2.12 The Zn flux measurements for the 60 cc conical cell as measured from crystal monitor readings, compared to the theoretical model (pink curve). The error bars represent 1 standard deviation from the mean.

differences observed can be adequately explained by experimental uncertainties such as the difference between real temperature and the thermocouple readings, as well as the accuracy of different parameters such as the dimensions and the Clausing factor. Practically, the theoretical prediction for the new cell is sufficient for everyday use, in that the flux curve can be readily used to predict the cell temperature required for different experiments.

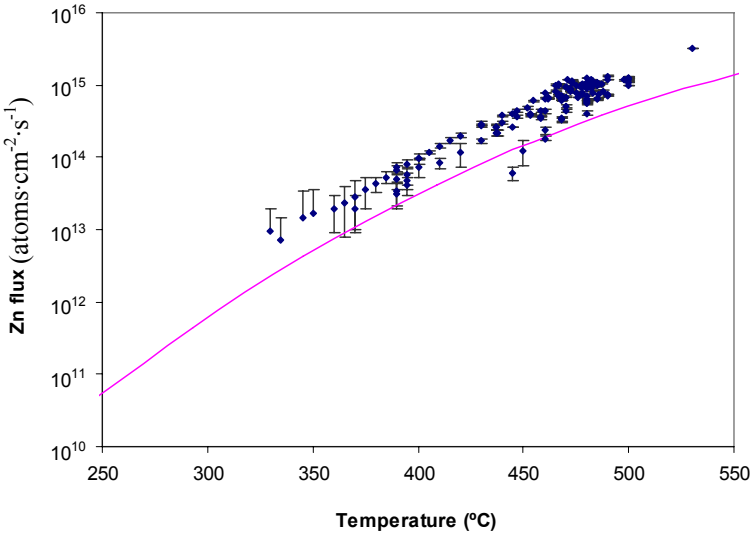

Figure 2.13 The Zn flux measurements for the dual zone cell as measured from crystal monitor readings, compared to the theoretical model (pink curve). The error bars represent 1 standard deviation from the mean.

2.2.3 Active Oxygen

The problem of introducing active oxygen in MBE dates back to the late 1980s, when several groups reported the use of MBE to grow copper-containing superconducting oxides. Prior to this it was realised that even with simple methods such as sputtering [108], oxygen gas was not sufficiently active to efficiently oxidise copper, necessitating high oxygen pressures to obtain superconducting films. In order to incorporate the advantages of MBE growth into superconductor fabrication and avoid high process pressures, Spah et al. [109] and other groups in the same period suggested the use of an atomic oxygen source to enhance the oxidation of the copper atoms. It was found that in general, the increase in atomic oxygen content provided during growth could be correlated with the lowered resistivity of the deposited films.

Other oxygen sources have also been considered. In particular, the use of atomic oxygen O [110], ionic oxygen O^+ [111], O_3 [112] and NO_2 [113] for oxide growth are discussed in the literature. Schlom and Harris [114] collected data from a number of reports on the use of these species for copper oxide growth, and compared their oxidation ability in terms of the growth temperature and the oxidant pressure required (see Figure 2.14). They found that in general, atomic oxygen required the lowest oxidant pressure for growth at a low temperature. Hence atomic oxygen can be regarded as the most beneficial active oxygen species for superconducting oxide growth. For ZnO, it has long been considered that the same logic can be applied. While there were attempts to grow ZnO with other oxidants such as NO_2 [115], ozone [116], and H_2O_2 [117], oxygen plasma sources, which are efficient at producing atomic oxygen, remain the dominant means of ZnO growth by MBE.

However, recent studies on the growth of GaN have cast doubts on the assumption regarding atomic oxygen. In particular, while it was believed for a long time that the growth of GaN needs an abundant supply of atomic nitrogen, VanMil et al. recently found that by optimising the content of metastable molecular nitrogen N_2^* instead of atomic nitrogen N as the primary growth species, the onset of the decrease in GaN growth rate with temperature associated with thermal dissociation can be delayed, suggesting that N_2^* plays an important role in growth [118]. This leads to the question of whether atomic oxygen is the only important species for ZnO growth, or

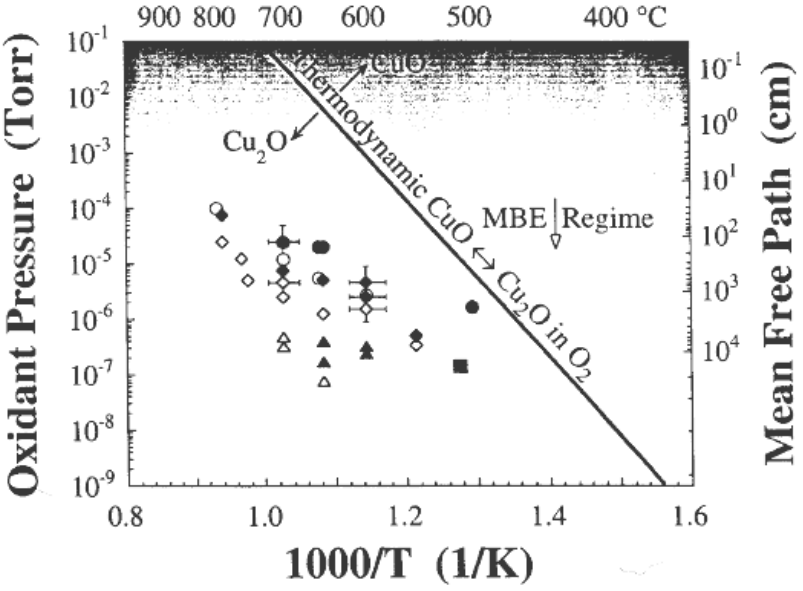

Figure 2.14 The evaluation of the oxidation ability by the formation of CuO and Cu_2O for atomic oxygen (triangles), O^+ (squares), ozone (diamonds) and NO_2 (circles) and molecular oxygen (straight line). The formation of CuO (solid points) and Cu_2O (hollow points) below the thermodynamic line implies an improvement in oxidation ability. Atomic oxygen requires the least pressure to obtain oxidation (From Schlom and Harris [114]).

other active oxygen species have a role in growth as well.

At the University of Canterbury, an inductively coupled plasma source from Oxford Applied Research, model MDP21, is used, with the original pBN plasma chamber components being replaced in-house with alumina equivalents. Figure 2.15 shows the schematic of an inductively coupled plasma source essentially identical to the MDP21 [119]. It operates by using an RF power supply to generate an ac current in the RF coil. This ac current creates a time-varying magnetic field inside the discharge tube, where the oxygen is kept at a relatively high pressure by the continuous in-flow of oxygen from the gas feed and the limited out-flow restricted by the beam exit plate. Under such RF fields, electrons and ions with high kinetic energy are formed through collisions of other charged particles present in the discharge. While some of these charged species recombine to form neutral (possibly excited) species, most of these charged species would go into collision with other particles creating an avalanche of charged species. Only when the pressure is sufficiently high that the generation rate and recombination rate of these charged species would reach equilibrium, leading to a stable plasma. The plasma species, which include both charged and atomic species, as well as neutral molecules, escape the beam exit plate and are directed towards the substrate to participate in growth. Note that many plasma

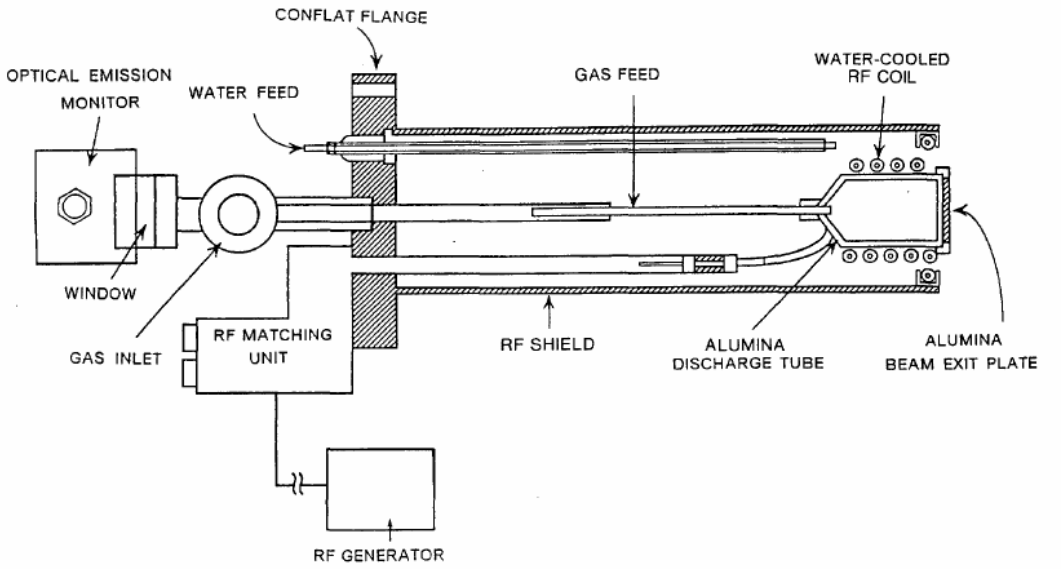

Figure 2.15 Schematic of one of the first inductively coupled plasma sources built for MBE (From Locquet et al. [119]).

sources have ion deflection plates installed at the beam exit plate to remove any ions generated from the plasma. The MDP21 does *not* have ion deflection plates, and therefore all of the oxygen species generated by the plasma were used for growth in this study.

Within limits, the relative amount of the various active oxygen species generated by a particular plasma source can be tuned. In particular, based on numerous studies of the relationship between GaN growth and plasma settings for similar types of plasma source [118, 120], it is expected that the oxygen species production can be optimised for ZnO growth by selecting an appropriate combination of RF power and oxygen flow rate, as well as through aperture plate geometry. The effect of the RF power is easy to envision: increasing the power supplied to the plasma results in more collisions, and hence more splitting of the oxygen molecules and increasing the atomic and ion content.

Ptak et al. offered the suggestion that the interaction between the plasma species and the side walls of the orifices can profoundly affect the ratio of N_2* to N emitted from the source [120]. They reasoned that by increasing the number of holes in the aperture plate while maintaining the same total aperture area accomplished by reducing the hole diameter, the aperture sidewall area is increased. This results in an increase in sidewall interaction, introducing extra collisions and reactions that leads to extra generation of metastable nitrogen N_2^* and also the reduction of ion energy.

O'Keeffe et al. [121] have studied the effect of exit aperture size in nitrogen ECR plasmas, and found that increasing the aperture diameter resulted in an increase in the relative ionic content (N_2^+/N_2^*), which they attributed to a decrease in pressure inside the discharge tube due to the larger exhaust velocity of the plasma from a large hole.

For an oxygen plasma, there are a limited number of studies on the effect of aperture interactions. One study on a microwave plasma source measured a smaller atomic oxygen density but a higher overall flux with a larger size orifice [122], which they attributed to the decrease in the sharpness of the atomic beam due to the defocusing effect of a large orifice. However, since the reported conductances of the small and large orifice designs were different, the applicability of this result is limited.

Thus, it is reasonable to surmise that the variation of applied RF power and aperture plate geometry might be utilised to tune the plasma to generate the optimal combination of oxygen species for growth. In particular, based on the study on nitrogen plasma [120], it is expected that for a constant conductance, an aperture plate with a large number of small holes should produce more molecular species with less ionic content, whereas for an aperture plate with a smaller number of large holes, a higher atomic flux with a larger ionic content should be generated. To investigate the effect of altered oxygen content on ZnO growth, two custom aperture plates — a 25 hole plate and a 1 hole plate — were manufactured such that the total orifice area or conductance of each was essentially identical to that of the default 276 hole plate which had 0.2 mm diameter holes. The dimensions of the plates are given in Table 2.

The effects of RF power and aperture plate variations on the active oxygen content were primarily characterised using optical emission spectroscopy, which is made possible by a window on the back of the plasma source directly opposite the aperture plate. In optical emission spectroscopy (OES), the optical emission of the plasma is analysed. This constrains the measurement to the observations of the excited states that are optically active. In particular, the integrated emission

Table 2: Specification of the aperture plates used in this study.

Configuration	Hole diameter (mm)	Sidewall area (mm^2)	Conductance (mm^2)
276 hole	0.20	216.7	8.67
25 hole	0.66	64.8	8.55
1 hole	3.30	12.9	8.55

intensity of a particular species x is given by [123]:

$$I_x = C_d(\lambda) n_{gx} n_e K_x Q_x b_{\lambda x} \qquad (2.16)$$

where C_d is the detector response, dependent on the wavelength range of the emission; n_{gx} is the density of ground state species, n_e is the electron density, K_x is the electron excitation rate from the ground state to the observed state, Q_x is the quantum yield of the photon emission, and $b_{\lambda x}$ is the emission branching ratio, i.e. the proportion of the species that emits through a particular emission peak or band. Therefore, the observation of the emission spectrum of the oxygen plasma provides information on the composition of the plasma, in terms of the density of different oxygen species present during growth.

To characterise the oxygen plasma generated by the MDP21 plasma source with different conditions using OES, a Jobin Yvon CCD-3000 spectrometer was used. An optical detector was placed at the back of the plasma source and connected via an optical fibre cable to the CCD, which was cooled to liquid nitrogen temperature to minimise thermal noise. The acquired optical spectra were then calibrated to the known positions of the O^* emission peaks [124] as well as to mercury emission lines at various positions [125].

Figure 2.16 shows the typical full emission spectrum of an oxygen plasma generated by the MDP21 from 250 nm to 950 nm. It can be seen that the plasma spectrum was dominated by the 777 nm triplet that corresponds to the $3p^5P$ atomic oxygen state [124]. This gives the plasma a predominantly pink colour. Because of its large electronegativity, oxygen can exist in a large number of excited states. In fact, a large number of reactions involving excited states and charged states of atomic and molecular oxygen are expected to occur in an oxygen plasma [128]. This is evident in the rich spectrum observed by OES. For example, a number of spectrum lines can be observed through out the scan range (eg at 533 nm), suggesting the presence of atomic oxygen of different states in the plasma. A band with triple peaks was also observed in the In the 330 - 366 nm range, corresponding to the Herzberg excited states of molecular oxygen [126]. The 1^{st} positive series of O_2^{+*} was observed in the the 500 - 536 nm range, and under certain conditions, traces of the atomic oxygen ions O^{+*} were also detected at different energies.

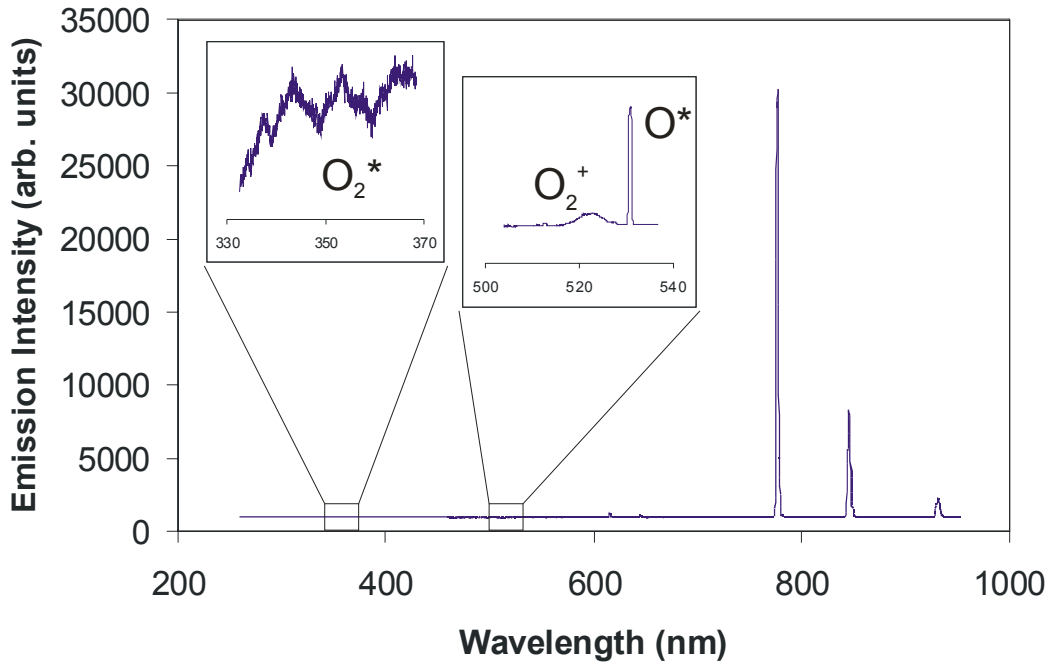

Figure 2.16 The full emission spectrum of an oxygen plasma generated with the MDP21 plasma source, showing the dominance of O^* emission. Much weaker emission for O_2^+ and O_2^* were also observed.

A clear indentification of all the excited states presented in the plasma, determination of their density, energy and their effects on growth is very difficult. That is because not all excited states or charged states can be observed optically. Even states that recombine optically can have different recombination rates which would affect the emission intensity. The lack of advance plasma diagnosis tools also prevents the determination of electron temperature and electron density, which is very important in determining the density of different plasma species. Further, some ground state species such as neutral atomic oxygen are expected to participate strongly in growth, which cannot be directly analysed with OES. From this, it can be seen that an oxygen plasma is a complex system where the full analysis falls outside of the scope of this thesis. In this thesis, a crude simplication is made where the different excited states are grouped into the four most obvious types: atomic oxygen O^*, molecular oxygen O_2^*, molecular ions O_2^{+*} and atomic ions O^{+*}, and the effect of each type of excited species is considered as a whole. It is also assumed that the density of ground state species is directly proportional to the excited state species observed from the OES.

To compare the variation of specific oxygen species in the plasma with varying RF power, the integrated emission intensity of each oxygen species (I_{533nm} for O^* 533 nm, I_{350nm} for O_2^* and I_{525nm} for O_2^{+*}. O^{+*} was omitted as the optical emission from atomic ions are rarely visible.) were normalised using I_{max}, the maximum intensity observed for that particular species for each aperture plate. Since data obtained from each aperture plate was obtained from one continuous experiment from the same wavelength range, $C_d(\lambda)$ and $b_{\lambda x}$ are constant. As Q_x is approximately equal to unity [123], the normalised intensity is equal to:

$$I_{normalised} = \frac{I}{I_{\max}} = \frac{n_{gx} n_e K_x}{n_{g\max} n_{e\max} K_{x\max}} = \frac{n_{x*} n_e}{n_{\max^*} n_{e\max}} \qquad (2.17)$$

The normalised integrated intensity therefore gives a measure of the variation of the density of the excited species in the plasma and the variation of electron density.

Figure 2.17 shows the normalised integrated intensities of O^*, O_2^* and O_2^{+*} emissions with varied applied RF power for the three plate designs. The figure shows that the normalised O^* intensity increased with RF power for all three aperture plates. This is consistent with previous observations [127]. It is well known that the electron density typically increases linearly with applied power for inductive discharges [128]. Hence, the linear increase in O^* emission with RF power for the 276 hole and 1 hole plate is consistent with an increase in atomic oxygen density. The saturation observed in the 25 hole plate emission suggests that as the RF power is increased, the O^* density was slightly decreased. The exact cause, however, is unclear as either a decrease in excitation rate and/or a decrease in dissociation rate can result in this observation.

Figure 2.17b shows the variation of the O_2^* emission intensity, which appears to be different amongst the three aperture plate designs. In particular, while a linear increase with RF power is again observed for the 276 hole plate, the plasma generated using the 25 hole plate showed an initial increase in the O_2^* emission, reaching a maximum at 300 W, then steadily decreasing with higher power. The O_2^* emission observed from the 1 hole plate plasma showed a sharp decrease from 375 W to 400 W, after which the emission was observed to stay virtually constant. While these complex trends seems to be puzzling to explain, one have to remember that compared

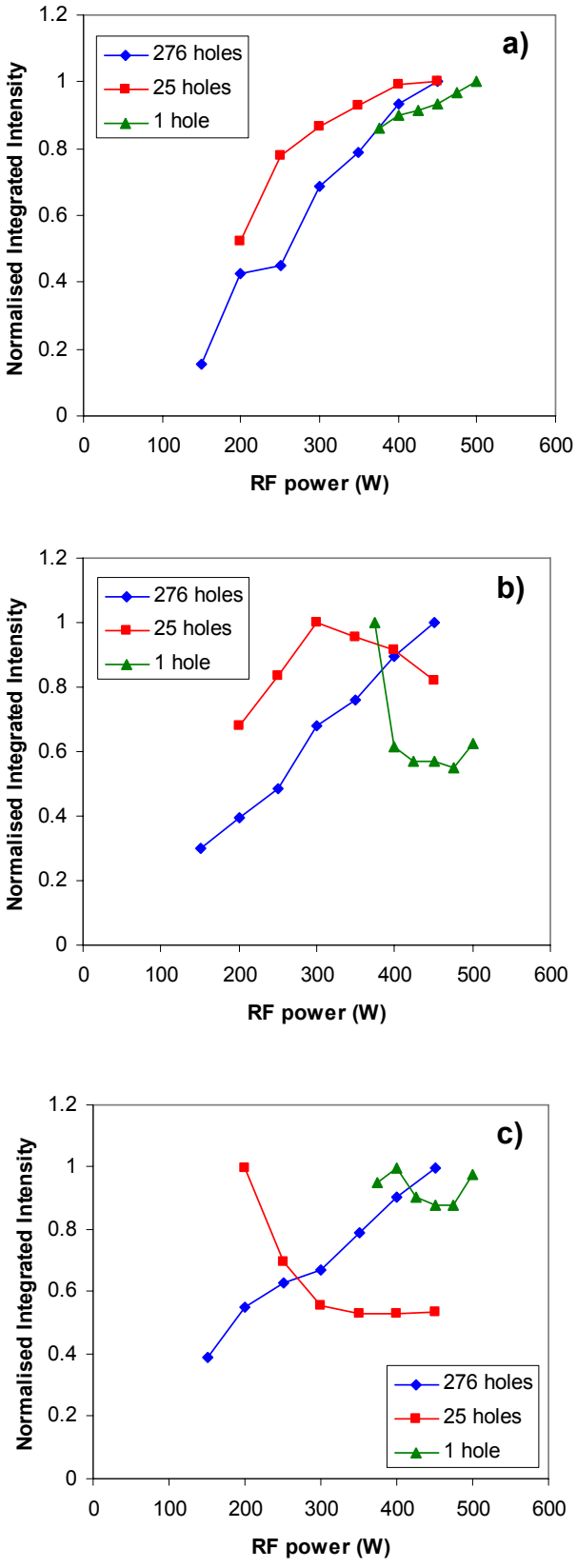

Figure 2.17 The normalised emission intensity of different active oxygen species in the plasma a) atomic oxygen O*, b) molecular oxygen O_2^*, c) molecular ions O_2^+.

to the O^* emission, the O_2^* emission is very weak. In fact, referring to Figure 2.16, it can be seen that the emission intensity of O_2^* is close to the noise level. This inevitably will generate uncertainties in the measurement data. These uncertainties must therefore be considered when analysing the trends. For example, from the relatively small decrease in O_2^* emission at high power for the 25 hole plate, it is quite possible that the O_2^* density is, in fact, saturating with increasing power. Similarly, for the 1 hole plate, the uncertainty gives a conclusion that the O_2^* density is practically constant for all applied power above 400 W, with the O_2^* density especially high at 375 W.

The variation of the O_2^{+*} ionic emission is shown in Figure 2.17c. It can be seen that a linear trend is again observed for the 276 hole plate, whereas the 25 hole plate gives a high ionic emission at low power, which decreases with power and becomes constant above 300 W. This opposite behaviour between the 276 hole and 25 hole plates is very interesting to note, although the origin for this observation is unclear. The O_2^{+*} emission observed for the 1 hole plate is virtually constant, with measurement variations most likely originated from uncertainties from the relatively more noisy data.

From the analysis in Figure 2.17, it can be seen that the behaviour of the 276 hole plate is the most predictable, with an increased excitation rate, dissociation rate and ionisation rate observed with increasing RF power, which is consistent with the theory and previous reports [120, 127, 128]. The 25 hole and the 1 hole plates, however, are behaving differently. In particular, the 25 hole plate showed a saturation of all three species at higher powers, suggesting that at high power, the excitation rate, dissociation rate and ionisation rates are constant. For the 1 hole plate, a virtually constant O_2^* and O_2^{+*} density was observed, which is consistent with the increased atomic emission observed with applied power. Note that this variation of behaviour between species in different aperture plate configuration is expected, as it is believed that the different nature of the excited species would interact differently with the sidewalls, and hence would be affect in different extend by changing the aperture sidewall area.

To provide more information on the variation in species density and comparison between plates, the intensity ratio can be used instead where the effect of electron density and experimental dependent factors are eliminated. For example, the intensity ratio of O^* and O_2^* is given by:

$$I_{ratio} = \frac{I_O}{I_{O_2}} = \frac{C_O(\lambda) n_{gO} K_O Q_O b_{\lambda x}}{C_{O_2}(\lambda) n_{gO_2} K_{O_2} Q_{O_2} b_{\lambda x}} \tag{2.18}$$

In a typical inductively coupled plasma, it is expected that the ratio presented in Equation 2.18 behaves in a similar fashion as the ratio n_O/n_{O2} [127].

Figure 2.18a shows the O^*/O_2^* emission intensity ratio. As the emission intensity ratio is expected to behave similarly to the absolute density ratio, this graph is essentially illustrating the variation in cracking efficiency of the plasma source with RF power and aperture plate design. It can be seen that in general the intensity ratio shows an increasing trend with applied power for all three plate designs, which is consistent with the expectations from the nitrogen plasma studies [129, 130] and is the direct result of the actual increase in cracking efficiency with RF power. The higher relative content observed for the 1 hole plate (almost twice the content observed for the 276 hole plate) is also consistent with nitrogen plasma studies, which reported an increase in N_2^* production with increased number of holes [120]. The deviation between the 25 hole and 276 hole plate, however, is inconsistent as it is expected that the 25 hole plate should give a higher atomic content compared to the 276 hole plate. Both the 1 hole plate and 276 hole plate showed a saturation in O^*/O_2^* at higher RF powers.

Figure 2.18b shows the O^*/O_2^{+*} emission intensity ratio. It can be seen that the relative O^* intensity compared with the O_2^+ emission increased with applied power, but appeared to saturate past 350 W, for all three aperture plates. This is consistent with what was observed by Seo et al. [127], who reported a saturation of the O^*/O_2^{+*} intensity ratio as the input power was increased. This saturation suggests that in general the increase in ion production with RF power is more significant than the increase in dissociation efficiency. The three curves have similar value, although the 276 hole plate has a higher atomic density (relative to the molecular ions). Comparing to the high O/O_2 ratio for the 1 hole plate in Figure 2.18a, the O^*/O_2^{+*} emission intensity suggests that the plasma generated by the 1 hole plate either has a significantly higher O_2^+ content or significantly lower O_2 content.

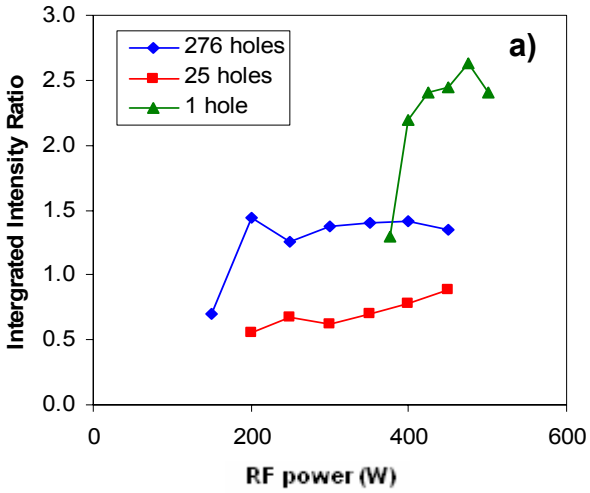

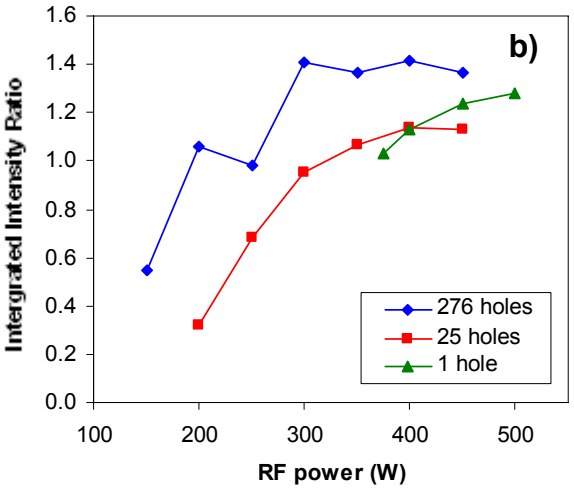

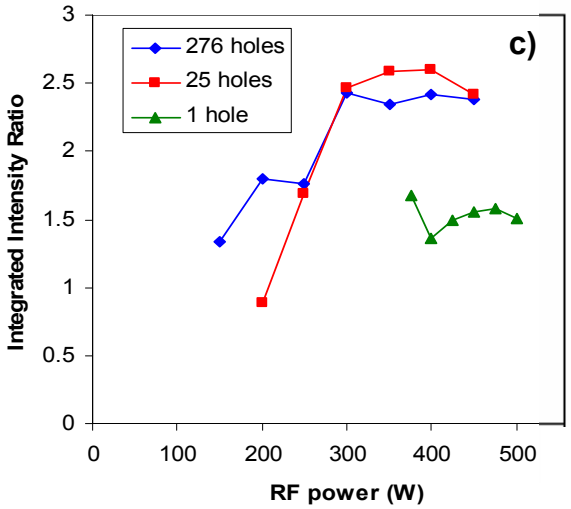

Figure 2.18 The emission intensity ratio between different active oxygen specie s in the plasma: a) O/O_2, b) O/O_2^+, c) $(O+O_2)/ O_2^+$.

Figure 2.18c gives an indication of the ion density of the plasma generated in terms of $(O^{*}+ O_2^{*})/O_2^{+*}$. It can be seen that the 1 hole plate was generating considerably more O_2^{+*} ions than the other two plate designs. This is consistent with the report of higher ionic density with larger aperture size [121]. Furthermore, it can be seen in Figure 2.18c that $(O^{*}+ O_2^{*})/O_2^{+*}$ of the 276 hole plate and the 25 hole plate are almost identical. This is also consistent with the observation in Figure 2.18a and Figure 2.18b, confirming that the 25 hole plate produces a higher O_2^{*} content than the 276 hole plate.

From Figure 2.18 a few conclusions regarding the behaviour of the plasma source can be drawn. Firstly, the results clearly suggest the highest atomic content is observed for the 1 hole plate, followed by the 276 hole plate, with the 25 hole plate having the lowest atomic content. Secondly, the ionic content in the plasma produced by the 1 hole plate is significantly higher then the other two. The results here demonstrate that by changing the RF power and the aperture plate design, the oxygen content in the generated plasma can indeed be varied. The inconsistency observed from the OES, especially the unusually low atomic content of the 25 hole plate as well as its erratic behaviour with RF power is puzzling and the available results cannot fully and conclusively explain the observation. However, it is recognised that variations in the pressure in the plasma discharge tube and the actual throughput of the discharge tube could play a role despite the total conductance of the aperture plate being kept as close to the original design as possible.

The limitation of the OES is that it is performed from the back end of the plasma source. As a result, the spectrum does not necessarily provide a fair or complete representation of the species that actually reach the substrate. Some systems allow OES monitoring of the plasma source from the front of the source by having a view port in the direct line of sight of the plasma outlet and the substrate. However, such a setup is not available in the Perkin-Elmer system. Therefore, as another measure of the plasma content, quadrupole mass spectrometry (QMS) was used to monitor the actual species emitted from the plasma source for two of the aperture plates (1 hole and 25 hole configurations). QMS operates by ionising gases, with the ions subsequently filtered based on their charge to mass ratio and collected in a Faraday cup, which provides an ion current representative of the density of the species present. Errors that must be accounted for in performing quantitative analysis include

the fraction of species which are multiply ionised, and differences in the ease of ionisation between species [131].

For the characterisation of oxygen plasmas, the QMS head was positioned at the direct line-of-sight of the plasma source outlet using the RHEED screen port. The plasma conditions were again varied within the operating region of the aperture plates, while the O and O_2 partial pressures were measured. By reducing the ionisation energy of the QMS to zero, the atomic and molecular oxygen ions were detected separately from neutral species.

Figure 2.19 shows a typical RGA scan showing the composition of the oxygen plasma generated by two aperture plates using 1.6 sccm oxygen flow and 450 W applied RF power. The plasmas generated by both plates contained a substantial amount of molecular oxygen (32 amu) and atomic oxygen (16 amu), although it must be noted that the peak at 16 amu is the sum of neutral oxygen atoms (O), ionic oxygen atoms (O^+) and doubly ionised oxygen molecules (O_2^{++}) detected by the Faraday cup. A measurement performed in the absence of a plasma suggested that approximately 5% of the molecular oxygen was doubly ionised. Therefore, Figure 2.19 confirms the

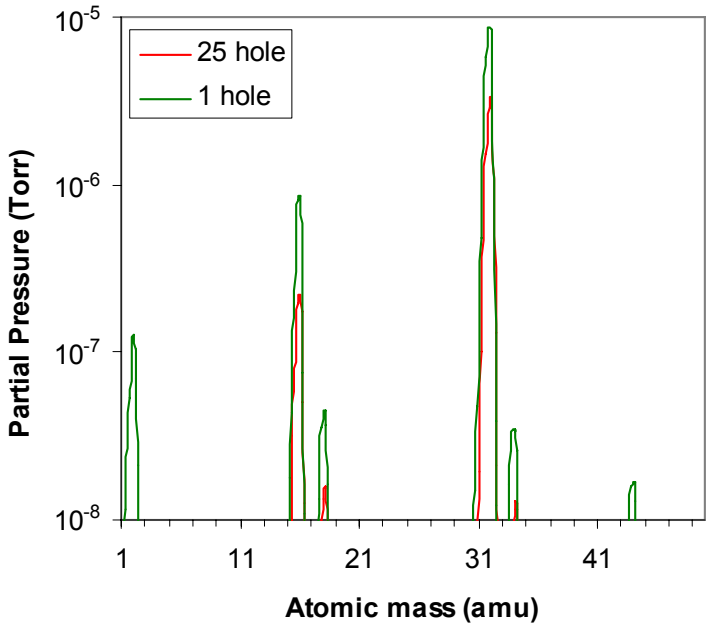

Figure 2.19 The composition of an oxygen plasma generated by the MDP21 source at 450 W, showing the O peak (16 amu) and O_2 peak (32 amu). Note that most of the other peaks such as that at 1 amu and 18 amu originated from water vapour inside the system and/or from the oxygen plasma.

creation of atomic oxygen by the plasma source, but it can be seen that the efficiency is not particularly high. In particular, for this particular case, the measured O_2 partial pressure for the 25 hole and 1 hole plates are 3.2×10^{-6} and 8.5×10^{-6} Torr, respectively, while the O partial pressures were measured to be 2.2×10^{-7} and 8.5×10^{-7} Torr, which are approximately 10% of the O_2 partial pressure, equating to roughly 5% dissociation. One can also see from the figure that at the same flow rate, the 1 hole plate provided more oxygen (both atomic and molecular) than the 25 hole plate. In fact, the sum of the partial pressure across the whole amu range for the 1 hole plate plasma was found to be 2.8 times larger than that of the 25 hole plate. This confirms the suspicion that the variation of orifice size changes the exhaust velocity or throughput of the plasma source despite the total orifice area being kept constant.

Figure 2.20 shows the spectra for the same plasmas with the QMS ioniser off, revealing the ion production of the plasma source. As can be seen, both plates produced molecular oxygen ions, but the 25 hole plate produced fewer atomic oxygen ions than the 1 hole plate. In fact, the ion production of the 1 hole plate was over an order of magnitude higher than the 25 hole plate. This confirms the increased ionic content observed from the OES. Interestingly, the 1 hole plate's ion spectrum showed

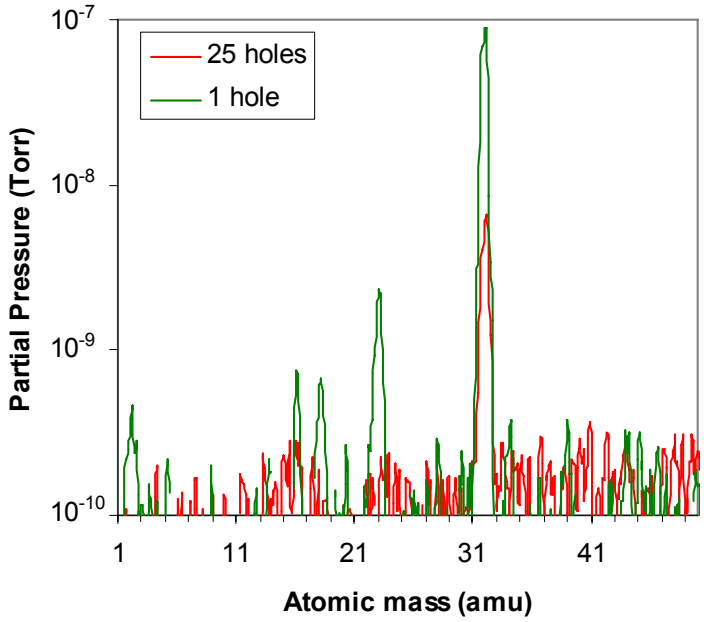

Figure 2.20 The ionic composition of an oxygen plasma generated using the 25 hole plate and 1 hole plate. The 1 hole plate produced dramatically more ions than the 25 hole plate, as evidenced by the much higher signal to noise ratio and the higher partial pressures measured for the 1 hole plate.

a distinct peak at 23 amu. This peak does not correspond to atomic nor molecular oxygen ions, and its origin is unclear.

Figure 2.21 shows the partial pressure ratio of O^+/O, O_2^+/O_2 and O/O_2. As can be seen from Figure 2.21a and b, the ion production efficiency increased considerably when the aperture plate was changed from the 25 hole plate to the 1 hole plate. In particular, the relative molecular oxygen ion content increased over 10 times, while the atomic oxygen ion content increased 3 times at the highest concentration. This observation is again consistent with previous reports [122] and confirms the higher ionisation efficiency of a larger orifice plasma source. The molecular ion content increased with applied RF power for both aperture plates. However, while for the 25 hole plate the O^+ content was essentially constant at 0.05%, the O^+ content for the 1 hole plate increased non-linearly with applied power. In particular, at an applied power below 450 W, no O^+ was observed in the plasma. Above 450 W, the O^+ content started to increase rapidly. This suggests that there might be an energy or a throughput threshold for sustaining atomic ion production. This observation provides a plausible explanation for the absence of O^{+*} in the OES. Note that the increase in ion content with RF power in oxygen plasmas has been previously reported [128]. The behaviour of the 1 hole plate observed here is consistent with the OES measurements. For the 25 hole plate, as the variation in the ion content observed with QMS is small, and no data is available for the lowest powers, the observed trend is also consistent with the OES measurements.

Figure 2.21c shows that the ratio O/O_2 does not vary substantially with RF power. For the 25 hole plate, the O/O_2 ratio varied from 0.0845 to 0.090, which corresponds to a change in cracking efficiency of 0.5%. This is similar to the trend observed by OES where the O^*/O_2^* ratio was essentially constant with applied power. A similar change in the O^*/O_2^* ratio is observed for the 1 hole plate. Note that no data was taken at 375 W for the 1 hole plate as the plasma was unstable for this aperture configuration. This suggests that the abnormally high molecular content at 375 W observed in Figure 2.17b from the OES was a result of the plasma operating at the limits of the stable region.

Overall, the characterisation of the plasma through OES and QMS provides evidence that the variation in active oxygen species can be achieved by changing the

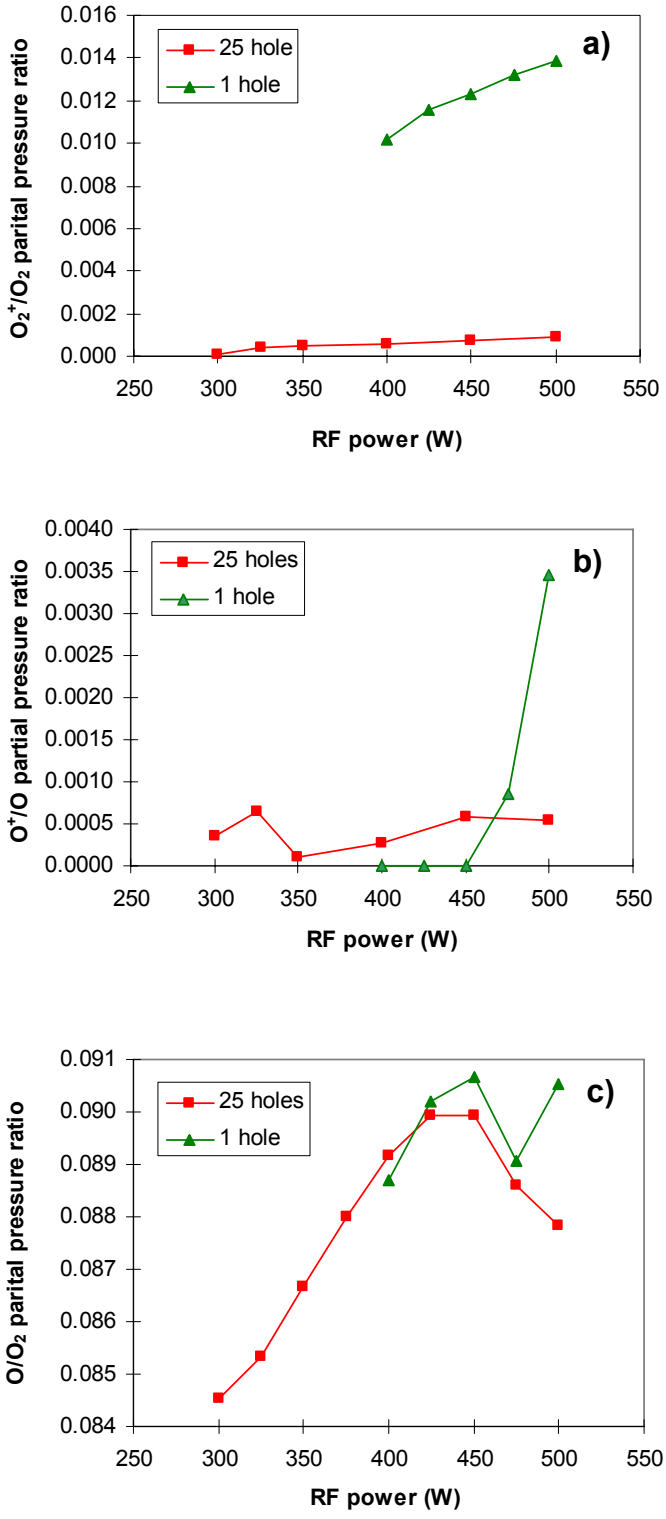

Figure 2.21 The partial pressure ratio for the different oxygen species a) O_2^+/O_2, b), O^+/O c) O/O_2.

RF power and the aperture plate design. In particular, by varying the RF power, a general increase in cracking efficiency can be achieved, accompanied by an increase in the ion content in the plasma. By increasing the orifice diameter on the aperture plate, the resulting plasma in general showed an increase in cracking efficiency, ion content as well as throughput, although the actual behaviour is much less predictable. While a more detailed plasma diagnostic such as a Langmuir probe and electron temperature measurements might give a better picture of the plasma dynamics, the ability to trace the differences in the plasma content using OES and QMS is sufficient for the investigation on its effect on ZnO growth.

2.2.4 Substrate Temperature

An elevated temperature, provided by an oxidation-resistant heater, is essential for ZnO growth. It is therefore necessary to provide the means to accurately measure the substrate temperature. The most common way to measure the temperature of the substrate for real time temperature control during deposition is by using a thermocouple (TC). A TC is typically two strips of metals with different Seebeck coefficients connected together. The differences in thermoelectric response with the same thermal gradient result in a voltage difference at the contacting point, which can be readily measured. Therefore, by keeping one of the contact points at a reference temperature such as room temperature and the other point directly in touch with the substrate holder, the voltage differences can be measured and converted to a substrate temperature. In most MBE systems, including the Perkin-Elmer 430, an extension alloy TC (Type D) system is used. Further details in the working of this and other TC systems can be found in reference [56]. Note that a similar TC is used to control the Zn cell temperature, although in that case it is not as critical as the QCM provides the main monitoring tool for the Zn flux.

Unfortunately, such a contacting TC setup is not always robust. A universal problem for all contact TC systems is the temperature difference between the measured temperature and the actual temperature of the substrate. In particular, since the TC is only in contact with the substrate holder, and the substrate is not a good conductor of heat, the measured temperature could be higher than the actual temperature of the substrate. Furthermore, there is a temperature difference between

the substrate and the actual growth surface which increases as the thin film gets thicker. Note that this kind of temperature mismatch is system dependent, and it is one of the main reasons why reproducibility between research groups is often hard to achieve.

One of the ways to examine this issue is to use a reference temperature as a calibration. A common way to calibrate the temperature is to place a eutectic on the surface of the substrate holder. As the eutectic changes form at a known temperature (the eutectic temperature), the observation of eutectic transition can be used to compare the measured temperature and the actual temperature of the substrate. In this work, the eutectic systems Au/Ge and Al/Si were used to calibrate the temperature measured by the substrate holder TC. The eutectic temperatures for the two eutectics are 361°C and 577 ºC, respectively. Each eutectic was placed on the substrate holder using indium bonding, and was slowly heated while changes were observed with the naked eye through the glass view port.

It was found that the measured eutectic temperature was approximately 60 ºC above the actual eutectic temperature for Au/Ge, while for Al/Si the measured temperature was approximately 30 ºC below the actual temperature. The difference between the temperature offsets suggests that the error of the TC is a function of temperature. Nonetheless, the temperature difference observed here is reasonable for a MBE system and it is much less than the temperature difference measured for indium free substrate mounting [132]. Therefore, for measuring substrates that are physically bonded to the substrate holder, contact TC readings should be interpreted as approximate to within 100 °C.

Unfortunately, contacting TC setups can also suffer from mechanical failures. Through the course of this work, two contacting problems were encountered. In the first instance, mechanical failure caused the TC to slip from its original position and resulted in the TC failing to contact the substrate holder. In the second instance, the connecting metallic strips for the TC were in electrical contact with ground due to the coating of the shielding ceramics with conducting material. In both cases, continuous electrical contacts meant that a failure was hard to identify, and as a result, not all temperature measurements were reliable. Because of this, a detailed comparison between growth temperatures is not available.

2.3 Crystal Growth Process and Growth Rate

2.3.1 Deposition and Growth Rate

Adequate control of Zn and O flux as well as substrate temperature, as outlined in the previous sections, provides a platform on which the MBE ZnO growth process can be investigated in detail. The deposition of thin films via MBE begins with nucleation, which occurs in the first few monolayers of growth. At this stage, the effect of the substrate is very important as the substrate surface lattice structure and dangling bonds determine where arriving atoms can bond to form clusters or islands on which further growth can occur. Eventually, these nuclei of material coalesce and form an essentially continuous layer. Once a sufficiently thick layer has been deposited, the effect of the substrate can be regarded as negligible as bulk effects dominate and the deposition enters the bulk growth stage. In this section, this bulk deposition process is studied.

The bulk crystal deposition process in MBE is similar to other vapour phase techniques such as CVD, where the participating species are in the vapour phase. As discussed by Smith [56], the crystal deposition process involves three steps: 1.) atoms approaching the surface and trapped in the potential well by van der Waal forces (physisorption); 2.) movement along the surface to an energetically favourable site (diffusion); and 3.) the chemical bonding between the trapped atom and the growing surface (chemisorption). Any species that are not incorporated are desorbed from the substrate into the surroundings. This growth process is shown in Figure 2.22. It can be seen that the most important aspect of the bulk crystal deposition is the chemisorption process, and the efficiency of the deposition is primarily determined by the chemisorption rate. This rate of reaction manifests itself as the growth rate of the thin film. Therefore, by considering the effect of different growth parameters such as Zn flux or active oxygen on the growth rate, one will gain insight in the interaction of these parameters in the reaction process during the epitaxial growth.

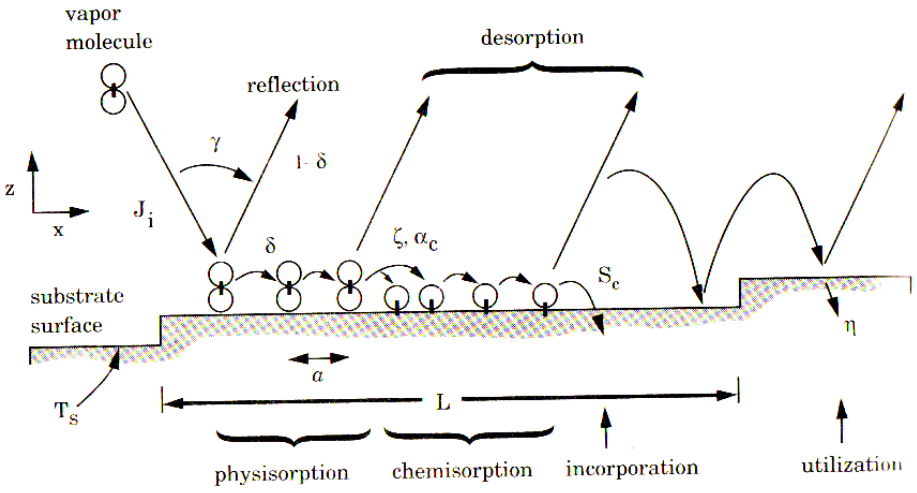

Figure 2.22 The deposition process. An adatom goes through physisorption, diffusion, and chemisorption before incorporation takes place. Unused adatoms are desorbed into the surroundings (From Smith [56]).

2.3.2 Growth Rate Measurements

Generally one can measure the growth rate of a particular thin film ex-situ or in-situ. In an ex-situ measurement, the final thickness of the thin film is determined post-growth and the growth rate is calculated from the measured thickness and the growth time. In an in-situ experiment, the growth rate is measured during the growth process by measuring the thickness change in real time. Ex-situ measurements by definition generally represent an average growth rate. Hence they lack the ability to detect any change in the growth rate due to changes in deposition conditions or in the growth mechanism. In contrast, in-situ measurements allow the real time monitoring of alterations to the growth rate during growth. In most cases, however, in-situ measurements are more complicated to perform and more expensive to set up. Because of the nature of these two types of measurements, they often serve as complementary techniques in determining the growth rate.

Two growth rate measurement techniques - ex-situ profilometry and in-situ laser reflection interferometry (LRI) - were used in this study. In profilometry, parts of the sample are etched off to form a step from the film to the substrate. The step height is then measured as the thickness of the film, from which the average growth rate is calculated. Usually, only a centre point in the substrate is selected for profilometry, and a few measurements are performed to assess the uniformity of the

sample across a small area. LRI is based on optical interference between the substrate and the surface of the film. As shown in Figure 2.23, when a coherent laser with energy below the bandgap of the thin film is targeted onto the surface of the growing film, part of it is reflected and part of it is transmitted. The transmitted beam eventually reaches the substrate and is (at least partially) reflected. These two beams then interfere and the superposition of the two is observed by the detector.

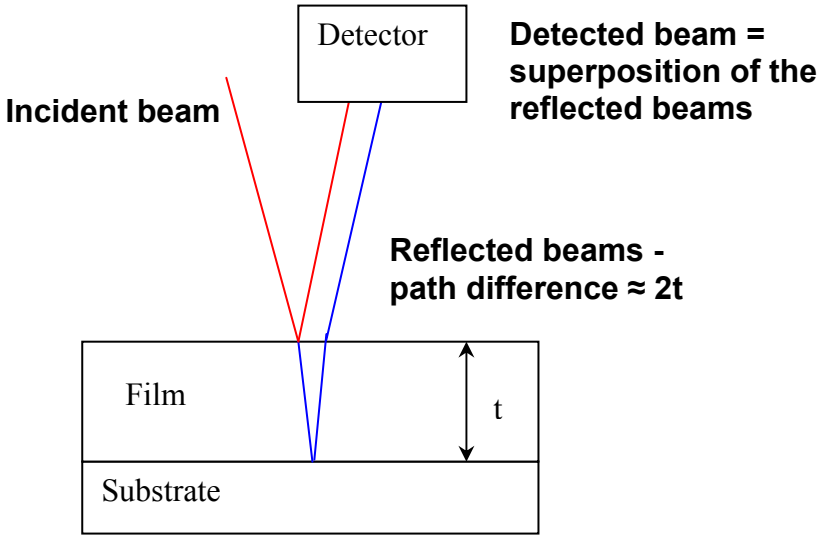

Figure 2.23 The principle behind laser reflection interferometry - the interference between reflected beams from the surface of the film and the surface of the substrate. For a nearly normal incident beam, the path difference of the reflected beams is approximately 2t. Therefore, by observing the occurrence of the constructive and destructive interference of the reflected beams the growth rate can be calculated.

In a typical LRI experiment, a red laser beam (625 nm) from a laser diode is targeted to the substrate at a slight angle to the normal of the substrate through a glass view port. The reflected beam is collected using a photodetector; as the thickness of the film increases during growth, an oscillatory intensity is observed at the detector, as shown in Figure 2.24, due to the change of the interaction between the reflected beams from constructive interference (when the path difference is $n\lambda$) to destructive interference (when the path difference is $n\lambda + \lambda/2$). As the path difference is roughly equal to twice the thickness, each oscillation (from peak to peak) corresponds to a thickness change of $\lambda/2$. The growth rate can then be calculated from the peak spacings in the time domain.

Note that the use of LRI is uncommon in MBE, due to the capability of the more widely used RHEED oscillations which can measure the growth rate with

monolayer accuracy. However, due to the need of high quality surfaces, RHEED oscillations can only be used for nearly optimised growths. Therefore, for exploratory experiments such as those considered here, LRI provides a more accessible approach for real time growth rate measurements.

Armed with these two growth rate measurement techniques, the effects of different growth parameters on the growth rate were studied to provide more insight into the MBE ZnO bulk deposition processes. In particular, the effects of Zn flux, active oxygen and temperature are presented in detail.

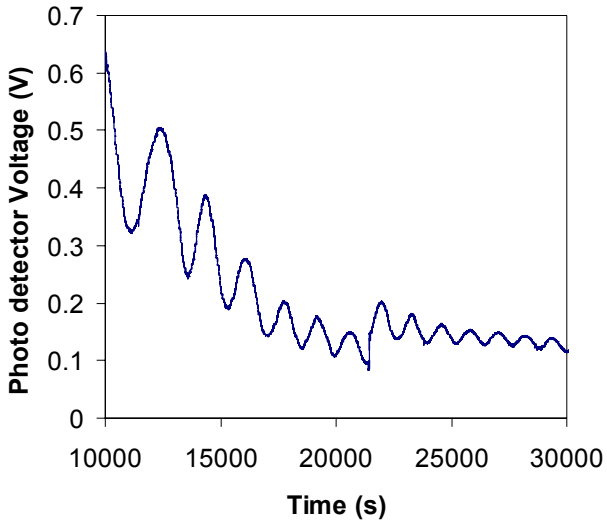

Figure 2.24 A typical signal in an LRI experiment. The peak to peak spacing represents the time it takes for the thickness to change by λ/2. Note that the discontinuity is due to an interruption of the experiment.

2.3.3 Growth Rate and Zn flux

Consider the growth of ZnO on sapphire at an elevated temperature. As the Zn species and oxygen species arrive on the surface of the substrate, the species become adatoms (mobile atoms physisorbed on the surface), and diffuse for a certain amount of time before they chemisorb and incorporate at a specific site on the substrate. In particular, it is expected that under perfect conditions, Zn atoms will only bond to an O atom and vice versa. Further, due to the high vapour pressure of Zn, it is expected that at an elevated temperature, any Zn adatoms not bonded to the surface will eventually desorb. This is also true for unused O adatoms. Then, it follows that an

increase in Zn flux will only result in an increase in growth rate given that there are enough O atoms on the substrate for the Zn adatoms to bond to. Therefore, it is expected that if the oxygen flux is fixed and the Zn flux is varied, the growth rate will initially increase linearly with Zn flux. This linear growth region is known as O-rich growth. As the Zn flux increases past the stoichiometric point where the O flux J_o is equal to the Zn flux J_{Zn} , the growth enters the Zn-rich condition, and the growth rate should then saturate and remain constant, independent of the Zn flux.

As the flux ratio (i.e. Zn-rich, O-rich or stoichiometric) is known to be important for MBE growth [133, 134], growth rate measurements were performed in-situ using LRI for different Zn fluxes at a fixed oxygen flux and substrate temperature to determine the growth window for the different stoichiometric conditions. In this experiment, the Zn flux was increased in steps, and for each step a number of oscillations were recorded to calculate the growth rate for that particular flux. This allowed the growth rate under different Zn fluxes to be measured in a single experiment, minimising the error between data points and also avoiding the need for multiple substrates and repetitive experiments.

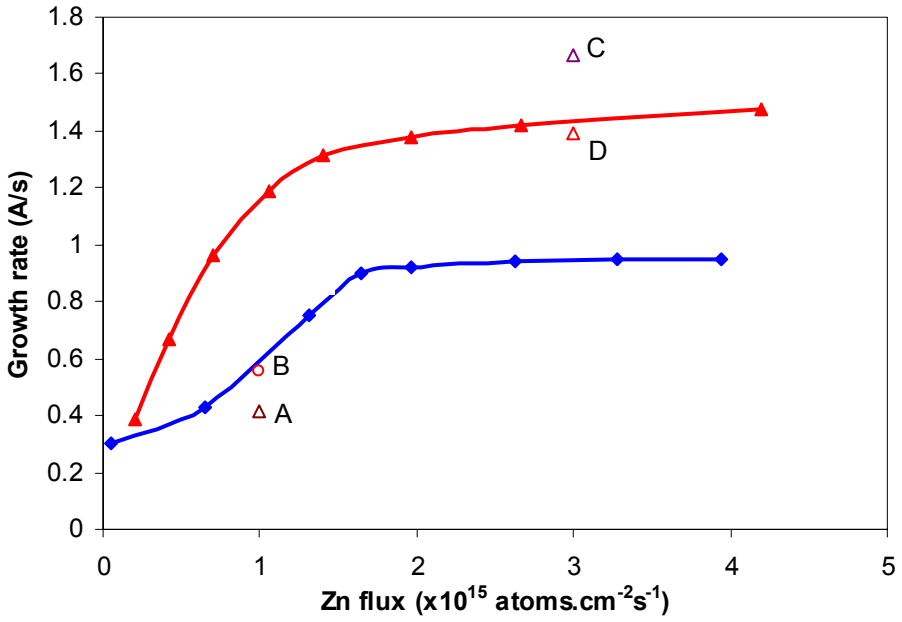

Figure 2.25 The growth rate as a function of Zn flux for different systems. The red curve represents the data taken in this study. The blue curve represents data from Ko et al. [135]; open symbols are data from selected groups (A -Murphy et al. [136], B - Jung et al. [83], C - Dong et al. [137] and D - Vigue et al. [138]).

The red curve in Figure 2.25 shows the growth rate of ZnO under various Zn fluxes with a 400 W plasma generated from a 1.6 sccm oxygen flow (which resulted in a process pressure of $\sim 8 \times 10^{-6}$ Torr), as measured using LRI. Because of the RF interference between the QCM and the plasma source generator, only the smallest and the largest fluxes were measured using QCM at the start and the end of the experiment, respectively. The other data points were estimated using the theoretical model presented in Section 2.2.2, utilising the cell temperature which was varied in uniform steps, and calibrated using the initial and final QCM reading. It can be seen that the general shape of the curve is consistent with what is expected, with the growth rate increasing linearly with Zn flux until the flux reached approximately 0.8×10^{15} atoms/cm^2·s, at which point the growth rate started to increase at a slower rate and essentially saturate after 1.8×10^{15} atoms/cm^2·s. The slight increase in growth rate observed at high Zn fluxes can be explained by roughening of the surface. As calculated in Section 2.2.2, growing ZnO at a growth rate of 1 Å/s requires 1.82×10^{14} Zn atoms/cm^2·s. This system needed a flux of 8×10^{14} atoms/cm^2·s for such a growth rate, giving a Zn sticking coefficient of 0.22 under the specified growth conditions.

Similar growth rate curves have been reported by Ko et al. [135], who used RHEED oscillations to measure the growth rate for different Zn fluxes using a fixed oxygen flow rate of 2.5 sccm. Their growth rate measurements are shown in Figure 2.25 as the blue curve. It can be seen that even though their oxygen flow rate was higher, the growth rate obtained was smaller. At the same time, the stoichiometric point $J_o = J_{Zn}$ occurred at a higher Zn flux than the present work. This suggests more active oxygen was provided by the larger flow rate, but the sticking coefficient was lower and hence the desorption rate was higher. This is consistent with the fact that they were growing at 750 ºC, higher than the growth temperature of 650 ºC used here. Generally, the growth rate of thin films in this study is comparable to but higher than typical MBE ZnO growth rates from other groups, as can be seen from open symbols in the graph. This can be explained by slight differences in system and growth parameters, such as the plasma source model, Zn cell design and position of the substrate.

2.3.4 Growth Rate and Active Oxygen

To study the effect of active oxygen on the growth rate, various plasma conditions, provided by varying RF power and aperture plates, were used to grow ZnO thin films. The films were grown using the same oxygen flow rate of 1.6 sccm, and a Zn flux of 1.6×10^{15} atom/cm^2·s was used to ensure a Zn-rich condition (based on Figure 2.25). Figure 2.26 shows the deviation in growth rate under these varying plasma conditions. Note that the growth rates were measured ex-situ by profilometry using a Dektec profilometry system. It can be observed that the growth rate in general increased with applied power to the plasma source. This means that by increasing the plasma power, the amount of growth-benefiting oxygen species increases. The

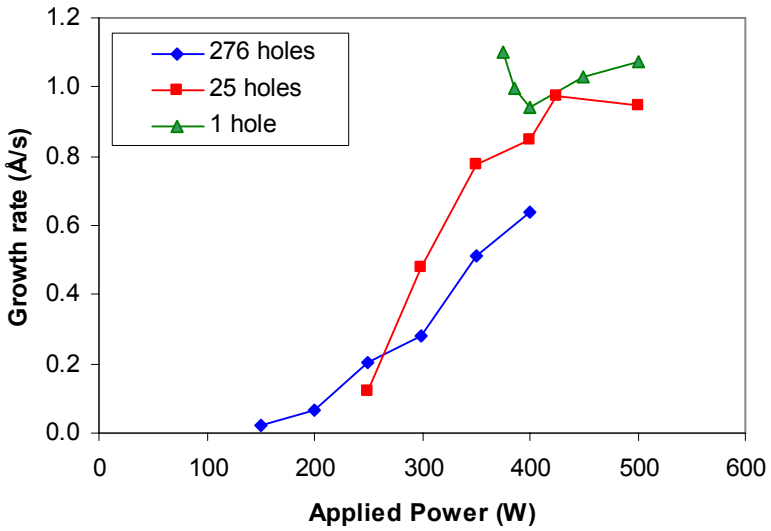

Figure 2.26 The growth rate as a function of applied power for the three aperture plate designs. The growth was kept under a Zn rich condition, and all other growth variables were kept constant.

densities of useful oxygen species also increased when the aperture plate was changed from the 276 hole to the 25 hole design, with almost a 50% increase in the maximum achievable growth rate. Apart from the unexpected high growth rate at the lowest plasma power, changing to the 1 hole plate only resulted in a slight increase in the growth rate compared to the 25 hole plate.

To confirm that the increased growth rate resulted from the 25 hole and 1 hole plates, growth rate versus Zn flux data were collected using LRI for each of the plates, using a fixed RF power of 400 W and a fixed flow rate of 1.6 sccm for all three aperture plates. As shown in Figure 2.27, these measurements strongly imply that the

amount of active oxygen produced by each plate design is different. In particular, the saturation Zn flux of the 1 hole plate was greater than the 25 hole plate, implying an increased amount of Zn flux was needed to bring the growth to a stoichiometric condition. Also plotted on the figure is the growth rate of a film grown under the same

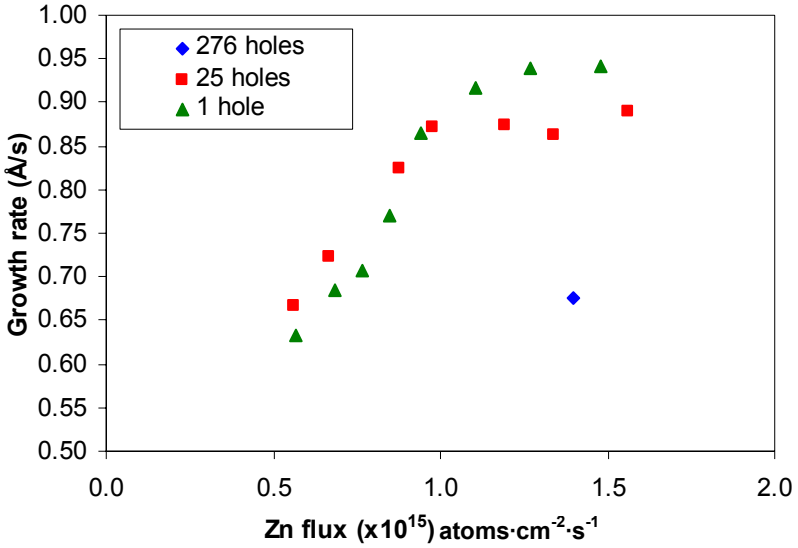

Figure 2.27 The growth rate as a function of Zn flux measured using LRI for the 25 hole plate and the 1 hole plate, showing a difference in the saturation Zn flux between the two. The growth rate of a ZnO film under grown with the 276 hole plate with the same applied RF power is also plotted for a comparison.

RF power but with the 276 hole plate as a comparison. It can be seen that this film is consistent with the increasing saturation flux trend expected from the two LRI curves. Recall that the OES actually suggested that the relative amount of active oxygen decreased by going from 276 hole plate to 25 hole plate. This is inconsistent with the 50% increase in achievable growth rate. The only plausible explanation would be an increase in throughput of the 25 hole plate compared to the 276 hole plate, similar to that observed between the 25 hole plate and the 1 hole plate. Similarly, the nearly three times increase in throughput observed from the 1 hole plate is more than sufficient to explain the increase in growth rate observed. However, it can be seen that the growth rate trends of the 1 hole plate and 25 hole plate are more complex than a simple offset from the 276 hole plate. Therefore, the observed variations in the growth rate involve more then just a simple increase in the total oxygen content.

While it is believed in general that O^* is the predominant species for oxide growth [114], the growth rate trend suggests that other species might also play a role.

In particular, although the increase in growth rate with RF power for the 276 hole and 25 hole plate followed the increase of O^* reasonably well as seen in the previous section, the 1 hole plate showed a distinctly high growth rate at 375 W which is not consistent with the O^* trend. If one compares the OES of the plasma (Figure 2.17) with the growth rate variation, one can observe that the non-linear growth rate trend for the 1 hole plate resembles the variation of O_2^* content for the 1 hole plate plasma. Therefore, it is possible that the O_2^* is actively involved in the growth process.

The variation in growth rate is related to the relative amount of oxygen species generated from the plasma. Under Zn-rich conditions, the growth rate should be independent of the Zn flux. Therefore, the growth rate should then be proportional to the active oxygen species that are participating in the growth. Further assuming ionic species do not actively participate in the reaction, the growth rate is directly proportional to the available O flux J_o and O_2^* flux J_{o2}, i.e.:

$$GR = K_1 J_O + K_2 J_{O_2} - R_v \tag{2.19}$$

where K_1 and K_2 are constants related to the incorporation rate of the two species, and R_v is related to the reevaporation of the incorporated material due to resputtering and desorption.

From Section 2.23, the density of different oxygen species is related to the integrated intensity of the emission spectrum of each oxygen species. Putting all the species dependent variables into one variable c, the situation can be simplified as:

$$GR = K_1 c_1 I_O + K_2 c_2 I_{O_2} - R_v \tag{2.20}$$

Introducing a factor *m* one can rewrite the above as:

$$GR = m(aI_O + bI_{O_2}) - R_v \tag{2.21}$$

where a = $K_1 c_1 / m$ and b = $K_2 c_2 / m$. are the weighting factors indicating the dominance of O and O_2, respectively. This equation predicts a linear dependence of the growth rate on the weighted sum of O and O_2 emission intensity.

To evaluate the validity of this model, the experimentally determined growth rates were plotted against the weighted sum of the integrated intensity of the emission peak I_O (533 nm) and the emission band I_{O2} (330 nm) measured at the corresponding plasma condition for growth. This is shown in Figure 2.28 where an additional scaling factor was used to allow a better comparison. The data can be fitted by a linear

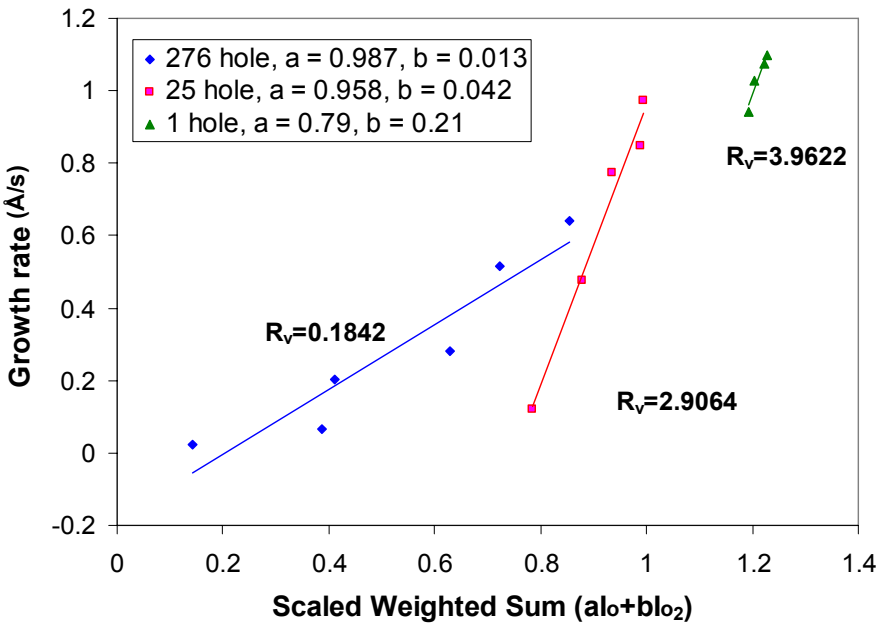

Figure 2.28 The growth rate of ZnO thin films as a function of a weighted sum of the O^* and O_2^* intensity, showing the participation of O_2^* in growth and the change in O^* dominance as well as the reevaporation rate with the aperture plates.

function, confirming that O and O_2^* are the only major participating species. The value of *a* was greater than 0.5 for all three aperture plates, suggesting that atomic oxygen is the dominating species in the growth of ZnO regardless of the aperture plate design, and unlike atomic nitrogen in the growth of GaN, the surface adatom scavenging effect of atomic oxygen in the growth of ZnO is limited [129]. This is consistent with the extremely strong polarised Zn-O bond formed from the large electronegativity differences. However, it can be seen that O_2^* was also involved in growth, especially in the 1 hole plate. In particular, if one calculate the total sidewall area A of each aperture plate, one can see that the ratio $A_{1\ hole} : A_{25\ hole} : A_{276\ hole} = 3 : 15 : 50$, whereas the weighting factor ratio $b_{1\ hole} : b_{25\ hole} : b_{276\ hole} = 50 : 10 : 3$. This means that, approximately, $b_{1\ hole} : b_{25\ hole} : b_{276\ hole} = 1/A_{1\ hole} : 1/A_{25\ hole} : 1/A_{276\ hole}$,

suggesting that the reduction in sidewall interaction has increased the relative importance of molecular oxygen species. From Equation 2.20 this suggests a relative increase of either the O_2^* content in the plasma and/or the incorporation rate of molecular species. This effect of the sidewall interaction is the exact opposite of that expected from nitrogen plasmas, where the metastable molecular nitrogen N_2^* content increases with increased sidewall interaction [120]. The origin of this discrepancy between the two plasma conditions and their effects is unknown, although it is possible that the difference in the formation mechanism of the metastable species had led to their difference in sidewall interaction dependence. Whatever the cause might be, this study in growth rate has shown for certain that even though the growth of ZnO dominantly involves atomic oxygen, the participation of molecular oxygen during growth cannot be neglected.

Note that there is also a discrepancy between the increased throughput observed to the increased growth rate observed, especially for the films grown with the 25 hole plate and 1 hole plate. In particular, the increase in growth rate is much smaller than expected from the observed 3 times increase in throughput. One possible explanation of this difference is the change in the reevaporation rate K_3. More specifically, if the reevaporation rate is much higher for the 1 hole plate than the 25 hole plate, then the increase in throughput will be offset by the increase in reevaporation, resulting in only a small increase in growth rate. This effect is illustrated by the reevaporation value calculated from the fitting shown in Figure 2.28 for the three plates. The origin of this variation of reevaporation rate is currently unclear. However, it is clear that the reevaporation rate for the 276 hole plate is much lower than the 25 hole plate, which suggests that the increase in throughput from the 276 hole plate to the 25 hole plate must have been substantial. The fact that the 276 hole plate used in this experiment was found later to be partially clogged may have been the major reason for this substantial difference.

2.3.5 Growth Rate and Temperature

To investigate the effect of temperature on growth rate, a series of LRI experiments was performed over three temperatures. Figure 2.29 shows the growth rate as a function of Zn flux for substrate temperatures of 300 °C, 400 ºC and 650 °C.

It can be seen that the maximum growth rate decreased with increased temperature as expected. From the limited data available it seems that the knee points for the three curves are almost identical, with the growth rate at 650 ºC saturating at a slightly lower Zn flux than the other two lower temperatures. This is very different compared to the observations of Ko et al. [135], who observed a shift of the knee point to a higher Zn flux with increased temperature, corresponding to the decreased sticking coefficient.

Recall from Figure 2.22, Zn atoms and O atoms that approaches the surface of the substrate goes through physisorption and chemisorption before it is truly become part of the epitaxial film. Further, a physisorbed adatom might also desorb and leaves the surface, without participating in the growth. In thermodynamic terms, one can represent this situation by a physisorbed state trapped between a chemisorption energy barrier and a desorption barrier from the bound, incorporated state and the free atom state respectively. As the growth temperature increased, the number of adatoms being physisorbed will increase due to the increased energy of the atom fluxes.

However, the desorption rate and the chemisorption rate would also increase, as more adatoms would have enough thermal energy to overcome the chemisorption and desoption barrier. Then, the overall growth rate of the film is related to the height

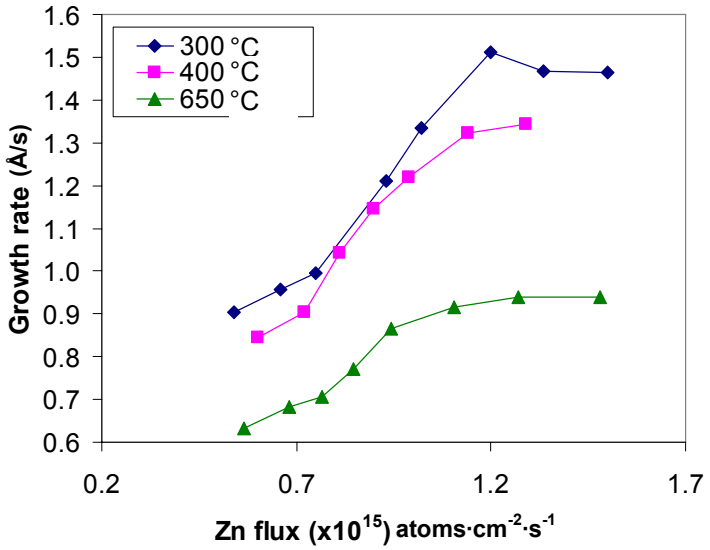

Figure 2.29 The growth rate as a function of Zn flux for various growth temperatures.

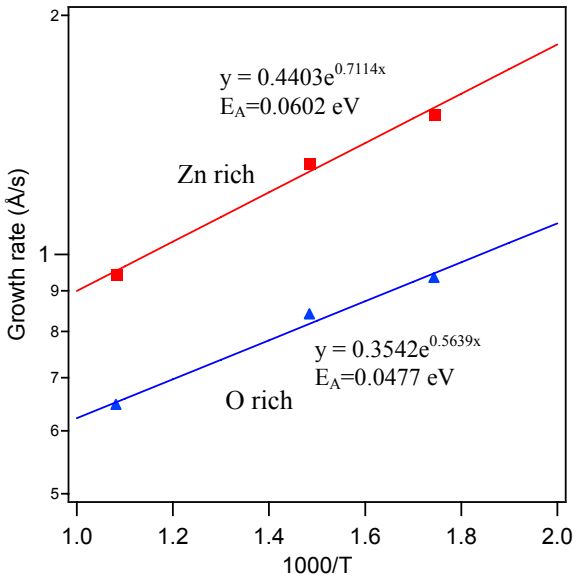

Figure 2.30 Plot of growth rate versus 1/T showing a straight line trend. The slopes of the curves are extracted as the energy difference between the chemisorption barrier and the desorption barrier.

difference between the two barriers - if the chemisorption barrier is higher, an increase in temperature would have a more important effect on the chemisorption of the adatom. Similarly, if the chemisorption barrier is relatively small, then the increase in temperature would have a stronger effect in increasing the desorption. Of course, this is a simplified version of the events as in a kinetically driven system such as MBE, the kinetic energy of the adatoms as well as the difference in the barrier height at different sites on the substrate can have a strong bearing on the actual thermal energy needed to overcome the barriers. Nevertheless, base on this model, the growth rate of a thin film is related exponentially to the difference between the effective chemisorption barrier and desorption barriers (taking into account of kinetic effects), i.e. $GR \propto e^{(E_d - E_r)/kT}$.

Therefore, by plotting the growth rate as a function of temperature for the Zn and O rich region in an Arrhenius plot, the difference in the reaction energetics between O and Zn adatoms can be determined. This is plotted in Figure 2.30. Although there are only three data points for each series, they can be fit reasonably well with a linear function. The activation energy calculated for Zn rich growth (red curve) was 0.0602 eV and for O rich growth (blue curve) was 0.0477 eV. These values are in the same order, but quite different to those observed by Ko et al. (0.028 eV for Zn rich and 0.138 eV for O-rich) [135]. More importantly, since the growth rate decreased with temperature under both Zn-rich and O-rich conditions, it can be

seen that the effective chemisorption barrier height is smaller than the effective desorption barrier height for both Zn and O adatoms on the surface. Therefore, the beneficial effects of increased temperature on the growth efficiency are limited.

The study of the individual effects of Zn flux, active oxygen and growth temperature on the growth efficiency has proved fruitful. It was confirmed that the growth rate is linearly dependent on both the Zn flux and O flux. The study on active oxygen showed that unlike what is commonly believed, both atomic and molecular oxygen species participate in ZnO growth. It was also found that in general, the growth activation is not a problem for ZnO growth, and increasing the substrate temperature will only reduce the growth efficiency. The effects of many system dependent variables, such as plasma source efficiencies, sticking and desorption coefficients, and adatom incorporation energies are also identified.

At this point, it is important to discuss the consistency of the system in order to justify the transferability of these knowledge. The consistency of a growth system can be divided into internal and external consistency. Internal consistency refers to the consistency of the system through a growth process within a single growth run, while external consistency refers to the repeatability in a run to run basis. In the Perkin-Elmer 430 system, it was observed that the internal consistency is very high. In particular, it has been observed experimentally that the Zn flux is very constant over a period of three hours of growth, and for LRI experiments, the Zn flux variation with temperature is very consistent with the temperature change. Similarly, it has been observed that the OES of the oxygen plasma exhibits only small hestersis with RF sweeps, suggesting the plasma source also have a high internal consistency. In terms deviation between film runs, the experimental data from this section is a good indication of the reasonable external consistency observed with this system. In particular, while it is expected that because of the kinetic nature of the process, finite statistical variation would exist between runs (as indicated by the scatter in the growth rate data presented in this chapter), it was observed that in many instances, very similar behaviour was observed during or after different growth under similar conditions. For example, by growing a film at 385 W after growing films at 375 W and 400 W for the 1 hole plate confirmed the abnormal growth rate trend observed, suggesting a good repeatability between films. Similar consistent observations were also made for other aspects such as the optical and electrical characteristics of many films (covered in the next Chapter). Because of this high internal and external

consistency, the trends observed in this chapter and in the rest of the thesis can be clearly regarded as real effects rather than statistical variations. Therefore, it is expected that the knowledge gained from these trends can be readily applied to other MBE systems.

Overall, this chapter confirms the capability of plasma-assisted molecular beam epitaxy for growing ZnO and that the growth efficiency is relatively easy to control by adjusting the Zn-flux, plasma parameters, and the growth temperature. However, the growth efficiency, although important, is not the only important trait that needs to be considered in the growth of thin films. The effect of different parameters on the structural, optical and electrical properties of the final ZnO thin film is also very important. In the next chapter, the effect of one particularly important factor - the flux ratio during growth - on the properties of the resulting thin films is presented.

Chapter 3

THE EFFECT OF FLUX RATIO

2.1 Determination of Flux Ratio

The flux ratio and the resulting stoichiometry of thin films grown by MBE have always been important issues. Due to the non-equilibrium conditions during MBE growth, it is possible for non-stoichiometric incorporation to take place. It is also possible for optimum stoichiometric incorporation to take place under a non-stoichiometric flux ratio. For example, for GaN, it is well known that growth in the Ga-stable region, i.e. using a very high Ga:N flux ratio, results in the best film quality [134, 139]. This has been associated with the presence of Ga droplets and surface Ga bilayers [140, 141]. For most II-VI materials such as ZnSe, this trend is not observed due to the relatively high vapour pressure of the cation at typical growth temperatures, which means nominally, all excess cations would be desorbed from the growth surface. However, the flux ratio is still an important factor. For instance, it has been shown that ZnSe films grown using different Zn flux, Se flux and substrate temperatures but with the same Zn:Se ratio can have nearly identical properties [133]. The same report also suggested that Zn stabilised conditions give rise to better film quality for the growth of ZnSe. For the growth of ZnO by MBE, only a small number of reports can be found on the topic of flux ratio, and furthermore, the reported observations varied greatly from paper to paper. For example, a number of papers have suggested that the optimum growth condition occurs at a stoichiometric flux ratio [81, 135], while other papers (e.g. [142]) suggest otherwise. Therefore, the actual effects of the Zn/O flux ratio on the growth of ZnO still warrant investigation.

As mentioned in section 2.3.3, it is expected that under a fixed oxygen flux, the growth rate is linearly dependent on the Zn flux until $J_{Zn} = J_O$, after which the growth rate saturates and becomes independent of the Zn flux. This means that a growth rate versus Zn flux curve can be divided into three regions: the linear region,

which represents growth under a $J_O > J_{Zn}$ regime, or the O rich region; the point of inflection or the knee point which represents the point $J_{Zn} = J_O$ or the stoichiometric condition; and the growth rate saturation region which represents growth under $J_{Zn} > J_O$ or the Zn rich region. Therefore, the investigation of growth rate verses Zn flux at a fixed oxygen condition and temperature is the most common way to identify the flux ratio during growth. In particular, a number of studies on MBE growth of ZnO used this method to determine and investigate the effects of flux ratio on film growth [135, 142].

This method of determining the flux ratio, however, is based on a very important assumption - that Zn and O incorporate in a 1:1 ratio during the ZnO MBE growth process. This is naturally assumed in ZnO as well as other II-VI materials such as ZnTe or CdTe, where both reactants are of high enough vapour pressures at the growth temperature that any excess, unused atoms are expected to leave the surface. To date, this issue has not been considered in the MBE growth of ZnO.

To confirm the validity of this assumption, growth rate was measured first with varying Zn flux then with varying oxygen flow. In the first experiment, the growth rate at varying Zn flux with a fixed oxygen flow rate of 1.5 sccm was measured using in-situ LRI. In the second experiment, a Zn flux in the linear region in the first experiment was chosen, and the growth rate variation with oxygen flow rate was observed using LRI, starting at 1.5 sccm and keeping the applied power constant at 400 W. If the assumption is correct, it is expected that no growth rate change would be observed in the second experiment, as it would typically be assumed from the first experiment that the growth condition is already O rich at the chosen Zn flux, and therefore the growth rate should not change with increasing oxygen flow.

Figure 3.1 shows the actual growth rate measurements using the 25 hole plate. In Figure 3.1a, it can be seen that the growth rate saturated at $\sim 1.0 \times 10^{15}$ atoms/cm^2·s, corresponding to the "stoichiometric" Zn flux. Figure 3.1b shows the growth rate variation with increasing oxygen flow rate, at a Zn flux of 8.8×10^{14} atoms/cm^{-2}·s^{-1}, which according to Figure 3.1a would give an O-rich condition at 1.5 sccm. It can be seen from Figure 3.1b that the growth rate continued to increase with oxygen flow, and saturated when the oxygen flow rate reached 3 sccm, twice the flow rate expected

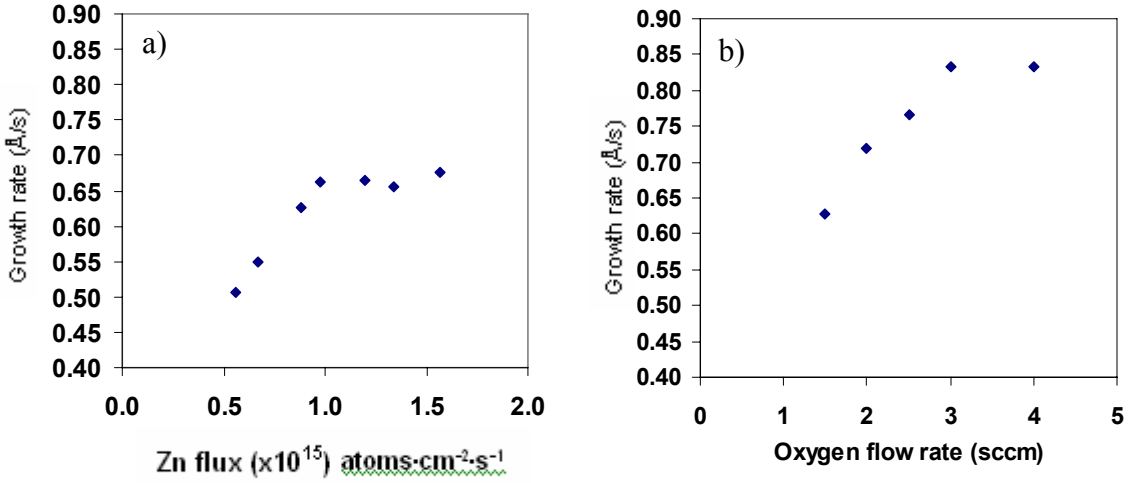

Figure 3.1 The LRI curve of a) varying Zn flux at 1.5 sccm O_2 and b) varying O flux at 8.8×10^{14} Zn atoms/cm^2·s. The mismatch in the knee point suggests non-stoichiometric incorporation.

from Figure 3.1a. This mismatch in the transition point cannot be explained by the assumption of perfect 1:1 incorporation. Interestingly, the occurrence of non-stoichiometric incorporation is supported by Rutherford backscattering spectrometry (RBS) in conjunction with nuclear beam analysis (NBA) performed by Dr. J. Kennedy at GNS Science (Lower Hutt, New Zealand) which showed that some ZnO films have a Zn:O composition ratio of up to 1.2.

The presence of non-stoichiometric incorporation means that in the region around $J_O = J_{Zn}$ the reaction rate becomes a non-linear function of both J_O and J_{Zn}. Consequently, the growth rate transition from linear to saturation is no longer abrupt. Rather, a curved transition between the two regions will take place. It is this curvature that caused the apparent mismatch in the knee point between the LRI Zn sweep and the LRI O sweep. Figure 3.2 illustrates the behaviour of a real growth rate curve compared to the theoretical growth rate curve. Because of the curvature, there is a slight increase in growth rate as the Zn flux is increased beyond the stoichiometric knee point. Therefore when the O flow is changed under a fixed Zn flux, the corresponding knee point will be higher than expected.

A consequence of non-stoichiometric incorporation has already been observed in the previous chapter. In particular, the curved growth rate vs Zn flux curve presented in Figure 2.25 is a typical signature of non-stoichiometric incorporation. The non-linearity can also be used to explain the apparent anomaly observed in Figure 2.29, where the apparent stoichiometric flux decreased with increasing temperature.

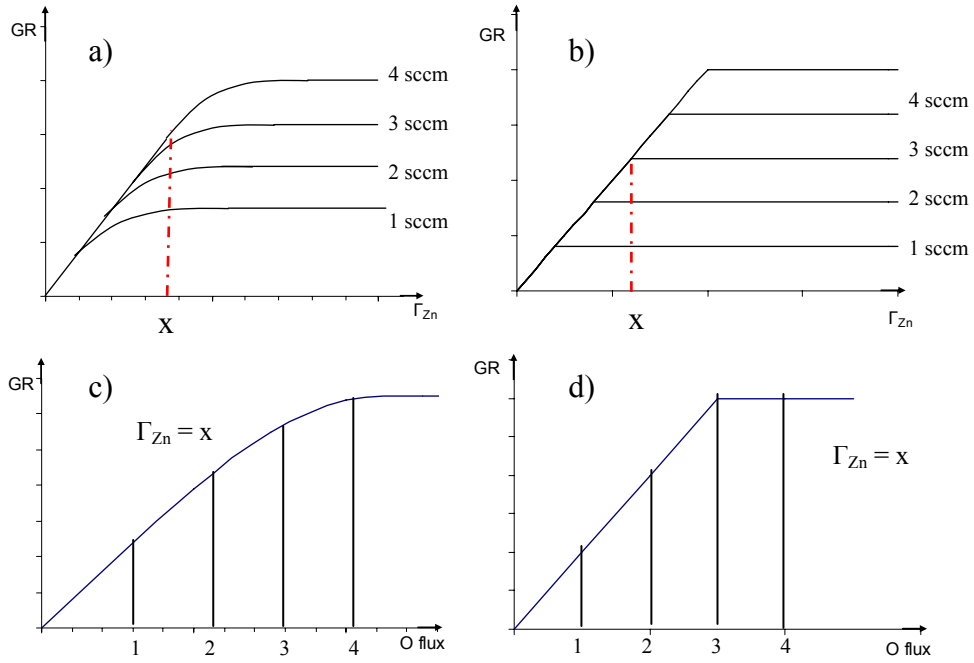

Figure 3.2 Growth rate behaviour of a) experimental LRI curves with gradual saturation and b) theoretical LRI curves with abrupt saturation. The curvature in a) results in a mismatch at the saturation point between the Zn and O sweeps (c and d).

It is possible that at low temperatures, the increased sticking coefficient results in a higher non-stoichiometric incorporation limit, increasing the amount of Zn that can be incorporated with a fixed amount of O, and therefore increasing the growth rate saturation point. Of more relevance here, however, is the effect of non-stoichiometric incorporation on the ability to determine the flux ratio. In particular, as the determination of the flux ratio involves the accurate determination of the transition point, the presence of non-stoichiometric incorporation means that it is almost impossible to determine the true stoichiometric point $J_O = J_{Zn}$. While this might be discouraging, the identification of the non-linear region on the Zn flux curve still allows accurate determination of the near-stoichiometric region. The ability to accurately determine the O-rich region and Zn-rich region is unaltered.

3.2 Effects of Flux Ratio on Film Properties

Based on the investigation in the previous section, the effects of flux ratio on film properties can be studied by first determining which growth region the film belongs to. In particular, to investigate the general effect of flux ratio on the growth of

ZnO, ZnO thin films grown in this work were systematically mapped onto a 2-D plot according to the Zn flux and O flow rate used. A "stoichiometric band" can then be drawn on the map assuming that the near stoichiometric region can be scaled linearly with O flow rate and Zn flux. A film on the left of the band represents a film grown under O-rich conditions, whereas a film on the right of the band represents a film grown under Zn-rich conditions. A film within the stoichiometric band indicates that it was grown under near stoichiometric condition.

Figure 3.3 shows selected ZnO thin films grown in this work mapped using the procedure outlined above. Note that the stoichiometric bands are simplified to stoichiometric lines representing what the stoichiometric point would have been if there was no non-stoichiometric incorporation. As observed in Figure 2.26, the growth rate with a fixed Zn flux varied with plasma conditions. Therefore, the near-stoichiometric regions under different plasma conditions are different. These are

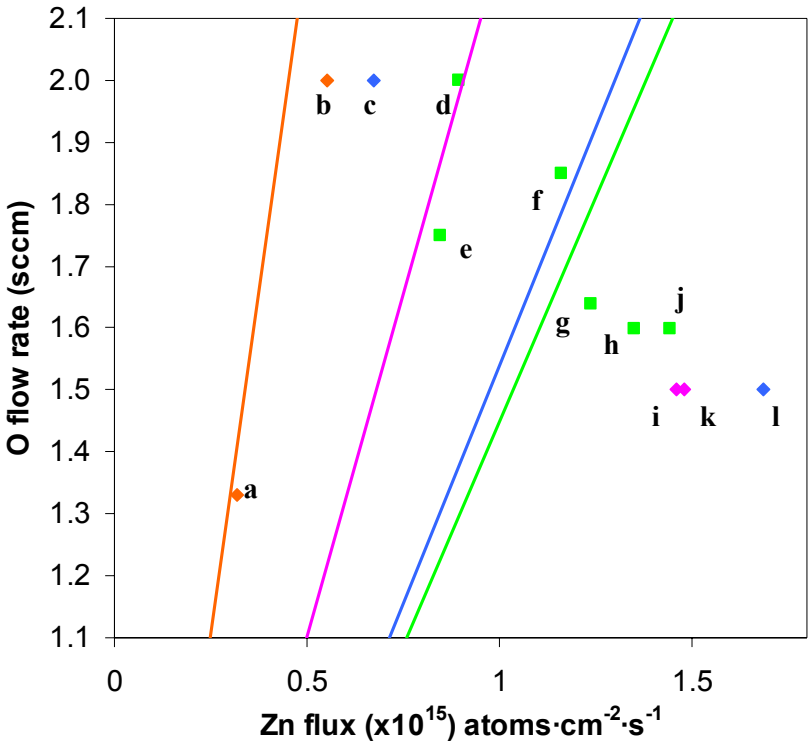

Figure 3.3 Selected ZnO thin films, arranged by the flux ratio during growth. The lines represent the theoretical stoichiometric condition for different aperture plate designs and applied plasma power: orange - 276 hole plate, 300 W; pink - 276 hole plate, 400 W; light blue - 25 hole plate, 400 W; green - 1 hole plate, 400 W. The data are colour coded according to the oxygen condition that was used. Each film labelled in the graph can be traced to the actual film identifier using Appendix B.

represented on the graph as stoichiometric lines of different colours. In particular, the orange line represents 300 W, 276 holes; pink is 400 W, 276 holes; light blue is 400 W, 25 hole; green is 400 W, 1 hole. The data points were colour coded according to the oxygen conditions used. The shape of the data points indicates the Zn condition; diamond points are films grown with the 60 cc conical Zn cell and square points are films grown with the new dual zone Zn cell with cylindrical crucible.

Figure 3.4 shows the RHEED pattern of these films taken after growth at room temperature. The RHEED patterns are arranged such that roughly all the images on the bottom and right hand side of the figure are from Zn-rich films, whereas the RHEED images on the top and left hand side of the figure are from O-rich films. All images were taken in the [1 $\bar{2}$ 1 0] direction. As indicated by the absence of arcs or rings in the RHEED patterns, all films presented are single crystal. A range of surface structures were observed for these films, as indicated by the different degrees of spottiness in the RHEED pattern. It can be seen that most of the samples with streaky RHEED were grown under a Zn-rich condition. This suggests that it is relatively easier to achieve a smooth surface using a Zn-rich condition.

Such a conclusion is confirmed by Figure 3.5, which shows AFM images of the films presented in Figure 3.4, arranged in a similar fashion. Figure 3.5 shows that most of the ZnO thin films grown were covered with surface features that were as high as 500 nm. Compared with the thickness of ~1 μm for most films, this implies a very rough surface. No large scale steps or terraces were observed, and the root mean square (rms) roughness of all samples was above 1 nm. Therefore none of the films can be considered atomically smooth over a large area. In general, the very rough films were grown under O-rich conditions, while the films grown under Zn-rich conditions were in most cases smoother with rms roughness below 10 nm. From these results, it can be seen that under the influence of other growth variables, the bulk of all films, regardless of the Zn:O flux ratio, were grown under a 3-D growth mode. However, the flux ratio acted to enhance or decrease this roughening. Although carrier concentrations ranging from 1×10^{16} cm^{-3} to 1×10^{20} cm^{-3} were measured for these films, no correlation was found between the measurements and the Zn:O flux ratio. The majority of the films have a carrier concentration between 1×10^{18} cm^{-3} to 1×10^{19} cm^{-3}, which is high for nominally undoped ZnO. Further, the carrier mobility was very similar for all samples, with μ_e = 10 to 50 cm^2/Vs.

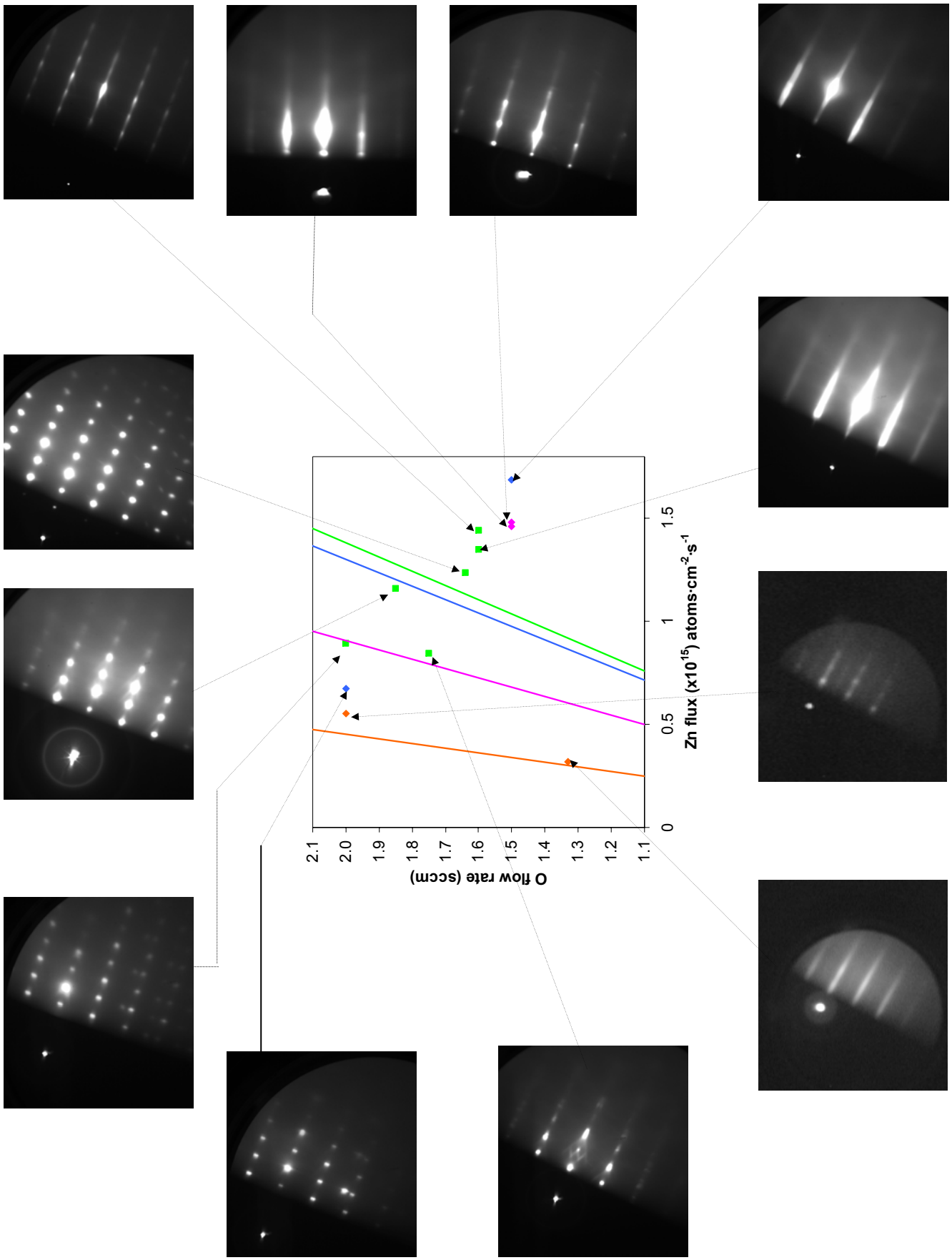

Figure 3.4 After growth RHEED images of ZnO thin films grown under different Zn:O ratios. In general, streaky RHEED pattern is more easily achieved with a Zn-rich condition.

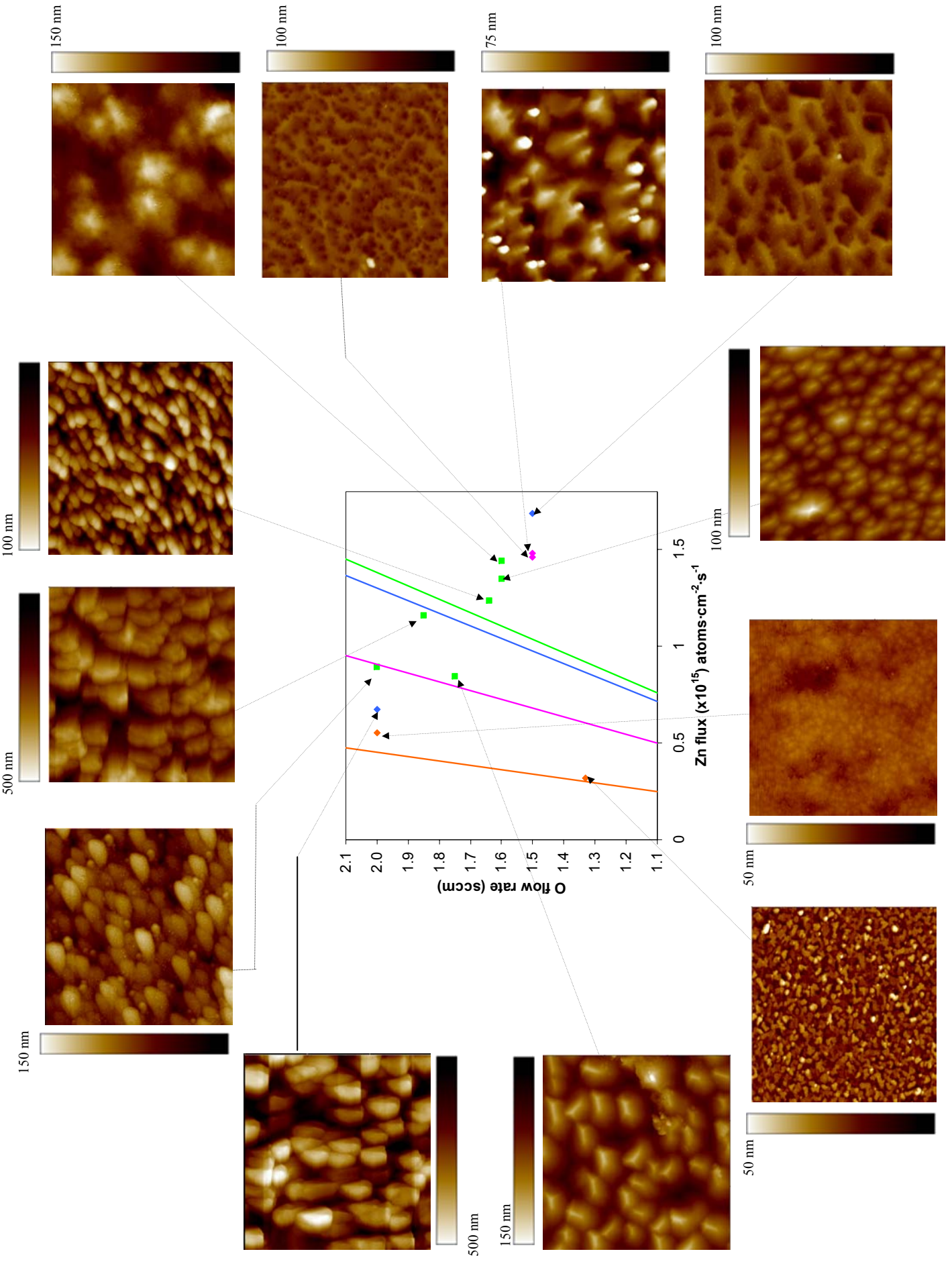

Figure 3.5 The AFM images of ZnO thin films grown with different Zn/O ratios. All images are 3 µm × 3 µm in area. Generally the surface of the ZnO thin films grown in this thesis is not smooth, regardless of the flux ratio, suggesting that other growth variables are more important in determining the surface structure. However, the roughness increases as the growth conditions tend toO-rich.

To investigate the effect of flux ratio further, a series of three films were grown under exactly the same conditions with the exception of the Zn flux to change the growth conditions from O-rich to near stoichiometric to Zn-rich. The values of the Zn flux were chosen based on the LRI experiment presented in Figure 2.25 and scaled for an oxygen flow rate of 1 sccm to give a slightly reduced growth rate (which could possibly improve the crystal quality [143]). The films were all grown with a ~50 nm low temperature buffer layer at 300 ºC directly on epi-ready (0001) sapphire substrates prior to the high temperature deposition at 650 ºC. Both the buffer and the HT layer were grown using an applied RF power of 400 W. The thickness of the films was kept constant (~500 nm) to eliminate thickness effects. Note that these three films were not mapped in Figure 3.3. This is because the aperture plate used in this experiment (and that used in Figure 2.25) was a new 276 hole plate that is different to the old 276 hole plate used in the experiments presented in Figure 3.3 (and in Section 3.3) which was partially clogged due to extensive usage. However, it is expected that apart from the increased growth rate due to the increased throughput of the new plate, the behaviour of the plasma source and its effects on the flux ratio and film properties would be the same as the old plate.

Figure 3.6 shows the RHEED image of the Zn-rich, O-rich and near stoichiometric films in the $(1\ \bar{2}\ 1\ 0)$ and $(1\ 0\ \bar{1}\ 0)$ orientations. It can be seen that all three films were single crystal, but the films were deposited in a 3-D growth mode, with the RHEED pattern dominated by spots for all three films. It is clear that the surface quality degraded as the growth condition was changed from Zn-rich to near stoichiometric to O-rich. Arcs were observed on the RHEED pattern of the O-rich sample, suggesting the existence of random rotation of columnar growth features [144]. The RHEED patterns for the $(1\ \bar{2}\ 1\ 0)$ and $(1\ 0\ \bar{1}\ 0)$ directions were essentially the same for the O-rich sample, further suggesting that the O-rich grown film has a high density of rotation domains, which are regions within the ZnO epilayer that are 30º rotated from the main crystal structure, and are associated with inferior crystal quality (see Chapter 4). This evolution from spotty streak to spotty arc RHEED patterns with decreasing Zn flux is consistent with the general trend observed previously, where Zn-rich films are typically smoother and of higher quality.

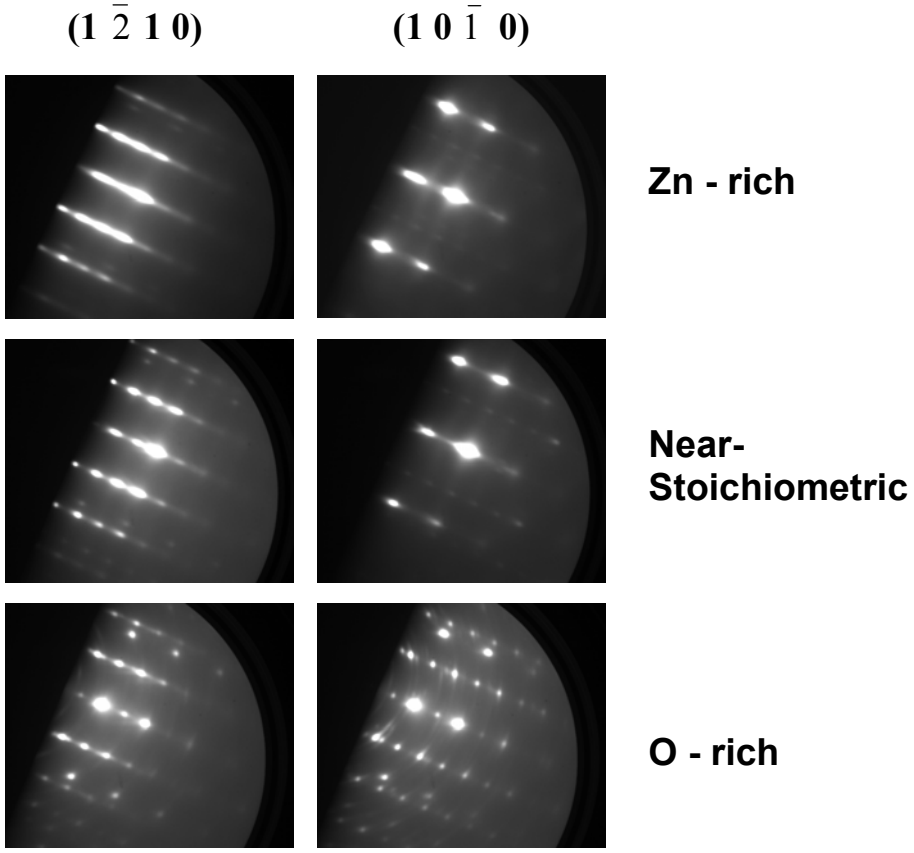

Figure 3.6 After growth RHEED images of the ZnO thin films grown under Zn-rich, near stoichiometric and O-rich flux conditions with other variables kept constant (The oxygen plasma was kept at 1.6 sccm and 400 W and T_g = 650 °C for all three films). The O-rich film is clearly inferior from the rotation domains and arcs visible in both directions.

Figure 3.7 shows SEM images of the three films. It can be seen that both the Zn-rich and stoichiometric films have smaller structures and a more regular surface than the O-rich film, which is consistent with the RHEED pattern variation observed. The structure of the surface changed from somewhat corrugated morphology under the Zn-rich condition, to a relatively flat pit surface with sparsely distributed irregular islands for the near stoichiometric condition, to an irregular 3-D island surface with large features under O-rich condition.

AFM was performed on the three films to observe the detailed features of the surface. Figure 3.8 shows the AFM scan of the three films over a 500 nm × 500 nm area and the corresponding cross section profile of the surface. It can be seen that the feature size and feature height increased from Zn-rich to near stoichiometric to O-rich. In fact the surface roughness was measured to be 3.22 nm,

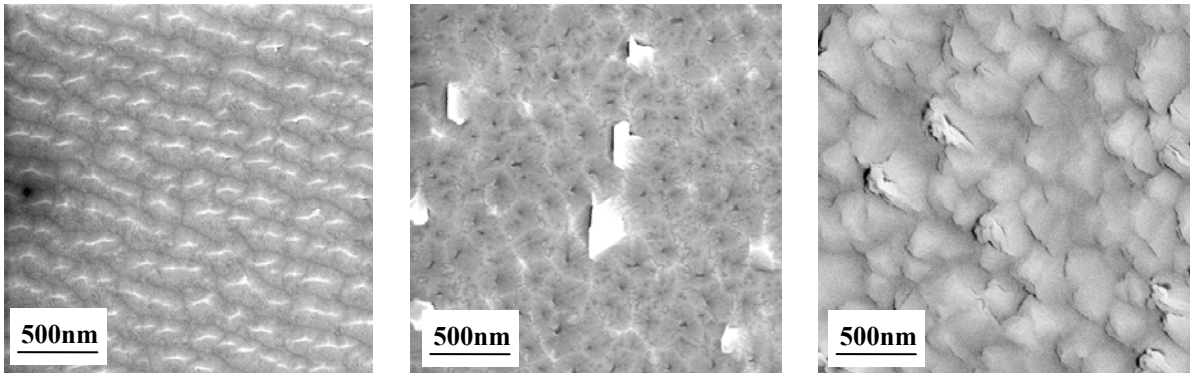

Figure 3.7 SEM images of the films grown with different Zn/O ratio (as shown in Figure 3.6), from the left: Zn rich, near stoichiometric and O-rich.

3.35 nm and 33.0 nm for the Zn-rich, near stoichiometric and O-rich grown films, respectively. From this, it is clear that although none of the films can be considered atomically smooth the O-rich film is considerably rougher than the films grown under the other two conditions. The Zn-rich film surface is covered by small islands of diameter ~150 nm with round peaks. These are distinctly different from the pits that formed on the film grown under a near stoichiometric condition, which have steeper sidewalls that meet at a point. None of the films showed any terracing or steps on the film surface.

This change in morphology is slightly different to that reported by Chen et al. [145], who observed a morphology change from irregular steps with islands to large regular terraces to hexagonal pits between atomically smooth steps as the growth condition was changed from O-rich to stoichiometric to Zn-rich. Murphy et al. have also investigated the effect of flux ratio, and found the exact opposite — that under Zn-rich conditions, features on the order of 100 nm in size and height are observed [146]. It would be desirable to link these different observations into a single model of ZnO growth.

The surface evolution of a thin film is closely related to the surface diffusion process, as illustrated in Figure 3.9. At any given time, the surface of the thin film will have a morphology predetermined by different growth variables (Figure 3.9a). As more reactants arrive on the surface, two possible processes can take place. Under a diffusion dominant regime, the diffusion rate is sufficiently high that the surface adatoms have enough time to diffuse to an energetically favourable site, such as kinks and step edges, before incorporation. Therefore as the growth progresses, the

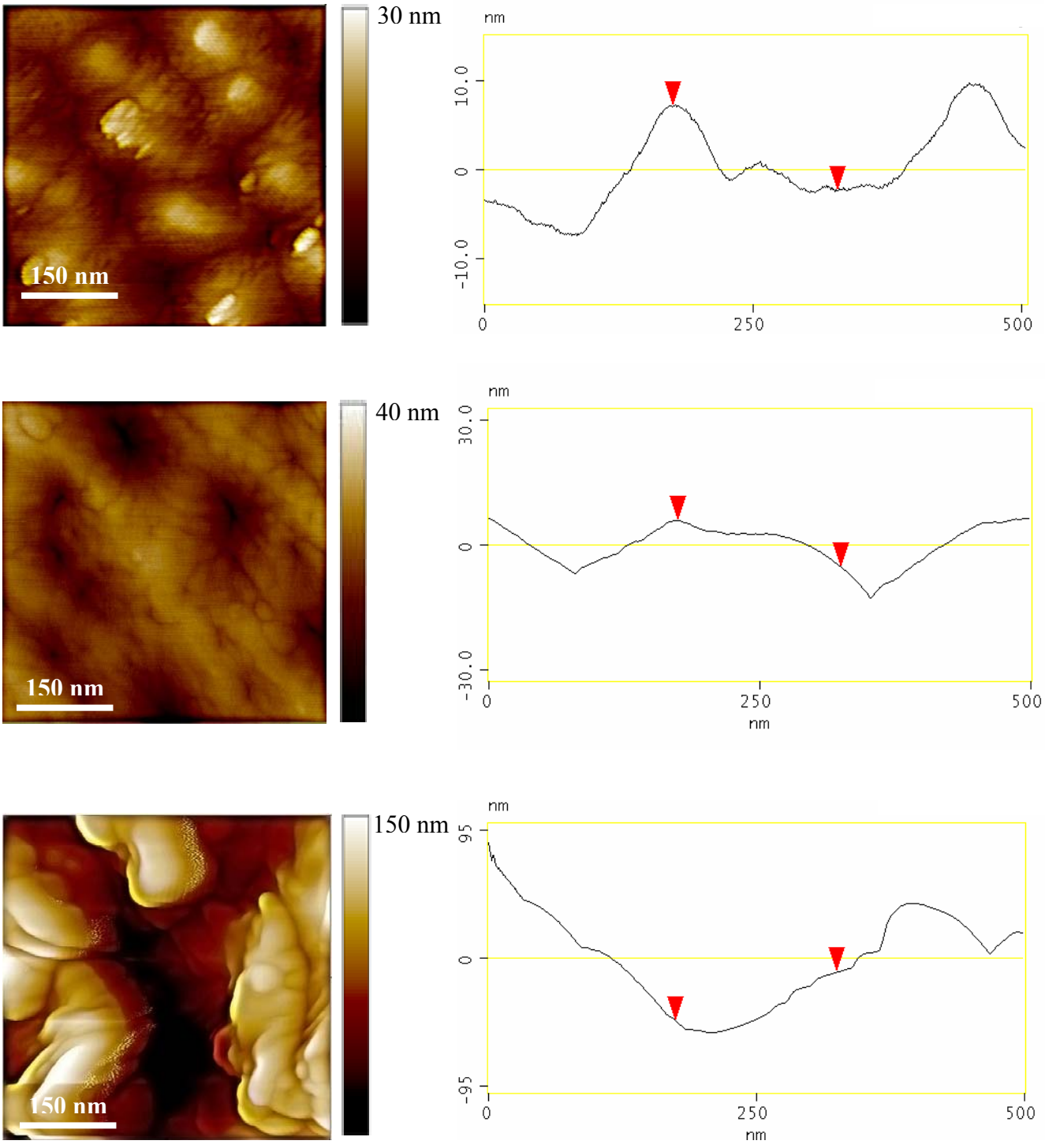

Figure 3.8 AFM images and line scans showing the height information of the films grown under different Zn/O ratio. From the top: Zn rich, near stoichiometric and O-rich.

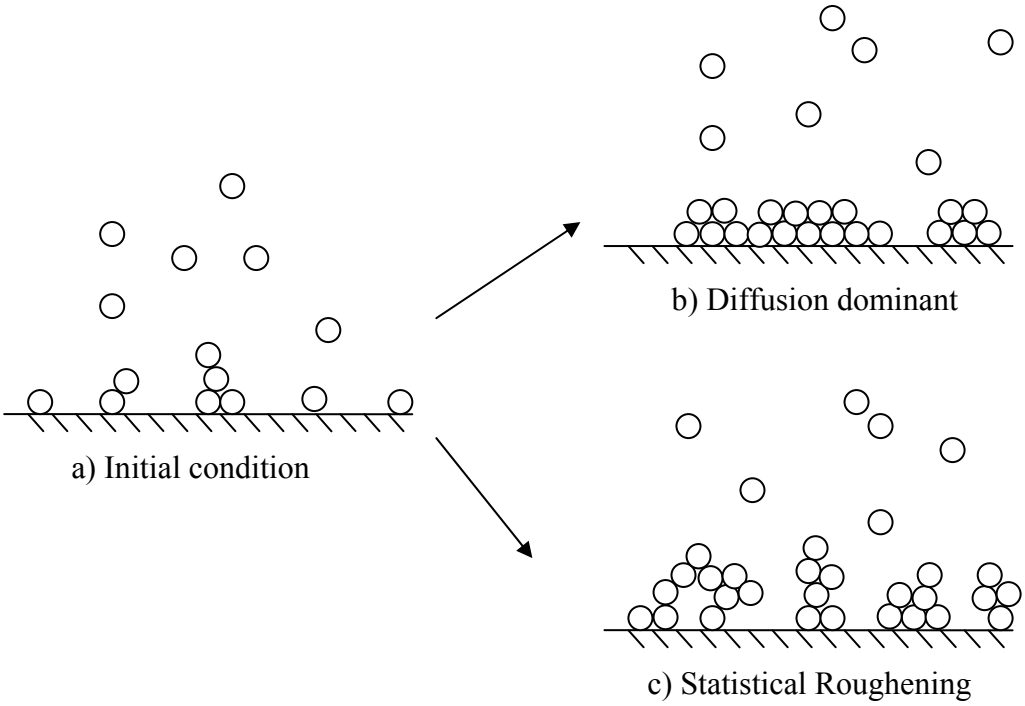

Figure 3.9 A simple diagram of a deposition process showing the effects of diffusion and statistical roughening. Under the diffusion dominant regime the adatoms can move to energetically favourable sites, usually at the edge of a step or a kink, and the atoms align in a smooth fashion. When the diffusion is severely limited, adatoms become immobile and stick to the sites they land on, resulting in statistical roughening.

morphology will become smoother (Figure 3.9b). This regime is the most desirable for thin film growth. However, when the diffusion is severely limited, deposition will occur under a statistical roughening regime, where the adatoms incorporate almost immediately upon reaching the surface. Therefore, the surface structure will be dependent on the position of adatom arrival (which is random in nature), resulting in an irregular surface (Figure 3.9c).

The surface irregularity and extreme roughness observed under O-rich conditions can be readily explained by statistical roughening. In particular, MBE grown ZnO films on c-plane sapphire are generally O-polar. With this surface polarity, O adatoms on the surface interact with three Zn (incorporated) atoms whereas Zn adatoms interact with only one O atom (see Figure 1.2). Therefore, the O adatoms move much slower than Zn adatoms, and hence the morphology is governed by the movement of Zn adatoms [145]. Under O-rich conditions, the diffusion of the Zn adatoms is limited due to the immediate stabilisation by the excess oxygen, resulting in statistical roughening which produces the extremely rough surfaces and poor crystal quality observed. This observation is consistent with previous reports on

other material systems such as GaN and ZnSe, where cation stabilised growth regimes were observed to perform better than anion stabilised growth [133, 134].

Under near stoichiometric or Zn-rich conditions, the relative O flux is reduced, which reduces the O adatom surface concentration, allowing Zn adatoms to diffuse further before incorporation. Hence, the Zn adatom diffusion rate is improved, resulting in the smoother and more regular surfaces observed, as predicted by the diffusion model in Figure 3.9. However, the diffusion model cannot explain the island and pit formations observed on these regular surfaces. Both the formation of islands and pits can result from the strain relaxation of thin films [147]. For example, Heying et al. observed the formation of pits in the MBE growth of GaN under nitrogen-rich conditions, and suggested that the pits originated from the termination of threading dislocations [116]. Chen et al. however observed pits under Zn-rich conditions for ZnO films [145].

The discrepancy of the two can be explained by the fact that the growth of GaN on a MOCVD GaN template results in a Ga-polar GaN surface, whereas the growth of ZnO on sapphire results in an O-polar ZnO surface. As explained previously, the faster Zn adatoms govern the surface morphology of O-polar ZnO surfaces. Using a similar argument, it can be deduced that N adatoms govern the surface morphology of Ga-polar GaN surfaces. Therefore, the effects of N-rich conditions on Ga-polar GaN studied by Heying et al. on surface morphology are in fact the same as that of Zn-rich conditions on O-polar ZnO thin films. Under these conditions, the increase in diffusion of the most mobile adatom type allows adatoms to travel upstep, magnifying small pits formed from dislocation termination into large, hexagonal pits, resulting in pit dominant surfaces [145]. This explains why most Zn-rich films grown in the present study had a pit dominant morphology (c.f. Figure 3.5). The pit morphology observed for the near stoichiometric film (Figure 3.7) can also be explained by the improvement of Zn adatom diffusion through the increased Zn flux. However, some Zn-rich films, such as the one shown in Figure 3.7, were observed to have an island dominant morphology. This is inconsistent with the explanation described here.

As mentioned previously, both islands and pits are capable of strain relaxation. In fact, theoretical treatments have shown that islands and pits can relieve strain equally well provided that the slope of the sidewalls is infinitesimal [147]. However, as the slope increases, pit formation becomes increasingly energetically favourable,

and therefore such features nucleate more quickly and become more abundant compared to islands [148]. Therefore, the formation of island dominant morphology requires the suppression of pit formation. Previous studies have shown that the formation of pits can be suppressed when there is a high concentration of adatoms [149, 150]. Therefore, the regular island morphology observed for the Zn-rich film in Figure 3.7 can be explained by an over-concentration in surface adatoms. In particular, even though the adatom diffusion rate is increased under Zn-rich conditions, an extremely high Zn flux coupled with a low desorption rate from a relatively low growth temperature can lead to an over-concentration of Zn adatoms on the growth surface. This results in the suppression of pit nucleation, leading to the formation of islands.

Murphy et al. reported the growth of ZnO thin films with extreme roughness under Zn-rich conditions, even though they have shown that the ZnO films were O-polar. By using a stochastic model, they attributed this roughening to a large lateral diffusion length (i.e. a high diffusion rate) [146]. This contradicts the observations here. However, if one examines their modelling technique closely it can be seen that a diffusion length close to the dimension of the simulation lattice was chosen, which means that edge or finite size effects cannot be ignored. This is not a very good representation of the real situation, as compared to an adatom, the substrate lattice is semi-infinite. According to the Das Sarma - Tamborenea (DT) model (the model used by Murphy et al.), finite size effects would lead to the saturation of feature heights [151]. This is evident in Murphy's paper. Further, the DT model actually suggests an increase in regularity and reduction in surface roughness with increasing diffusion length [151]. Consequently, the roughening observed by Murphy et al. was not due to an increased diffusion length. Rather, the roughening observed by them resembles statistical roughening caused by a reduced diffusion length. At this stage, it is not clear how the increased Zn flux has led to the roughening observed by Murphy et al. However, similar rough surfaces were observed in this work on films grown under extremely Zn-rich conditions (details of which are provided in the next section). This suggests that extremely high Zn flux might lead to a reduction in adatom diffusion.

Other than the structural properties and surface morphology, the flux ratio was also observed to affect the optical properties of the ZnO thin films grown. Figure 3.10 shows the low temperature PL of the three films in the study. The near bandedge

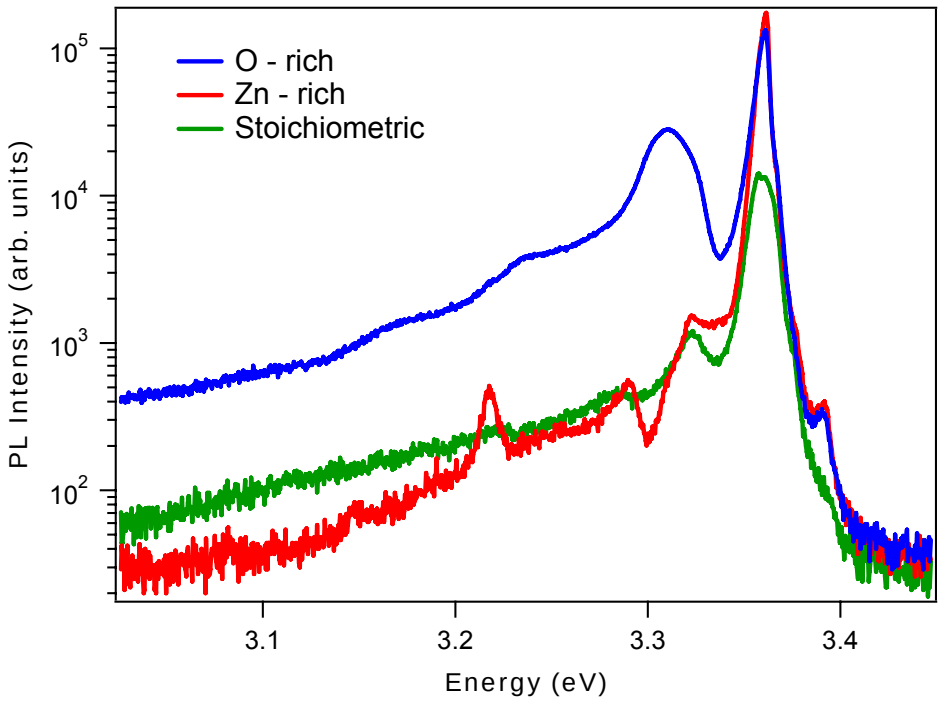

Figure 3.10 The low temperature (4 K) PL for the ZnO films grown under different Zn/O ratio, showing the near bandedge emission only. The defect band emission was found to be negligible at low temperatures.

emission (NBE) at 4 K of all three films is dominated by the donor bound exciton emission at 3.3615 eV. The Zn-rich and O-rich films, however, are more feature rich than the film grown at near stoichiometric condition. In particular, apart from the dominant donor bound exciton emission, B exciton emission can be observed at 3.3918 eV for both Zn-rich and O-rich samples. It can also be seen that there are shoulders on the donor bound exciton peak for these two samples, suggesting the presence of multiple bound exciton states. At energies below the excitonic emissions, the PL response of the Zn-rich sample and the O-rich sample start to differ. A large band of unknown origin at 3.3112 eV is observed on the O-rich sample, which has previously been described as a LO-phonon replica [152] and surface state related emission [153]. This peak was observed on all O-rich films that were characterised in this work. A ripple like structure can be observed below this band, which can be attributed to the 1st and 2nd LO-phonon replicas of the band from the 72 meV spacing between the peaks of the ripple [154].

For the Zn-rich sample, the band is replaced by two peaks at 3.3232 eV and 3.2906 eV, with a distinct asymmetrical dip in between. The two peaks have been previously and unambiguously identified as the two electron satellite and the 1st LO phonon replica of the excitonic emission [155], respectively, whereas the dip has been

attributed to the Fano resonance effect which is usually observable in high quality polar semiconductors [156]. The Zn-rich sample also has a distinct 2nd LO phonon replica at 3.2180 eV. The observations of distinct LO phonon replicas, Fano resonance and the B-exciton emission on this sample as well as in many other samples grown under Zn-rich conditions suggest that a Zn-rich condition is more beneficial for the optical emission of ZnO thin films. The FWHM of the Zn-rich film exciton emission is 4.7 meV. This is smaller than the 6.0 meV FWHM measured for the O-rich sample and 14.3 meV measured for the near-stoichiometric sample. This confirms the superior crystal quality of the Zn-rich sample compared to the other two samples. Note that a FWHM of 2.2 meV was reported by Ko et al. [135], 5 meV by Murphy et al. [136] and 8 meV by Jung et al. [83]. This shows that the optical quality of the samples here in this work is comparable to other reports in the literature.

The effect of the Zn/O ratio on the low temperature PL of ZnO films observed here is quite different to what was previously reported. In particular, Ko et al. reported that while films grown under Zn-rich conditions have the best optical quality (which is consistent with this work), the optical quality was found to improve with Zn flux, i.e. an improvement in optical emission from O-rich to stoichiometric condition was observed [135]. This is different from that observed here, where the near stoichiometric film was found to have the worst optical quality. Unfortunately, the origin of this discrepancy is undetermined, as many factors affect the optical response of a material.

Figure 3.11 presents the room temperature PL of the three films, showing both the NBE and the defect band emission (DBE). All three samples have a NBE peak at the same position, originating from exciton-related recombination. It can be seen that the FWHM (101 meV for O-rich, 81 meV for Zn rich and 89 meV for the near stoichiometric film) of the three films is very similar. This similarity of the shape, intensity and FWHM of the NBE of the three samples suggests that the flux ratio has limited effect on the room temperature NBE. The slightly higher intensity observed for the O-rich sample is possibly due to surface effects. The DBE is also very similar for the three samples. This suggests that the flux ratio has limited effects on the generation of deep level defects. Note that for all three samples, the NBE peak intensity is approximately 10 times stronger than the DBE intensity, which is higher than that reported by Murphy et al. [136]. This dominance of NBE even at room temperature is very desirable for optoelectronic applications.

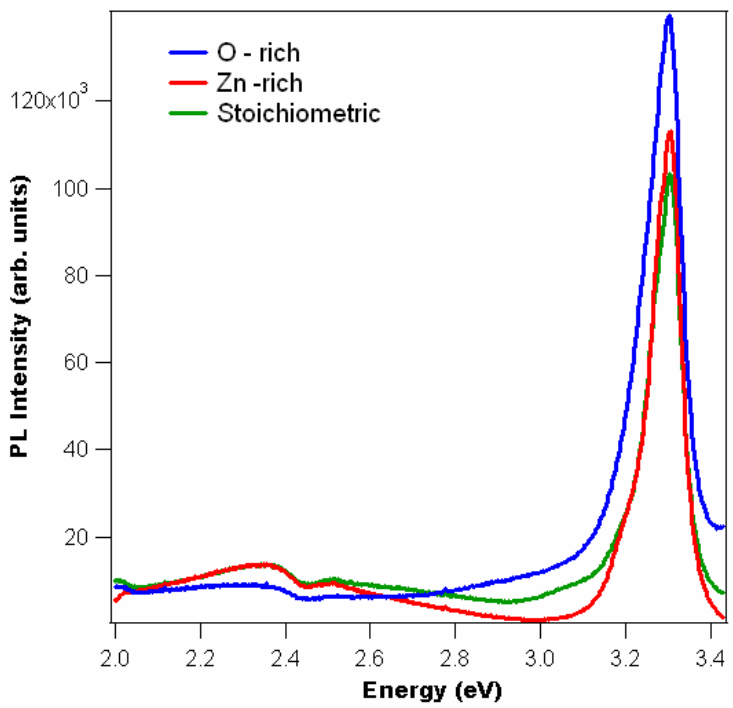

Figure 3.11 Room temperature PL of the ZnO films grown under different Zn/O ratio, showing the near band spectrum (3.0 - 3.4 eV) and defect band spectrum (2.0 eV - 3.0 eV). The large NBE/DBE ratio suggests these films have high optical quality.

Table 3 shows the electrical measurements of the three films. All three films have a carrier concentration of $\sim 1 \times 10^{17}$ cm^{-3}, which is comparable to other reports of MBE grown ZnO [83, 136]. All three films were found to be n-type. The maximum mobility observed was 19 cm^2/Vs from the ZnO film grown under near stoichiometric condition, while an extremely low mobility of 0.9 cm^2/Vs was measured for the O-rich film. Although it is significantly lower than the best mobility reported for MBE films (~140 cm^2/Vs) [86], this low mobility is not uncommon for MBE grown ZnO or ZnO thin films in general. An increase in resistivity from Zn-rich to near stoichiometric to O-rich condition was also observed. Overall, there is a clear reduction in electrical quality by growing under O-rich conditions, but there are limited differences between the Zn-rich and near stoichiometric grown films.

From these, it can be seen that the flux ratio greatly affects the properties of ZnO thin films. It was observed that because of the cation stabilisation effect under O-rich conditions and roughening effect under extremely Zn-rich conditions, there is indeed an optimal growth region where the surface diffusion rate is high enough to sustain a diffusion dominant growth without an over concentration of surface adatoms. The experimental data suggests that the optimum surface morphology is

Table 3: Electrical characteristics via conventional Hall effect measurements for the ZnO thin films grown under different Zn/O flux ratio.

Flux ratio	Carrier Concentration (cm^{-3})	Mobility (cm^2/Vs)	Resistivity (Ωcm^{-1})
Zn rich	4.3×10^{17} (n-type)	15.6	0.93
Near stochiometric	2.0×10^{17} (n-type)	19.1	1.63
O-rich	1.1×10^{17} (n-type)	0.910	13.9

obtained under Zn-rich conditions. Similar observations were made in regards to the optical properties of the ZnO films, where the low temperature optical emission of a Zn-rich sample was found to be superior to films grown in the O-rich or near stoichiometric conditions. The flux ratio seems to have limited effects on the room temperature PL or the electrical characteristics of the ZnO thin films.

3.3 Flux ratio and Active Oxygen

In Section 2.3.4, it was found that the amount of active oxygen generated by the plasma source was affected by both the RF power and aperture plate configuration, and has a non-negligible effect on the growth rate of ZnO thin films. Therefore, it is expected that varying the plasma condition will have noticeable effects on the properties of these ZnO thin films. In addition, the effects of the different oxygen species on the actual flux ratio would also play an important part in determining the properties of the films grown. In this section, the interactive effects of active oxygen species and the flux ratios on the structural, optical and electrical properties of ZnO thin films are described.

To investigate the effects of active oxygen on film properties, the films studied in Section 2.3.4 were characterised using the methods outlined in Section 1.4. These films were grown using different RF power and aperture plate designs to alter the oxygen content, and grown under Zn-rich condition to emphasise the effect of the active oxygen over the flux ratio. All films were grown at 650 ºC with an oxygen flow rate of 1.6 sccm and a Zn flux of 1.2×10^{15} atoms·cm^{-2}·s^{-1} for three hours (most of the films were grown with the 60 cc Zn cell except those grown with the 1 hole plate which used the new Zn cell). Figure 3.12 shows the RHEED pattern of the ZnO thin

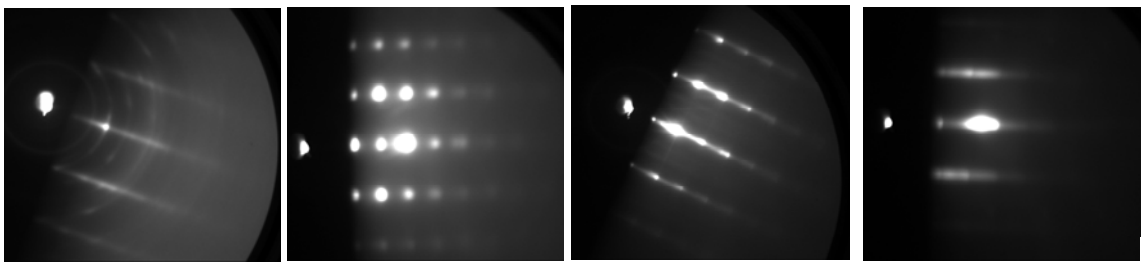

Figure 3.12 After growth RHEED images for samples grown with the 276 hole plate with a fixed Zn flux of 1.2×10^{15} atoms·cm^{-2}·s^{-1}and temperature of 650 ºC. From the left: 200 W, 250 W, 300 W, 400 W.

films grown using the 276 hole plate at different RF powers, taken at room temperature after growth. Generally, it can be seen that with increasing applied RF power the RHEED pattern changed from spotty to streaky. At 400 W, a strong specular spot and a purely streaky pattern was observed, indicating a 2-D surface of very high quality. A similar improvement of surface quality with RF power has been previously reported by Sakurai et al. [82]. This improvement suggests an increase in Zn adatom diffusion with applied RF power.

Figure 3.13 shows the SEM images of the films, displaying the surface morphology. At 200 W, the film surface was relatively uniform, with the formation of irregular hexagonal structures randomly distributed on the surface. As the RF power was increased, the growth became more 3-D, with islands appearing on the surface that almost resemble grains in a polycrystalline film. In this region, the increase in applied power resulted in an increase in the feature size. However, as the RF power was increased from 350 W to 400 W, the surface transformed from an island dominant morphology to a pit dominant morphology, resulting in a smoother surface.

Based on the experimental findings and the diffusion model presented in the previous section, the observed morphology change with applied RF power can be readily explained by the change in adatom behaviour due to the effects of the

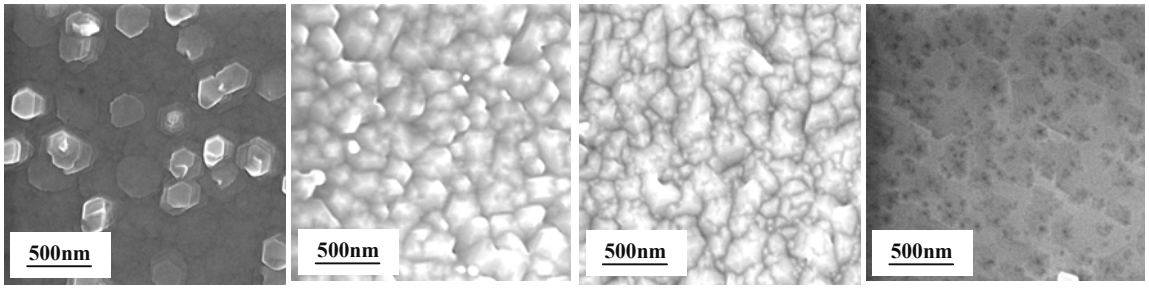

Figure 3.13 SEM images of the ZnO thin films grown with the 276 hole plate. From the left: 200 W, 250 W, 300 W and 400 W.

increased active oxygen on the flux ratio. At low power, the active oxygen content is low, resulting in an extremely Zn-rich growth that, via a mechanism that is unclear at this stage, reduces the adatom diffusion and results in a rough surface with large, irregular features similar to that observed by Murphy et al. [146]. As the amount of active oxygen is increased with increased applied RF power, the Zn/O ratio reduces, improving the mobility of the adatoms. However, the adatom concentration is still too high for pit formation. Therefore, the ZnO surface has an island dominated morphology. As the RF power is further increased, the increased growth rate leads to the coarsening of islands through Ostwald ripening, resulting in generally larger islands with increasing RF power. Above 350 W, the surface adatom concentration is sufficiently reduced that pit formation becomes energetically favourable, resulting in the smooth pit morphology for films grown at 400 W and above.

This proposition is supported by the AFM images in Figure 3.14, which shows that pits started to form even at 300 W. Therefore, the change from island to pit morphology is not abrupt. Rather, it is a smooth transition from island dominated morphology to pit dominated morphology. For the film grown at 200 W, the surface is actually covered with small islands between the large hexagonal structures, resembling the films grown at higher power. This is consistent with the island formation model described previously, and confirms the occurrence of island coarsening with increased applied power.

Figure 3.15 shows the SEM images of a set of ZnO thin films, comparing the effects of RF power and different aperture plate configurations. By using a 25 hole plate, the applied power needed for the onset of hexagonal pit formation was reduced, with a pit dominated morphology observed at 300 W. This is consistent with the

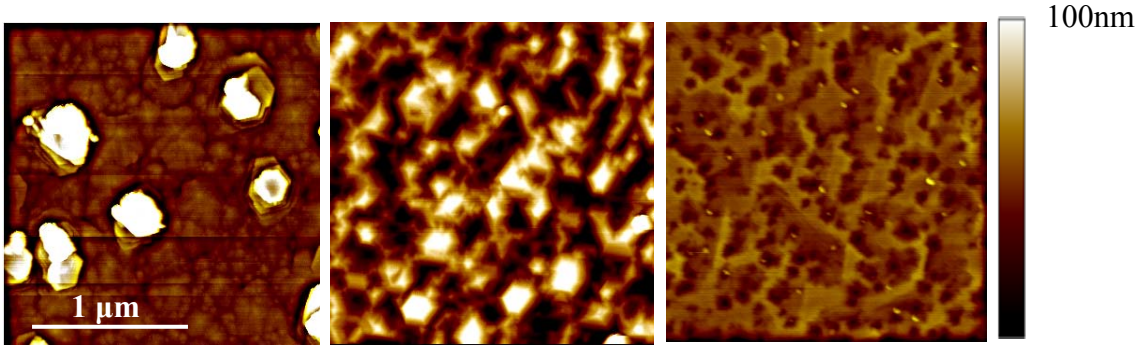

Figure 3.14 AFM images of ZnO thin films grown with the 276 hole plate under different RF power. From the left: 200 W, 300 W, 400 W. All images are 3 µm x 3 µm.

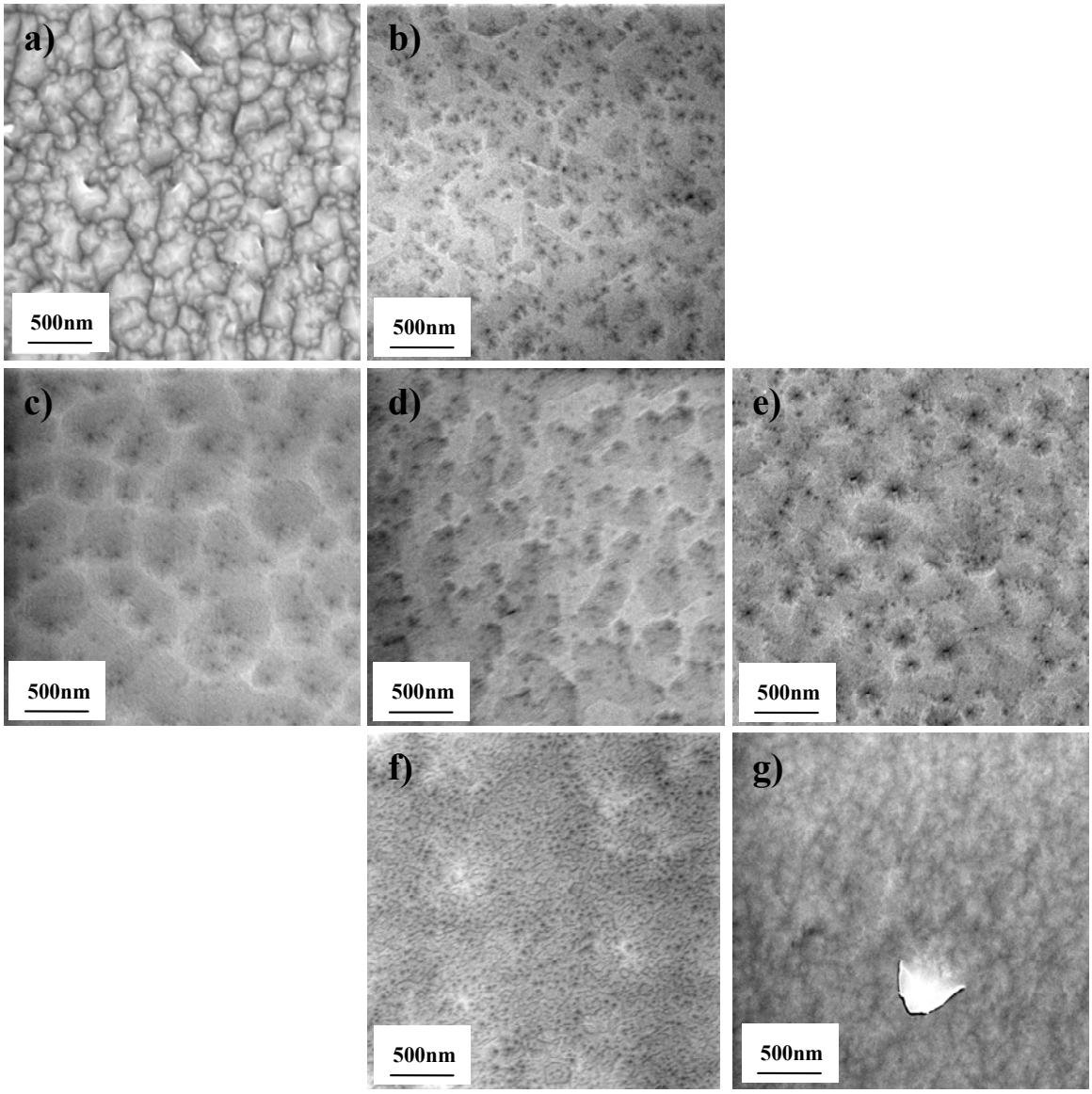

Figure 3.15 SEM images of ZnO thin films grown under different plasma power and aperture plate designs ($\Gamma_{Zn} = 1.2 \times 10^{15}$ atoms·cm^{-2}·s^{-1}and T_g = 650 ºC) : a) 300 W, 276 holes; b) 400 W, 276 holes; c) 300 W, 25 holes; d) 400 W, 25 holes; e) 500 W, 25 holes; f) 400 W, 1 hole; g) 500 W, 1 hole.

growth rate experiment in Section 2.3.4 which suggested that the amount of active oxygen provided was increased by using the 25 hole plate. The surface stayed essentially the same with a further increase in applied RF power, but from the differences in the image contrast it appears that the pits became larger and steeper. Above 400 W, it was observed that some pits were no longer terminated at a point (cf. Figure 3.7), but terminated at enlarged holes of ~10 nm in diameter. At 500 W, the domination of these "terminating holes" is apparent. These holes are remarkably similar to the small pits observed in GaN, and can be associated with the surface

termination of threading dislocations [157]. The increased density of holes with high power therefore implies that the dislocation density increased or the dislocations propagated closer to the surface with increased RF power. Figure 3.15f and Figure 3.15g show the surface structure of two films grown with the 1 hole plate. The surface features observed for these two films were much smaller than that of the other films, even though the RHEED suggested a much rougher surface. Neither of the films have the expected pit morphology.

Figure 3.16 shows the AFM images of three films grown at the same RF power but with different plate designs. It can be seen that the pit size (diameter) increased from ~100 nm for the 276 hole plate grown film to ~500 nm for the 25 hole plate grown film. This increase in pit size can be explained by the coarsening of the pits, similar to the island coarsening process [158]. The film grown with the 1 hole plate, however, has a substantially different surface morphology. In particular, unlike the irregular island morphology previously observed with an O-rich or excessively Zn-rich films, the surface of the film is covered with irregular clusters of ZnO. It seems that this cluster morphology, unlike the pits or island morphologies that was observed, is not an effect of the varying flux ratio on the growth surface. Rather, it is an effect related to the 1 hole plate, and its origin is unclear.

The surface roughness of the ZnO thin films grown under different applied power for the three aperture plates, normalised with the film thickness, is shown in Figure 3.17. It can be seen that the surface roughness decreased exponentially with increasing RF power for all three aperture plates. This decrease in surface roughness suggests that the adatom diffusion rate increased with increasing active oxygen.

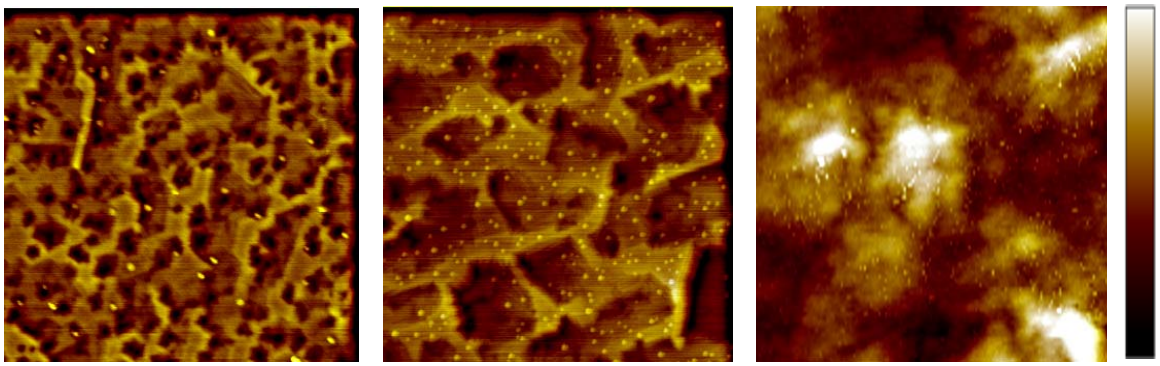

Figure 3.16 AFM images of ZnO thin films grown at 400 W using different aperture plates. From the left: 276 hole plate, 25 hole plate and 1 hole plate. All images are 2 µm x 2 µm. The height scale is to 100 nm for the 276 hole plate and 25 hole plate, and 150 nm for the 1 hole plate.

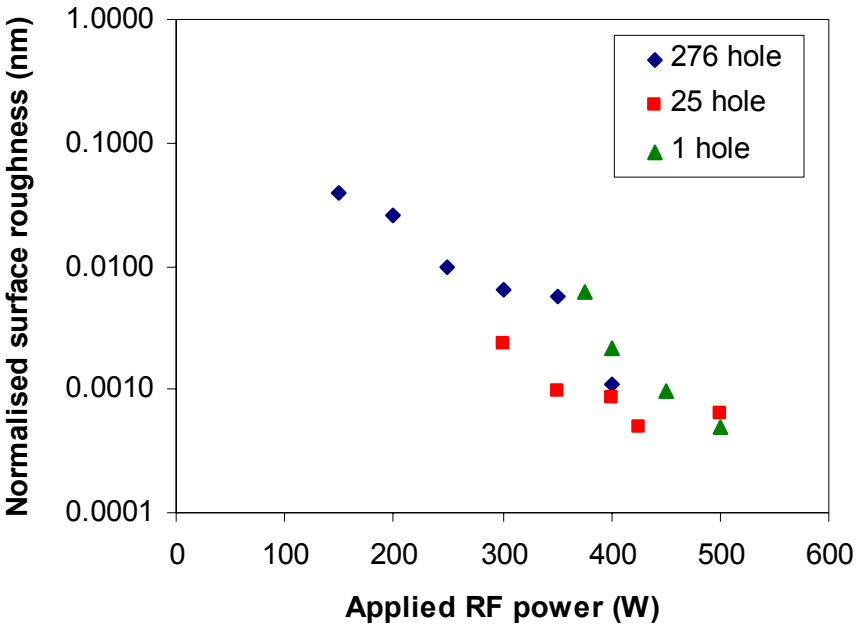

Figure 3.17 The normalised surface roughness for ZnO thin films grown under identical conditions except for the different different plasma conditions.

Furthermore, the exponential decrease of the surface roughness with RF power can be correlated with the saturation of atomic oxygen content with RF power observed in Figure 2.17. Figure 3.18 shows the relationship of the normalised roughness with the normalised O^* emission. The direct overlap of the experimental data points for the 25 hole plate and 1 hole plate suggests that there is indeed a correlation between surface morphology and atomic oxygen content in the plasma. Such a correlation between OES intensity and surface morphology cannot be observed for O_2^*, even though O_2^* was shown to participate in growth from the growth rate experiments. This suggests that O_2^* has a limited effect on the surface morphology of the film, even though it participates in growth. Figure 3.18 highlights the importance of atomic oxygen in the improvement of the surface quality of ZnO thin films.

Note that there is an abrupt change of slope in the graph as indicated by the lines on the figure. It was found that apart from the films grown with the 1 hole plate, every film that lies after the transition point has a pit morphology. As the island or pit density and size increase with RF power (c.f. Figure 3.13 and Figure 3.15), this slope change at the island to pit transition suggests that pit formations are better at reducing the surface roughness than island formations.

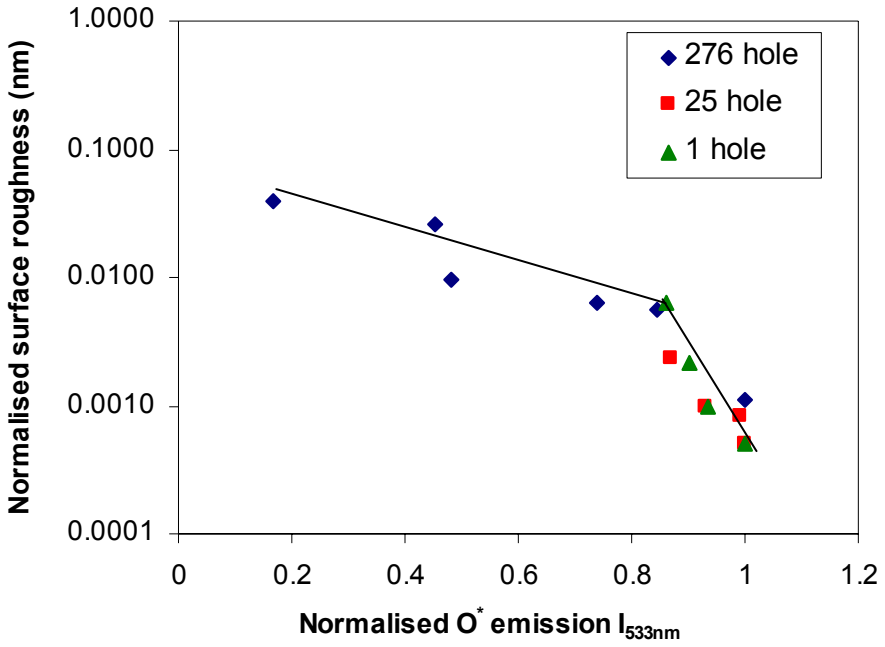

Figure 3.18 Normalised surface roughness compared to the O* emission, showing a strong relationship between the two. The line is a guide for the eye only. However, there is a distinct change in the slope of this line, which interestingly corresponds to the change from island to pit morphology.

Even though a relatively smooth surface was observed for films grown with the 1 hole plate, the RHEED of these films suggests that the crystal quality of these films is much lower than the films grown with the other two plate designs. This shows that the surface roughness value does not always give a good indication of the crystal quality. The degrading effect of the 1 hole plate can be confirmed by XRD measurements. Figure 3.19 shows the θ-2θ curve for the sample grown with the 1 hole plate and the sample grown with 25 hole plate, both grown at 400 W. By using the 1 hole plate, the quality of the crystal was significantly decreased with a much broader and weaker diffraction peak detected for both the ZnO (0002) and ZnO (0004) directions. In fact, a FWHM of ~2000 arcsec was observed for the XRD rocking curve of the 1 hole plate film, compared to 388.4 arcsec for the 25 hole plate film. This huge increase suggests that samples grown with the 1 hole plate have a high concentration of defects and dislocations.

While the flux ratio was observed to have limited effect on the electrical characteristics in the three samples studied in the preceding section, the variation in active oxygen seems to have a substantial effect on the electrical quality of the ZnO thin films. Figure 3.20 shows the carrier concentration and the mobility variation with

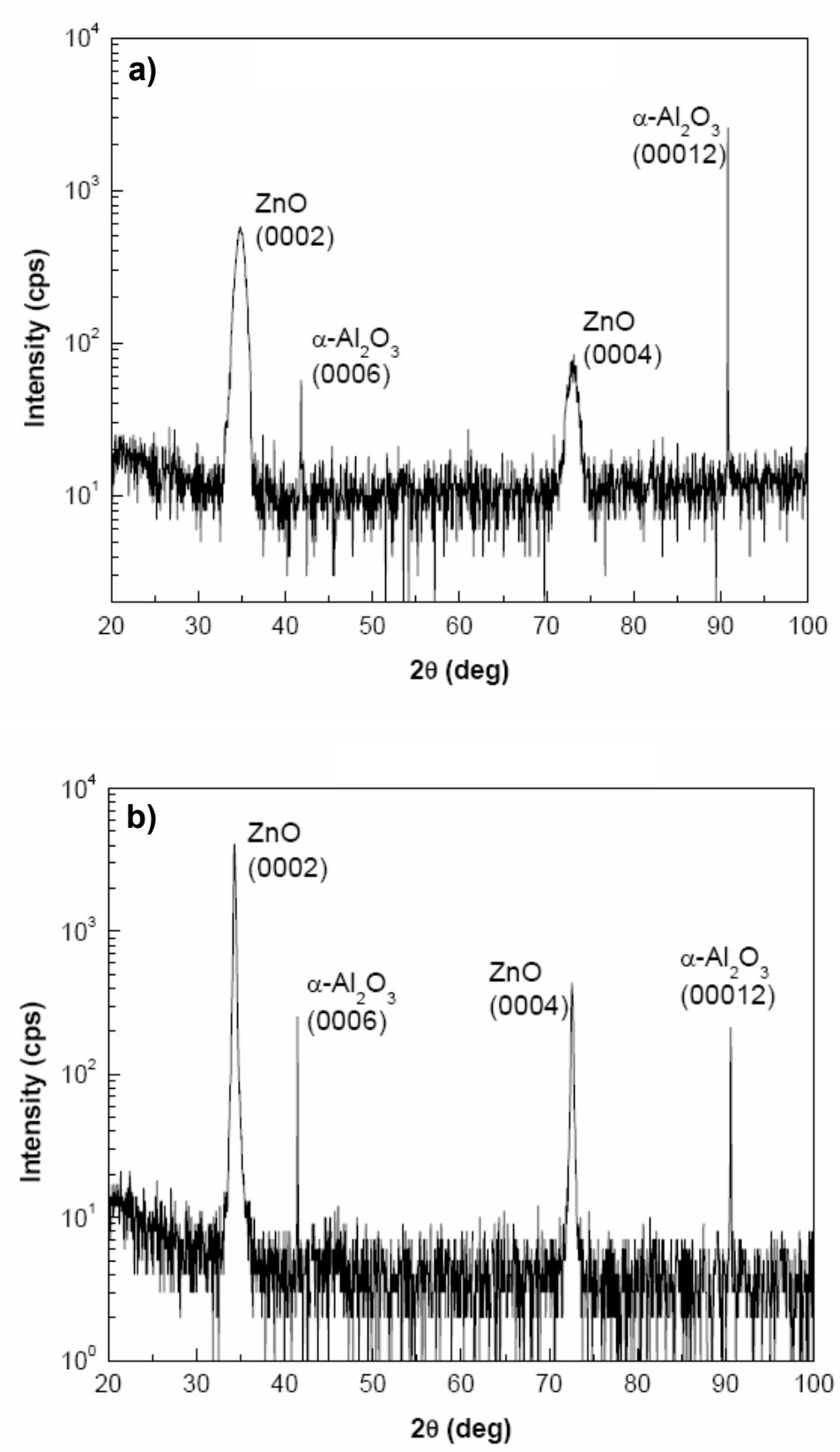

Figure 3.19 The θ-2θ of ZnO thin film grown at a) 400 W, 1 hole plate and b) 400 W, 25 hole plate.

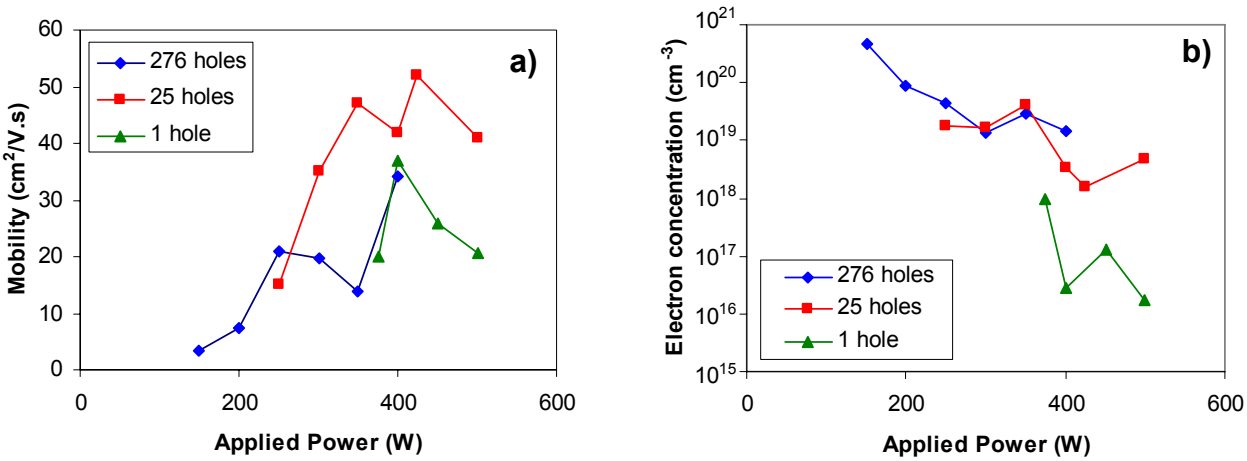

Figure 3.20 The a) carrier mobility and b) concentration of ZnO thin films grown using different plasma conditions as measured from conventional Hall effect measurements.

RF power for the three aperture plate designs. It can be seen from Figure 3.20a that the mobilities of the samples are not drastically different between the different plasma condition, with considerable scatter present in the data for all three aperture plates. This is due to uncertainty in the measurements as the mobility values are relatively low. In particular, it is expected that in some of the trends, for example, the decrease in mobility at high RF powers for 25 hole and 1 hole plate, the small change in mobility can be readily explained by the experimental errors and statistical variation between measurements. However there are some variations evident that can be attributed solely to the change in active oxygen, not the change in flux ratio. For example, the mobility for the 25 hole plate obtained was higher compared to the other two plates, suggesting that the active oxygen provided by the 25 hole plate is more beneficial for improving the electrical quality. However, even with the 25 hole plate, the maximum mobility achieved was 52 cm^2/Vs, still much lower than the expected (bulk) value.

The carrier concentration showed a very clear trend with active oxygen. By varying the RF power with the 276 hole plate, the carrier concentration was reduced from $\sim 5 \times 10^{20}$ cm^{-3} to $\sim 1 \times 10^{19}$ cm^{-3}. Using the 25 hole plate, the carrier concentration was reduced further to a minimum of $\sim 1 \times 10^{18}$ cm^{-3} at 400 W. Changing to the 1 hole plate distinctly resulted in a major reduction in carrier concentration. In fact, two orders of magnitude of carrier concentration reduction was observed, giving a minimum carrier concentration of $\sim 1 \times 10^{16}$ cm^{-3}. Again, this type of variation is inconsistent with the effect of flux ratio observed in the last section, and is therefore contributed by the variation in the oxygen content of the plasma.

Comparing the dramatic decrease in carrier concentration with the increase in ion content observed for the 1 hole plate plasma in Figure 2.18, it seems that the reduced carrier concentration observed is related to the increased ion production. To confirm this hypothesis, the sheet resistivity of the samples was compared to the relative ion content measured from OES - the intensity ratio between the ionic emission O_2^{+*} and the total neutral emission $O^* + O_2^*$. Note that the sheet resistivity was used instead of the bulk resistivity as sheet resistivity offers a fairer comparison between thin films with different thickness. The results are plotted in Figure 3.21. From the figure, it can be seen that even though there is considerable scatter in the data, the sheet resistivity in general is proportional to the relative ion content. This strongly implies that an increase in resistivity is linked to an increase in the plasma ion content. Note that this is consistent with previous reports of electrical isolation in ZnO thin films deliberately bombarded by ions. Such electrical isolation has been attributed to an increase in point defect creation due to ion damage [159] [160].

Although the change in flux ratio has almost no effect on the room temperature PL of the ZnO thin films, it was observed that films grown under different plasma conditions has vastly different room temperature optical response. Figure 3.22, Figure 3.23 and Figure 3.24 display the room temperature PL of the

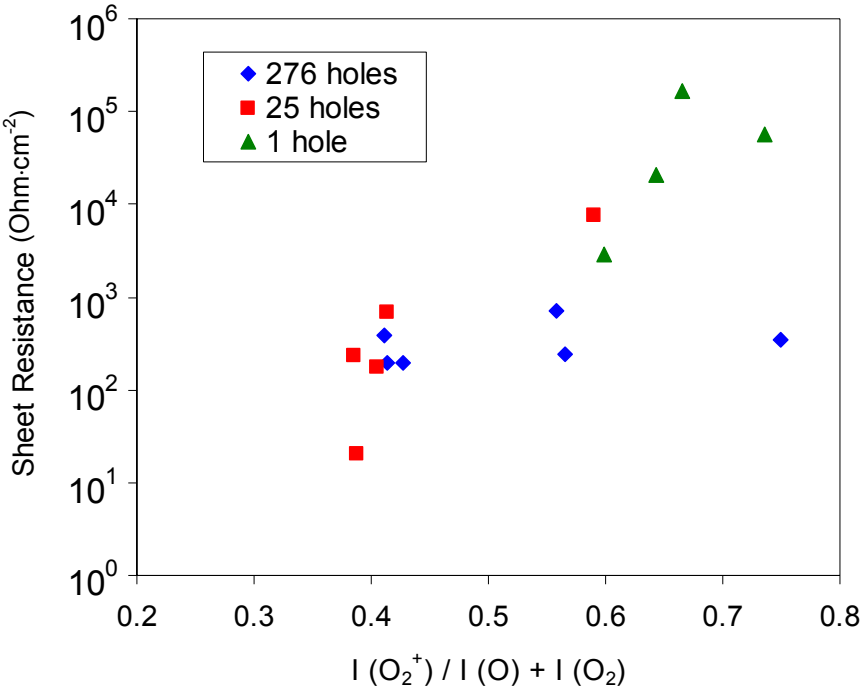

Figure 3.21 The sheet resistance of the ZnO thin films grown under different plasma conditions, plotted again the ion content of the plasma used.

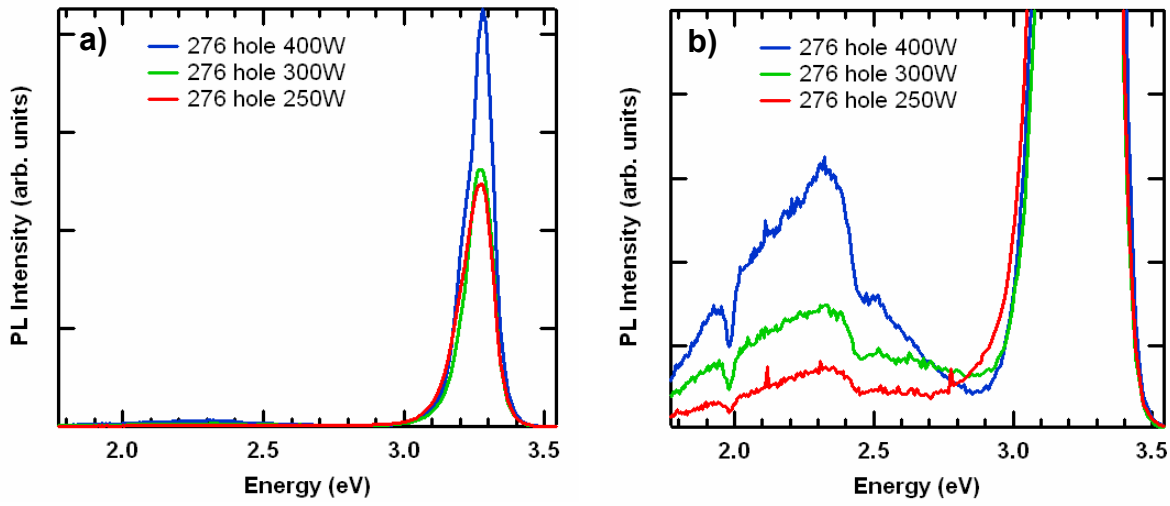

Figure 3.22 The room temperature PL of the ZnO thin films grown with the 276 hole plate: a) full spectrum and b) defect band emission.

ZnO thin films grown with 276 hole plate, 25 hole plate and 1 hole plate, respectively. From Figure 3.22, it can be seen that for the 276 hole plate, there is a strong correlation between the applied RF power and the NBE intensity and FWHM. In particular, it was observed that the NBE intensity of the film grown at 400 W is almost doubled that of the film grown at 300 W, which in turn has a stronger NBE than that of the film grown at 250 W. At the same time, the DBE intensity was observed to increase with the applied RF power. Note that the two side features at ~ 2.5 eV and ~ 2.0 eV on the defect band are actually spectrometer artefacts, and therefore the defect band is in fact a symmetrical band centred at 2.3 eV. This DBE has been previously attributed to a number of impurities such as Cu [161], and defects such as V_o [162] and V_{Zn} [163] and their complexes. In the case here since a change in the impurity level is unlikely as the films were prepared and grown the same way except the plasma conditions, it is reasonable to believe that the DBE observed in this work is due to structural defects rather than impurity associated deep levels.

Figure 3.23 shows the variation in PL with applied power for the 25 hole plate. The variation in the NBE emission between the samples does not follow a distinct trend, with the brightest emission observed at 300 W and weakest at 500 W. More distinct features can be observed in the NBE of the samples grown with the 25 hole plate compared to those grown with the 276 hole plate. In particular, features can be seen on the NBE of most films at 3.28 eV, 3.24 eV and 3.19 eV. Most 25 hole plate films also have a stronger DBE emission compared to films grown with the 276 hole

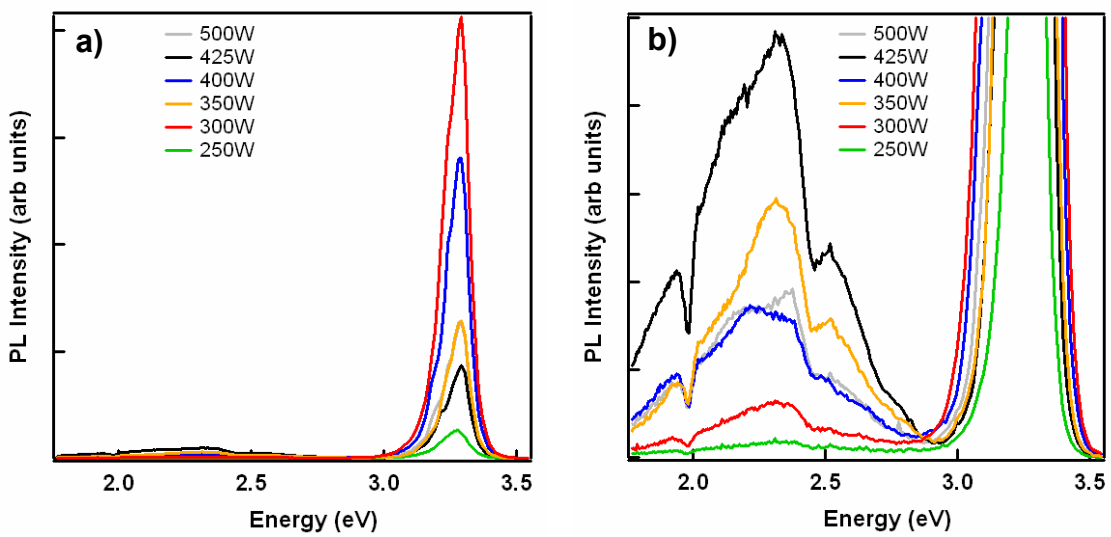

Figure 3.23 The room temperature PL of ZnO thin film grown with the 25 hole plate: a) Full spectrum and b) defect band emission.

plate. However, the overall NBE to DBE ratio was still quite large. At 400 W, the integrated intensity of the NBE is 10 times higher than the DBE, while the ratio between the peak intensity of the NBE and DBE is close to 300. Note that as a comparison, the NBE emission observed for a film grown at 400 W with the 276 hole plate (as displayed in Figure 3.23) has an intensity approximately 75% of that observed from a film grown at the same power but with the 25 hole plate.

Figure 3.25 shows the RT PL spectrum of films grown using the 1 hole plate at various applied power. It is apparent that the 1 hole plate clearly produces the most

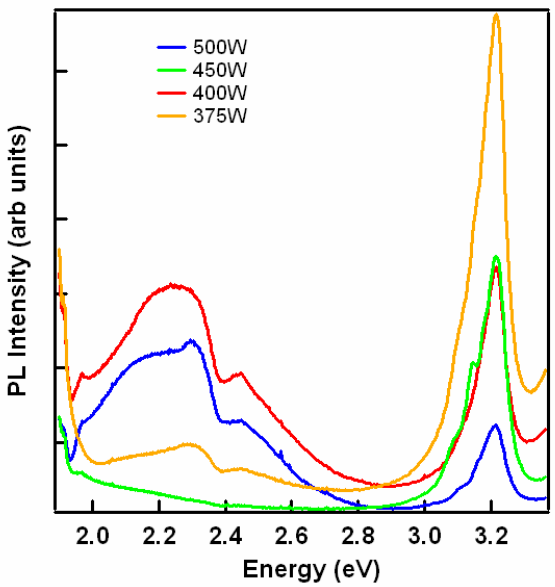

Figure 3.24 The room temperature PL of films grown with the 1 hole plate.

optically inferior films of the three aperture plate, which can be seen clearly in Figure 3.24. In particular, a substantial increase in the DBE can be observed, with the integrated intensity of the DBE comparable, and in some cases greater, than that of the NBE. Again, as a comparison, the NBE intensity of the film grown at 400 W with the 1 hole plate is approximately 50% of the intensity observed from the film grown with 276 hole at 400 W.

In general, the optical quality of ZnO thin films can be quantify by the FWHM of the NBE and the intensity ratio between the NBE and the DBE. Figure 3.25a and 3.25b show the variation of these two values as a function of applied plasma power for the three aperture plates. It can be seen from Figure 3.25a that the NBE FWHM varied from a maximum of 132 meV to a minimum of 97 meV. These FWHM values for room temperature PL are comparable to that reported in the literature [136, 164], and the small variation observed suggests that the FWHM is largely dependent on growth independent parameters, i.e. thermal broadening. Figure 3.25b shows that the NBE:DBE ratio (NDR) in general decreased with increasing RF power, although a high level of scatter can be observed in the data.

While there is clear variation in the optical properties between films grown at different plasma conditions, the correlation between the plasma species and the optical response of these ZnO films is much more complex than just a "cause and effect" type relation. This is clearly shown by the large scatter observed in the NDR, and the lack of trend in the PL observed from 25 hole plate films. This complexity arises from the indirect effect of the variation in the plasma condition in other aspects of the film growth. For example, it was found that the variation in the plasma condition has the power to change the surface morphology of the films. Although the observation of similar PL response between films grown with different Zn/O ratio suggests that the pit or island morphology should have minimal effect on the PL, it is nevertheless a possible variable that could change the optical response. Another change that was observed was the growth rate of these films with plasma conditions. As a result, the thickness of the films studied in Figure 3.22 - 3.25 are different. While the pentration depth of a He-Cd 325 nm laser is short enough (90 nm) and it can be guaranteed that the PL probes the same volume of material in each film, the increase in thickness may have decreased the dislocation density on the surface of the film (See Chapter 4), therefore possibly changing the optical response.

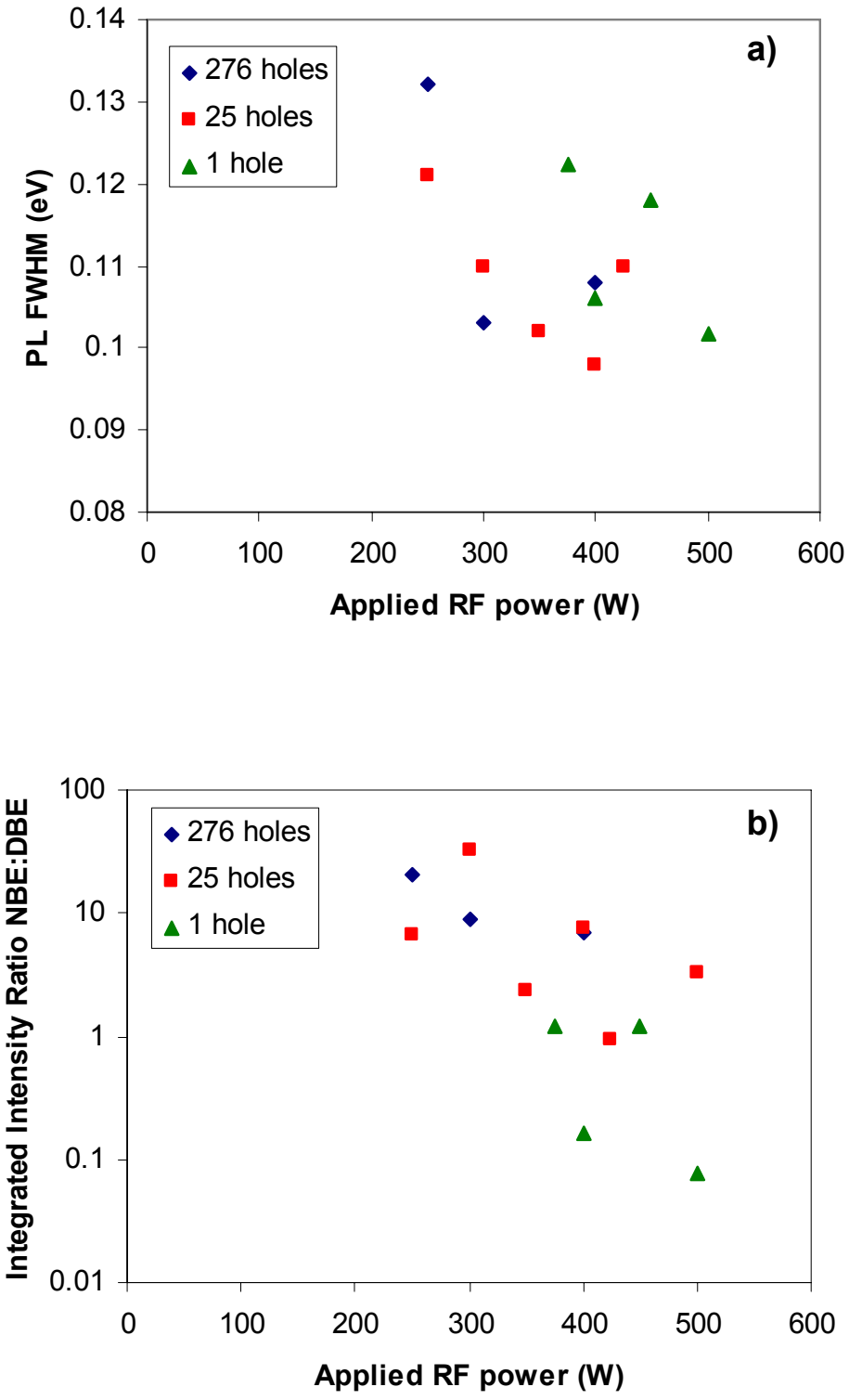

Figure 3.25 The quantitative optical characteristics of the ZnO thin films grown under different plasma conditions, measured at room temperature a) FWHM of the NBE, and b) Ratio of the integrated intensity of NBE and DBE.

Although these various secondary effects prevent the clear extraction of the relation between the oxygen species and the optical properties, a number of clear trends can be deduced. Firstly, it is clear that 1 hole plate does give the worse PL, with NBR lower than most films grown at 25 hole and 276 hole, even though the thickness of these films are quite similar to that grown with the 25 plate. This degradation in optical properties is consistent with both the structural and electrical degradation, and it is very likely the effect of the increased ion content in the plasma. Secondly, it is clear that 25 hole plate in general gives films with better optical quality. Even though the NBR of 25 hole plate films are only similar, and in some cases less, than that observed for the 276 hole plate, it is observed in general that films with similar thickness (c.f. Figure 2.26) has higher NBE intensity and more defined NBE peaks with more resolvable excitonic features. However, the data available cannot pinpoint the role of the change in oxygen species in this improvement of optical quality.

In summary, it can be seen that the variations in the active oxygen content change the effective flux ratio during growth, and as a result lead to a change in the film properties. This has the most prominent effect on the surface structures of the films. In particular, it was found that the increase in atomic oxygen led to a reduction in Zn adatom concentration under Zn-rich conditions, resulting in the transition from island to pit morphology and reduction of surface roughness as the RF power was increased. Note that molecular oxygen seems to have no part in improving Zn adatom diffusion on the surface even though it was observed to participate in growth. This possibly means that molecular oxygen is more likely to interact with already stabilised species, which points to a higher chance of non-stoichiometric incorporation. Currently, the experimental data available here is not sufficient to confirm this speculation. Nevertheless, it is clear that when considering the flux ratio, it is the zinc-to-atomic oxygen ratio that is important for ZnO thin film growth. The oxygen content of the plasma also has its own effect on the quality of the films. It was found that the variation in the oxygen content affects the electrical and optical quality greatly. For example, the increase in ion content (by using a 1 hole aperture plate) led to an increase in the sheet resistivity and carrier concentration of the resulting thin films. In addition, a change in the plasma condition has a dramatic effect on the room temperature PL emission of the ZnO films, with variation in both the NBE and DBE observed with RF power and aperture plate design. Although this variation cannot be

directly related to a particular oxygen species, evidence suggests that increased ion content might have led to the increased DBE and decreased NBR observed.

Overall, the study here suggests that the best plasma for ZnO growth should have high atomic oxygen content, low molecular oxygen content and low ion content. It was found that the 25 hole plate operating at a 300 - 400 W provided the best plasma for growth in this work. However, a 276 hole plate (new and unclogged) may also be beneficial for growth, as it allows a finer control of the different species by having a larger operable range of flow rate and RF power.

3.4 Growth Temperature and Other Variables

While the flux ratio and the active oxygen are two very important variables, there are other variables that are also important in the growth of ZnO. As observed from the effects of Zn/O ratio and active oxygen, adatom diffusion and stabilisation are the two main factors determining the structural quality of MBE grown ZnO thin films. Since the diffusion rate is directly dependent on the thermal energy provided, the substrate temperature has significant effects on the film properties. In Section 2.2.4 it was pointed out that the accurate measurement of the substrate temperature is difficult and problematic, and several intermittent problems with thermocouples were encountered over the course of this research. However, different substrate temperatures were used for various investigations in this work, and although these films cannot be compared quantitatively, they can be used to illustrate the general trends that one can expect from changing the growth temperature.

Figure 3.26 shows the RHEED after growth of four films, grown at (approximately) 400 ºC, 550 ºC, 650 ºC and 750 ºC. It has to be emphasised that these films were grown under similar but not identical conditions, and therefore direct comparison has to be treated with caution. The RHEED pattern shows that a low

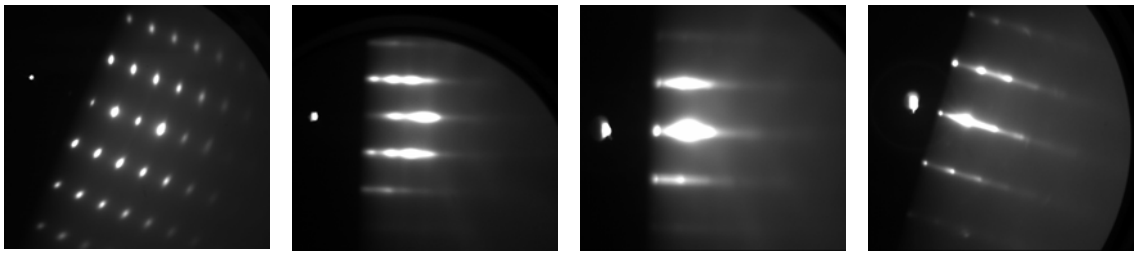

Figure 3.26 After growth RHEED for ZnO thin films grown under different temperatures. Note that the Zn and oxygen conditions used for each film are different. From the left: 400 °C, 550 °C, 650 °C and 750 °C.

growth temperature in general gives a rougher surface. In fact, from the slightly elongated spots in the RHEED, it can be said that the 400 ºC film has a high density of surface defects and misoriented domains. This is generally true for low temperature growth, with all growth attempts at 400 ºC resulting in films that showed some degree of polycrystalline composition. As the growth temperature was increased, considerable improvement in the film surface was observed, with good surface quality achieved for all three higher temperatures.

Figure 3.27 shows the planar SEM images of the four films presented in Figure 3.26. At low temperature, the surface was extremely irregular but directional with long ridges dominating the surface. Films with smaller features and more regular surfaces can be achieved with higher growth temperatures, with a very grainy surface observed for the film grown at 550 ºC, and a pit covered surface for the 650 ºC film. For the film grown at 750 ºC the surface is dominated by pits, with observable steps on the surface suggesting some degree of 2-D growth. The degrading effect of low temperature growth is consistent with the insufficient diffusion expected at low temperature, which results in statistical roughening. As the diffusion coefficient is proportional to $e^{(-1/T)}$ [56], the diffusion rate increases and saturates with increasing temperature. Hence a dramatic improvement was observed by going from 400 °C to 550 °C, but improvement in increasing the substrate temperature from 550 °C to 650 °C to 750 °C is less noticeable.

Note that Jung et al. have studied the effect of temperature and observed the best quality film at 720 ± 10 ºC [83]. Also note that annealing experiments in this work have shown that the best film quality can be achieved by ex-situ annealing at 750 ºC for 1 hour. Therefore, it is likely that a growth temperature of ~ 700 - 750 °C is a good choice for the MBE growth of ZnO. Unlike GaN, ZnO does not suffer from dissociation at these growth temperatures. However, based on annealing studies in this work, it is suspected that a growth temperature above 850 °C will increase the bulk diffusion and cause undesirable roughening (more detail is provided in Section 4.46).

Apart from the flux ratio, active oxygen and growth temperature, there are other growth variables that substantially affect the properties of MBE grown ZnO thin

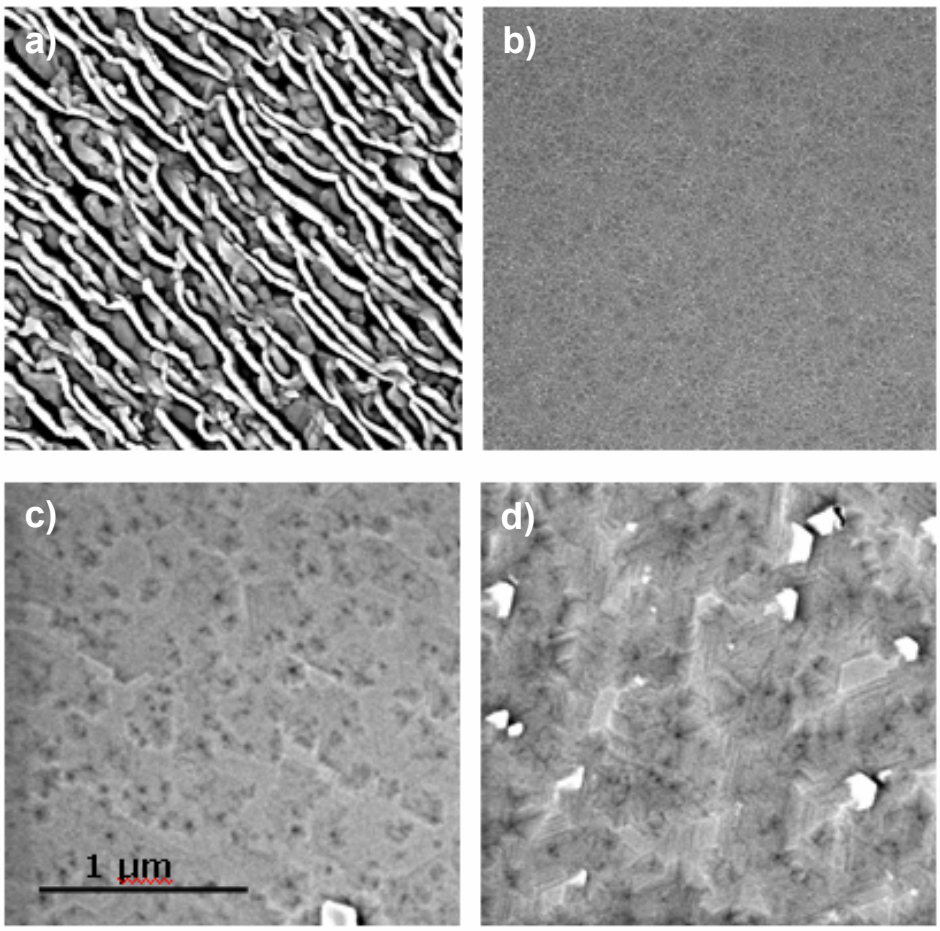

Figure 3.27 The SEM images of the ZnO thin films grown at a) 400 °C, b) 550 °C, c) 650 °C, d) 750 °C under different Zn and O conditions.

films. This is especially evident when comparing films grown in this work with that reported by others. Even though an optical quality comparable to the best reported was achieved in this work, most films studied have a rough, 3-D surface and a mobility that is much lower than that of bulk ZnO material. Even with a reduced growth rate (via a reduction of flow rate) the resulting films, as seen in Section 3.2, still suffered from low electron mobility. Although additional growth or processing steps such as slow cooling after growth [165], in-situ annealing [166], and more complicated heating - cooling - growing procedures [45] may improve the situation, ultimately the issue is the large lattice mismatch between ZnO and the sapphire substrate. It is therefore crucial to study ways to overcome this incompatibility between the two. This is investigated in the next chapter.

Chapter 4

STRAIN AND STRUCTURES

In Chapters 2 and 3 the process of bulk crystal growth in a heteroepitaxial process was studied and the effect of adatom diffusion on the quality of the films was described. It was found that the properties of the ZnO can be tuned by varying the flux ratio, active oxygen content and growth temperature. However, it was also found that the incompatibility between ZnO and sapphire ultimately limits the achievable film quality. Even still, sapphire remains one of the best substrates available for ZnO epitaxial growth due to its cheap cost compared to bulk ZnO material. Therefore, various interface conditioning techniques, in particular, buffer layer systems, are needed to improve the film growth. In this chapter, the growth and effects of two buffer layer systems, LT-ZnO and MgO buffers, are described.

4.1 Epilayers and Strain

Prior to the study of buffer layers, the effect of lattice mismatch on heteroepitaxy must be recognized. In heteroepitaxy (as oppose to homoepitaxy), the material of interest is grown on a substrate of another material, as in the case of ZnO on sapphire. The thin film layer is then expected to conform to the crystal lattice structure of the substrate template as it nucleates. However, each material has its own preferred crystal lattice structure (sometimes more than one) that minimises the energy of the lattice. Therefore, when one forces a thin film to follow the crystal lattice of the substrate, the thin film will try to achieve a lattice structure as close to its preferred structure (or the most compatible structure if more than one preferred structures exist) as possible. The mismatch between the two crystal lattice structures therefore leads to strain in the thin film.

To quantify this mismatch between the substrate and the epilayer, the lattice mismatch *f* is used [51]:

$$f = \frac{a_e - a_s}{(a_e + a_s)/2} \approx \frac{a_e - a_s}{a_s} \tag{4.1}$$

where a_s and a_e are the lattice constant of the substrate and the epilayer, respectively, and it is assumed that $a_e \approx a_s$. When *f* is less than 0.1% the epilayer and substrate are known as lattice-matched, a desirable condition as lattice matching leads to low amounts of strain in the crystal lattice. Typically, however, a lattice matched substrate is hard to find or very expensive. Therefore, traditionally, a substrate with lattice mismatch of ~1% to 5% is commonly used for heteroepitaxial growth, such as Ge on Si [167]. For ZnO on sapphire, a lattice mismatch of 18% is observed [168]. Although this is a high *f* value, the cheaper cost of sapphire compared to better lattice matched substrates overrides this disadvantage. The large lattice mismatch therefore needs to be dealt with when growing ZnO thin films.

Lattice mismatch has substantial effects on the thin film nucleation process. In particular, it affects the bonding between the substrate and the epilayer. In extreme cases, if interface bonds are sufficiently weak, a large mismatch can induce a strong enough strain that prevents chemical bonds from forming. The epilayer would therefore float on the substrate surface (Figure 4.1a) and would be connected to the substrate through weak van der Waal forces [56]. This growth mode is known as an incommensurate growth, and it commonly occurs in 2-D layered systems, for example, graphite and MoS_2 [56]. In the other extreme, perfect bonding between the substrate and the epilayer may occur under certain conditions. In this case the epilayer is perfectly aligned to the substrate lattice, and is therefore strained (Figure 4.1b). Such pseudomorphic growths are generally very desirable because of the resulting defect free lattice. In other cases when the lattice mismatch is very large, the extreme strain means that a pseudomorphic layer is not possible. This leads to a relaxed growth with a high density of lattice defects (Figure 4.1c). For ZnO on sapphire, the strong O-Zn bond means that it is unlikely for incommensurate growth to occur. However, it is possible for ZnO epilayers to take the form of pseudomorphic growth or relaxed growth, depending on the growth parameters and substrate conditions. Note

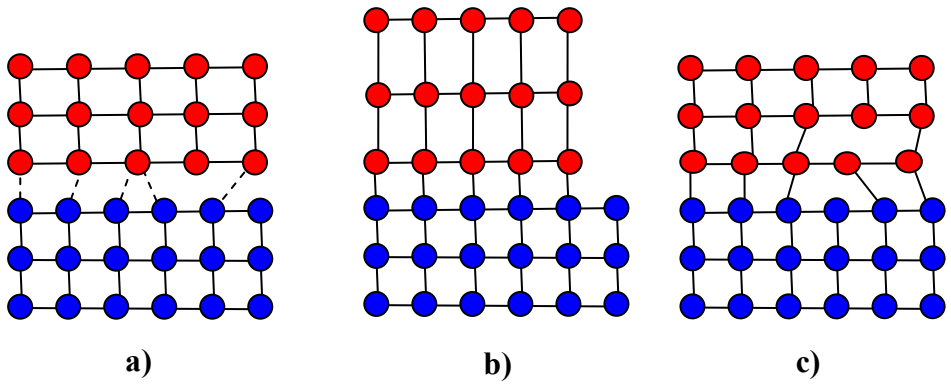

Figure 4.1 Atomic model showing three situations under lattice mismatched film growth: a) incommensurate growth where the over-layer is "floating" on the substrate by van der Waal forces; b) pseudomorphic growth where the over-layer is strained to match the substrate lattice, forming a coherent crystal; c) relaxed growth where the lattice is distorted to accommodate the strain. Note that pseudomorphic growth eventually transforms to relaxed growth once a critical thickness, as determined by the elastic coefficient of the film, is reached.

that in most cases, as the thickness of the film increases, pseudomorphic growth will eventually transform into a relaxed growth once a critical thickness is reached.

For either pseudomorphic growth or relaxed growth, the behaviour of the nucleation process is dependent on the minimisation of surface energies. There are three different surface energies in consideration in a substrate-film system: substrate free surface energy γ_s; film free surface energy γ_f; and interface free energy γ_i [56]. The total system energy U is given by the sum of all these energies in the system:

$$U = \sum \gamma_s + \sum \gamma_f + \sum \gamma_i + U_{nucleation} \qquad (4.2)$$

where $U_{nucleation}$ is the energy prerequisite for a particular mode of nucleation to occur. Equation 4.2 governs the thin film nucleation in that the nucleation process will attempt to minimise this system energy by following one of the three regimes illustrated in Figure 4.2. In the first instance (Figure 4.2a), no nucleation occurs. Both γ_f and γ_i are zero as neither a film nor an interface exists. For this nucleation mode to occur, an extra energy U_{desorb} is required to desorb all incoming reactants. Hence, the total system energy becomes:

$$U = \sum_{surface} \gamma_s + U_{desorb} \qquad (4.3)$$

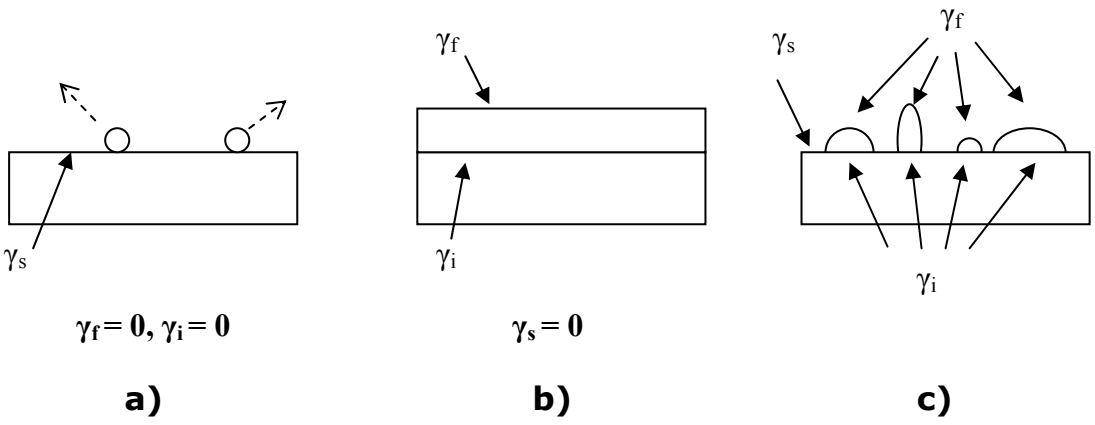

Figure 4.2 Three possible modes of thin film nucleation: a) No nucleation ; b) Frank-van der Marwe mode giving a coherent interface; c) Volmer-Weber mode.

Because of the generally high desorption barrier, Equation 4.3 is unlikely to give the minimum surface energy unless the growth temperature reaches the dissociation temperature of the growing film.

If, in the opposite extreme, the nucleation progresses under a coherent, uniform and strained 2-D nucleation regime, as shown in Figure 4.2b, then the entire substrate is covered by the thin film, giving $\gamma_s = 0$. While there is no energy requirement for adatom desorption, extra energy is needed to maintain the coherently distorted lattice. This is stored in the lattice as strain energy U_{strain}. Therefore, the total system energy is given by:

$$U = \sum_{surface} \gamma_f + \sum_{surface} \gamma_i + U_{strain} \qquad (4.4)$$

Such formation of a uniform, strained interface is known as the 2-D or the Frank - van der Marwe growth mode, and the spreading of the film across the surface of the substrate is known as wetting [56]. Note that while pseudomorphic growth requires 2-D nucleation, in general 2-D growths can be sustained to a much greater thickness given that U_{strain} can be relieved in a proper way (see next section).

In the third case, a 3-D nucleation or Volmer-Weber growth mode (Figure 4.2c) occurs, where a free substrate surface exists across most of the substrate. However, at localised sites such as steps and kinks, nucleation occurs and these nuclei eventually coalesce into larger 3-D islands. In this case, the substrate is not wetted,

and there is no continuous growth. However, the resulting clusters of islands will be strain free (within the island). The total system energy of this 3-D growth is given by:

$$U = \sum_{surface} \gamma_s + \sum_{localised} (\gamma_f + \gamma_i) + U_{upstep} \qquad (4.5)$$

where U_{upstep} is the energy required for an adatom to travel inter-plane to an energetically favourable site such as the top of a growing island.

Unfortunately for ZnO on sapphire, the 3-D growth mode described by Equation 4.5 is more favourable than 2-D growth. This is because under a large lattice mismatch of 18%, both U_{strain} and γ_i increase due to the increased difficulty in bond formation. An example of this is Figure 4.3, which shows a ZnO "thin film" deposited directly on sapphire at a temperature of 550 °C. Discrete rod-like islands are evident on the surface, consistent with a 3-D nucleation. Even though these 3-D islands or nuclei will eventually coalesce to form a continuous layer after sufficient deposition, their irregularity will result in severe surface roughening. This poor wetting of the sapphire substrate by ZnO is therefore undesirable.

To improve the wetting during epitaxial growth, a common method that has been used in the growth of GaN [169, 170] and other material systems [171, 172] is to use a buffer layer — a continuous interface layer between the substrate and the bulk

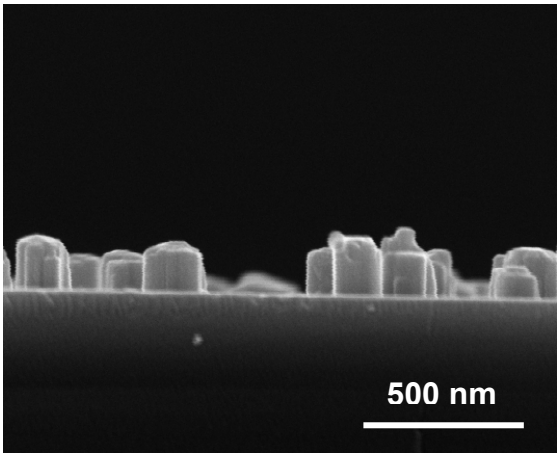

Figure 4.3 Cross section SEM image of a ZnO sample grown directly on sapphire, showing the discrete, discontinuous nature of growth. Because of the large mismatch, ZnO would nucleate in the Volmer-Weber mode under typical growth conditions if directly deposited on sapphire.

high quality layer. A buffer layer improves the wetting by increasing the energy requirement for 3-D nucleation. The use of buffer layers in the growth of ZnO has been reported previously, with promising results [173, 174]. In this work, the effects of low temperature ZnO buffer layers and MgO heteroepitaxial buffers on the MBE growth of ZnO on sapphire have been investigated.

4.2 Homoepitaxial Buffer Layer and Strain

4.2.1 Homoepitaxial Buffer and ZnO Growth

One common buffer layer for sapphire-based growth is a homoepitaxial buffer — a buffer layer of the same material as the growth material. A homoepitaxial buffer is attractive as it minimises the interface energy between the epilayer and the buffer layer. Furthermore, by using homoepitaxial buffers, the need of introducing new buffer material or processes into the already established growth process can be avoided. Homoepitaxial buffers in most cases utilise a low growth temperature to improve wetting. In particular, to increase the "wetting" of the substrate it is necessary to increase the energy requirement for a 3-D nucleation mode. Since the chemical bonding energy cannot be changed, the only way to increase this energy according to Equation 4.5 is by either reducing the interface energy using different growth conditions, or lowering the substrate temperature such that extra energy is needed to provide the upstep diffusion energy U_{upstep}. Under a sufficiently low substrate temperature, the buffer layer will be forced to nucleate in a 2-D growth mode as the adatoms do not have enough energy to traverse through multiple atomic planes [56]. As a consequence, a continuous buffer layer can be formed. Once the buffer layer is complete, the deposition can then continue at a higher temperature as the interface free energy has been greatly reduced.

Figure 4.4 and Figure 4.5 show RHEED and AFM images, respectively, for two films grown under the same conditions, except for a 50 nm thick low temperature (LT) ZnO buffer grown at 300 °C for 15 minutes for one film. From Figure 4.4, it can be seen that the insertion of this buffer layer led to a smoother surface, as indicated by the streaky RHEED. The AFM images in Figure 4.5 illustrate the improvement much

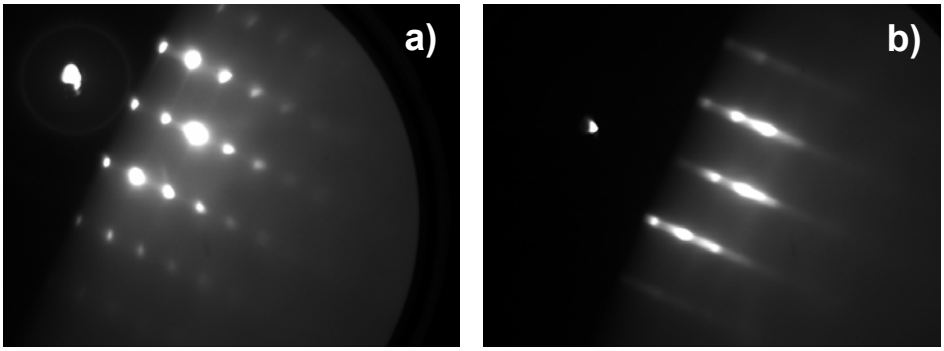

Figure 4.4 RHEED image taken after deposition for sample grown a) without and b) with a low temperature buffer layer, showing the surface smoothing effect of the buffer layer.

more clearly, with the surface changed from a rough, irregular island morphology to a flat, pit dominant morphology. The rms surface roughness substantially decreased from 75 nm to 8.2 nm.

The employment of a low temperature homoepitaxial buffer also has beneficial effects on the optical properties of the resulting ZnO films. Figure 4.6 shows the low temperature PL of the two films shown in Figure 4.4 and Figure 4.5. From the graph it can be seen that by employing a LT- buffer layer, sharper peaks and more features can be observed in the bound exciton emission complex, suggesting an improvement in crystal quality. In particular, the free exciton emission at ~3.37 eV was detectable in the film grown with a LT-buffer but not the other film.

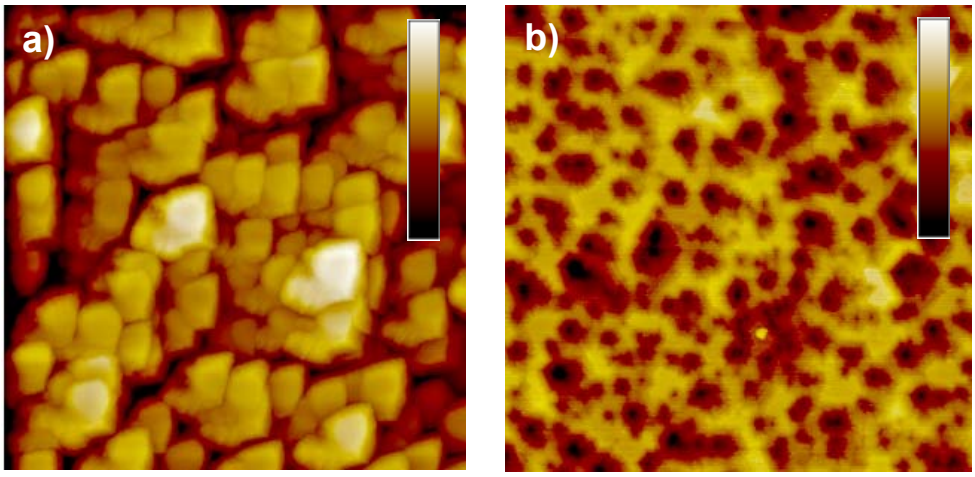

Figure 4.5 Corresponding AFM images of the surface of the sample growth a) without and b) with a buffer layer. Both images are 3 µm × 3 µm, but the colour scale for the left image is 300 nm, whereas for the right image is 100 nm, illustrating clearly the improved surface morphology.

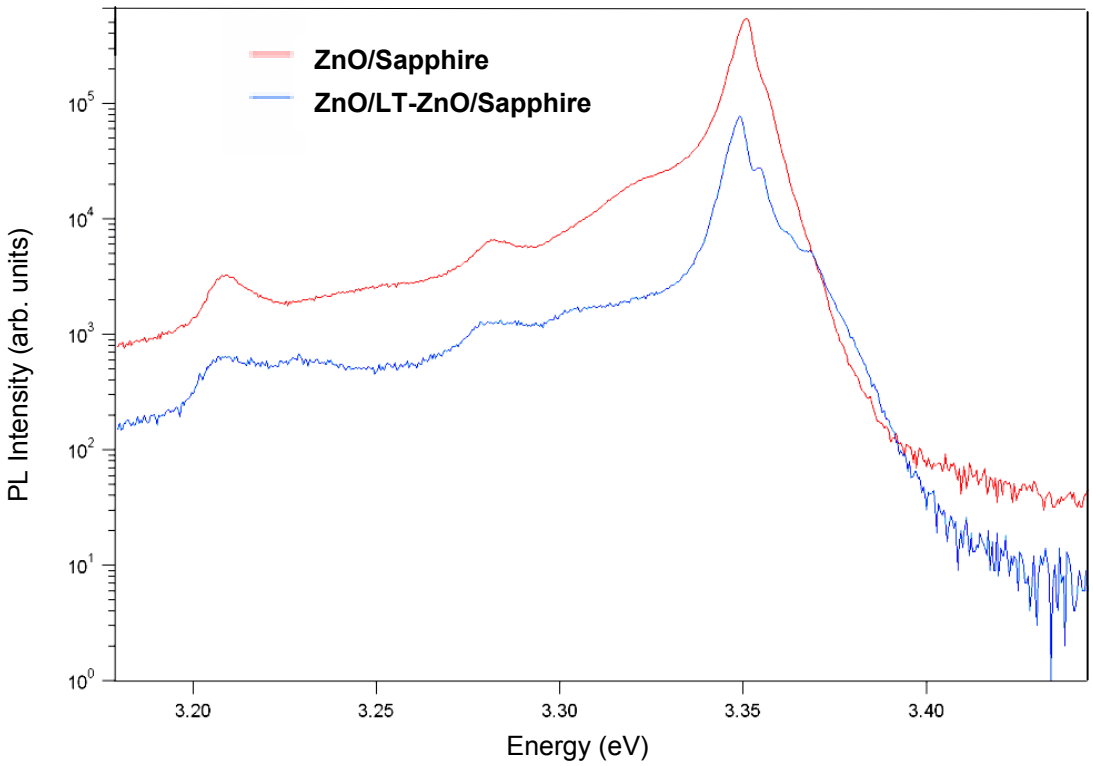

Figure 4.6 4 K PL of sample grown with and without LT-ZnO buffer, showing the improvement of crystal quality via LT-buffer employment.

In contrast, using conventional Hall effect measurements, it was found that the electrical quality of the ZnO thin film apparently degraded. An increase in the carrier concentration from 1×10^{18} cm^{-3} to 1×10^{19} cm^{-3} and a decrease in mobility from 30 cm^2/Vs to 10 cm^2/Vs was observed. This is inconsistent with the improved structural and optical quality that was observed with the employment of a buffer layer. A similar discrepancy between the optical and electrical properties of an epilayer has been previously reported in GaN as well as ZnO, especially when buffer layers were involved [175, 176]. This discrepancy has been attributed to a degenerate layer formed from the poor quality interface due to the low temperature growth [176], which dominates the electrical measurement, giving unrepresentative results. Therefore, even though electrical measurements suggest that the carrier concentration increased and the mobility decreased with the employment of a LT-ZnO buffer layer, it is likely that the electrical properties of the high temperature ZnO epilayer have actually improved (see Chapter 5).

From these experimental results, it can be seen that the employment of a LT-ZnO buffer is almost essential for the growth of ZnO epitaxial layers on sapphire. It should be noted here that this was in fact realised very early on in this work, and as a

consequence, almost all ZnO thin films grown in this work, including those presented in the previous chapters, were grown with a nominally 50 nm thick LT-ZnO buffer layer grown at 300 °C.

4.2.2 Strain Relief in ZnO Epitaxial Layers

From the preceding section it was observed that substantial improvement in the film quality can be obtained by using a LT-ZnO buffer layer. In particular, an order of magnitude improvement in the surface roughness of the resulting ZnO epilayers was obtained. However, even with this improvement, the resulting ZnO thin films are still dominated by 3-D surface morphologies, such as that observed in Figure 4.5b. In fact, results from previous chapters suggest that so far no films can be classified as perfectly 2-D, which is the most desirable form of an epilayer. Apart from the fact that LT buffers suffer from statistical roughening due to the low growth temperature (such as that shown in Figure 4.7), the dominance of 3-D morphology even with significant wetting can be attributed to the strain in the lattice.

As it was recognised in Chapter 3, (regular) surface roughening originated from strain in the crystal lattice. It is now clear that this surface roughening is the result of the strain build-up from the lattice distortion due to the mismatch between ZnO and sapphire. With the employment of a LT-ZnO buffer, the ZnO is forced to nucleate in the 2-D growth mode, and the strain caused by the coherent distortion of the ZnO lattice is stored as strain energy in the system (c.f. Equation 4.4). As the thickness increases, this strain energy eventually becomes sufficiently large that a 2-D strained film is no longer energetically viable. Upon a critical thickness, the thin film would spontaneously break up and delaminate, unless the strain can be relieved less catastrophically.

One possible strain relief mechanism is the transformation from a 2-D to a 3-D growth. This allows an initially smooth but strained surface to deform into islands that have essentially the equilibrium lattice constant of the growth material, and in the process releases the strain energy, leading to a relaxed film. This initial 2-D growth mode coupled with a transformation to 3-D growth mode upon reaching a critical thickness is known as the Stranksi-Krastanov (S-K) growth mode.

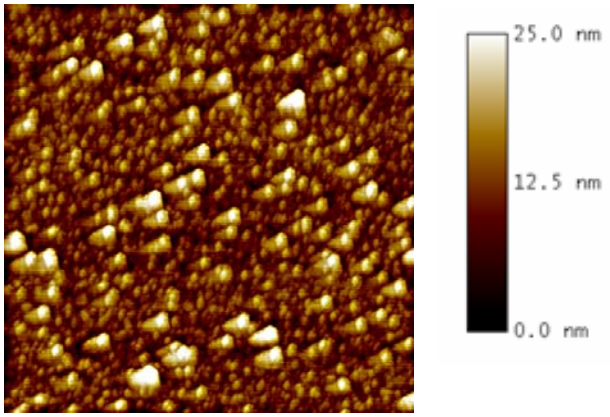

Figure 4.7 The AFM image of the surface of a low temperature buffer layer, showing the 3-D island morphology of the buffer.

There is, however, another possible strain relief mechanism: the formation of misfit dislocations. A dislocation is simply a fault in the crystal lattice. Through the formation of misfit dislocations, some of the strain can be relieved by the relaxation of localised regions in the lattice towards the true lattice structure of the material (c.f. Figure 4.1c). The formation of dislocations and the transformation to 3-D growth are in fact two separate but related processes. Tersoff et al. [147] have pointed out that 3-D roughening of the surface due to the strain field of the mismatched lattice can create efficient dislocation nucleation sites. Furthermore, islands formed through surface roughening can also introduce localised strain that will decrease the formation barrier of dislocations. This allows dislocations to form readily after the onset of surface roughening in large mismatch systems to further relieve the residual strain in the film [147, 177]. From this, it can be seen that roughening and misfit dislocation generation can be considered as competing processes where in one case dislocations are a result of strain relaxation roughening, and in the other case dislocations are formed spontaneously (or from existing dislocations), directly relieving the strain in the lattice. These two competing processes lead to two important critical thicknesses - the critical thickness for the onset of misfit dislocation (t_{MD}), and the critical thickness for the onset of 3-D growth (t_{3D}) [51].

In the case of ZnO thin films grown on sapphire, the observations from Figure 4.4 and Figure 4.5 suggest that surface roughening is the dominant strain relief mechanism. That is, if misfit dislocation was dominant, the formation of misfit dislocations would occur prior to surface roughening, i.e. $t_{MD} < t_{3D}$, resulting in a relaxed 2-D film that does not need surface roughening for residual strain relief. The

dominance of rough ZnO thin films therefore suggests that $t_{3D} < t_{MD}$ in the ZnO/sapphire system. To confirm this hypothesis and to further understand the strain evolution in the ZnO/sapphire growth system, the critical thickness values for selected films grown in this work were determined.

While there is no theoretical modelling of ZnO for the evaluation of t_{3D} has been reported, theoretical treatments has been applied to show that for a large misfit as in the ZnO/sapphire system the misfit critical thickness amounts to only a few monolayers [178, 179]. Even so, it has been observed in many materials that a strained 2-D growth without dislocations can be sustained to a thickness that is orders of magnitude higher than that predicted by theory [51]. Therefore, the most useful way to determine both critical thickness values is by studying the strain evolution of the epilayer experimentally.

A mean of studying the strain evolution in an epitaxial layer and evaluating the critical thickness is to use RHEED to monitor the change of the thin film surface during the first few minutes of growth. This temporal RHEED data provides two important pieces of information: the critical thickness for the 2-D to 3-D transition and the critical thickness at which lateral relaxation occurs. By comparing these two critical thickness values, the relative importance of surface roughening and misfit dislocation nucleation can be evaluated [51].

The determination of the 2-D to 3-D transition usually involves the observation of RHEED oscillation damping during the initial growth sequence [180, 181]. However, as RHEED oscillations were not observed in this work, an alternative method was used where the thickness at which the RHEED pattern changed from streaky to spotty is identified as the 2-D to 3-D transition point, as it is well known that 2-D surfaces result in reflection diffraction streaks whereas 3-D islands cause transmission related diffraction spots [51]. Figure 4.8 shows the transformation from a 2-D RHEED to a 3-D RHEED pattern for three samples grown under different oxygen conditions, hereby named as sample A, B and C for convenience, during the initial growth sequence (i.e. during buffer layer growth). Note that because of the lack of RHEED oscillations, the thickness values were estimated from the growth rate at 650 °C, scaled to 300 °C according to previous experiments (c.f. Figure 2.29). In addition, the data in between the two horizontal dashed lines represent RHEED patterns where both streaks and spots were observed, and were plotted based on the

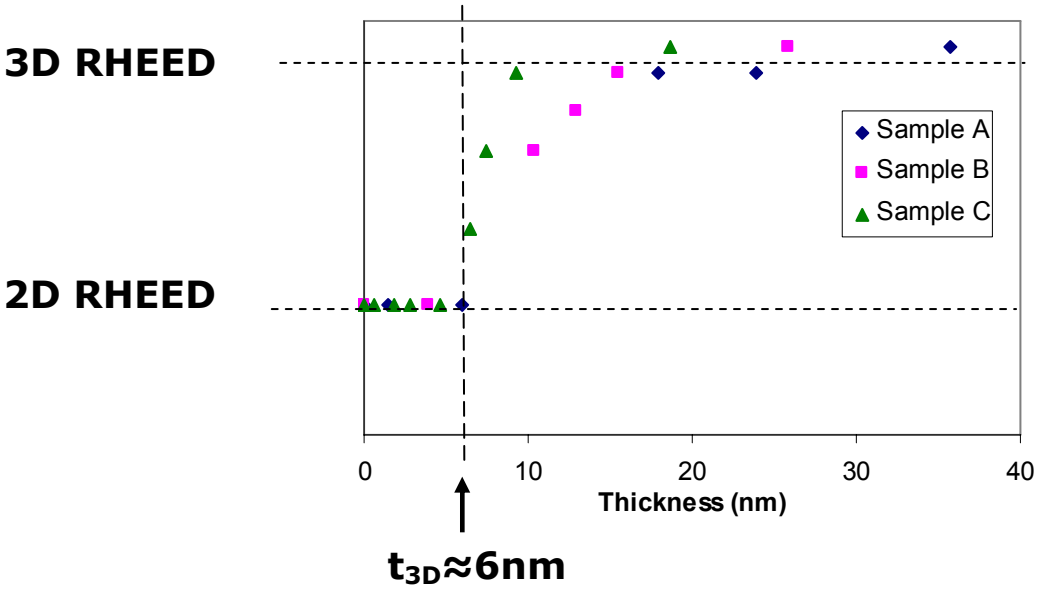

Figure 4.8 The transition of 2-D RHEED pattern (streaks) to 3-D RHEED pattern (spot) observed for three samples grown under oxygen different conditions - A, B and C, during the buffer layer growth. The graph suggests a critical thickness of ~6 nm.

number of spots observed on the RHEED pattern at a particular thickness compared to that observed when the sample is well into a 3-D growth regime. From Figure 4.8, it can be seen that the onset of the 3-D island formation occurred at $t_{3D} \approx 6$ nm. The perfect matching of this t_{3D} amongst all three samples indicates that this thickness is independent of the growth conditions. This t_{3D} value is also very similar to that reported by Jung et al., who observed a 2-D to 3-D transition at 5 nm when growing ZnO on c-plane sapphire [182].

The lateral relaxation of a strained film can be detected from a change in the RHEED streak spacing [180, 183]. The streak spacing corresponds to the rod spacing in the reciprocal lattice, which is inversely proportional to the lattice spacing between atomic planes of the crystal in real space. From this lattice spacing or d-spacing, the lattice constant can be determined via geometrical arguments. Since the lattice constant changes as the lattice relaxes, a distinct change in the streak spacing indicates a lattice relaxation event.

The behaviour of a lattice relaxation event depends on the mismatch and the atomic arrangement at the interface. Consider ZnO grown directly on sapphire. From Figure 4.9, it can be seen that by a 30° rotation the Zn sublattice can be aligned with the O sublattice of the sapphire surface, with the oxygen atom spacing given by $a_{sapphire}/\sqrt{3} = 2.747$ Å. Assuming room temperature and using $a_{ZnO} = 3.241$ Å [36],

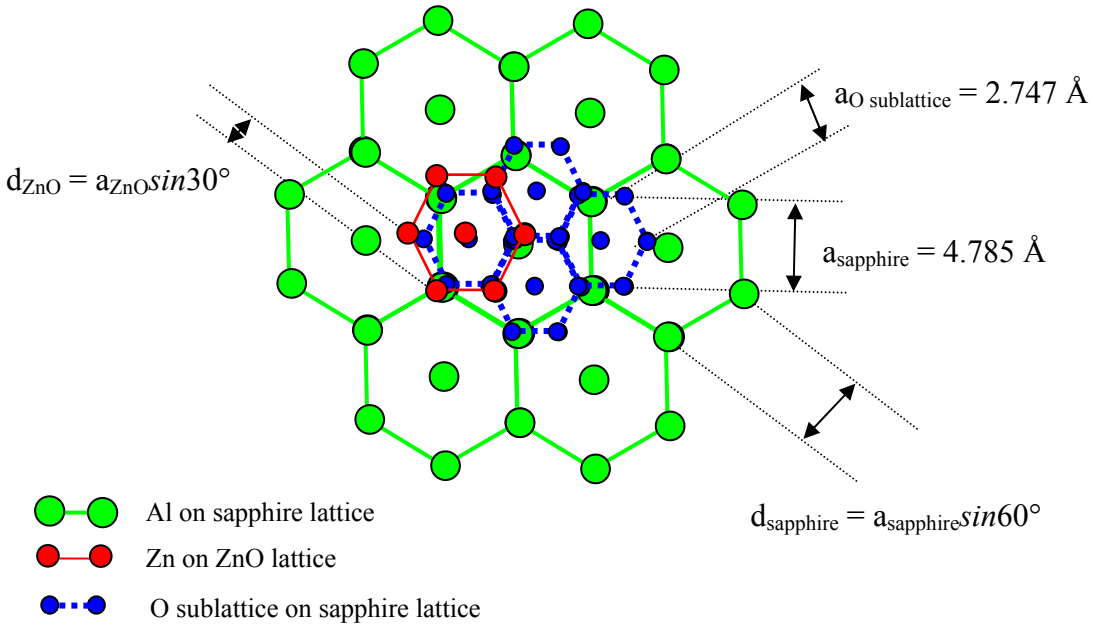

Figure 4.9 Theoretical epitaxial relationship between ZnO and Al_2O_3. Because of the large mismatch the ZnO lattice is rotated with respect to the Al lattice, reducing the mismatch to 18%. This figure also shows the expected d-spacing for ZnO and sapphire in the $[1\bar{2}10]$ RHEED direction with respect to the sapphire.

this gives a lattice mismatch of 17.9%, which is half of that expected from a non-rotated growth. Therefore, even though both the sapphire and ZnO lattices are hexagonal, ZnO films tend to have a crystal lattice rotated 30º with respect to the sapphire lattice. This has been confirmed experimentally by RHEED, with all ZnO films grown in this work showing a 30° rotation. Note that under this rotation, the strain becomes compressive as the Zn lattice is compressed to match the sapphire O sublattice. Thus, for a strained layer of ZnO it is expected that the experimental lattice constant a'_{ZnO} measured from RHEED would relax from 2.747 Å towards 3.241 Å as growth progresses.

The lattice spacing is dependent on the both the lattice constant and the direction of the diffraction beam, which is $[1\bar{2}10]$ with respect to the sapphire substrate in this case. Therefore, referring to Figure 4.9, the d-spacing of sapphire is related to the lattice constant by $d_{sapphire} = a_{sapphire} \sin 60º$. For ZnO, because of the 30º rotation, the lattice spacing becomes $d_{ZnO} = a'_{ZnO} \sin 30º$. From this, it is expected that initially the RHEED streak spacing would be constant, proportional to $1/d_{sapphire}$. As the lattice relaxation takes place at the critical thickness, a sharp transition in the

RHEED streak spacing would be observed where the lattice spacing abruptly changes from $d_{sapphire}$ to d_{ZnO}. As the growth progresses past this point, the RHEED streak spacing should decrease gradually as a'_{ZnO} increases eventually to 3.241 Å as the film fully relaxes.

Figure 4.10 shows the change in RHEED spacing with respect to the initial sapphire streak spacing for three samples A, B and C over the first 15 nm of buffer growth. Since the evaluation of the actual d-spacing requires precise knowledge of the geometry of the beam and the sample, as well as the effects of thermal expansions, the uncalibrated data were used instead, which were normalised to the sapphire streak spacing observed in each experiment to allow comparison amongst the three samples. All three samples showed the abrupt change in the streak spacing as expected, which corresponds to the onset of strain relaxation. However, it can be seen that this transition occurred at different thickness values for the three samples. In particular, the transition occurred at ~ 4 nm for sample A, ~ 1.5 nm for sample B and ~ 2 nm for sample C. Furthermore, it can be seen from the figure that the abrupt change in streak spacing saturates above 5 nm for all samples, although different variation is observed for the three samples past this saturation point. This saturation point corresponds well

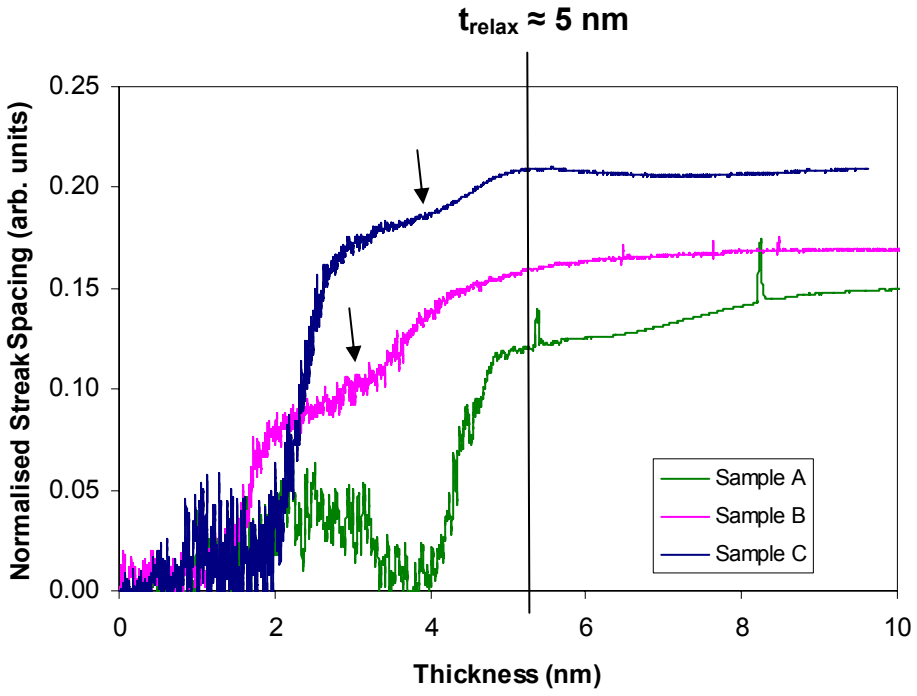

Figure 4.10 RHEED spacing evolution for the first 10 nm of LT-ZnO buffer growth for samples A, B and C which were grown under different oxygen conditions. The arrows indicate the existence of inflection points which suggests a two-stage relaxation process.

with the t_{3D} value determined previously, suggesting that surface roughening and island formation are the dominant strain relief mechanisms. Note that this result suggests that a ZnO buffer layer must be thicker than 6 nm to have a strain relaxation effect. Experiments on the buffer layer samples in the present work actually showed that when the buffer thickness is greater than 60 nm, surface roughening results in unacceptably rough buffer layers (similar to that in Figure 4.7). However, a reduction of carrier concentration with increasing buffer layer thickness was also observed. As a compromise between these two trends, the buffer layers used through out this work are nominally ~50 nm.

Interestingly, samples B and C showed a two-stage transition from the initial RHEED spacing to the saturated RHEED spacing. In particular, as indicated by the arrows in the figure, there exists an inflection point in the transition region for both samples B and C. The origin of this two-staged transition is unknown. However, from the early onset of the transition observed for sample B and C, which is close to the critical thickness observed in the literature [179], it is possible that the two stage transition originated from the involvement of misfit dislocation nucleation prior to the 3-D relaxation of the samples. From the data it is not clear whether this transition has occurred in sample A, although it is possible that the extremely noisy nature of the RHEED at the start of growth and the subsequent averaging of the experimental data may have resulted in the discrepancy observed. Note that it is expected that the RHEED spacing would gradually decrease past the saturation point as the ZnO lattice fully relaxes. The observed increase of RHEED spacing in sample A therefore suggests a further increase in compressive strain as growth progressed, possibly due to an increase in surface roughening originated from the higher growth rate of sample A.

From the RHEED analysis, it was confirmed that a 2-D to 3-D transition is the dominant strain relief mechanism in the ZnO/sapphire growth system under typical growth conditions used in this work. However, it was observed from the spacing change that the actual strain evolution process is not straightforward, and it is possible that after 1 - 2 monolayers of growth, misfit dislocations start to appear prior to the 2-D to 3-D transition. The experimental results observed here are different from that predicted by theoretical models [51]. In particular, it is expected that for a low temperature growth or small mismatch system, $t_{MD} < t_{3D}$ and the nucleation of misfit dislocation dominates, while $t_{3D} < t_{MD}$ for large mismatched systems. Here, it was

observed that $t_{MD} < t_{3D}$, but still the 2-D to 3-D transition dominates. It seems that the low temperature growth might have decreased the critical thickness for misfit nucleation, but the large mismatch prevented misfit dislocations from dominating. From this, it can be seen that the difficulty in obtaining high quality 2-D ZnO epilayers in this work can be attributed to the fact that surface roughening dominates over misfit dislocation generation under the large mismatch strain in the ZnO/sapphire system. This is the ultimate limitation of a homoepitaxial buffer system.

4.3 Reduction of Strain via MgO buffer

4.3.1 Motivation

As seen from the last section, the employment of a LT-ZnO buffer layer does not solve all the issues arising from the lattice mismatch. Because of the need for a low substrate temperature to obtain good wetting of the sapphire surface, a LT-ZnO buffer layer often possesses poor electrical quality, altering the observable carrier concentration and mobility. Furthermore, the lattice mismatch between the buffer and the substrate is still large, resulting in extensive surface roughening. Therefore, the possibility of using another material as a buffer layer for strain relief purposes is very appealing. Several groups have investigated MgO, a common oxide material that is chemically compatible to both ZnO and sapphire. Taking into account the epitaxial alignment, the lattice mismatch between MgO (111) and sapphire is ~9% [174]. Therefore, it is expected that MgO would be a good buffer layer for ZnO thin films. Very thin MgO buffer layers have been used for the plasma assisted MBE growth of ZnO thin films [145, 184], as well as for MBE ZnO growth using H_2O_2 [117, 185], with promising results. It is therefore interesting to determine whether the same buffer layer system can be applied in this work to improve the quality of the ZnO epilayers.

4.3.2 Growth of MgO Buffer Layers

For the growth of MgO, Mg was provided by the evaporation of 4N purity Mg pieces using a 60 cc conical effusion cell. Figure 4.11 shows the theoretical flux

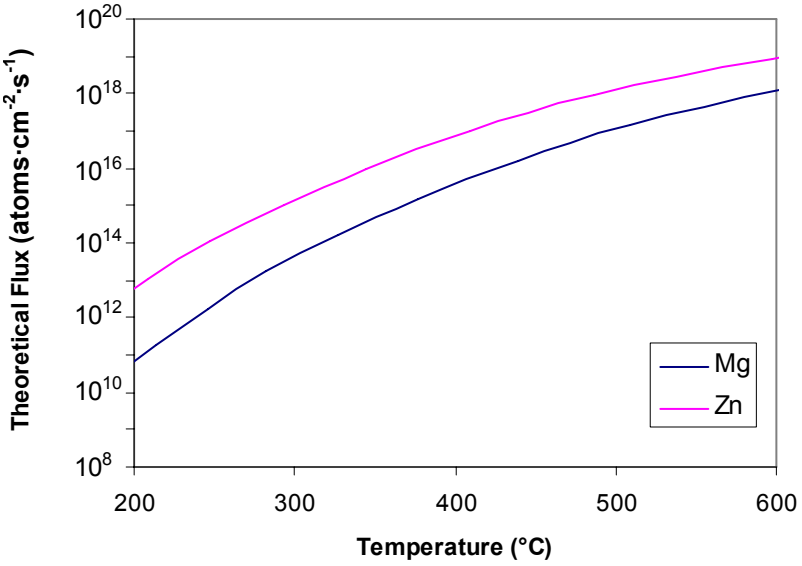

Figure 4.11 The theoretical flux curves of Mg and Zn.

curves versus temperature for Mg and Zn, showing that a roughly 80 °C higher cell temperature compared to the Zn cell is required to obtain a comparable Mg flux. To identify the growth rate of MgO thin films under typical growth conditions, a MgO layer was grown directly on sapphire at 570 °C for 2 hrs. It was found that the growth rate of the MgO thin film was approximately 100 nm/hr under a Mg flux of $\sim 2\times 10^{14}$ atoms·cm^{-2}·s^{-1} and an oxygen flow of 2 sccm at 400 W. Compared to ZnO (typically 300 nm/hr at 1.4×10^{15} atoms·cm^{-2}·s^{-1} and 1.6 sccm) the growth rate of MgO is approximately 1.8 times higher. This is consistent with the higher reactivity and larger sticking coefficient of Mg.

Figure 4.12 shows the RHEED of a typical 200 nm thick MgO film after growth. A 60º symmetry was observed for the RHEED pattern, suggesting that the MgO layer is predominantly hexagonal. However, comparing the RHEED pattern of the MgO layer in the $(1\bar{2}10)$ direction with that previously observed on other ZnO films (e.g. Figure 3.4), it can be seen that the periodicity of the RHEED spots is quite different to that expected for a pure hexagonal crystal lattice. This suggests that an alternative crystal structure is present in the MgO layer. In fact, the cross like pattern formed by the labelled spots as shown in Figure 4.12a is a well-known diffraction signature of the cubic (111) phase in the $(1\bar{2}10)$ direction [186, 187].

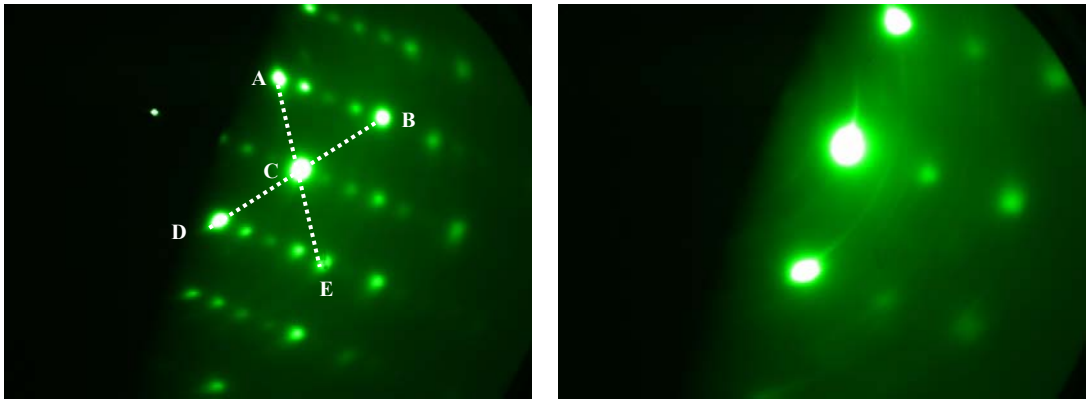

Figure 4.12 RHEED of MgO on sapphire taken after growth in the a) $(1\bar{2}10)$ direction and b) $(10\bar{1}0)$ direction. A 60° symmetry was observed suggesting a predominant hexagonal structure, but the cross pattern formed by the labelled spots indicates the co-existence of the cubic (111) phase.

According to Chen et al., the optimum thickness for the MgO buffer can be obtained by halting the MgO buffer growth just after the onset of 3-D island formation [184], i.e. when $t_{MgO} = t_{3D}$. However, since no real time RHEED was available during the majority of the experiments, it was very difficult to monitor the evolution of the MgO surface during growth. Therefore to investigate the surface evolution of MgO buffer layers, four MgO layers with thicknesses ranging from 0.5 nm - 3 nm were grown. The growth time for each was estimated using the growth rate of the thick MgO buffer layer by assuming a constant deposition rate over time. Figure 4.13 shows the RHEED of these ultra-thin MgO films, compared with the sapphire substrate surface. It can be seen that below 1 nm, the MgO film was strained with a perfect alignment to the sapphire lattice. The 2-D to 3-D transition occurred between 1 nm to 2 nm, with the MgO RHEED pattern superimposing on the sapphire pattern observable on the 2 nm thick layer. It is evident that a 30º rotation in the surface crystal lattice has occurred. As the thickness increased, the cubic features represented by the cross-like pattern became clearer, suggesting a further roughening of the surface. Note that the observation here is consistent with that of Minegishi et al., who observed a transition from 2-D to 3-D at ~1.5 nm [188].

The actual change in the surface morphology is illustrated by AFM scans shown in Figure 4.14. It can be seen that with the shortest deposition time, which is nominally 0.5 nm, the surface is not as smooth as expected. In particular, it is difficult to determine whether there is a complete coverage of the substrate. It is expected,

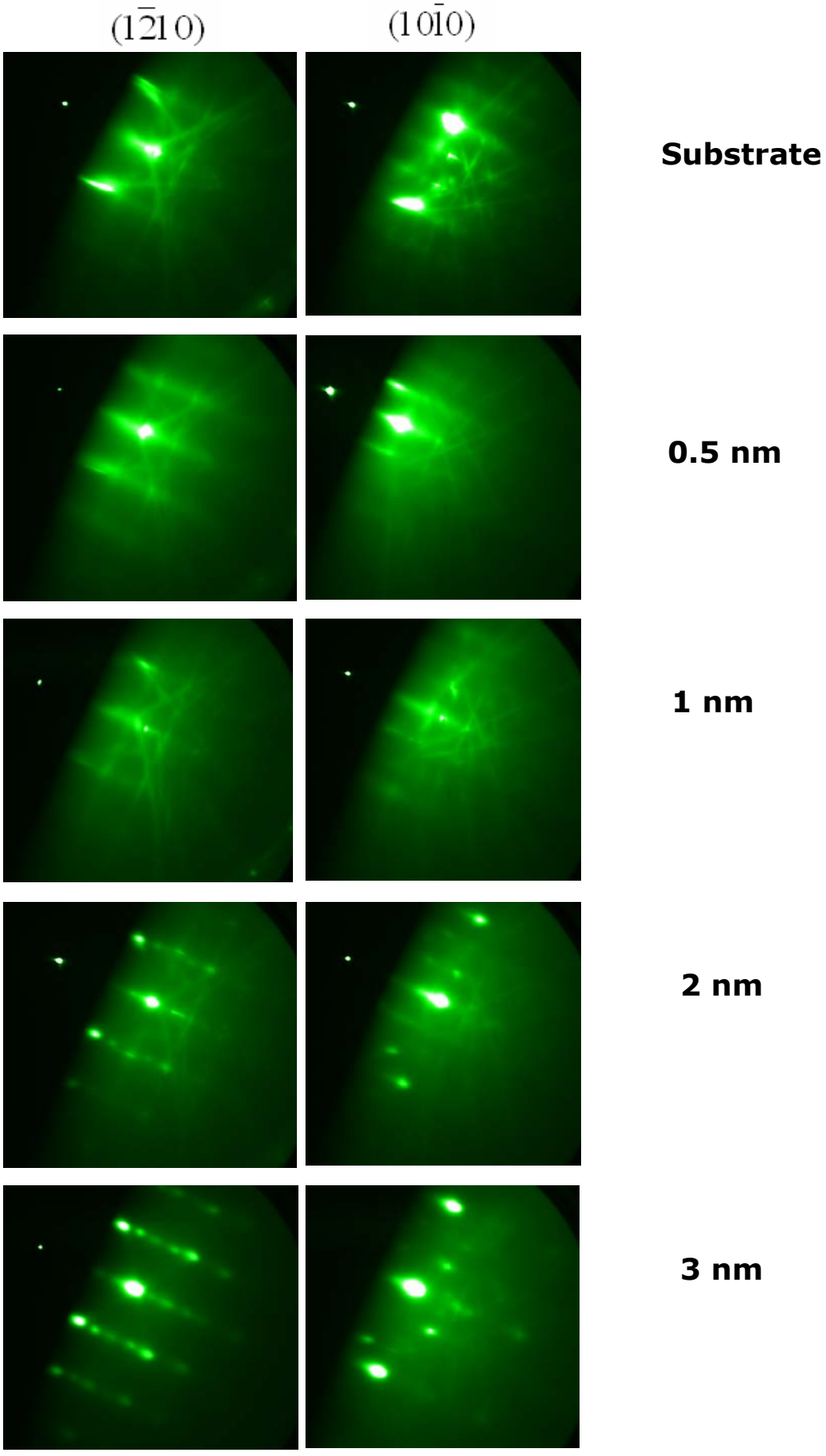

Figure 4.13 RHEED image of MgO buffers grown on sapphire with varying thicknesses. It can be seen the buffers are 30° rotated with respect to the sapphire. Above 1 nm, spots start to appear in both direction indicating the onset of surface roughening. The cubic "cross" pattern is also evident above 1 nm.

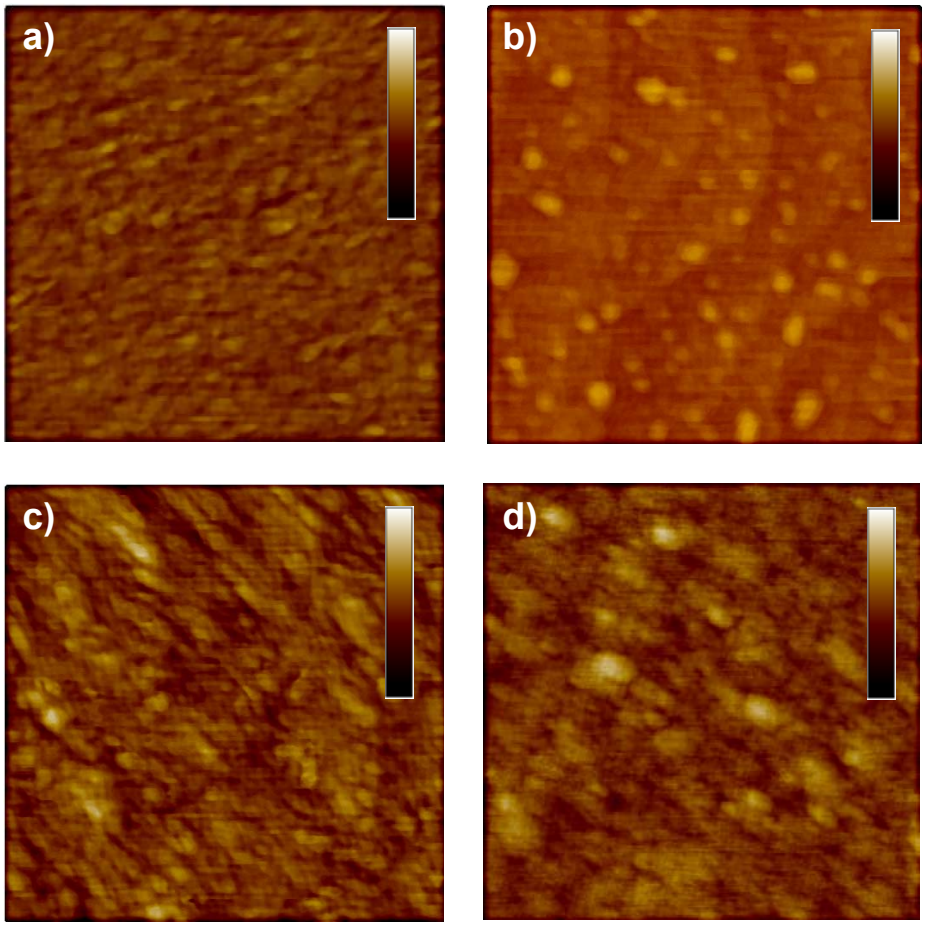

Figure 4.14 AFM images of MgO buffer layers of thickness a) 0.5 nm, b) 1 nm, c) 2 nm and d) 3 nm. All scans are 500 nm × 500 nm in area and the vertical scale is 10 nm for all scans except d) which has a 20 nm scale.

however, that the layer would be coherent and strained regardless of the surface coverage. At 1 nm, the MgO surface was covered with the random formation of island of < 50 nm in diameter, along with a very smooth underlying layer. The increased smoothness of the 1 nm layer compared to the 0.5 nm thick layer coupled with the random formation of small islands observed strongly suggests that the onset of strain relaxation occured at 1 nm [51], i.e. t_{3D} = 1 nm. Above 1 nm, the roughening of the surface became more evident, with the formation of clusters of islands with an average height of ~10 nm. This is extremely high compared to the nominal thickness of 3 nm. Such a transformation, possibly due to the tendency of cubic MgO formation, is not desirable for achieving 2-D growth. From this, it is apparent that a 1 nm MgO buffer layer would give the best surface as a buffer layer for subsequent ZnO growth.

4.3.3 ZnOThin Film with MgO Buffer

To investigate the effect of a MgO buffer on ZnO growth, a 1.2 μm thick (as measured using profilometry) ZnO layer was grown on a 1 nm MgO buffer, with an oxygen flow of 1.6 sccm, excited using a 1 hole plate plasma at 400 W. A Zn flux of 1.4×10^{15} atoms/cm^2·s was used, which should give a Zn-rich condition according to Figure 2.27. Prior to high temperature growth, a low temperature ZnO buffer was first deposited on top of the MgO layer to improve the wetting. Unlike Chen et al. [145], high temperature annealing after the low temperature buffer layer was omitted to allow a more direct comparison with previous film growths.

Figure 4.15 shows the after growth RHEED images of the ZnO thin film, hereby known as sample M. The RHEED pattern in the $(1\bar{2}10)$ direction showed a very coherent streaky RHEED, indicating the high quality of the surface. The RHEED pattern in the $(10\bar{1}0)$ direction, however, was dominated by spots and chevron features, suggesting the presence of islands. The asymmetry between the RHEED in the two directions suggests that these islands are very directional, and the chevron appearance suggests these features have well developed facets and are well structured [189].

The structure of sample M was further investigated by using HRXRD. Figure 4.16 shows the θ-2θ scan of sample M. Similar to films grown without MgO buffer (c.f. Figure 3.19), the strongest peak observed was ZnO (0002), implying a strong c-axis orientation. The 2θ values of 33.7° and 72.2° were determined for the (0002) peak and (0004) peak respectively. From these two values, the c-axis lattice

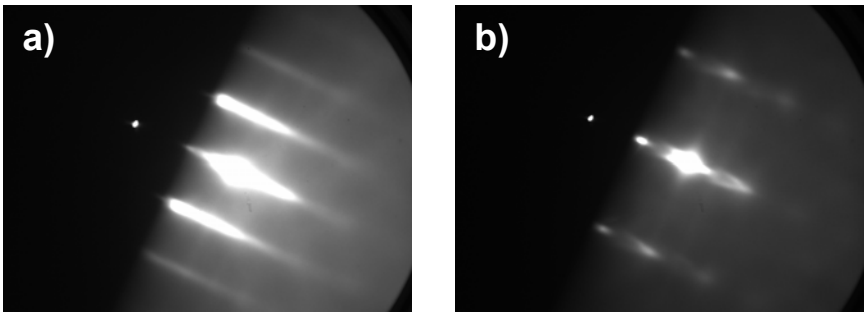

Figure 4.15 End of growth RHEED of the ZnO thin film grown on a MgO buffer layer, showing the a) $(1\bar{2}10)$ direction and b) $(10\bar{1}0)$ direction.

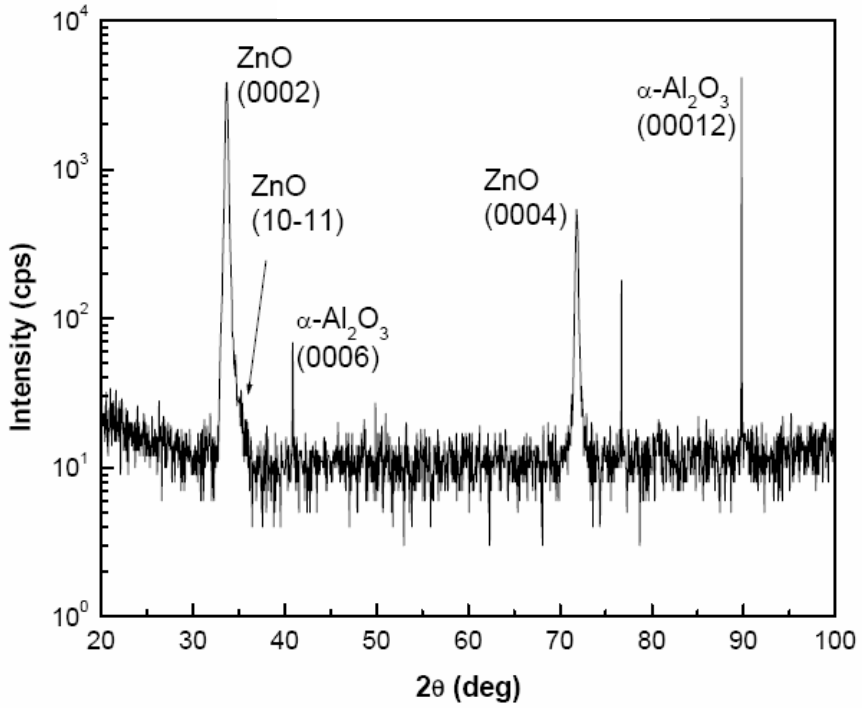

Figure 4.16 θ-2θ scan of ZnO thin film grown on MgO buffer, showing that the film is predominantly c-oriented. The width of the (0002) and (0004) peak was used to calculate the strain and the coherent distance of the sample.

constant can be calculated by Bragg's law:

$$c = 2d = \frac{\lambda}{\sin\theta} \qquad (4.6)$$

which gives c = 5.297 Å for sample M. Comparing this to a lattice constant of 5.206Å for freestanding ZnO [32], it can be seen that a tensile stress of 1.7% was experienced by the ZnO lattice in the c-axis direction. Note that this tensile stress was not observed for samples grown without a MgO buffer, which suggests that this tensile strain was introduced by the MgO layer. Examining the θ-2θ scan of sample M further, it can be seen that the (0002) peak is distinctly asymmetrical. This can be interpreted as the contribution of a small side peak corresponding to ZnO $(10\bar{1}1)$, indicating the existence of domains within the sample that deviated from the c-axis orientation. In particular, the $(10\bar{1}1)$ orientation corresponds to a 45° tilting of the crystal from the c-axis. This $(10\bar{1}1)$ peak of sample M is nearly 3 orders of magnitude lower than the (0002) peak, which suggests that the density of these $(10\bar{1}1)$ domains is low.

The FWHM of the (0002) peak and (0004) peak are approximately 0.21° and 0.34°, respectively. As mentioned in Section 3.3, the FWHM is related to the crystal quality in that the linewidth is inversely proportional to the crystal quality. In particular, the linewidth of the θ-2θ curve is mainly dependent on three factors: instrumental (experimental) widening; crystalline size; and inhomogeneous strain in the crystal [190, 191]. By taking the experimental widening into account through comparison with pure specimens, the separate effect of crystalline size and strain can be extracted by using Fourier analysis on two diffraction peaks from the same plane [184], in this case here, the (0002) and (0004) peak. A good estimation of the Fourier analysis can be evaluated by using Schoening's method, where the integral width (commonly known as the breadth) of each of the components are assumed separable, giving [191]:

$$\beta_c = \frac{\lambda}{D\cos\theta} \quad \text{and} \quad \beta_s = 2\varepsilon\tan\theta \tag{4.7}$$

for the crystalline size component β_c and the inhomogeneous strain component β_s, respectively, with D being the crystalline size and ε the strain in the lattice. These two components are related to the observed breadth according to the distribution of each component. For a Cauchy or Lorentzian distribution, the overall breadth is the sum of individual breadths; whereas for a Gaussian distribution, the sum of the squares of the individual breadths gives the square of the overall breadth [191]. Since in most cases the peaks are a mixture of both distribution types, a Cauchy-Gaussian mean is usually used where the average of the calculated values from a pure Gaussian and a pure Cauchy is used as the approximate value for *D* and ε [191].

By using FWHM/2 as an approximation of the integral breadth for θ [191], and applying Equation 4.7 to the (0002) peak and (0004) peak, it was found (using a Cauchy-Gausian approximation) that ε = 0.102 and *D* = 140 Å for sample M. The value of ε implies that there is approximately 10% non-uniformity in the strain (in the (0001) direction) throughout the sample. The value *D* is traditionally associated with the grain size, which has no meaning in a single crystal. Chen et al. suggested that *D* could be the coherence length of the crystal [168]. However, as their reported *D* value is not consistent with the XRD data displayed, this assignment may not be applicable. Note that it has been demonstrated that stacking faults have a similar effect on the

broadening of linewidth as crystalline sizes [192, 193]. Therefore, the value of D can possibly be interpreted as the mean distance between stacking faults in sample M. According to this, the D value suggests that on average a stacking fault occurs after every 30 monolayers.

Figure 4.17 shows the XRD rocking curves of a number of ZnO samples, including sample M, as well as a bulk ZnO sample from Tokyo Denpa. It can be seen that the FWHM of sample M is approximately the same as sample E - the best sample grown without a MgO buffer layer. The rocking curve for sample M is more symmetrical with a higher intensity, suggesting that sample M is more homogeneous. Sample F was grown under exactly the same conditions as sample M but without a MgO buffer. From the large FWHM of sample F compared to sample M, it can be seen that the improvement by simply adding an ultra thin layer of MgO buffer is very significant.

Compared to the reports in the literature, the FWHM values measured here are considerably higher. In fact, the FWHM of the best ZnO thin film grown on a MgO buffer layer reported by Cho et al. (18 arcsec) [184] was lower than that observed for

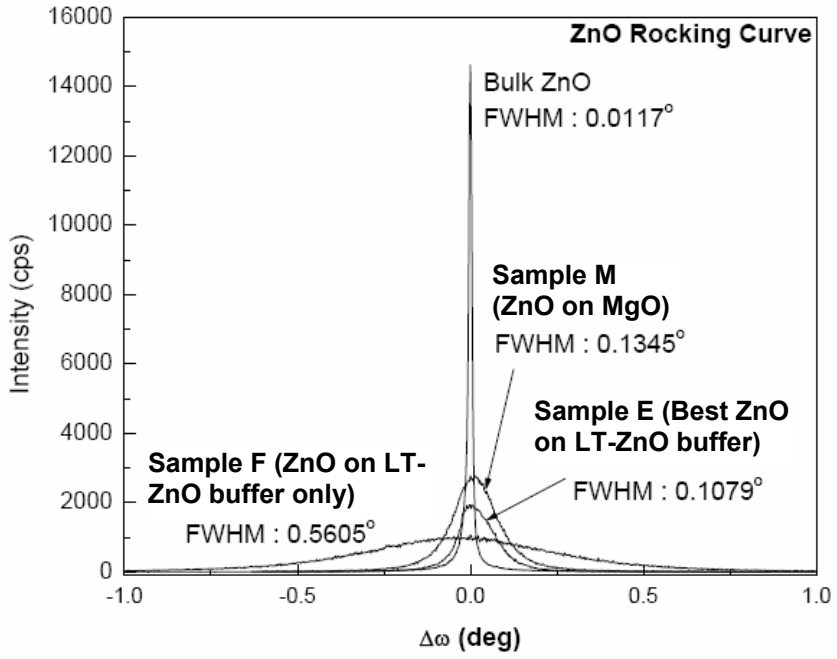

Figure 4.17 XRD rocking curve of ZnO crystal comparing the crystal quality of MBE grown thin films and bulk (Tokyo Denpa) ZnO material. The crystal quality improvement via using a MgO buffer layer is clearly illustrated.

a bulk ZnO sample (27 arcsec). Such high crystal integrity highlights the capability of the MgO buffer system, but also illustrates that the employment of a MgO buffer is only one of the many variables that need to be controlled for producing high quality material.

Figure 4.18 shows the SEM image of the surface of sample M. It can be seen the sample has a very distinct island morphology, similar to that observed on the surface of the Zn-rich film studied in Figure 3.7. Sample M, however, is covered by much larger islands. In particular, the island size is not as regular as that observed in Figure 3.7, with a diameter ranging from 200 nm to 500 nm observed for sample M. This larger island size represents a larger coherent region, consistent with the improved RHEED observed as the absence of small features is expected to reduce the amount of transmission diffraction. Additionally, irregular features extruding from the surface were observed sparingly on the surface of sample M (as labelled in Figure 4.18a). These features are not c-axis oriented and could possibly be one of the sources of the $(10\bar{1}0)$ side peak observed in XRD.

The directionality and the hexagonal nature of the pyramid-like islands can be seen more clearly with the AFM image shown in Figure 4.19. It can be seen that these pyramids are on average 80 nm high, which is small compared to the thickness of the sample (1.2 μm), thus the sample is relatively smooth. The directionality of these pyramids and the well developed facets are consistent with the observed asymmetry in

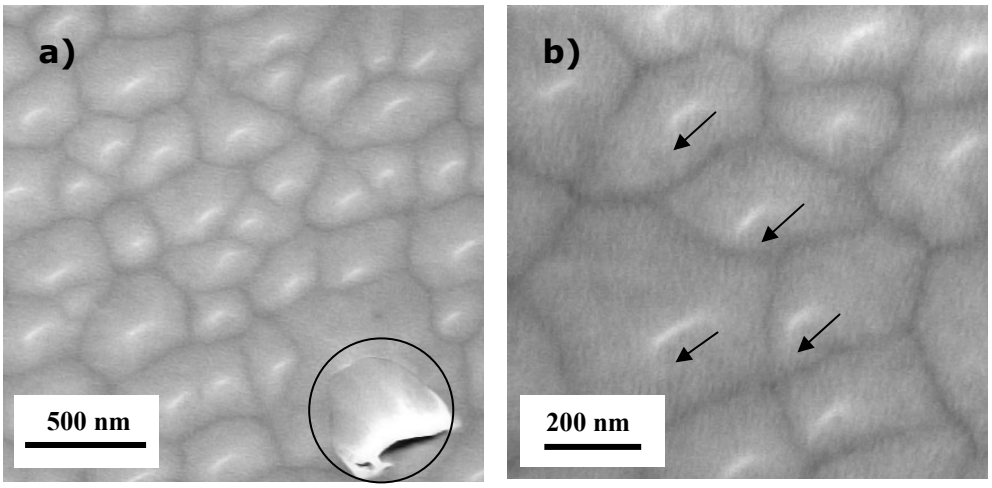

Figure 4.18 SEM images of a) 25000x and b) 50000x magnification, showing the features of the hillocks on the surface of film grown with MgO buffer. The circle shows an irregular domain on the surface, while the black arrows are showing the directionality of the ridges on the surface of the film.

the RHEED pattern. In particular, when the RHEED beam is parallel to the ridge direction the beam would predominantly be reflected from the ridges, resulting in a streaky pattern, whereas a beam perpendicular to one of the other faces would go through the different facets on the pyramids resulting in chevron features originated from transmission diffraction.

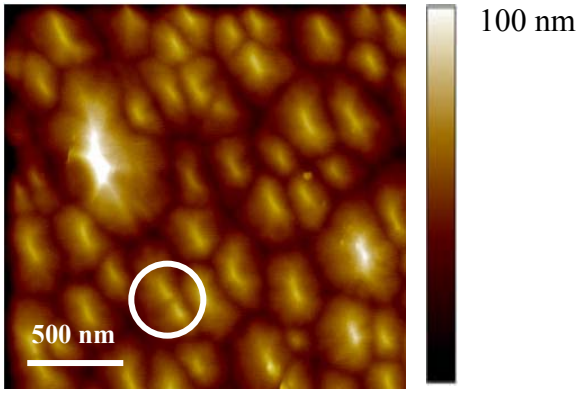

Figure 4.19 AFM image of the surface of ZnO/MgO showing the faceted natures and directionality of the islands. The circle shows an example of the incomplete coalescence of two islands.

4.3.4 Dislocations and Strain

The island formation observed from sample M is the direct result of strain relief in the sample. However, as mentioned in Section 4.2, even though surface roughening is the dominant strain relief mechanism in the ZnO/sapphire epitaxial system, dislocations can also form. In order to study the formation and effects of dislocations in more detail, transmission electron microscopy (TEM) (performed by Dr X. Weng at the Pennsylvania State University) was used to study sample M. Figure 4.20 shows the bright field (BF) TEM image of sample M and the corresponding transmission diffraction pattern. The BF image shows that the surface of the sample was quite smooth, with no evidence of discontinuities in the film. This suggests that the islands observed with SEM were coherent and oriented, and formed purely from misfit strain. The diffraction pattern (in $[1\bar{1}00]$ direction) showed only 0002_{ZnO} and $11\bar{2}0_{ZnO}$ diffraction spots, confirming that the single crystal structure is

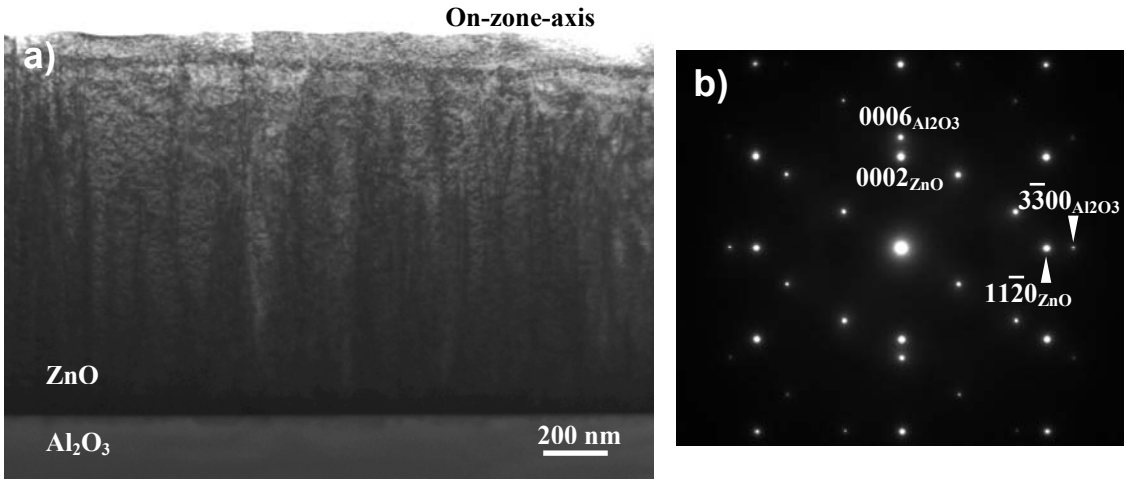

Figure 4.20 a) Bright field TEM and b) TEM diffraction pattern of the sample grown with a MgO buffer on zone axis. The limited contrast in the bright field TEM suggests limited defect density in the sample, whereas the lack of irregular diffraction spots suggests that the sample is a high quality single crystal with hexagonal structure.

purely hexagonal, dominantly consisted of a single phase. Furthermore, the diffraction spot alignment suggests that the $[11\bar{2}0]$ direction of ZnO is aligned with the $[1\bar{1}00]$ direction of sapphire, confirming the existence of 30° rotation even with a MgO buffer layer. Note that the actual MgO layer cannot be seen in Figure 4.20a, as it is expected that a 1 nm buffer layer would not be visible in the scale of the bright field scan. For a similar reason, the diffraction from the MgO buffer was too weak to be observable in the diffraction pattern in Figure 4.20b.

There are three types of dislocations - screw, edge, and mixed type. These can be identified as white lines in the dark field (DF) TEM image. In particular, screw dislocations can be seen in a DF image in the (0002) direction but not the $(11\bar{2}0)$ direction; edge dislocations appear only in the $(11\bar{2}0)$ direction; and mixed type dislocations appear in both directions [194]. Figure 4.21 shows the dark field (DF) TEM images for sample M in the (0002) and $(11\bar{2}0)$ directions. It can be seen from the line density in the two directions that the dislocations in sample M are predominantly edge type. This is consistent with previous reports on ZnO thin films [138, 184] as well as GaN thin films [195]. To determine the density of each type of dislocation, the two beam images were overlapped as shown in Figure 4.22. The blue colour lines represent edge dislocations, pure yellow lines represent screw

Figure 4.21 Dark field TEM of the ZnO/MgO sample in the (0002) and $(11\bar{2}0)$ directions. It can be seen that the sample has a relatively high dislocation density ($\sim 2\times 10^{10}$ cm^{-2}) compared to that reported in the literature. More dislocations are observed in the $(11\bar{2}0)$ direction, suggesting the predominance of edge dislocations. White circles identify a number of dislocation interactions.

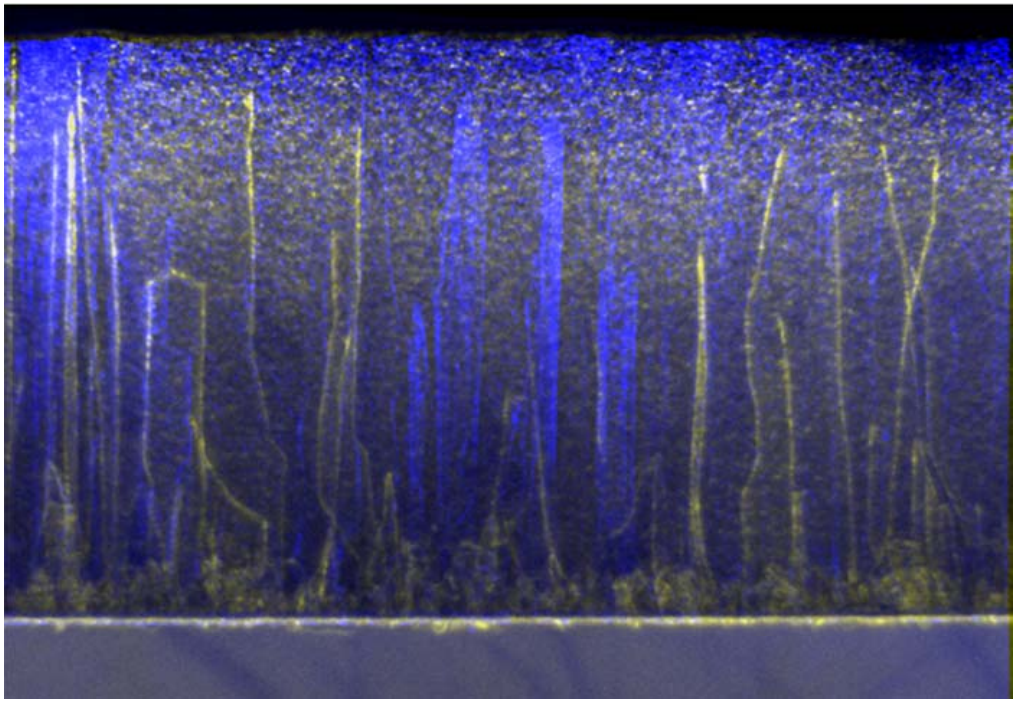

Figure 4.22 The overlapping of the two images shown in Figure 4.21. The blue is the edge dislocation, yellow are the screw dislocations, and dislocations with a white tint are mixed type that appeared in both weak beam directions.

dislocations, and dislocations that appear white are mixed type dislocations that are visible in both directions. It can be seen that over half of the dislocations that are visible in the (0002) direction are mixed type, while quite a few are ambiguous due to the much higher density of dislocations that appear on the $(11\bar{2}0)$ image. Only a few of the pure screw dislocations propagated in the c-axis direction.

Using the DF images, the dislocation density can be approximated by D = n/Lt, where n is the number of dislocations shown across an image of length L, and t is the foil thickness. Figure 4.23 shows the dislocation density estimated from the two beam images, assuming a uniform change in foil thickness from 300 nm measured at the interface to 50 nm measured near the surface. The estimated density plot shows that both the screw type and mixed type dislocation density reduced as the film growth progressed. The screw dislocation density decreased from $\sim 4\times10^{9}$ cm^{-2} to $\sim 5\times10^{8}$ cm^{-2}, and similarly the mixed type dislocation density decreased from $\sim 4\times10^{9}$ cm^{-2} to $\sim 2\times10^{9}$ cm^{-2}. In contrast, the edge dislocation density is virtually constant with increasing distance from the interface, with the density varying between 8×10^{9} cm^{-2} to 1.4×10^{10} cm^{-2}.

The dislocation density observed here is slightly higher than typically reported in the literature, which suggests that the crystal quality of the ZnO films in this work is slightly poorer. For example, Cho et al. reported a dislocation density of 1×10^{5} cm^{-2} and 1.1×10^{10} cm^{-2} for screw and edge dislocations respectively using XRD analysis (sample thickness unspecified) [184], while Miyamoto et al. reported a dislocation density of $\sim1\times10^{8}$ cm^{-2} for screw, $\sim1.3\times10^{9}$ cm^{-2} for edge and 5.4×10^{8} cm^{-2} for mixed type using TEM analysis (sample thickness ~ 1 μm) [86]. A dislocation density similar to that observed here was reported by Vigue et al. for a ZnO thin film grown without a MgO buffer layer [138]. The relatively high screw dislocation density observed here is consistent with the large FWHM observed for the (0002) rocking curve compared to previous reports as the (0002) rocking curve is only affected by screw and mixed type dislocations.

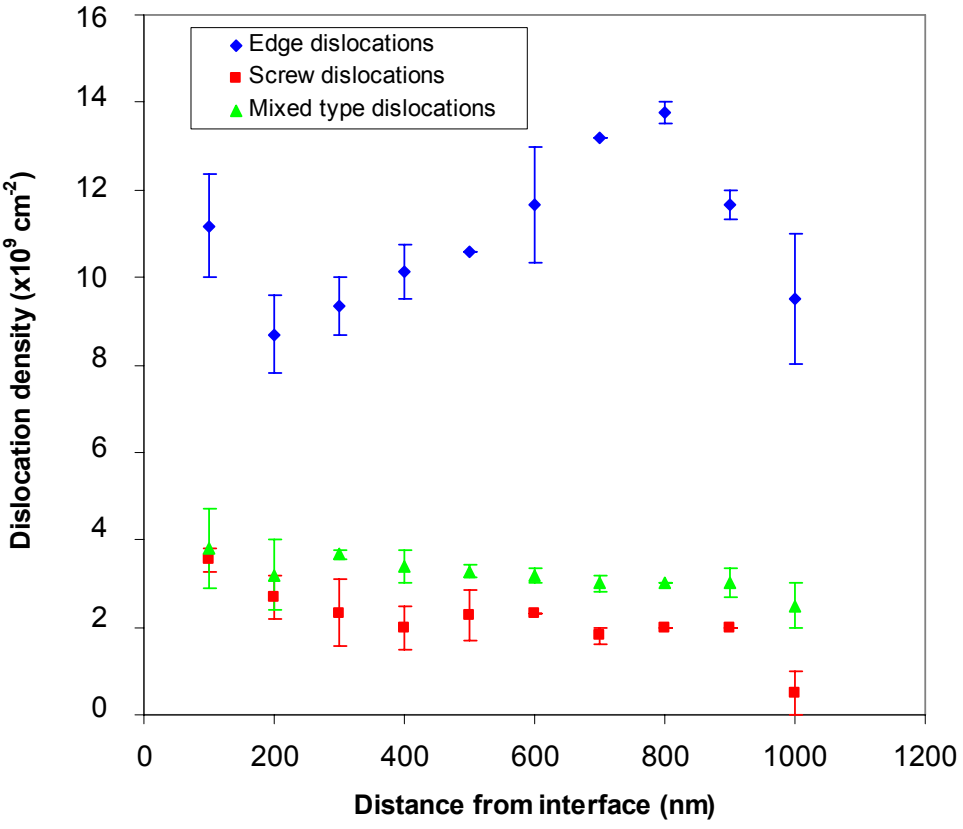

Figure 4.23 Dislocation density estimated from the DF TEM images and the foil thickness of the sample. A distinct reduction of dislocation density is seen for screw and mixed type dislocations but not for edge dislocations.

The reduction in dislocation density in an epitaxial layer with thickness is most likely due to the termination of dislocations. Since dislocations cannot abruptly self extinguish, the reduction of the dislocation density is mainly through the annihilation or fusion of dislocation pairs. According to Speck et al., the most probable way for threading dislocations to interact is for two dislocations that nucleated on parallel or intersecting planes to approach each other through gliding and inter-planar motion as growth progresses [196]. Upon reaching a threshold distance, the two dislocations attract each other to start the annihilation or fusion process. These kinds of interactions are readily observed in Figure 4.21 for screw dislocations, particularly for those that have deviated from the c-axis orientation, as labelled in the figure. This can be attributed to the fact that dislocations with a screw component have a greater tendency to change direction and move between planes, and thus are more likely to participate in annihilations [197].

The annihilation of dislocations with increased sample thickness has been described by a scaling law in a number of reports stating that the threading dislocation density is inversely proportional to the thickness of the layer [196, 198, 199]. Such a trend cannot be observed for sample M. This is expected as the scaling law is typically only applicable when the layer thickness is much greater than the annihilation radius (> 1 μm) [196]. It is expected that with a further increase in sample thickness a more distinct reduction in both the screw and the edge type dislocations may be observed.

The DF images in Figure 4.21 also indicate that the dislocation density for the first 50 nm of the thin film is extremely high as seen in both beam directions. This high density of non-directional dislocations originated from the highly strained interface layer, and these dislocations are sometimes known as basal plane dislocations [184]. An abrupt reduction of the dislocation density can be observed at around 50 nm. Similar behaviour has been observed previously and was attributed to the non-directionality of the basal dislocations which allow them to quickly annihilate each other [184]. However, this does not fully explain how most of the dislocations from the interface distinctly terminated after 50 nm of growth, which is, interestingly, the approximate thickness of the LT-ZnO/MgO buffer system. A possible cause of this behaviour is the dislocation pinning effect: the "pinning" of a threading dislocation to a certain point of minimum energy in the epilayer, thereby immobilising the dislocation and halting dislocation propagation [200]. It has been

shown that a sacrificial buffer layer can lead to dislocation pinning either by providing a minimum energy at the buffer layer surface through growth interruption, or by reducing the driving force of the dislocation propagation to zero via the formation of orthogonal interfacial dislocations at the buffer-epilayer interface during the bulk growth [201]. Therefore, it is possible that the employment of the LT-ZnO buffer layer suppresses the propagation of any dislocations that have not been annihilated in the early stages of growth, thereby leading to a distinct reduction of dislocation density within the first 50 nm of the film.

Figure 4.24 shows the HRTEM image of the ZnO/MgO/Al_2O_3 interface along the $[1\bar{1}00]$ and $[11\bar{2}0]$ zone axis. The MgO buffer cannot be clearly identified, although it is clear that two monolayers of atoms near the interface separate the substrate from the ZnO layer. This implies that the MgO buffer does exist, but it is not as thick as expected. In addition, the MgO buffer is coherent, strained and 2-D, as evident from the matching of the atomic arrangement to the sapphire substrate. The

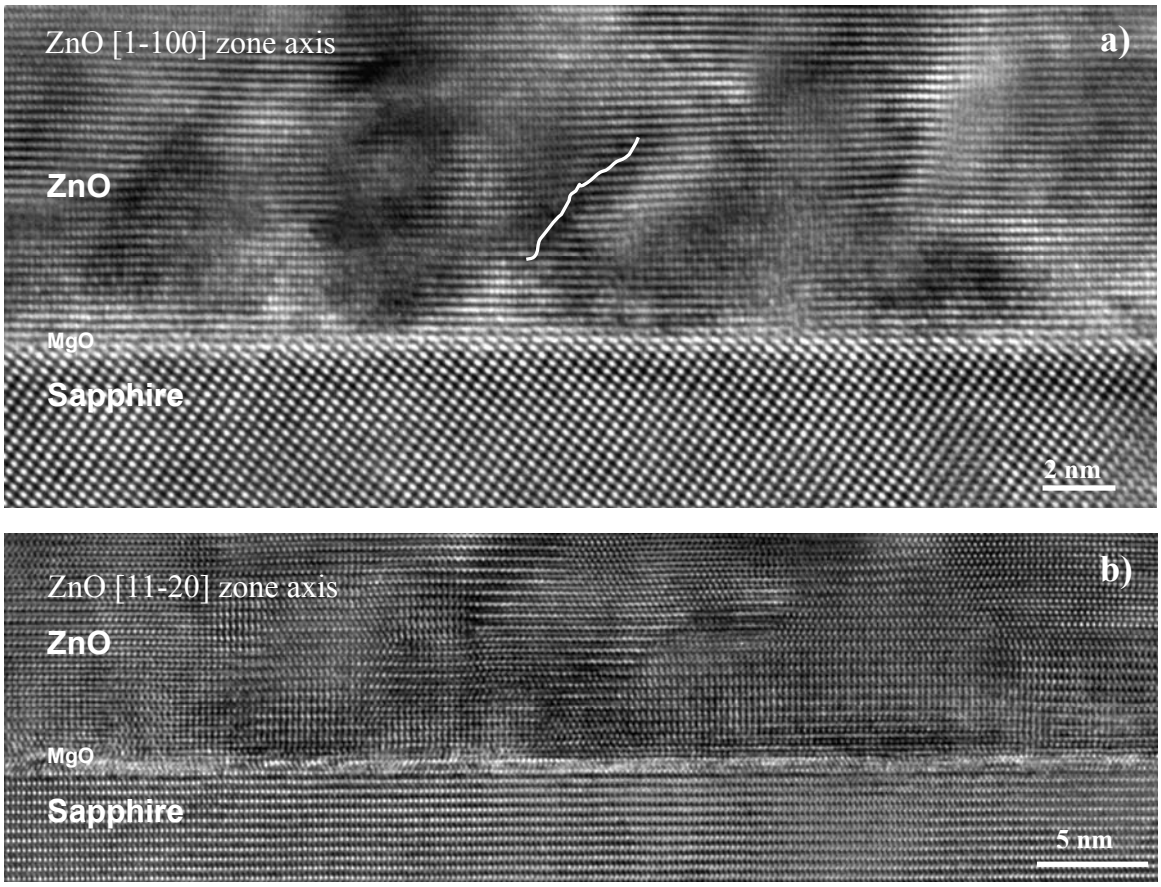

Figure 4.24 HRTEM of the interface between the sapphire, MgO and ZnO in the a) $[1\bar{1}00]$ direction and b) $[11\bar{2}0]$ direction. The images in both directions show that the MgO layer is thinner than expected, but is clearly 2-D and coherent. The white line shows an example of dislocation nucleated close to the interface that is not propagating in the c-direction.

high quality of the ZnO sample observed is inevitably dependent on these facts. There were dislocations nucleating after approximately 2 nm of growth, which is consistent with the RHEED analysis presented in Figure 4.10. Most of the dislocations observed near the interface are not fully (0002) oriented (as labelled), supporting the hypothesis that interfacial dislocations annihilate at a faster rate because they are tilted.

4.3.5 Optical and Electrical Characteristics

Figure 4.25 shows the 4 K PL of sample M, showing the NBE. Compared to the PL observed in previous films without a MgO buffer (c.f. Figure 3.10) it is obvious that the emission spectrum of sample M has many more features, implying sharper excitonic emissions. In particular, the bound exciton emission can be clearly separated into three features at 3.3568 eV, 3.3606 eV, and 3.3658 eV, corresponding to the I_9, I_6 and I_{3a} lines respectively [155]. Both the A exciton and B exciton emissions are visible at 3.3775 and 3.3925 eV, respectively. These peak positions are

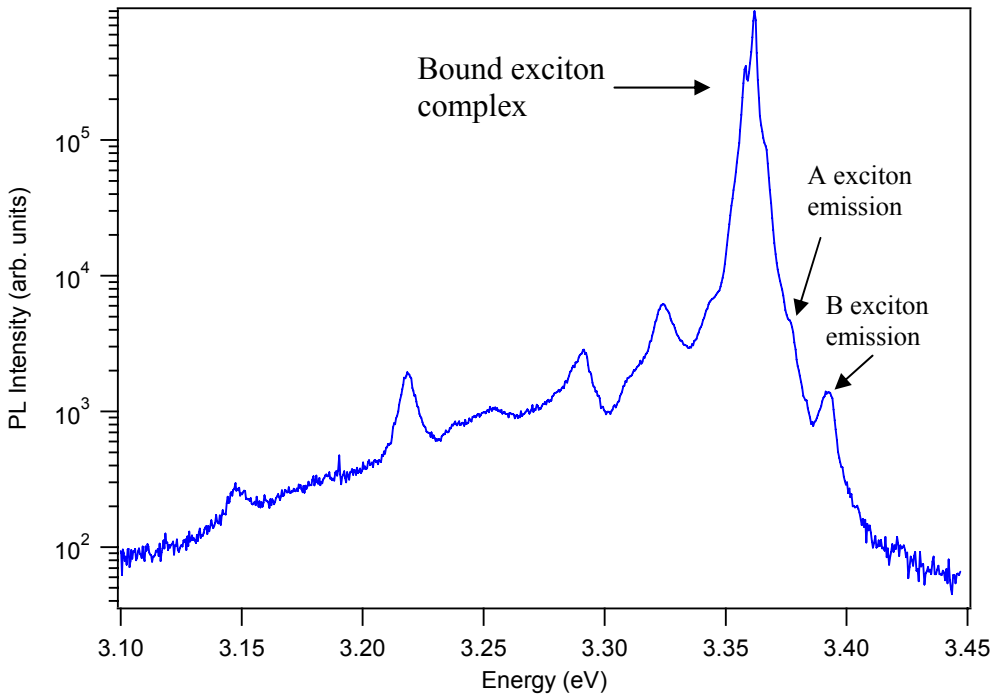

Figure 4.25 4 K PL of the ZnO/MgO thin film, showing the multi-excitonic features in the bandedge region, which indicates its superior crystal quality. Note also the sharp B-excition emission observed here which is rarely observed in other samples.

in exact accordance with the reported exciton positions for freestanding bulk ZnO crystal, which implies that the ZnO film is totally relaxed [155]. Furthermore, the clear separation of these different features in the bound exciton complex suggests that the crystal quality of sample M is very high, consistent with other measurements. In fact, the FWHM of the bound exciton complex for sample M is ~2 meV, which is identical to the best value reported in the literature for ZnO thin films [135].

Figure 4.26 shows the PL of sample F (no MgO buffer) compared with sample M, both samples grown under identical conditions. It can be seen that by using the MgO buffer, a dramatic improvement in the crystal structure was observed, with a substantial decrease in bound exciton complex FWHM from 12 meV to 2 meV. Multiple LO phonon replicas were also observed on sample M's emission but not in the spectrum of sample F. Such a huge improvement under the same growth condition highlights the beneficial effect of MgO buffer layers on the growth of ZnO thin films.

The room temperature PL of sample M is shown in Figure 4.27, along with the PL of the Zn-rich sample studied in Section 3.2 as a comparison. A larger NDR can

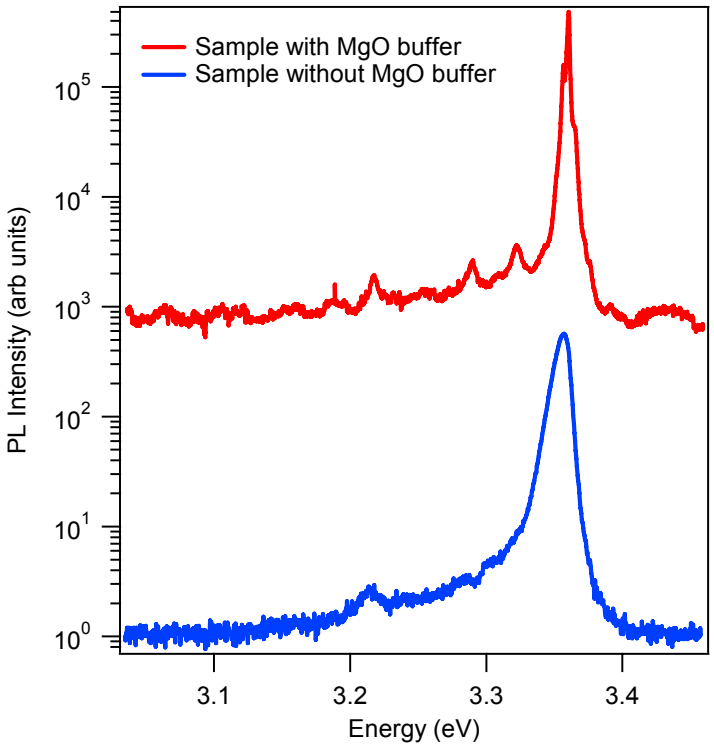

Figure 4.26 The 4 K PL of two samples grown under exactly the same conditions except for the employment of a MgO buffer layer. The improvement of optical quality with the use of the MgO buffer is clear.

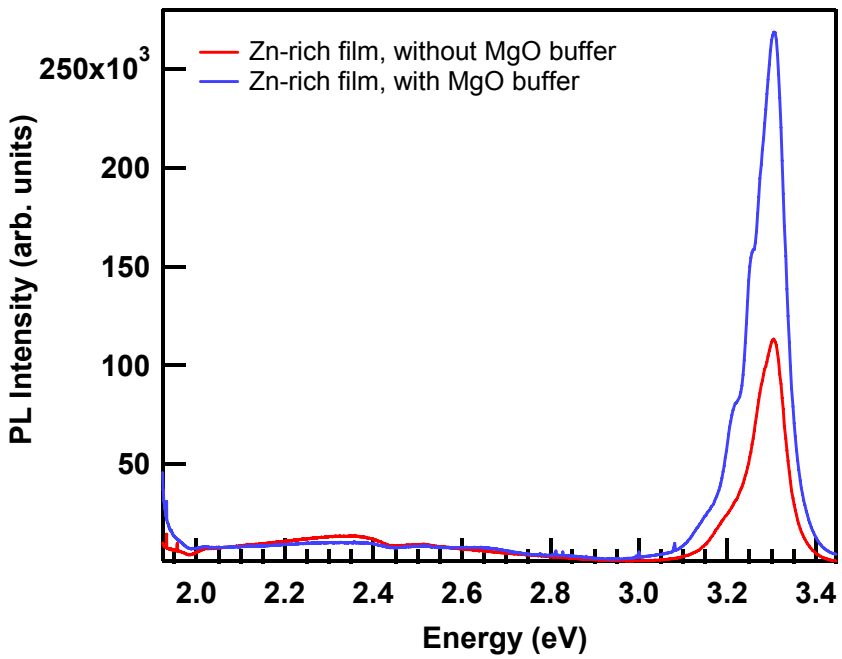

Figure 4.27 Room temperature PL of the ZnO/MgO sample compared with the PL observed in a Zn-rich sample grown with only a LT buffer. Again, the improvement in optical emission is significant.

be seen for sample M (up to 2.5 times higher) compared to the other sample, even though the actual DBE of the two samples are similar. This suggests that the employment of MgO buffer improves the free excitonic emission significantly, but has limited effects on the reduction of optical defects in the thin film. Multiple features were observable from sample M's room temperature PL, similar to that observed in Figure 3.23a. Again, the structured excitonic emission at room temperature indicates the high quality of the sample.

All MgO films grown in this study were measured to be insulating, not surprising given its 8.0 eV bandgap. Therefore, unlike ZnO/LT-ZnO or ZnO/sapphire, the MgO ultra-thin buffers should not affect the electrical measurements of the bulk of the ZnO film. Using conventional Hall effect measurements, the carrier concentration of sample M was determined to be ~ 8×10^{15} cm^{-3}, with a mobility of ~17 cm^2/Vs and a resistivity of ~44 Ω·cm. Although low mobility limited the accuracy of the measurement, it is evident that the carrier concentration was significantly reduced by employing the MgO buffer. During the course of the Hall effect measurements, it was found that the Hall voltages increased with time. This indicates the presence of persistent photoconductivity (PPC), which originated from the illumination of the sample with ambient light prior to the Hall effect measurements. This PPC indicates that photocarriers had contributed to the initial

measurements, suggesting that the background carrier concentration of sample M is even lower than the measured value. To eliminate this PPC effect the sample was left in the dark for over 24 hours, after which a resistivity of 2000 Ω·cm was measured, with a corresponding carrier concentration of $\sim 3 \times 10^{14}$ cm^{-3} and mobility of ~8 cm^2/Vs. Note that because of the very small change in Hall voltages observed, the actual mobility might be even lower, which implies that the carrier concentration is possibly higher than the value quoted here. However, even with a mobility of 0.1 $cm^2/V \cdot s$, the carrier concentration would be $\sim 1 \times 10^{16}$ cm^{-3}, still very low compared to that reported in the literature.

The PPC and the low mobility observed here strongly indicate a high density of deep level traps in sample M that did not contribute to the carrier density, but caused a high level of carrier scattering through the trapping and detrapping of carriers. In particular, these deep level traps capture photocarriers and release them with a long decay time constant, resulting in a long lifetime PPC. Such trapping is highly undesirable. From its effect on the conductivity measurements, it can be seen that the PPC observed in this work only generates a small amount of carriers (on the order of $\sim 1 \times 10^{16}$ cm^{-3}) in the sample, and therefore, it can only be observed when the background carrier density is low. As the PPC described here is generally observable in most films grown using a MgO buffer layer but not in other samples, one can conclude that the employment of a MgO buffer eliminated most of the donors (most probably structural defects) that were present in the ZnO/LT-ZnO thin films. It should also be noted that similar PPC behaviour is also present in recently acquired bulk samples from Tokyo Denpa, which were observed to have a carrier concentration of 1×10^{13} cm^{-3} [88]. This similarity to the bulk material confirms the relatively low concentration of defect related donors in the ZnO/LT-ZnO/MgO films.

4.3.6 MgO Buffer and Epilayer Polarity

Previous reports have also identified another function of the MgO buffer, namely, controlling the polarity of ZnO thin films [188, 202]. It has been observed in this work through etching experiments that without any substrate treatment, ZnO thin films grown directly on c-plane sapphire are almost always O-polar. While the polarity of ZnO thin films in most cases has limited effects on the electrical or optical

properties, it can affect impurity incorporation [203]. There is also evidence which suggests that Zn-polar surfaces provide a better platform for the formation of Schottky diodes [204]. Because of these device related differences between the polarities, it is advantageous to be able to control the polarity of the ZnO thin films grown by MBE. A number of substrate preprocessing procedures such as nitridation [205], O irradiation [206] and Ga irradiation [207] were shown to alter the polarity of the resulting ZnO. Similarly, Minegishi et al. has shown that by varying the thickness of the MgO buffer the polarity of the resulting ZnO can be controlled [188]. In particular, they found that there is a distinct transition from O-polar to Zn-polar when the MgO buffer thickness exceeds 2.7 nm, the critical thickness that marks the MgO hexagonal to cubic transition. In the present work, it was observed that cubic phases start to appear when the MgO buffer exceeds 2 nm (c.f. Figure 4.13), slightly lower than that observed by Minegishi et al. This slight discrepancy between the two values can be explained by a number of factors such as the growth conditions and the thickness measurement technique used. The important thing to note is that the observation of a hexagonal to cubic transition in this work suggests that the polarity of the films grown by the current system can be controlled using the thickness of the MgO layer.

Figure 4.28 shows the SEM of the as grown (Figure 4.28 a,c) and etched surface (Figure 4.28 b,d) of two ZnO/MgO thin films. Both films were grown under O-rich conditions; one was grown with a MgO buffer thickness of ~1 nm, while the other with a MgO buffer thickness of ~3 nm. The surfaces of both films were extremely rough, mainly due to the O-rich condition and possibly the unoptimised buffer growth conditions used. The light etching of the surfaces of the two films with diluted hydrochloric acid (<0.05%) revealed different features. In particular, disregarding the irregular etch pits (orange labels) which originated from the irregular features that were intruding from the surface (islands for the first film and narrow ridges for the second film), it can be seen that for the film with a thin MgO buffer, the rest of the etched surface was covered with small hexagonal structures, whereas for the film with a thick MgO buffer, pits were observed from the etched surface (green labels). According to Tampo et al. [208], this suggests that a thin buffer layer resulted in an O-polar film, whereas a thick buffer layer produced a Zn-polar film. This is consistent with the observations by Minegishi et al. [188].

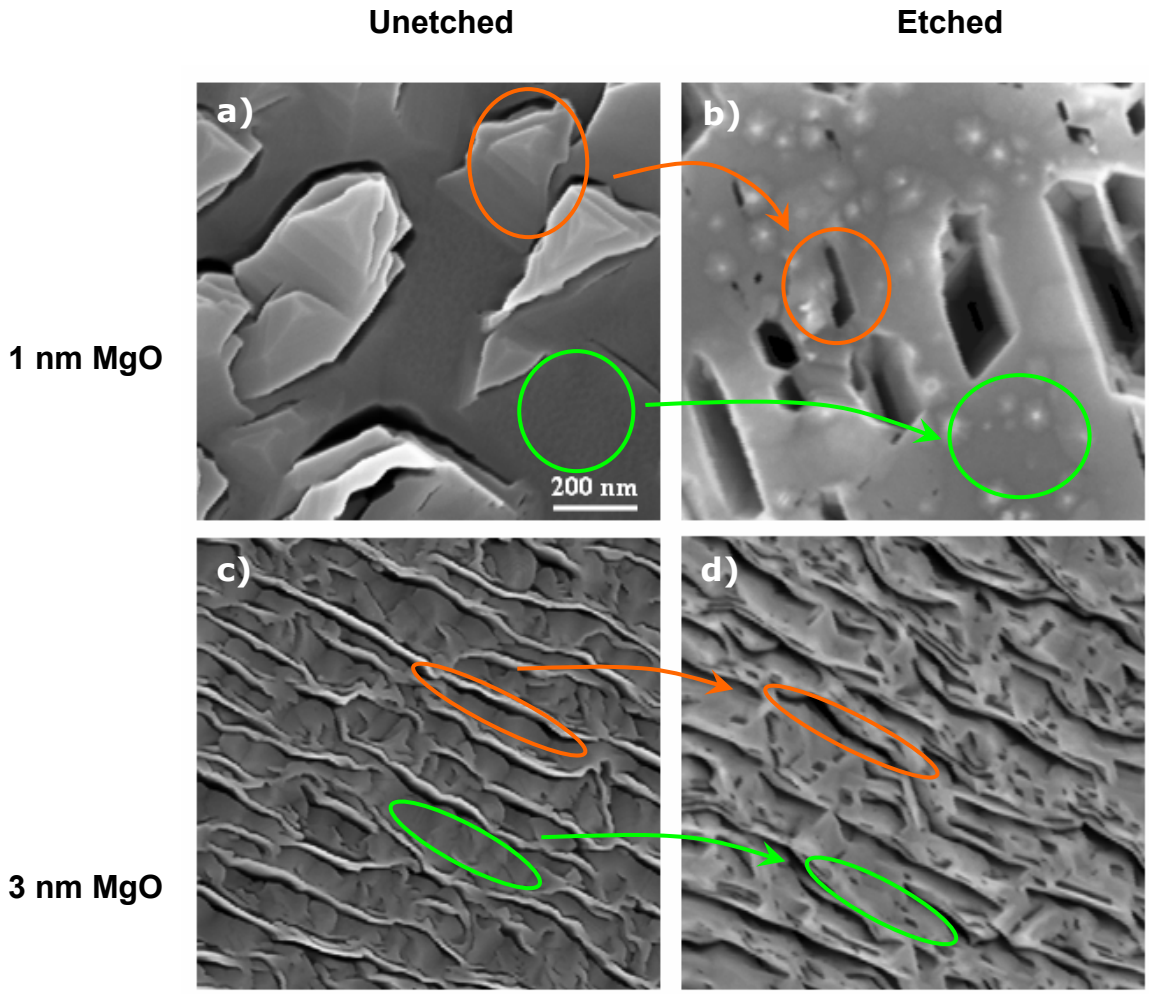

Figure 4.28 SEM images of sample surface before and after etching for samples grown with: a, b) 1 nm MgO buffer, and c, d) 3 nm buffer layer. The orange labels illustrate an example of the etching of irregular surface features, whereas green represents the etching of the underlying regular surface. The different etching behaviours illustrated by the green labels suggest that is a change in polarity with MgO buffer thickness.

One might argue that the roughly etched surface and the dominance of the irregular features masked the expected trend and are giving etching results that are not the most convincing. However, apart from the difference in the etch behaviour, an increase in growth rate was also observed with the increase in the MgO buffer thickness. In particular, with the same growth condition and growth time, the thickness of the film with the thin MgO buffer layer is 0.85 μm compared to 1.45 μm for the film grown with a thick MgO buffer. Note that Kato et al. observed a doubled growth rate for ZnO thin films grown with a thick MgO buffer layer, which were also found to be Zn-polar [202]. They have attributed the increase in growth rate to the extra dangling bonds on the surface of a Zn-polar film. Therefore, the 1.7 times

increase in growth rate observed here provides strong evidence that polarity has been changed by increasing the MgO buffer thickness from a hexagonal growth regime to a cubic growth regime.

Even though polarity control by MgO buffer thickness is possible, it can be seen from Figure 4.28 and from the AFM images in Figure 4.14 that a thick MgO layer can result in the degradation of crystal quality from the extreme roughening of the buffer. Therefore, Zn-polar ZnO thin films grown using this method might not be suitable for device applications.

4.4 Strain Reduction Through Structural Variation

The previous sections have shown that by using a buffer layer, a large part or even all of the strain caused by the lattice mismatch can be accommodated. However, while the appropriate buffer layer can lead to an improvement in the crystal quality, strain relief does not solely rely on the buffer layers. Other mechanisms of strain relaxation have been observed in this work. In this section, some of these observations will be discussed and their relevance to growth optimisation will be evaluated.

4.4.1 Domains

Thin film crystal structures can take different forms, depending on the amount of disorder present in the crystal lattice. If only small amounts of disorder exist, virtually all atoms in the thin film would be aligned into a continuous crystal lattice (Figure 4.29a). These single crystals may have localised, very small scale disruptions such as dislocations, but overall the crystal lattice structure, orientation and symmetry are virtually identical everywhere in the thin film. Such a perfect single crystal can only form under certain optimal growth conditions. Under conditions that are far from optimal, polycrystalline thin films can form where the thin films are made of a large number of discrete crystals each having slightly different structure and orientation, separated by grain boundaries (Figure 4.29b). Most crystalline thin films, however, are neither polycrystalline nor pure single crystal. In particular, pockets of disordered

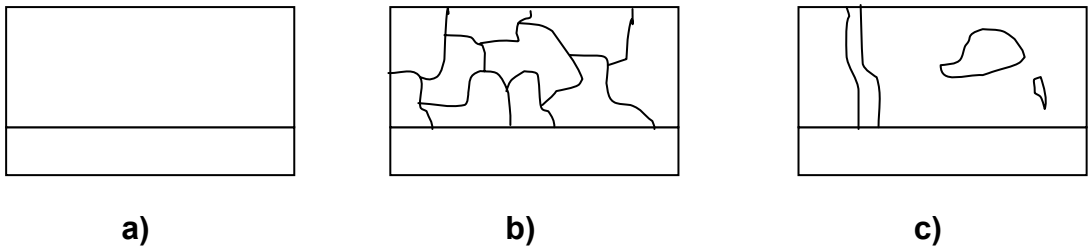

Figure 4.29 Three possible thin film crystal structures: a) Single crystal - a perfect crystal throughout the film; b) Polycrystalline - a conglomeration of grains with different crystal structures; c) A thin film that is predominantly single crystal, with domains of different lattice structures embedded.

regions may form within a single crystal film under non-optimal conditions (Figure 4.29c). These regions of varying crystal structure are known as domains. Because of their small volume compared to the main crystal lattice, these domains in most cases are considered as structural defects in a single crystal lattice. It is evident that many of the ZnO thin films grown in the present work have different types and densities of domains. These domains mostly originated from the strain in the epilayer.

As mentioned in the last two sections, misfit strain can be relieved via surface roughening and dislocation formation. However, these two mechanisms may not completely relieve the strain in the lattice. Furthermore, dislocations and island formations, along with inadequate diffusion, can induce additional localised strain due to the deformation of the crystal lattice. Therefore, even with the occurrence of dislocation nucleation and roughening, it is very possible that a thin film is still strained, most likely in a localised fashion. As growth progresses, the strain in these localised regions builds up, and eventually becomes so large that atoms in the vicinity are forced to align and orient differently to the rest of the lattice, creating regions of alternative crystal structure. Since atom realignment requires energy, the formation of these local domains results in the release of strain energy. Further disruption of the crystal lattice would lead to an increase in the density of domains. Eventually, the crystal ceases being a single crystal and becomes polycrystalline. Note that polycrystalline is not the end of the disorder continuum. Even larger disruption would result in the loss of crystal structure in the entire sample, turning it amorphous.

There are different types of domains, classified by the relationship of their structure to the bulk crystal structure. Each type of domain forms under different conditions and has different effects on the crystal lattice and other properties of the thin film. Throughout this work, different types of domains were encountered in ZnO films grown with or without buffer layers. These will be described in more detail.

4.4.2 Rotation Domains

As mentioned in Sections 4.2 and 4.3, both RHEED and TEM showed evidence that ZnO grown on sapphire has a 30º rotation with respect to the substrate lattice. However, there is also evidence which suggests the existence of regions in the crystal lattice that are not rotated with respect to the sapphire substrate. These regions are known as rotation domains, and are 30º rotated with respect to the bulk ZnO crystal lattice.

The existence of rotation domains can be readily observed with RHEED. Figure 4.30 shows the RHEED of one of the many samples that has rotation domains. It can be seen that in the $(11\bar{2}0)$ direction, a secondary streak can be observed adjacent to the top streak A and the bottom streak E. In addition, in the $(1\bar{1}00)$ direction, intermediate streaks (G and I) were clearly observable in between the three main streaks. Note that these intermediate streaks resemble secondary streaks from surface reconstruction, which should be equally spaced between the main streaks. From the line profile, it can be seen that this is not the case. In particular, by plotting the line profile of the RHEED pattern and aligning the central streak that is present in both directions (Figure 4.30b and d), it can be observed that the side streak spacing in the $(11\bar{2}0)$ direction is actually the same as the spacing of the main streak in the $(1\bar{1}00)$ direction and vice versa. The fact that these side streaks are 30° out of phase with the main streaks indicates that they are from 30° rotation domains. The intensities of the diffracted pattern from the rotation domains are much lower than the diffraction from the main crystal, which suggests that only a small density of rotation domains exists in this sample. There are other samples such as that

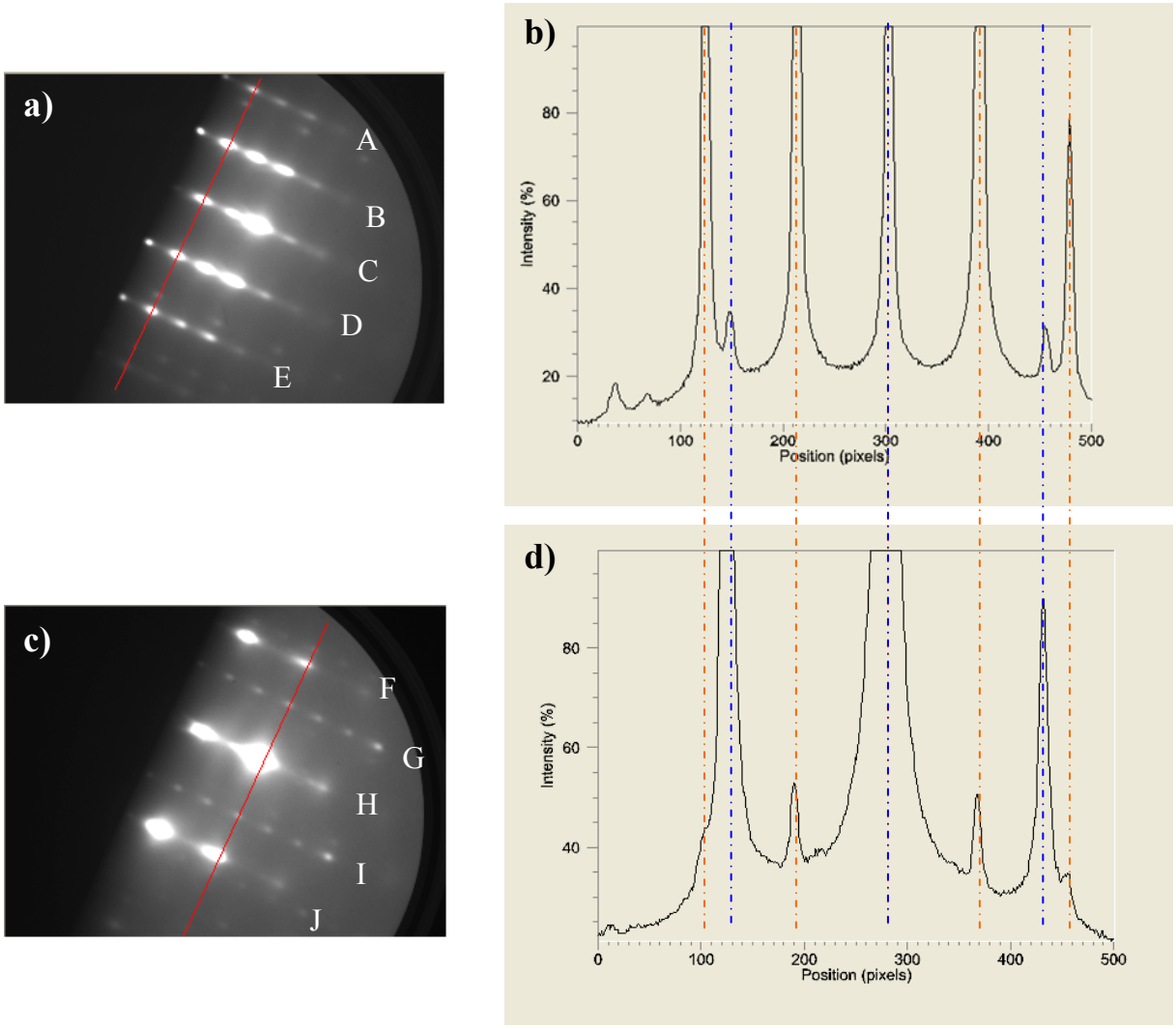

Figure 4.30 RHEED images of a) (11 $\bar{2}$ 0) direction and b) (10 $\bar{1}$ 0) direction diffraction patterns and their respective line profile (c, d) showing the existence of rotation domains. The nature of the side streaks between the main streaks are identified as rotation domains. This is confirmed by the clear correspondence of the secondary streak in one direction to the main streaks in the other direction (orange and blue lines).

shown in Figure 3.6c where the intensity of these side streaks are comparable to the intensity of the main streaks. In such cases, the rotation domain density is large, and a larger fraction of the volume is rotated. In effect, the sample can no longer be considered a single crystal.

Rotation domains have been observed previously in ZnO and GaN. Yamaguchi et al. reported the existence of 11° rotation domains in GaN thin films grown on sapphire and was able to suppress it using a nitridation process [209]. Yoshikawa et al. reported 30º domains in ZnO grown directly on sapphire, as well as less pronounced 21.8° domains when the sapphire surface was treated with atomic hydrogen prior to growth [210]. From the effect of surface treatments on the domain

formation, both reports suggested that these rotation domains originated from the interface. This is consistent with the observations in this work, where RHEED from very early stages of growth for a number of samples showed evidence of rotation domains. Yoshikawa et al. have attributed the formation of these 30º domains to the bonding of the oxygen atom (from the ZnO lattice) with the Al on the sapphire lattice (i.e. $O_{(ZnO)}$-$Al_{(sapphire)}$, rather than the typical $Zn_{(ZnO)}$-$O_{(sapphire)}$ bonding). This argument suggests that samples grown under O-excess conditions are more likely to form rotation domains as there will be a higher probability of O-Al bonding. This is also consistent with observations in this study, where many O-rich films were observed to have rotation domains. However, not all O-rich samples have rotation domains. Similarly, there are films grown with the same interface conditions as samples with domains that do not have rotation domains. Therefore, there are other variables that affect the formation of rotation domains.

The strain relief effects of rotation domains originated from the atomic rearrangements along the domain boundaries, where the strain energy is released from the lattice and used as the formation energy of the rotation domains. In particular, Liu et al. have shown that for interfacial rotation domains, the domain formation can take place prior to the misfit critical thickness t_{MD} [211]. This suggests that under conditions where rotation domains are favoured, the strain relief through rotation domain formation would dominate over misfit dislocation formations.

It has been shown by a number of reports that the formation of rotation domains is undesirable [209, 211]. Since the occurrence of rotation domains are quite common, it is necessary to take them into consideration when optimising the growth of ZnO thin films. Observations in this work suggest that there is a higher chance for rotation domains to form under O-rich conditions. Therefore, growing under Zn-rich conditions is expected to reduce the probability of rotation domain formation in ZnO thin films.

4.4.3 Twinning

In a number of samples, RHEED images that are similar to Figure 4.31 were observed, where two closely spaced secondary streaks (B, C, E and F) can be seen

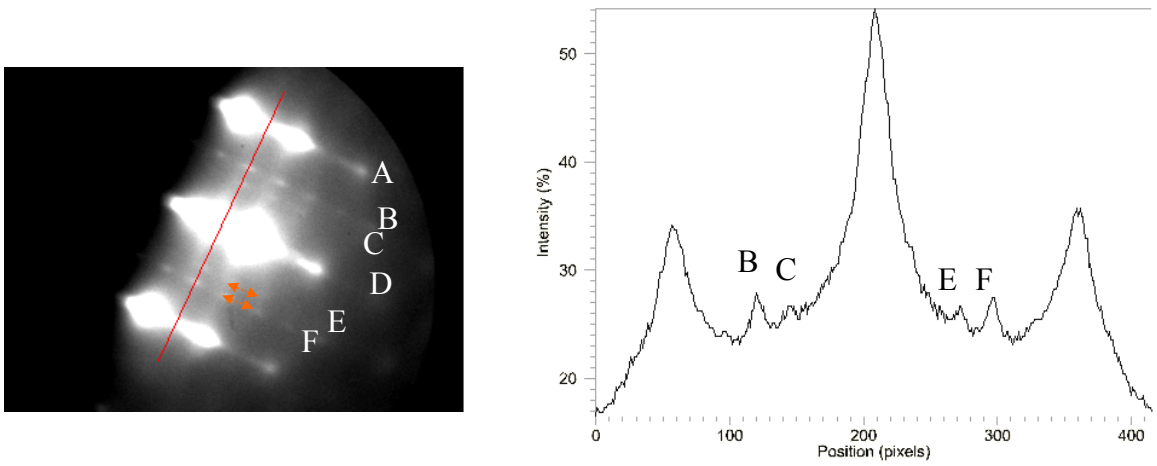

Figure 4.31 RHEED image and line profile of the diffraction pattern showing crystal twinning. The double streaks in between the main streaks are identified as twins from the extremely small spacing between them. Note that this twin diffraction pattern represents the twinning of the rotation domain, and is the most commonly observed twinning in ZnO thin films.

inbetween the main streaks. The spacing between these secondary streaks is much smaller than expected for rotation domains, yet the film surfaces were too rough to have reconstruction. Furthermore, these double secondary streaks have identical features. In particular, the spot spacing within each of these secondary streaks is identical (as indicated by orange arrows in Figure 4.31a). It seems that these closely spaced streaks were split from a single RHEED streak.

RHEED streak splitting has been previously reported in MnTe [212], and is similar to the splitting of the diffraction spots observed in the TEM of $LaAlO_3$ [213]. Such splitting of the diffraction streak or spots can be attributed to crystal twinning. Twinning is a deformation of the crystal structure where the deformed domains have a lattice structure that is related to the main crystal lattice through a reflection operation or a 180º rotation [214]. Because of the symmetry between the twin crystal and the main crystal lattice, the domain boundaries between the two (the twin boundaries) are usually coherent, straight and parallel [215]. Twinning is strongly related to stacking faults and slips. In particular, slip and twinning are two competing mechanisms in the plastic deformation of a crystal under stress [214-216]. Figure 4.32 shows schematically the difference between slip and twinning. Since most slips are generated through dislocation creations and movements, twinning can be considered as an alternative strain relief mechanism to dislocation formation. Twinning is a common phenomenon amongst epitaxial thin films [217].

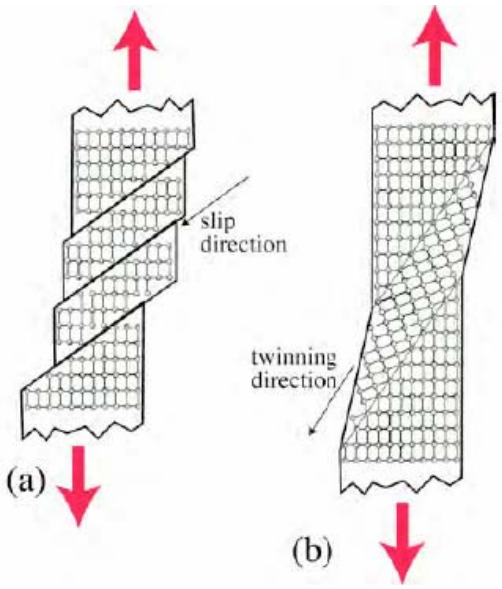

Figure 4.32 Schematic showing the behaviour of an ideal lattice under a) slip and b) twinning. Twinning results in a coherent domain boundary while slips generate less ideal dislocations (from Clyne [215]).

Apart from reports which mistakenly labelled 30º rotation domains as twin crystals (e.g. [174]), there are rarely any reports on the observation of twinning in ZnO thin films grown on sapphire (eg. [94]). That is because even though calculations have shown that the twin boundary formation energy, γ_T, of ZnO (40 mJ/m^2) is relatively low compared to other wurtzite semiconductors such as GaN (107 mJ/m^2) or AlN (109 mJ/m^2) [218], the compressive strain experienced by the ZnO lattice means that the critical thickness for twin formation t_{TF} is higher than the critical thickness for misfit dislocation t_{MD} [216]. In particular, Liu et al. have identified that under compressive strain, t_{TF} would only exceed t_{MD} when the specific twin boundary energy (STBE) is less than 0.0004 [216]. By analysing the experimental data, they also found that the STBE can be calculated empirically by $\gamma_T/10\mu a$, where μ is Young's modulus and a is the lattice constant. Therefore, by taking μ = 100 GPa [219], the STBE of ZnO can be calculated to be approximately 0.007, which is greater than 0.0004. From this, it can be seen that under compressive strain, misfit dislocations are expected to dominate over twin formation in a ZnO thin film. The low probability of twin formation compared to dislocations is evident from the fact that twinning is not commonly observed in this work. In particular, the occurrence of twinning was substantially less than the occurrence of rotation domain formation. Furthermore, from the typical intensity of the split streaks compared to the main

streaks as seen in Figure 4.31, it is evident that even when twin domains are present, the domain density is very small in most cases.

Interestingly, the split RHEED streaks observed from the ZnO thin films are predominantly the splitting of secondary streaks originated from rotation domains. This suggests that twin formations are more probable in rotation domains, which is consistent with the observations made by Kim et al. [94]. The higher probability of twin formation in rotation domains can be attributed to the fact that rotation domains are under tensile stress with respect to the substrate lattice, and therefore STBE = 0.007 (as calculated above) actually gives $t_{TF} < t_{MD}$, favouring twin formation over misfit dislocations [216]. Note that not all rotation domains in this work showed twinning. This is because twinning tends to occur on a larger scale (see Figure 4.32) and therefore requires more energy to form. Therefore, if the strain within the rotation domain is small, it may be more energetically viable to relieve the localised strain through dislocation formation even if $t_{TF} < t_{MD}$.

From the experimental observations and theoretical considerations, it was observed that twin formations, in most cases, are unfavourable in compressive epitaxial systems. Favourable conditions for twin formation include low substrate temperature where dislocation mobility becomes low; and extreme localised stress (generated by rapid temperature change) which causes sudden strain in the lattice. In these cases, twinning provides a much faster and therefore more efficient way to relieve the strain compared to dislocation nucleation [215]. However, as low substrate temperature reduces surface diffusion, and rapid temperature change has been associated with increased point defect density [165], both of these conditions are undesirable in terms of growth optimisation. Therefore, even though twinning may not significantly affect electrical properties [218], and hence may be less troublesome then dislocation formation, it is very difficult to reduce dislocation formation through increasing the occurrence of twin boundary formation in the epitaxial growth of ZnO on sapphire.

4.4.4 Surface Irregularities, Etch Pits and Nanopipes

As seen in previous sections, the surface of many ZnO films grown in this work is sparsely covered with irregular features that extend outward from the surface. While

these features do not seem to have a noticeable effect on the RHEED pattern, optical properties or electrical properties, there is evidence which suggests that these features affect the performance of Schottky diodes [220]. Figure 4.33 shows an extreme example where the density of these features is very high. From the irregularity of these features compared to the underlying surface morphology, it is quite obvious that these features were not caused by simple surface roughening from misfit strain. Most of these irregular features are partially faceted islands, even though the distribution, size and shape are often random in nature. In most cases, at least one side of these irregular islands is surrounded by voids. As the shape of these surface features resembles pyramids originated from inversion domains in GaN [221], it is possible that these features are associated with regions of polarity inversion within the ZnO thin films.

To confirm the relationship between these surface features and inversion domains, the surfaces of selected ZnO thin films were lightly etched using dilute HCl (~5 % concentration). It is expected that if the surface features are indeed inversion domain related, the irregular islands will be partially etched, revealing the inversion domains (in the form of an etch pit) at the centre of half etched pyramids due to the etch anisotropy of the two polarities [222]. Figure 4.34 shows the etching behaviour of one of the selected ZnO samples (grown with LT-ZnO buffer only under Zn-rich conditions) with irregular surface features. It can be seen that after the etching, the surface morphology became dominated by a grain like morphology, corresponding to the behaviour of an O-polar surface [208], with sparse, regular hexagonal etch pits.

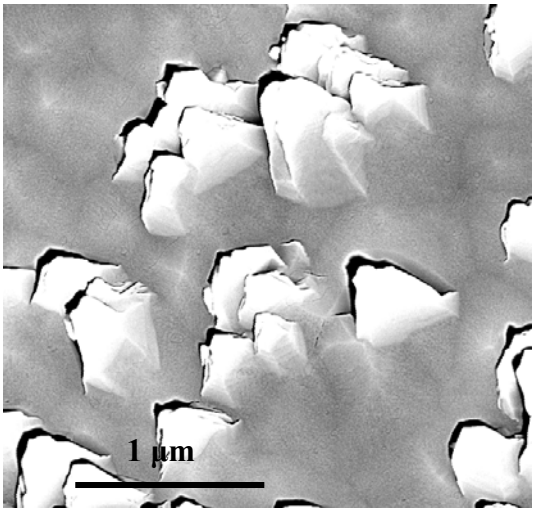

Figure 4.33 SEM image of the surface of a ZnO sample (grown with a LT-ZnO buffer layer) under non-optimal condition showing a high density of irregular features on the surface.

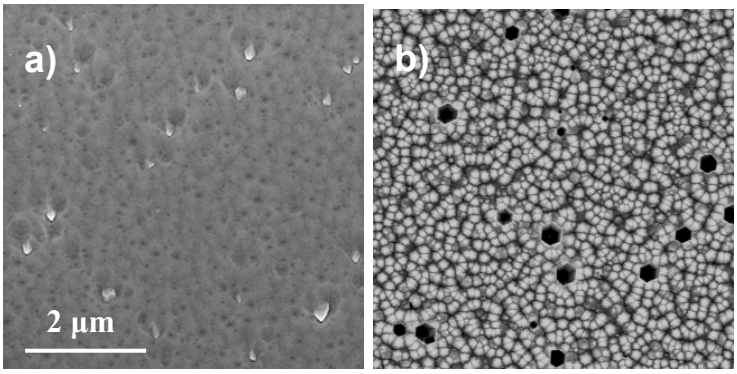

Figure 4.34 SEM of a ZnO sample grown with a LT-ZnO buffer layer a) before and b) after light etching. The grain morphology after etching suggest an O polar surface, while hexagonal pits identify dislocations (both images have the same scale).

Although the density and the distribution of the etch pits are similar to the features of interest for the sample shown in Figure 4.35, the size of the pits ranges from <50 nm to ~200 nm, while the surface features are predominantly ~200 nm. It is also clear that these etch pits are not positioned at the centre of any irregular features. More importantly, similar hexagonal etch pits were also observed on samples with no irregular surface features, and the density of etch pits in other samples far exceeded the density of surface domains, as shown in Figure 4.35. This strongly suggests that the regular hexagonal etch pits are not related to the irregular surface features. In fact, an SEM image of an etched surface feature (Figure 4.36) shows that the etch behaviour is uniform over the whole surface domain and is the same as the rest of the sample surface. This etching behaviour is different from the expected behaviour of inversion domains. From this, it can be seen that there is no evidence to suggest that these irregular features are inversion domains. While the nature of these surface

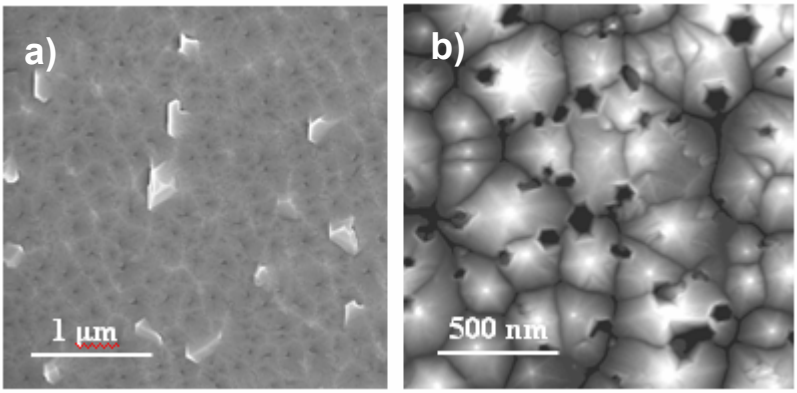

Figure 4.35 SEM image of another ZnO film (different from that shown Figure 4.35) which is also covered with irregular islands, showing the sample surface a) before and b) after etching. The difference in the density of the etch pits and the irregular surface features proves that the hexagonal pits are not associated with the surface irregularity.

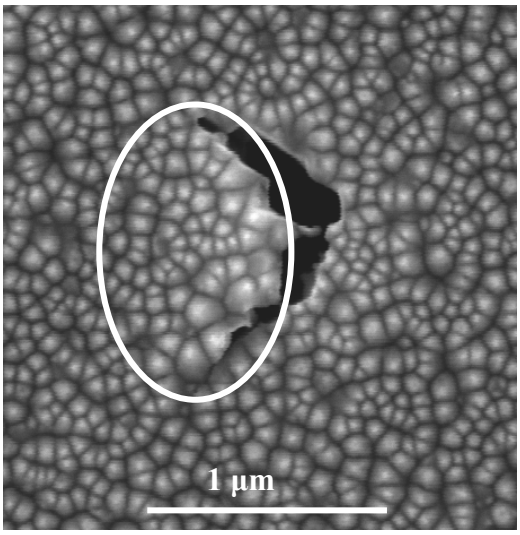

Figure 4.36 An irregular island after etching (circled), showing the same etch behaviour as the rest of the film. This suggests that these features have crystal structures similar to the bulk of the film. Note that the voids surrounding the feature were present as grown and were enlarged by the wet etching.

features cannot be confirmed, the experimental data have shown that the formation of these surface irregularities is strongly related to the growth condition. In particular, a high surface domain density was observed on pit morphologies under Zn-rich conditions with low applied RF power and relatively low oxygen flow. A possible origin of such features could be domains of different phase as observed in the previous sections, where the growth anisotropy of the different growth directions resulting in the extrusion of the domain from the surface.

Note that in Figure 4.28 it was observed that the etching of the irregular surfaces resulted in a distinctly non-uniform etched surface with large etch pits appearing on both samples. The difference in the etching behaviour of these features compared to those observed in Figure 4.34, Figure 4.35 and Figure 4.36 can be attributed to the fact that these features have a different origin. In particular, the irregular features observed on the surface of the sample in Figure 4.28a and Figure 4.28c are not faceted islands. For the sample with thinner MgO buffer (Figure 4.28a), the features clearly show a layered pyramidal shape, whereas the surface irregularity is in the form of ridges for the sample with thicker MgO buffer (Figure 4.28c). From these different observations between samples, it can be seen that surface irregularity on ZnO epilayer surfaces can be a complex problem, and the identification and elimination of these undesirable features might be difficult.

Even though the etching could not identify what the surface domains are, it revealed the presence of the hexagonal etch pits. Hexagonal etch pits have been

observed in GaN frequently, and have been associated with dislocations on the surface [223-225]. Reports with TEM and AFM have shown that hexagonal etch pits, also known as nanopipes, were formed from termination of screw and mixed type dislocations [223-225]. Therefore, using the density of the etch pits, one can estimate the dislocation density of a sample. As an example, the dislocation density of ZnO thin films grown with different RF power was studied using etch pits. Figure 4.37 shows the etched surface for a sample grown at 300 W and a sample grown at 500 W. In general, it was found that the etch pit density increases with increasing RF power, indicating an increase of dislocation density. In particular, from Figure 4.37, it can be seen that the dislocation density increased from 1×10^{9} cm^{-2} for a sample grown at 300 W to 4×10^{9} cm^{-2} for a sample grown at 500 W. Note that this dislocation density is approximately the same as, but slightly higher than, the dislocation density of sample M obtained from the TEM image in Figure 4.21, which is consistent with the narrower XRD rocking curves observed for sample M (see Figure 4.17) compared to the other samples. The agreement between TEM, XRD and the etch pit density shows that the etching of ZnO thin film surfaces is a valuable tool for structural evaluation when TEM or XRD cannot be used to characterise the thin films.

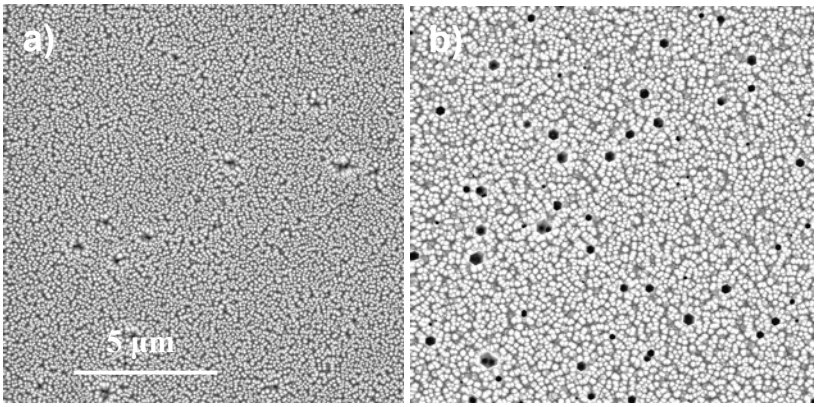

Figure 4.37 Etched surface of samples grown with the 25 hole aperture plate, using a) 300 W and b) 500 W. It is evident that the increase in power resulted in an increased etch pit density, which indicates an increase in dislocation density.

4.4.5 Other Domains

A common trait for the previously mentioned domain types is that even with various orientation differences, these domains still have the same crystal structure as

the bulk of the film, namely, a wurtzite crystal structure. This is very much expected since the wurtzite structure is the preferred crystal arrangement for ZnO. However, if there is very strong localised strain present in certain regions in the lattice, it may be more energetically favourable for these regions or even the entire film to rearrange into a different crystal structure.

As an example, the behaviour of ZnO thin films grown under a rough interface was studied. In particular, ZnO thin films were grown on a rough MBE grown GaN template. As GaN has almost the same lattice constant as ZnO, any strain experienced by the ZnO epilayer would most likely be due to localised strain originated from the rough interface. Figure 4.38 shows the surface of one such sample. It can be seen that rather than a continuous epilayer, the resulting film is highly porous with nearly 50% void volume. This self assembly of a nanoporous network was non-catalytic as no external catalyst was introduced in the growth process. Therefore, it is clear that localised strain originated from the rough interface led to the void formations. Figure 4.39 shows the HRTEM image of the porous ZnO at the bottom of one of the pores. It can be seen that the atom arrangement is abnormal in the entire region. While the sidewalls of the void are in regular hexagonal structures, these well behaved regions are separated by a number of domains with unclear crystal structures. These domains are separated from each other by dislocations, similar to the white boundaries shown in the figure. It can be seen that these irregular domains span the entire base of the void, strongly implying that the formation of the void is due to the incompatibility between the hexagonal sidewalls and the irregular non-hexagonal inclusions.

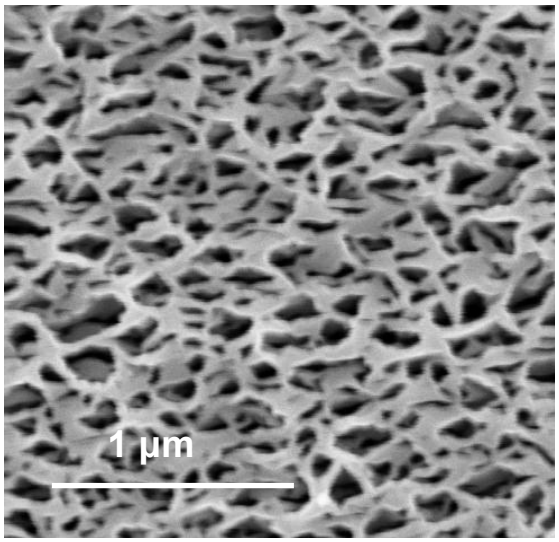

Figure 4.38 SEM image of a self-assembled nanoporous ZnO thin film grown on a MBE GaN template, showing a layered pore structure.

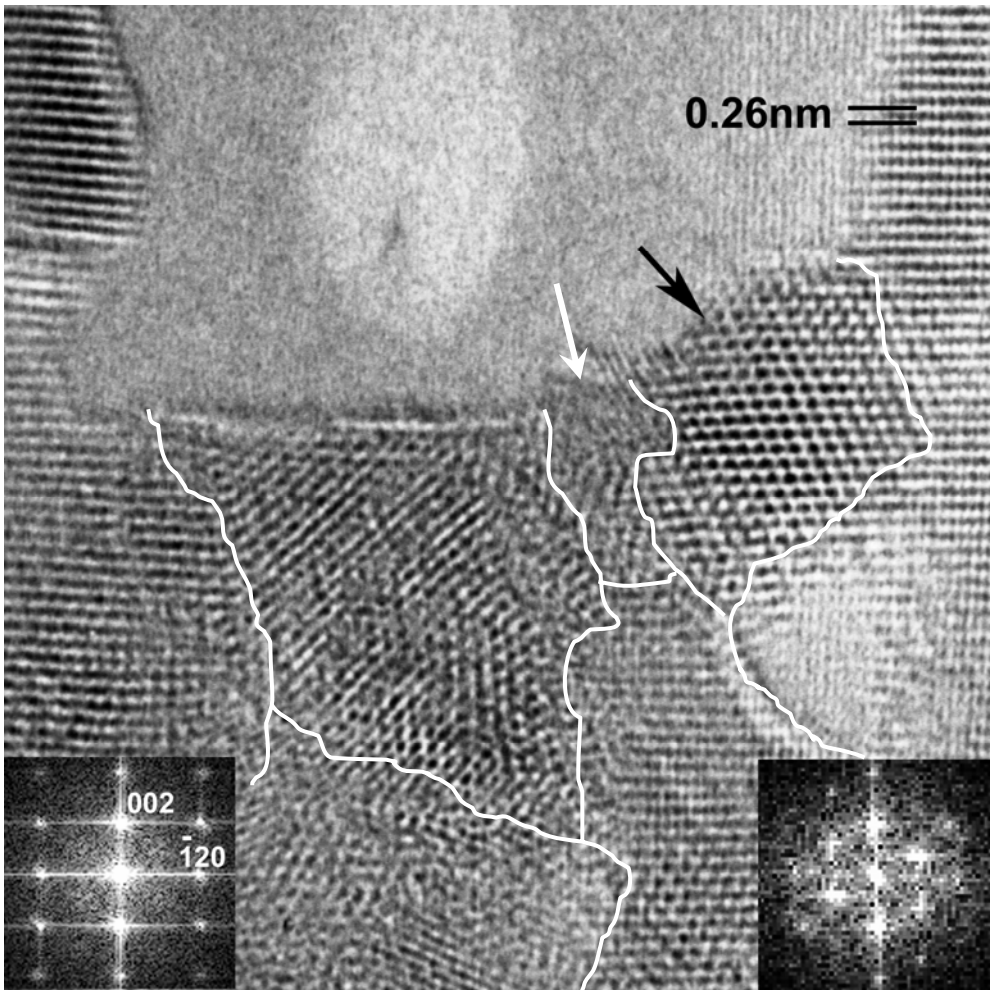

Figure 4.39 HRTEM of a pore of the porous ZnO thin film grown on a MBE GaN template. The chaotic crystalline structures at the bottom of the pore suggest that the formation of this void is possible through the incompatibility of these various crystal structures. In particular, nano-cubic inclusion is detected through nano TEM diffraction. The black arrow shows the nano-cubic inclusion, whereas the white arrow shows an amorphous region. The white lines represent domain boundaries.

Further analysis showed that some of these domains, as indicated by the black arrow, are cubic inclusions - i.e. nanodomains of cubic ZnO. This is supported by the localised diffraction image as shown in Figure 4.39 (left inset). Since cubic ZnO is only viable under extreme conditions, and the growth temperature is much lower than the temperature criteria for cubic formations [32], it is most likely that the cubic nano-inclusions were formed under the extreme localised stress originated from the rough interface strain, and this cubic formation leads to a partial release of the strain energy in the lattice. It is evident from Figure 4.39 that in some cases, the localised strain was so intense that the local lattice was distorted into an amorphous state (white arrow).

It can be seen that these crystal disorders destroy epitaxy and are therefore undesirable just like other domain structures. Fortunately, the occurrence of these irregular domains is not very frequent. Even when a large lattice mismatch is present, domains with crystal structures other than hexagonal are rarely observed. In fact, there are virtually no reports of direct observation of cubic phase inclusions in hexagonally grown ZnO thin films. Therefore, during a typical ZnO growth, the elimination of alien structured domains would not be an important factor to consider. However, as the observation of cubic inclusions has shown here, the lattice mismatch is not the only factor that affects the strain in epitaxial growth. It is therefore very important to have a smooth interface to ensure the growth process takes place without extreme localised strain.

4.4.6 Thermal Rearrangement

As mentioned previously, many ZnO thin films grown on sapphire are considerably strained. As the sample is cooled down after growth, further strain might be introduced from the thermal mismatch between the substrate and the film. Normally after the growth and cooling process the film would not have a chance to further relax. However if enough thermal energy is provided, for example through external annealing, the surface or even bulk atoms may be able to diffuse and further roughen to relieve the residual strain. Such after-growth strain relaxation has been observed in the ex-situ annealing of MBE grown ZnO samples. In one experiment, a sample (300 nm thick) was annealed at various temperatures to investigate the surface and bulk diffusion behaviour.

Figure 4.40 shows the variation of morphology with annealing temperature for a film grown at 550 ºC directly on sapphire without a buffer layer, annealed under an oxygen atmosphere for 1 hr. It can be seen that below 750 ºC, the surface of the sample remains unchanged. For annealing temperatures of 750 ºC and above, islands were observed on the surface (Figure 4.40b). Since no reactants were provided during the annealing process, the formation of these islands originated from the rearrangement of the surface of the film. Above 850 °C, island size increased, while island density decreased with increasing annealing temperature (Figure 4.40e).

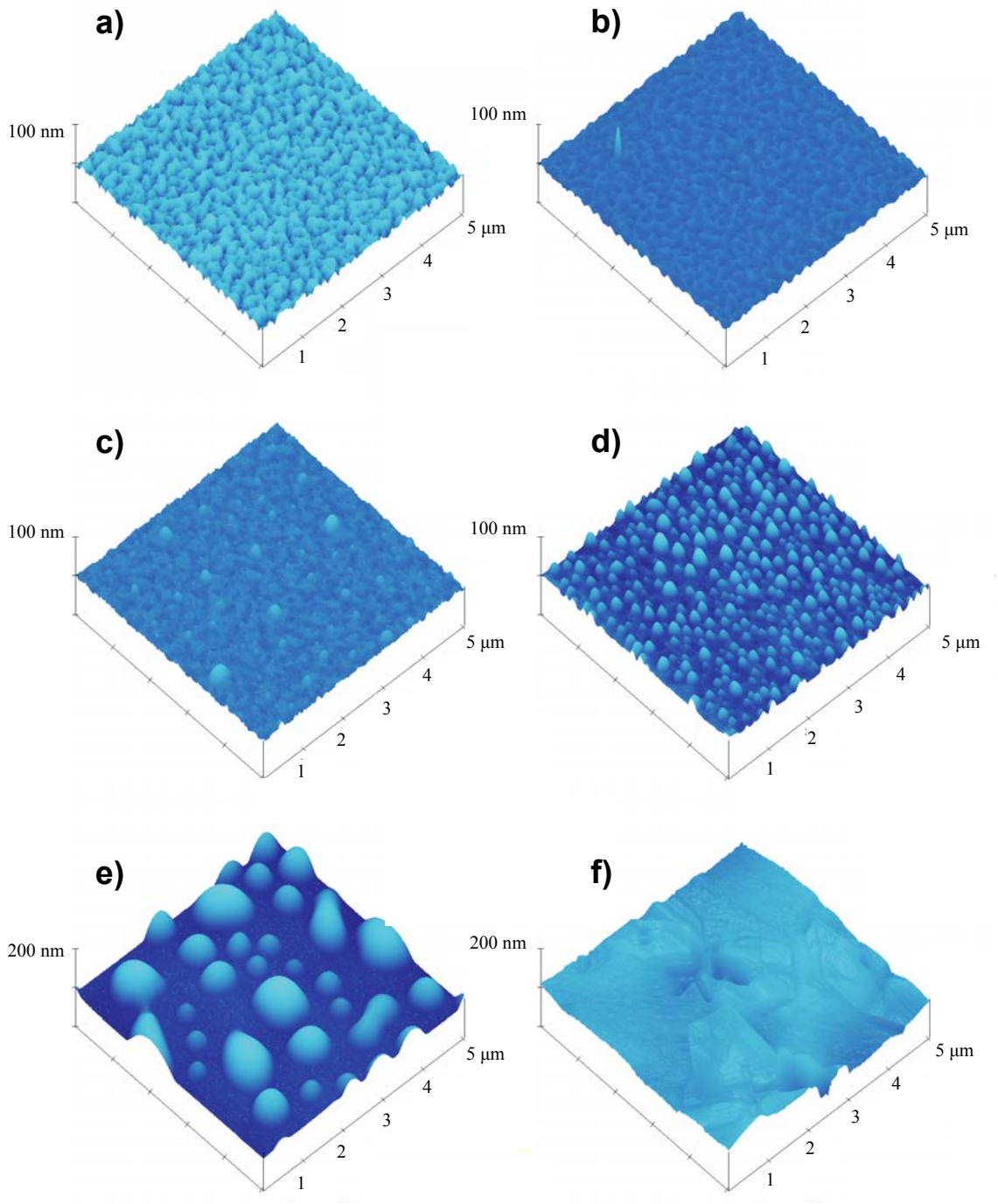

Figure 4.40 3-D AFM images of a ZnO sample grown directly on sapphire a) as grown; b) 750 ºC; c) 850 ºC; d) 950 ºC; e) 1050 ºC; f) 1100 ºC

This coarsening of the islands can be sustained until 1100 ºC, at which point the deformation was so great that the film was no longer continuous and isloated plateaus were formed (Figure 4.40f). As 1100 ºC is below the melting point of ZnO [32], this deformation is suspected to be due to extensive surface and bulk diffusion driven by the relaxation of either the thermal stress or the remaining misfit strain in the film.

The intrinsic biaxial stress σ_0 caused by the lattice mismatch between ZnO and sapphire is given by:

$$\sigma_0 = \varepsilon M \tag{4.8}$$

where M is the biaxial elastic modulus of the ZnO thin film and ε is the strain caused by the lattice mismatch, which is equal to the lattice mismatch between ZnO and sapphire. Taking values for Young's modulus and Poisson ratio of ZnO as 100 GPa and 0.36, respectively [219], the stress can be calculated as:

$$\sigma_0 = 0.17 \times \frac{100 \times 10^9}{1 - 0.36} = 26 \text{ GPa} \tag{4.9}$$

This large compressive stress would be present in a maximally strained, dislocation free film. It is expected that the actual strain would be lower, as all ZnO films would be at least slightly relaxed by the formation of dislocations and surface roughening during growth. During annealing, thermal stress is present due to the difference in the expansion coefficient of the ZnO thin film and the sapphire substrate. The thermal stress due to the thermal mismatch during annealing is given by [226]:

$$\sigma_{TH} = \Delta\alpha \ \Delta T \ M \tag{4.10}$$

where $\Delta\alpha$ is the difference in thermal expansion coefficient between ZnO and sapphire, and ΔT is the change in temperature. Using $\alpha_{ZnO} = 2.9 \times 10^{-6}$ /K and $\alpha_{sapphire} = 7.2 \times 10^{-6}$ /K [227], it can be calculated that the thermal stress exerted on the ZnO thin film during annealing is $1.14 \times 10^5 \ \Delta T$. Therefore for an annealing temperature of 850ºC and an initial temperature of 25ºC, the thermal stress is 94 MPa. Thus, the thermal stress due to annealing at 850ºC is two orders of magnitude smaller than the

intrinsic stress in the thin film. Therefore, it is unlikely that the observed surface roughening and island formation were due to thermal stress. A more plausible explanation is that the surface roughening is the product of the intrinsic residual strain and the increased surface atom diffusion due to the elevated temperature [228]. This is supported by the fact that the island formation through annealing was not observed for films grown with a buffer layer, which has much lower intrinsic stress in the crystal lattice but would be experiencing the same thermal stress under the same annealing condition.

In addition, the increased temperature triggered the process of island ripening. Figure 4.41 shows the mean island size and island density as a function of annealing temperature. It can be seen that the island size increased exponentially and the island density decreased exponentially as the annealing temperature was increased. This is a typical characteristic of Ostwald ripening [229], where large islands grow at the expense of small islands. One can therefore attribute the observed surface evolution to the Ostwald ripening of strain related surface roughening, which activates at a threshold temperature of around 850 °C.

According to Zinke-Allmang et al., the temperature dependence of island growth can be expressed as [229]:

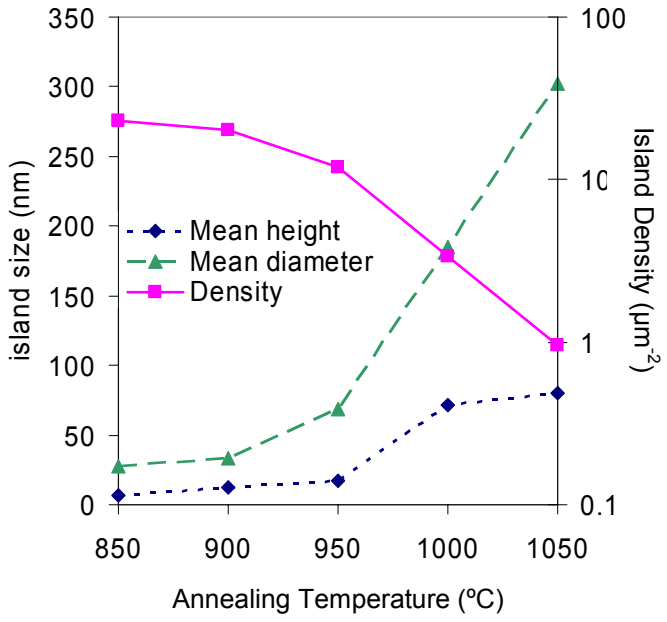

Figure 4.41 The evolution of island density and size with increasing annealing temperature. The non-linear decrease in density and increase in size is a signature of Ostwald ripening.

$$K = \frac{K_0}{T} e^{\frac{-E}{kT}} \tag{4.11}$$

where $K = dr^3/dt$ is the rate of change of critical island radius for a surface diffusion process. Linearisation gives:

$$\ln KT = \ln K_0 - E/kT \tag{4.12}$$

Therefore, by plotting ln KT against $1/T$, one should be able to find the activation energy of this diffusion process. Assuming circular islands and that K is constant for each temperature, one can approximate KT by [229]:

$$KT = R^3 T/t = T(\sqrt{A/\pi})^3/t \tag{4.13}$$

where A, t and T are the island area, annealing time (1 hour) and annealing temperature respectively. Using Equations 4.12 and 4.13, a linear fit through the experimentally derived values (Figure 4.42) yielded a surface diffusion activation

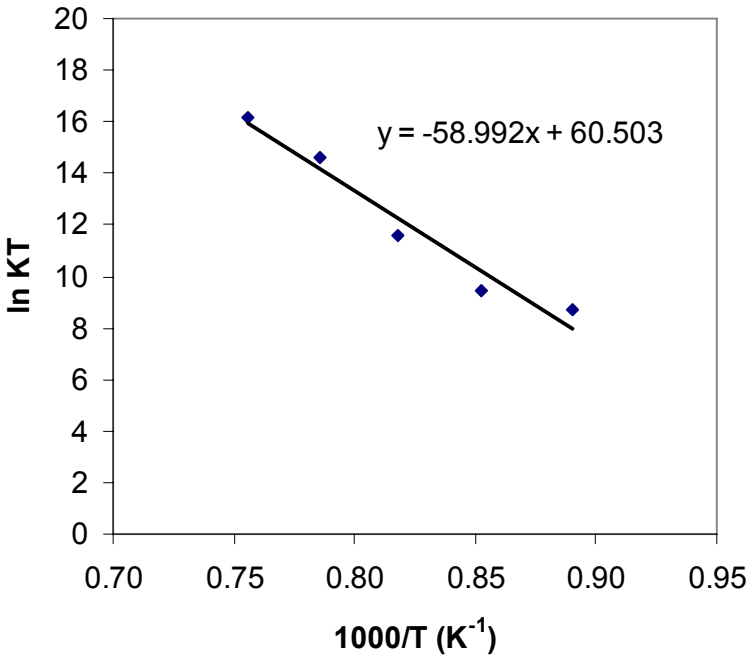

Figure 4.42 Arrhenius plot showing the temperature dependence of island growth under Ostwald ripening according to Equation 4.12. From the slope *m* of the linear fit, the activation energy can be calculated to be 1000*m*k = 5.08 eV.

energy of 5 eV. This high activation energy suggests that ZnO thin films are thermally very stable compared other materials such as Si (1.4 eV) [230]. Note that this is the barrier for the diffusion of Zn and O atoms that are already incorporated. This energy therefore implies that once incorporated onto the surface, the diffusion of sub-surface atoms or bound surface atoms is limited. It is expected that during growth the diffusion barrier for surface adatoms would be much smaller than 5 eV.

4.4.7 Importance of Buffer Growth Conditions

The past few sections have outlined a number of strain relief mechanisms for misfit, thermal and interfacial strain other than the predominant dislocation nucleation and surface roughening. While the occurrences of these different phenomena are not as dominant compared to dislocation formation or surface roughening, they provide extra information on the structural behaviour of ZnO. One important thing to note from this section is the importance of an optimised buffer layer. Even with a proper substrate and proper buffer material, the resulting ZnO thin film may not have the desirable qualities if the combination of growth condition and localised strain lead to the formation of undesirable domains and other defects. A good example is shown in Figure 4.43 which shows the TEM of a sample grown on a non-optimised MgO buffer. As can be seen from the HRTEM, because of the 3-D interface, the large misfit strain has resulted in the dominance of domain formation over dislocations. The film therefore has extensive defects, inversion domains, as well as other domain features that can only be identified with more detailed TEM studies. This highlights the importance of the optimisation of the buffer layer growth process in the fabrication of high quality ZnO thin films.

Throughout this chapter, the structural characteristics of PAMBE grown ZnO thin films were discussed, with arguments presented regarding strain as the main source of the structural variety observed. The dislocations, defects and rotation domains etc. all have fundamental effects on the structural, electrical and optical properties of the epilayers. The employment of buffer systems, both homoepitaxial ZnO buffer and heteroepitaxial MgO buffer have been shown to improve the ZnO growth by improving the wetting, preventing dislocation propagation and relieving

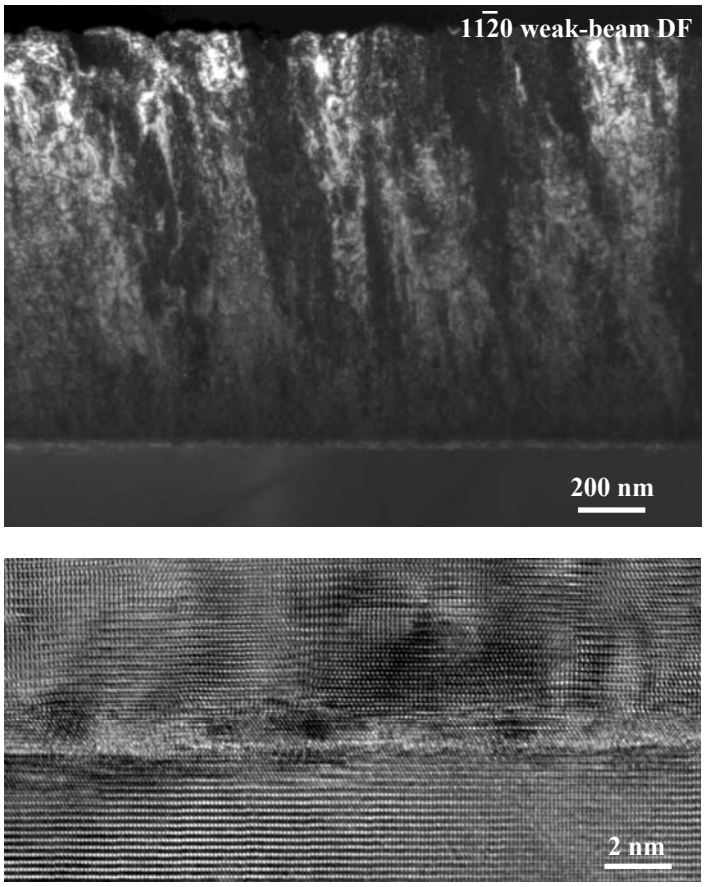

Figure 4.43 DF TEM and HRTEM of sample grown with an unoptimised MgO buffer layer showing high density defects, a rough surface and a 3-D interface, highlighting the importance of growth conditions on strain relaxation.

the lattice mismatch strain. However, it was observed that both buffer layer systems have disadvantages. In particular, while the employment of a MgO buffer resulted in ZnO thin films with low defect density, strong excitonic emission and low carrier concentration, it was observed that the quality of the ZnO epilayers is strongly dependent on the MgO buffer thickness and integrity, which are very hard to control due to the small thickness of the layer. In fact, even with the recent installation of an oxygen resistant RHEED system allowing real-time monitoring of the MgO buffer layer growth, it was found that growing perfect 2-D MgO buffer layers is still difficult. Therefore, ultimately a MgO buffer may not be able to fully replace LT-ZnO homoepitaxial buffer systems. In that case, efforts must be put into solving the problem of parallel conduction due to degenerate interface layers that result in the inaccurate characterisation of ZnO/LT-ZnO thin films.

In the next two chapters, an in-depth exploration of two quantitative measurement techniques, variable magnetic field Hall effect and time-resolved photoluminescence, are presented as a means of understanding the behaviour of

carriers in a multilayered system such as ZnO/LT-ZnO, to allow a more accurate characterisation of ZnO epilayers.

Chapter 5

SEPARATING CARRIERS IN MULTILAYER ZNO STRUCTURES

5.1 Carrier Densities and Carrier Transport

Carrier concentration and carrier mobility are the two key figures of merit in terms of electrical characteristics of a semiconductor. Measuring them, however, can be problematic in an inhomogeneous sample, such as a multilayered structure. In this chapter, the limitations of conventional measurements on determining these two values in an inhomogeneous epilayer are described, and the application of an alternative measurement technique in determining the true electrical properties of ZnO thin films grown with a degenerate interface layer is evaluated.

The carrier concentration or the carrier density is the number of free carriers available in the material. Due to the quantum nature of electrons, "free" electrons in reality occupy discrete states in the conduction band. Similarly, holes (empty states) occupy discrete states in the valence band. At thermal equilibrium, i.e. without external fields, the carrier density is related to the density of states ($g_c(E)$ for electrons in the conduction band and $g_v(E)$ for holes in the valence band) and the probability of the states being occupied. Note that because ZnO is normally n-type, only electrons (majority carriers) will be considered here. The electron density of a semiconductor at equilibrium, i.e. the intrinsic electron concentration, is given by [231]:

$$n_0 = \int_{E_c}^{\infty} g_c(E) f(E) dE = \int_{E_c}^{\infty} \frac{8\pi\sqrt{2}}{h^3} m_e^{*3/2} \sqrt{E - E_c} \frac{1}{1 + e^{(E-E_F)/kT}} dE \quad (5.1)$$

where E_F is the Fermi level and E_c is the conduction band minimum.

This integral can be simplified if the semiconductor is non-degenerate, i.e. when E_F is at least 3kT below the conduction band minimum, at which point $(1 + e^{(E-E_F)/kT}) > 1$ and therefore the Fermi-Dirac function $f(E) = 1 / (1 + e^{(E-E_F)/kT})$

can be approximated by a simple exponential function, enabling the equation to be solved analytically:

$$n_0 = N_c e^{(E_F - E_c)/kT} = 2\left[\frac{2\pi m_e^* kT}{h^2}\right]^{3/2} e^{(E_F - E_c)/kT} \qquad (5.2)$$

where N_c is the effective density of states in the conduction band. The measured carrier concentration compared with the intrinsic carrier concentration gives an indication of the amount of extrinsic carriers present in the semiconductor sample. For ZnO, it is expected that the intrinsic carrier concentration would be very low as the wide bandgap makes the thermalisation of valence electrons difficult. In fact, by using an effective electron mass of $0.24m_e$ [232] and a room temperature bandgap of 3.37 eV, the intrinsic carrier concentration for ZnO at 300 K can be calculated to be $\sim 1 \times 10^{-8}$ cm^{-3}. This extremely low value suggests that pure ZnO should be insulating. The nominally n-type doping commonly observed is then caused by impurities and structural defects such as dislocations and point defects. Some of these impurities and defects cause localised disruption of the band structure, creating mid-gap states close to the conduction band, i.e. shallow donors. The thermal activation needed to ionise these donors results in the temperature dependence of the extrinsic carrier concentration.

The accuracy of Equation 5.2 breaks down when the electron density is so high that E_C - E_F < 3kT. In that case the carrier density cannot be adequately approximated by an exponential function. For ZnO, this point of degeneracy is $\sim 1 \times 10^{17}$ cm^{-3} at 300 K. Note that this particular definition of degeneracy is somewhat arbitrary and does not have physical significance. The term degeneracy or degenerate carrier is often reserved in the literature for situations when the Fermi level is above the conduction band. Under such circumstances no thermal activation is necessary for the creation of free electrons, and the material behaves like a metal with carrier density independent of temperature. Degenerate conduction starts to occur when $E_F = E_C$, which for ZnO corresponds to a carrier concentration of $\sim 3 \times 10^{18}$ cm^{-3} at 300 K.

While a description of a material in thermal equilibrium using carrier concentration gives the basic electrical behaviour of the material, the carrier dynamics in the material determine its usefulness for electronic devices, as all devices involve

energy transfer via movement of carriers. The carrier transport is governed by the Boltzmann transport equation (BTE) [233]:

$$\frac{\partial f}{\partial t} + v \cdot \nabla_r f + \mathbf{F} \cdot \nabla_p f = \left.\frac{\partial f}{\partial t}\right|_{collision} + s(\mathbf{r}, \mathbf{p}, t) \qquad (5.3)$$

where f is the Fermi-Dirac function for a carrier located at position r with a momentum p at time t, v is the carrier velocity, F is the force applied that caused the carrier movement and s is a carrier source. By using the relaxation time approximation where the collision time of individual carriers is approximated by a relaxation time τ, and recognising that carriers can be moved by both an electric field and a magnetic field, the BTE becomes:

$$\frac{\partial f}{\partial t} + v \cdot \nabla_r f + (-qE + -qv \times B) \cdot \nabla_p f = \frac{f_A}{\tau} + s(\mathbf{r}, \mathbf{p}, t) \qquad (5.4)$$

At steady state, $\partial f / \partial t = 0$, and assuming there are no constant carrier sources, the BTE can be simplified as

$$v \cdot \nabla_r f + (-qE + -qv \times B) \cdot \nabla_p f = \frac{f_A}{\tau} \qquad (5.5)$$

This is the general form of the steady state relaxation time approximated BTE. It can be used to predict carrier transport behaviour under different circumstances. In particular, under no magnetic influence, i.e. $B = 0$, the equation can be solved analytically to give the carrier velocity under a uniform, low electric field:

$$v = \frac{-q\tau E}{m^*} \qquad (5.6)$$

The electron current J, defined as $J = -qnv$, is then given by:

$$J = -qn \cdot \frac{-q\tau}{m^*} E = nq\mu_n E \qquad (5.7)$$

where $\mu_n = -q\tau/m^*$ is the electron mobility. The mobility is therefore a measure of the relaxation time of the carriers which in turn is a measure of the carrier scattering in the material. Note that from the mobility, the conductivity can be calculated by $\sigma = nq\mu_n$. This gives the well known current equation,

$$J = \sigma E \tag{5.8}$$

Since the carrier scattering is affected by temperature, it is expected that the mobility also varies with temperature. In particular, for thin films with dislocations, the mobility is governed by five scattering mechanisms: ionised impurity scattering, deformation phonon scattering, piezoelectric (acoustic phonon) scattering, polar optical phonon scattering and dislocation scattering [234]. Each of these scattering mechanisms results in a mobility component, and the overall electron mobility is given by the Matthiessen's rule [234]:

$$\frac{1}{\mu} = \frac{1}{\mu_{impurity}} + \frac{1}{\mu_{deform}} + \frac{1}{\mu_{piezo}} + \frac{1}{\mu_{polar}} + \frac{1}{\mu_{dis}} \tag{5.9}$$

The dominance of each of these terms is dependent on the material's intrinsic properties, the quality of the material of interest, and temperature. In particular, impurity concentrations, deformation potentials and dislocation densities are sample dependent. Therefore, the mobilities calculated from Equation 5.9 for ZnO materials can vary greatly depending on the sample parameters used. For example, by assuming a relatively high impurity concentration and dislocation density Jung et al. calculated a maximum mobility of ~105 cm^2/Vs at 300 K for ZnO grown by MBE, which adequately modelled the experimental mobility reported [234]. Makino et al. modelled the abnormally high mobility they observed for ZnO thin films grown on SCAM, by using the polaron effective mass instead of the electron effective mass and a very low impurity concentration. They calculated a room temperature mobility of 430 cm^2/Vs [235], twice the value reported by Look et al. for bulk ZnO material [87]. In general, it was found that the mobility in ZnO is mainly limited by impurity or dislocation scattering at low temperature and optical phonon scattering at high temperatures [234, 235].

5.2 Limitations of Conventional Hall Effect

The measurement of carrier transport has been established for decades. Conventionally, the carrier density and the carrier mobility are measured by using the Hall effect [236]. The Hall effect is the induction of an electric field when a current through a conducting sample is subjected to a magnetic field perpendicular to the current flow, with the resulting electric field normal to both the applied magnetic field and the current direction. The Hall effect is the direct result of the Lorentz force experienced by an electron as it moves through a magnetic field. Consider a sample with current flowing as in Figure 5.1. When a magnetic field B is applied normal to the current, the electric field generated is given by solving the BTE [233]:

$$E = J\mu B\rho \tag{5.10}$$

which can be rewritten as:

$$\frac{E}{JB} = -\rho\mu_H = R_H \tag{5.11}$$

where R_H is known as the Hall coefficient. From Equation 5.11, it can be seen that by

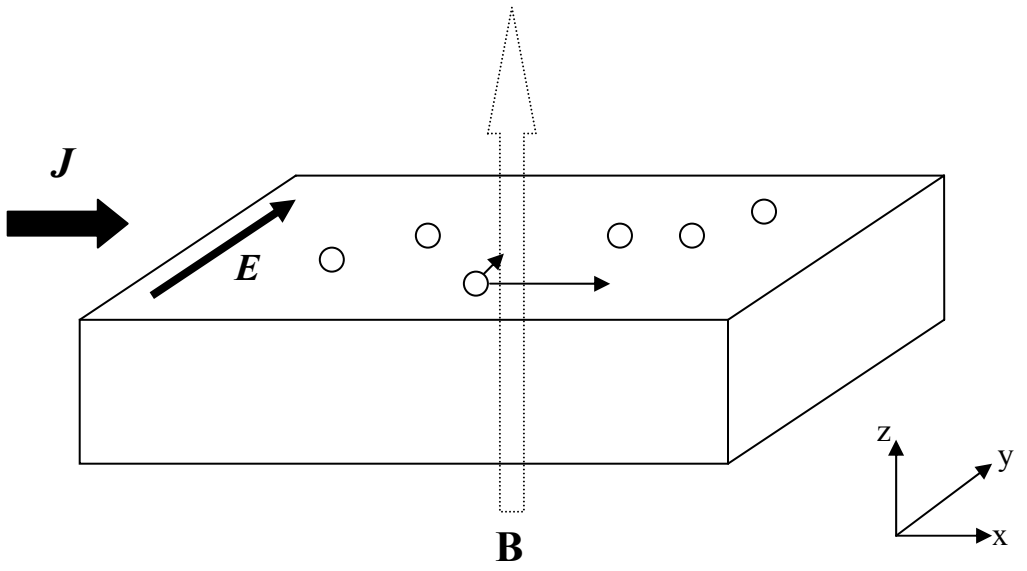

Figure 5.1 Schematic showing the Hall effect phenomenon. By applying a magnetic field B, the electrons from the current J are deflected, creating an induced electric field E.

measuring the Hall coefficient and the resistivity, the carrier mobility can be estimated. The carrier density can also be estimated from the Hall coefficient via the relationship:

$$R_H = \frac{r_H}{-nq} \tag{5.12}$$

where r_H is the Hall factor which is dependent on the dominant scattering mechanism in the material and has a value between 1 and 2. Therefore, conventional Hall effect measurements are based on measuring the Hall coefficient of the sample. In particular, the electric field generated causes the electrons to preferably move to one side of the sample, creating a voltage difference. Hence the Hall coefficient can be readily evaluated by measuring the voltage generated when a known magnetic field is applied to a sample with a known current passing through.

As mentioned in Chapter 1, samples were measured using the van der Pauw geometry. With this geometry, contacts are placed at the four corners of a nominally square sample. A current I is then forced through each pair of the contacts while the voltage difference between the remaining two contacts is measured. In particular, referring to Figure 5.2, the voltage differences V_{12}, V_{13}, V_{24} and V_{34} under no magnetic field influence are used to calculate the resistivity ρ, whereas the difference between the voltages measured with and without magnetic field for V_{14} and V_{32} gives the Hall voltage V_H. The carrier density and mobility can then be calculated from the Hall voltage by:

$$n_s = \frac{r_H}{q} B_z V_H I \qquad \text{and} \qquad \mu_H = \frac{V_H}{I R_s B_Z} \tag{5.13}$$

where R_s = ρ/t is the sheet resistance of the layer.

As mentioned in previous chapters, most of the ZnO films grown in this work have an apparant carrier concentration of $\sim 1\times10^{18}$ cm^{-3} to 1×10^{19} cm^{-3}, which means almost all samples are degenerate as measured by the conventional Hall effect measurements. This is inconsistent with the generally high crystal quality observed for most samples. In addition, as mentioned in Chapter 4, the employment of a

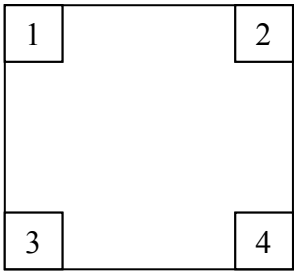

Figure 5.2 Schematic of the van der Pauw geometry. Opposite contacts are used for the measurement of Hall voltages, while adjacent contacts are used for resistivity voltages.

LT-buffer layer was observed to improve the structural and optical properties of ZnO films, yet a higher carrier concentration and lower mobility compared to films without a LT-buffer layer were measured. Such anomalies can be attributed to the existence of a degenerate layer at the interface, which alters the measurable carrier concentration and mobility [176, 237].

The observation of erroneous measurements due to degenerate layers is not new. In fact, it has been reported in other semiconductors such as GaN and InN. For example, a degenerate interface layer was previously observed in MBE and MOCVD grown GaN thin films, with its origin identified as the LT wetting layer [237]. For InN thin films, a degenerate surface layer created by surface electron accumulation has been shown to affect the mobility measurements [238]. Degenerate interface layers in MBE grown ZnO have also been observed by Tampo et al. [176]. The existence of a degenerate layer in MBE grown ZnO on sapphire can be attributed to the poor quality interface due to the large mismatch between ZnO and sapphire. Although a LT-ZnO buffer layer improves the quality of the interface (as described in Section 4.2), the low substrate temperature used for the buffer layer growth still results in a poor quality intermediate layer. Therefore, most ZnO films grown in this study suffer from this degenerate measurement problem (except for thin films grown with a MgO buffer layer, as described in Section 4.3).

The failure of conventional Hall effect measurements originates from the inherent assumption that there is only one majority carrier homogeneously distributed in the material, which allows averaging techniques to be used. Such single carrier models fit traditional semiconductors (such as Si and Ge) very well when the samples are uniformly doped. However, the assumption of homogeneity fails when multiple carriers exist within a material system, for example, in a multiple layered structure

such as a multilayer quantum well or a LT-buffer/HT-epilayer system. Consider a two layered system such as that shown in Figure 5.3. When a current is forced through the sample using the van der Pauw configuration, the current component in each layer is dependent on the resistivity of the layer. The voltage measured is therefore the weighted average of the two layers. In fact, the two layers can be treated as resistors in parallel, and the overall resistance measured is given by $1/R = 1/R_1 + 1/R_2$. Since a degenerate layer is likely to have a high conductivity, its presence will dominate the measured resistance. Hence, the mobility and carrier density obtained will not truly represent the *bulk* layer of such sample.

One way to separate the carriers in the different layers is by multilayer analysis [237]. In this technique, the apparent carrier density and mobility are evaluated normally using Hall effect measurements, and these apparent values are corrected with a layered model. In particular, for a two layer model consisting of a top bulk layer and an interface layer, the apparent carrier concentration and mobility can be shown to obey [237]:

$$\mu_H = \frac{\mu_1^2 n_1 + \mu_2^2 n_{S2}/d}{\mu_1 n_1 + \mu_2 n_{S2}/d} \tag{5.14}$$

and

$$n_H = \frac{(\mu_1 n_1 + \mu_2 n_{S2}/d)^2}{\mu_1^2 n_1 + \mu_2^2 n_{S2}/d} \tag{5.15}$$

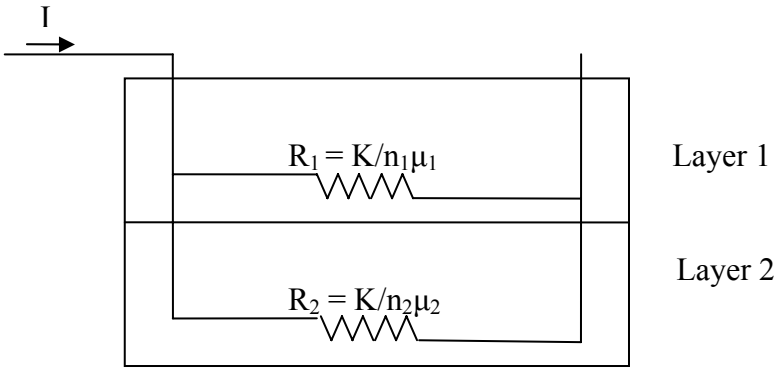

Figure 5.3 The equivalent circuit of a two layered system when a current is applied. The current sees a resistance equal to the equivalent resistance of R_1 and R_2 in parallel. If one of the resistances is very small, e.g. as in degenerate layers, then the overall resistance would be dominated by that layer.

where layer 1 is the bulk layer and the layer 2 is the interface layer, n_{s2} is the sheet concentration of the interface layer, and *d* is the measured thickness of the whole sample, which includes both the bulk and the interface layer. It follows from Equation 5.14 and Equation 5.15 that if the parameters of one of the layers are known then the parameters for the other layer can be calculated from the apparent Hall measurement.

The carrier density of a degenerate semiconductor is essentially independent of temperature, whereas carriers freeze out in a non-degenerate semiconductor at low temperature. Therefore, at low temperatures, the layered sample becomes a single carrier system where the carrier density and mobility from the Hall measurement represents the parameters for the degenerate layer. Using these low temperature measurements, and assuming the parameters of the degenerate carrier is constant with temperature, the higher temperature measurements can then be corrected using Equation 5.14 and Equation 5.15 to evaluate the bulk carrier density and mobility value. Such an analysis has been used in GaAs [239], GaN [237] and ZnO [60] to separate the bulk carrier component from the degenerate layer either from the interface or surface accumulation.

This multilayer analysis relies on one assumption: that the degenerate carrier properties are independent of temperature. However, there is evidence that this is not always the case. For example, Swartz et al. observed that the mobility of degenerate layers in HVPE GaN exhibit clear temperature dependence, with the actual mobility at 10 K higher than the mobility obtained from the multilayer model [240]. In addition, the multilayer model only applies if one of the carriers is degenerate. Therefore, if more than one type of non-degenerate carrier is present, for example in a layered device, then the mobility of each layer cannot be separated using the multilayer technique. Therefore, for more accurate measurements of materials or devices with more than one carrier, an alternative technique is needed. One possibility is to use mixed conduction analysis.

5.3 Mixed Conduction and Variable Field Hall Effect

Mixed conduction analysis (also known as multiple carrier analysis) makes use of the fact that the Hall effect induced conductivity has multiple components.

Referring to Figure 5.1, it can be seen that under the influence of the magnetic field and electric fields, the electron movement has multiple components. In particular, under the influence of the "main" electric field E_x (which generates the current ***J***), electrons predominantly move in the x-direction, but also move in the y-direction due to deflection from the magnetic field. Similarly, electrons under the influence of the induced electric field E_y move predominantly in the y-direction, but also have an x-direction component due to the deflection from **B**. One can therefore define conductivity components σ_{xx}, σ_{yy}, σ_{xy}, σ_{yx}, with $1/\sigma_{ij} = \rho_{ij}$ being the resistivity seen by the carriers when travelling in the *i* direction under the influence of the electric field in the *j* direction. Then, one can write a matrix equation:

$$\begin{bmatrix} J_x \\ J_y \end{bmatrix} = \begin{bmatrix} \sigma_{xx} & \sigma_{xy} \\ \sigma_{yx} & \sigma_{yy} \end{bmatrix} \begin{bmatrix} E_x \\ E_y \end{bmatrix} \tag{5.16}$$

that models the current density in the material under the influence of a magnetic field B_z. Note that σ_{xx} and σ_{yy} are the conductivities directly generated from the electric fields, whereas σ_{xy} and σ_{yx} can be regarded as conductivity components generated from the deflection of carriers from the applied magnetic field. Assuming that the material is isotropic and homogeneous, $\sigma_{xx} = \sigma_{yy}$, and $\sigma_{xy} = -\sigma_{yx}$. Therefore, the Hall coefficient and the sample resistivity can be evaluated using only two parameters σ_{xx} and σ_{xy}:

$$R_H = \frac{\sigma_{xy} / B}{\sigma_{xx}^2 + \sigma_{xy}^2} \tag{5.17}$$

and

$$\rho = \frac{\sigma_{xx}}{\sigma_{xx}^2 + \sigma_{xy}^2} \tag{5.18}$$

from which the carrier density and mobility can be calculated.

For a material with a single carrier, this approach is identical to Equation 5.12, as σ_{ij} can be measured directly as I_i/V_j. For multiple carriers or mixed conduction system, however, σ_{xx} and σ_{xy} are summations of the components from each of the carrier in the system, and therefore, the voltages measured have different components contributed by each of the carriers present. By solving the BTE, assuming the same

relaxation time, velocity and effective mass for each individual electron or hole in a given layer, the conductivities are evaluated as:

$$\sigma_{xx} = \sum_j \frac{n_j e_j \mu_j}{1 + \mu_j^2 B^2} \tag{5.19}$$

$$\sigma_{xy} = \sum_j S_j \frac{n_j e_j \mu_j^2 B}{1 + \mu_j^2 B^2} \tag{5.20}$$

From these two equations, it can be seen that the conductivity of each carrier in the system σ_j is proportional to the mobility and the carrier density of that particular carrier j. Furthermore, the conductivity is also dependent on the magnetic field B. In particular, given two carrier components of certain mobilities the difference between their conductivity increases with increasing magnetic field. Hence, by utilising this difference in magnetic field dependence of each carrier's conductivities, the carrier concentration and mobility of each carrier present in the sample can be modelled and separated. This variation on the Hall effect technique is known as the variable magnetic field Hall effect measurement (VB Hall).

While this mixed conduction analysis has been known for decades, the difficulties in generating strong, variable magnetic fields prevented its wide spread application. With the development of superconducting high field magnets it is now possible to apply this technique to novel materials that warrant the need. VB Hall measurements have been applied to HgCdTe, GaN and InN for the separation of degenerate layers [240], characterisation of active layers [241], as well as identifying existence of holes in seemingly n-type materials [242]. In the rest of this chapter, the first ever attempt in applying VB Hall on ZnO is presented.

5.3 Conductivity Curves and Multicarrier Fit

Since the low mobility of ZnO necessitates a high magnetic field to resolve the mobilities, it was necessary to conduct measurements using the superconducting 12 T magnet at West Virginia University. Samples were bonded onto an electrically insulated ceramic plate, and electrical feedthroughs were connected to four corners of

the nominally rectangular samples in the standard van der Pauw configuration via indium soldering. Each mounted sample was then lowered in turn into a reservoir of liquid helium which allowed the temperature of the samples to be varied from 5 K to 300 K for the measurement to take place. To obtain the magneto-transport measurements, the resistivity voltages and Hall voltages were measured at 22 logarithmically spaced magnetic field points from 0.1 T to 12 T for a number of temperatures. From these measurements, the conductivity tensor components σ_{xx} and σ_{xy} of the sample were calculated.

Figure 5.4 shows the dependence of σ_{xx} and σ_{xy} on the magnetic field for a typical MBE ZnO thin film grown with a LT-buffer. It can be seen that both σ_{xx} and σ_{xy} show well-behaved magnetic field dependence. The variation of σ_{xx} with magnetic field is small, with ~3% difference between 0 T and 12 T. This is because the electric field induced by the magnetic field is relatively small compared to the field induced from the applied current. Also, it was observed that σ_{xy} is negative, as expected for an n-type sample. Further, while σ_{xx} decreased with increasing magnetic field, σ_{xy} increased in magnitude with magnetic field. This is intuitive as increasing the magnetic field is expected to create more deflection of the carriers, and therefore increases the deflection driven σ_{xy}.

To find the concentration and mobility of the different carriers that exist in the sample, these two conductivity curves can be fitted with Equations 5.19 and 5.20. This approach is known as multicarrier fitting or MCF. In most cases, MCF is simply the evaluation of the least squares fit of the conductivity curves. In a multilayer structure, this requires an estimation of the number of carriers present and assigning arbitrary initial n and μ values for each carrier. At each iteration, n and μ are varied in steps until the least squares error between the calculated conductivity curve and the measured data is minimised.

To analyse data from the variable field Hall effect measurements, the least squares MCF algorithm was implemented using Labview (written by Dr. Craig Swartz), requiring initial n and μ values as well as the type of each carrier as fitting parameters. Figure 5.5 shows the fitting of the conductivity data from Figure 5.4 using the Labview algorithm. It can be seen that with a given set of fitting parameters, σ_{xy} can be fitted better compared to σ_{xx} even though the same algorithm is used. This is generally true as in most cases the variation of σ_{xx} with magnetic field is small,

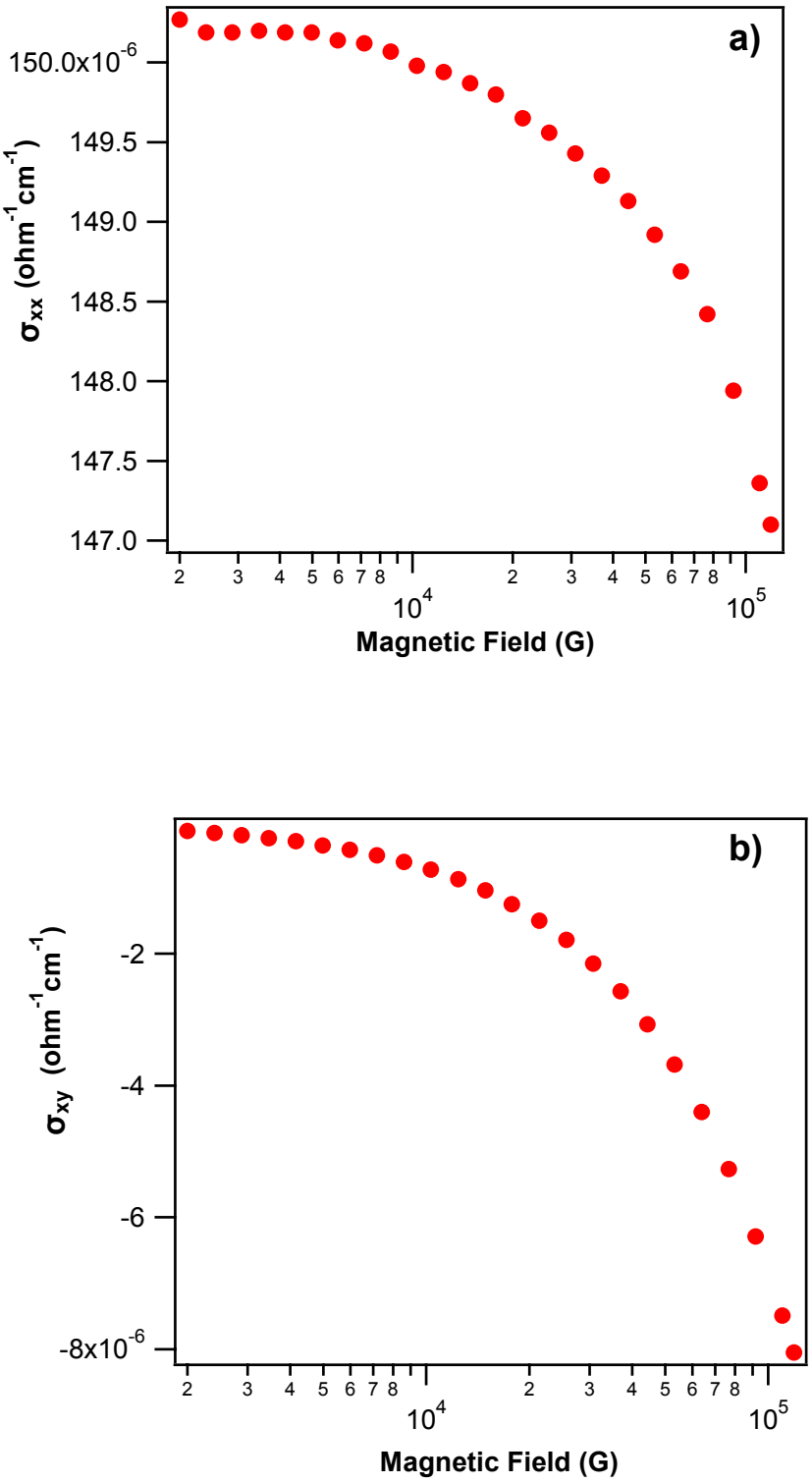

Figure 5.4 The conductivities of a typical MBE grown ZnO sample as a function of magnetic field: a) σ_{xx}; b) σ_{xy}.

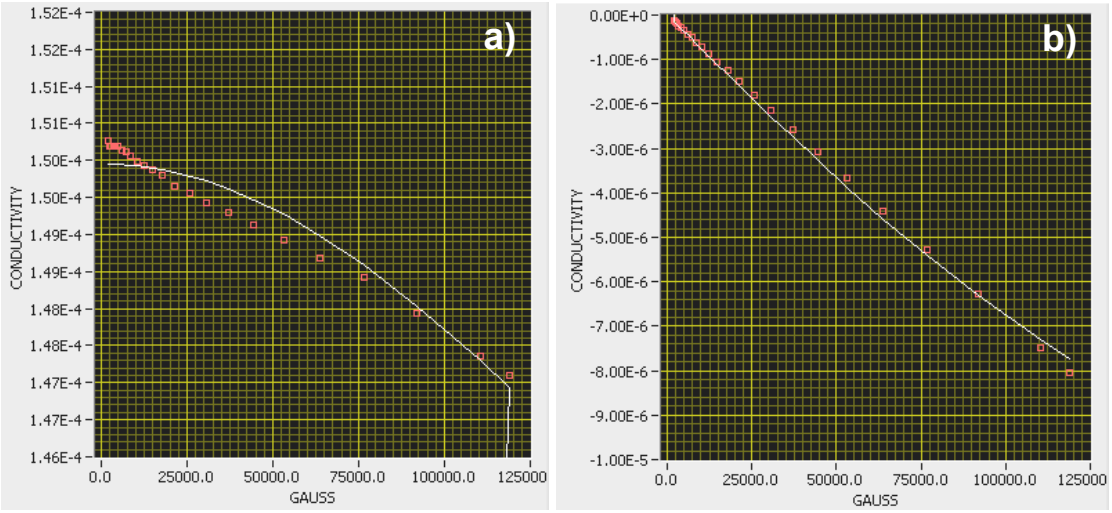

Figure 5.5 Conductivity curves in Figure 5.4 fitted using a multicarrier fitting algorithm with arbitrary initial values and a single carrier model: a) σ_{xx}; b) σ_{xy}.

making the fitting of σ_{xx} susceptible to noise in the data. It should also be noted that MCF may in some cases fail to resolve the carrier concentration and mobility of a particular carrier, possibly due to noise in the data and/or a very low carrier mobility. The presence of the unresolvable carrier in such cases is represented in the analysis by a non-zero residual conductivity.

Table 4 shows the carrier density, mobility, and the residual conductivity for four ZnO samples analysed by the MFC algorithm assuming a single carrier, compared to the values measured by the conventional (single magnetic field) Hall effect technique. The initial n and μ values for the MFC algorithm were chosen arbitrarily within sensible limits (i.e. $10^{11} < n < 10^{20}$ and $0 < \mu < 500$). It can be seen that three samples showed a significant residual conductivity, suggesting the existence of more than one carrier in these samples. Note that the MCF diverges for all four samples if a two carrier model is used. This suggests that the properties of the extra carrier in these samples cannot be resolved by MCF. Considering sample A, it can be

Table 4 The electrical measurements of selected samples via conventional and VB Hall effect. Sample A was measured before and after annealing at 750 °C.

	Conventional Hall		Variable field Hall, Multicarrier fitting		
Sample Name	μ_H (cm^2/Vs)	n_H (cm^{-3})	μ_1 (cm^2/Vs)	n_1 (cm^{-3})	Conductivity ($\Omega^{-1}cm^{-1}$)
Sample A	34	1.42×10^{19}	151	1.08×10^{18}	4.18×10^{-3}
Sample A annealed	15	5.30×10^{17}	329	8.64×10^{15}	1.27×10^{-4}
Sample F	37	2.79×10^{16}	40.0	2.92×10^{16}	4.50×10^{-11}
Sample D	35	1.65×10^{19}	46.1	1.27×10^{19}	2.54×10^{-5}

seen that the MCF of the as-grown and annealed sample gave a resolvable carrier at mobilities of 151 cm^2/Vs and 329 cm^2/Vs respectively, with a corresponding carrier concentration of 1.08×10^{18} cm^{-3} for the as-grown sample, and 8.64×10^{15} cm^{-3} for the annealed sample. This is very different from that observed from conventional Hall effect measurements, and is comparable to the mobility values reported in the literature [86]. While the exact location of this high mobility carrier cannot be unambiguously confirmed, it most likely originates from the high quality HT-ZnO epilayer that formed the bulk of the sample, based on previous reports [240] and the consistency of this measurement with the high crystal quality observed for these samples. The low mobility and higher carrier concentration measurements obtained from the conventional Hall effect then clearly belong to another carrier that exists in the system, represented by the unresolvable residual conductance. This is confirmed by the fact that the sheet conductivity observed from the conventional Hall effect measurement (for example, $\sigma = n\mu e = \sim4\times10^{-3}$ $\Omega^{-1}cm^{-1}$ for as-grown sample A) is almost identical to the residual conductivity obtained from MCF. Again, while the identity of this low mobility carrier cannot be confirmed, it most likely originated from the low quality buffer layer, based on the low crystal quality and high dislocation density observed previously (see Chapter 4) for these buffer layers.

Note that the mobility value for the annealed sample is very high compared to the best bulk value reported. This extremely high mobility value is most likely to be an artefact from the fitting algorithm, and strongly suggests that an additional analysis technique is required to confirm these results (as described in the next section). Nevertheless, it is clear that the MCF supports the existence of a high mobility bulk carrier in the sample. The MCF also shows that the concentration of the bulk carrier layer was reduced by three orders of magnitude via annealing, compared to the two orders of magnitude observed from the conventional Hall effect. This again illustrates the limitations of conventional measurements.

Examining sample F, it can be seen that the MCF using a single carrier model resulted in a carrier with similar mobility and carrier concentration to that measured with conventional Hall effect, with a negligible residual conductivity. This suggests that only one carrier exists in sample F. However, the fitting used for sample F (with an initial $n = 10^{17}$ and $\mu = 10$) actually resulted in a very poor fitting for σ_{xx}. This suggests that the σ_{xx} data was strongly affected by noise, possibly due to the much higher resistivity of sample F. This poor fitting therefore places doubt on the MCF

results observed for the sample. If MCF is performed on σ_{xy} only, a perfect fitting can be achieved for sample F (using a single carrier model) with a carrier mobility of 227 cm^2/Vs. The discrepancy between the two fitting attempts suggests the possible existence of a high mobility carrier in sample F, and highlights the need of additional analysis for the confirmation of the MCF results. For sample D, reasonably well-fitted data for both σ_{xx} and σ_{xy} can be achieved with the MCF of both conductivities, giving a mobility and carrier concentration that is almost identical to the degenerate measurements observed with conventional Hall effect. There is also a non-zero residual conductivity of $\sim 2.5 \times 10^{-5}$ $\Omega^{-1}cm^{-1}$. Again, the existence of a significant residual conductivity strongly implies the existence of two carriers in the sample. Note that the sheet conductivity of the resolvable carrier is $\sim 1 \times 10^{-2}$ $\Omega^{-1}cm^{-1}$, much higher than that of the unresolved carrier. Therefore, it is reasonable to suggest that the residual conductivity in this case belongs to the high mobility, low concentration carrier originated from the bulk of the sample.

As a comparison between the MCF analysis with variable field Hall effect and the multilayer analysis with conventional Hall effect described in the previous section, temperature dependent measurements were performed on sample D. For each temperature, the Hall voltage measurements from a single magnetic field (~ 0.51 T, the magnetic field used for all other Hall measurements presented in this work) was extracted and analysed as conventional Hall effect measurements, whereas data from the 22 magnetic field points were analysed using MCF.

Figure 5.6 shows the carrier concentration evaluated using conventional Hall effect, multilayer analysis correction of the raw measurements using Equation 5.14 and Equation 5.15, and the MCF of the conductivity curve from the variable magnetic field measurements. Conventional Hall effect measurements show no change in carrier concentration with temperature, confirming the existence of a degenerate layer, which dominated the measurement at all temperatures. Using the multilayer analysis, the bulk carrier was successfully separated from the degenerate carrier at all temperatures, and an activation energy of 26.7 meV was extracted. This activation energy is consistent with the common 30 meV shallow donor reported in the literature [243]. The MCF analysis, however, failed to extract the non-degenerate carrier at most of the temperatures used. The carrier concentration values calculated from MCF are similar to the conventional Hall effect measurements for most temperatures

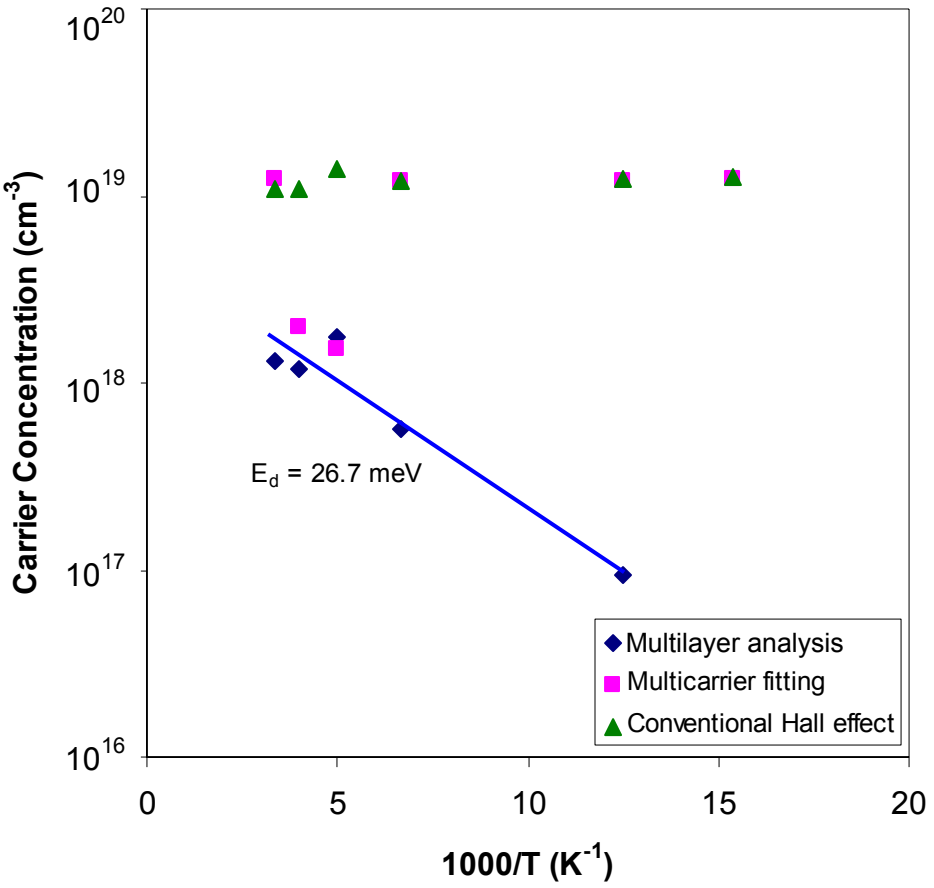

Figure 5.6 The carrier density of sample D (grown at 300 W with 25 hole plate) as a function of temperature, comparing between conventional Hall measurements, multilayer analysis of the conventional Hall data, and multicarrier fitting. A donor energy of ~26.7 meV is implied by both the multilayer correction and MCF.

except at 200 K and 250 K. At these two temperatures, the carrier density measured from MCF is comparable to the bulk carrier predicted by the multilayer analysis. In particular, the MCF gave a mobility of 127 cm^2/Vs for 200 K and 66 cm^2/Vs for 250 K, with a residual conductivity of 54 $\Omega^{-1}cm^{-1}$ and 2.5 $\Omega^{-1}cm^{-1}$, respectively, compared to a small residual conductivity of $\sim 1 \times 10^{-9}$ $\Omega^{-1}cm^{-1}$ measured for the lower temperatures. It can be seen that the carrier mobility for the bulk carrier at these two temperatures is quite low. This mobility value is expected to be even lower at room temperature. Considering the mobility measured using conventional Hall effect for this sample is ~50 cm^2/Vs at 300 K, it is clear that as the sample approaches room temperature, the mobility of the bulk and the degenerate layer become very similar.

The variation of the MCF results with temperature observed in Figure 5.6 can be explained by the variation of bulk carrier concentration and mobility with temperature. At low temperatures, the freeze out of the non-degenerate bulk carrier implies that the measurement solely depends on the degenerate interface carrier.

Therefore, the bulk carrier cannot be identified. Above 150 K, the bulk carrier concentration started to increase. Initially, the mobility of the bulk carrier is much higher compared to the degenerate layer. The difference between the two mobilities is significant enough that the conductivity difference between the carriers is observable with magnetic field, allowing the high mobility carrier to be resolved by MCF at 200 - 250 K. At higher temperatures, the mobility decreases due to polar phonon scattering. Because of the relatively high carrier density and low carrier mobility of the bulk layer, the bulk carrier and the degenerate carrier are too close in mobility to be separated. This leads to the low mobility and high carrier concentration observed at 300 K. From this, it can be seen that the MCF breaks down when the mobility of the two layers are too close to each other. Note that since the multilayer method explicitly subtracts the degenerate carrier from the measurements, the bulk carrier can be extracted from the measurements even if the mobilities of the two carriers are similar at high temperatures.

From these experiments, it can be seen that MCF provides an alternative means of evaluating the carrier concentration and mobility of a material, complementing the conventional measurements. MCF performs very well in separating carriers with large mobility differences, and has successfully confirmed the existence of a degenerate interface carrier and a high mobility bulk carrier in MBE ZnO thin films grown on LT-ZnO buffer layers. However, from the results of certain samples at various temperatures, it was found that MCF suffers from a number of limitations. Firstly, when the overall conductivity is low (such as sample F), the MCF becomes very susceptible to noise that leads to poor fitting; secondly, MCF breaks down when the mobilities of the different carriers in the sample are very similar; and thirdly, as observed in some measurements, unrealistically high mobilities or even multiple solutions can result from the arbitrary nature of the MCF algorithm. Therefore, to extract the electrical properties of a thin film from variable field Hall effect measurements more accurately, an additional method should be applied to complement the MCF analysis. One such method is mobility spectrum analysis.

5.4 Mobility Spectra

Mobility spectrum (MS) analysis was first described by Beck and Anderson [244], who suggested that rather than one discrete value, the mobility of a carrier should be treated as a range of values. This is a more physically satisfying theory as it preserves the statistical distribution of different carrier velocities. By using MS to analyse variable field Hall effect measurements, they showed that the arbitrary nature of MCF can be avoided [244]. Calculating a mobility spectrum also inherently takes uniformity into account, with the spread of mobilities within a layer associated with the uniformity of the sample.

In MS analysis, rather than treating the mobilities as discrete values, they are treated as a continuous function. Therefore, by definition, the summations in Equation 5.19 and Equation 5.20 can be generalised as an integral:

$$\sigma_{xx}(B) = \int_{-\infty}^{\infty} d\mu \frac{s(\mu)}{1+\mu^2 B^2} \tag{5.21}$$

$$\sigma_{xy}(B) = \int_{-\infty}^{\infty} d\mu \frac{s(\mu)\mu B}{1+\mu^2 B^2} \tag{5.22}$$

where the positive mobility domain (integrating from 0 to ∞) represents holes and the negative mobility domain (integrating from 0 to -∞) represents electrons, and s(μ) is the "conductivity density", which is the mobility spectrum function. The aim is to find a spectrum s(μ) that satisfies both equations. While Equation 5.21 and Equation 5.22 are generalisations of the mixed conduction analysis and take into account dependence of the relaxation time on mobility and mass anisotropy [245], such integrals can rarely be solved analytically, and therefore need to be approximated by a finite summation series. Different ways of approximating and evaluating this integral lead to various MS analysis algorithms.

One of the most common methods is the improved quantitative mobility spectrum analysis (iQMSA). The complete treatment of this technique can be found in reference [246]. Essentially, all MS algorithms rely on approximating the integral by replacing the continuous spectra with a fine grid, and summing the conductivity at each mobility μ_i:

$$\sigma_{xx}(B) = \sum_{i}^{M} \frac{s_p(\mu_i) + s_n(\mu_i)}{1 + \mu_i^2 B^2} \tag{5.23}$$

$$\sigma_{xx}(B) = \sum_{i}^{M} \mu_i B \frac{s_p(\mu_i) - s_n(\mu_i)}{1 + \mu_i^2 B^2} \tag{5.24}$$

where M is the number of grid points. The degree of accuracy of the spectrum depends on how finely the mobility grid is divided. Carriers from different layers with different mobilities are represented in MS analysis as distinct peaks or bands, while the deviation in mobilities for carriers from the same source would be represented by the spread or the broadening of the corresponding peak. The goal of a MS procedure then is to fit the experimental data with the finite summation by varying both $s_p(\mu)$ and $s_n(\mu)$ at each mobility μ_i to minimise the least squares errors $(\sigma_{xx}^{\exp} - \sigma_{xx}^{i})^2$ and $(\sigma_{xy}^{\exp} - \sigma_{xy}^{i})^2$. In iQMSA, a further step is taken to minimise the least squares error of the slope of the spectrum [244, 246].

Figure 5.7 shows a typical MS of a ZnO sample grown in this work obtained from the Lakeshore QMSA programme, a commercial package that uses the iQMSA routine for the evaluation of variable magnetic field Hall data (for simplicity, the iQMSA will be referred to as QMSA from now on). The QMSA routine calculates the mobility spectra which are plotted in terms of the conductivity at each mobility. One drawback of the MS procedure is illustrated in the figure, namely, the existence of artefacts or ghost peaks. In particular, high mobility peaks labelled A and B in the figure are often observed in many simulations, even though they are physically unrealistic as the mobility limit of ZnO is below 1000 cm^2/Vs at room temperature. These artefacts originate from the interpolated data used in the procedure. While such ghost peaks make interpretation difficult, the identification of peaks can be aided by MCF on the same data and from the general properties of the material. Even though ghost peaks and artefacts exist, the fitting of the conductivity curve using QMSA introduces less error compared to the MCF routine.

Figure 5.8 shows the fitting of the conductivity curve by QMSA for the same sample shown in Figure 5.5. It can be seen that the QMSA routine fits the experimental conductivity data very well for both σ_{xx} and σ_{xy}, unlike MCF which only yielded a good fit to σ_{xy}.

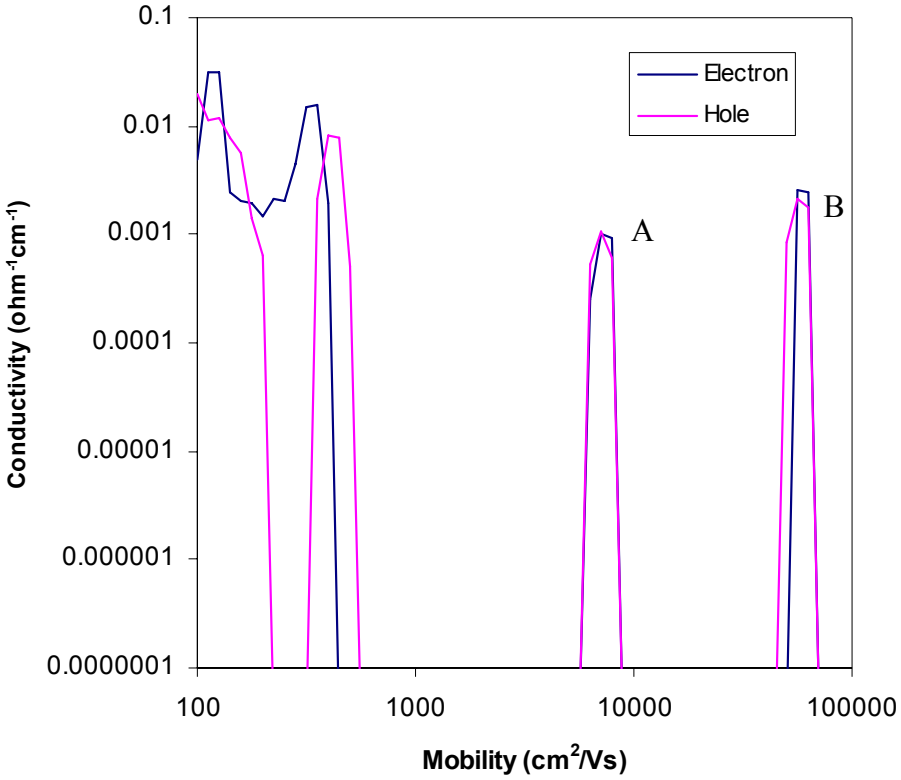

Figure 5.7 A typical mobility spectrum of an MBE grown ZnO sample, obtained using the Lakeshore QMSA program, showing electron and hole peaks. For ZnO, most high mobility peaks and hole peaks are artefacts from the algorithm.

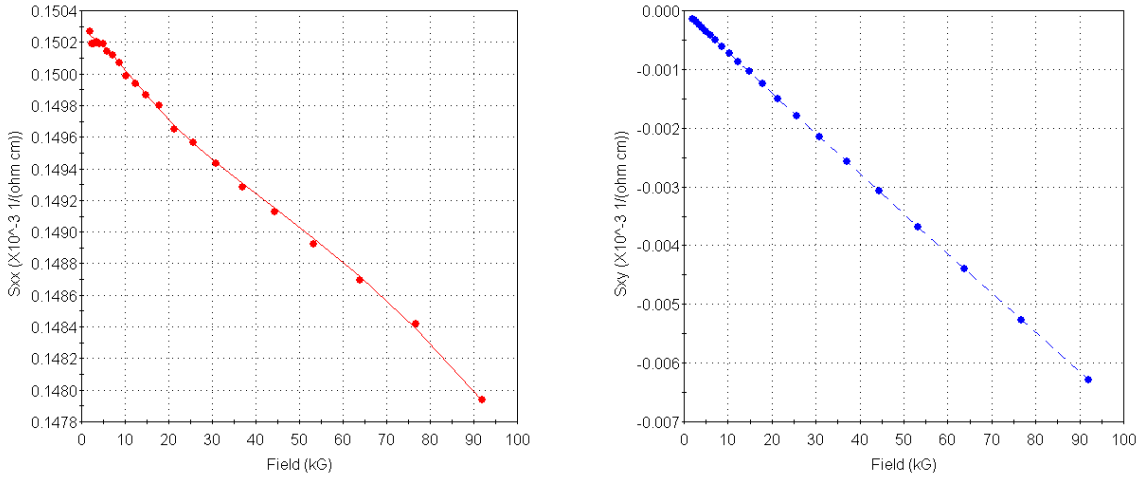

Figure 5.8 The fitting of the conductivity curve using the QMSA procedure. Compared to Figure 5.5, the fitting obtained by QMSA is superior ($S_{xx} = \sigma_{xx}$, $S_{xy} = \sigma_{xy}$).

Figure 5.9 shows the MS of sample A both as-grown and annealed. Note that the carrier concentration was calculated by the relation $\sigma = n\mu e$ at each mobility point. It can be seen that there are clearly two different carriers present in the sample. In particular, for both as grown and annealed samples there exists a low concentration electron layer with mobility above 100 cm^2/Vs, as well as a higher concentration electron layer with a mobility < 100 cm^2/Vs, indicated by the steep increase in conductivity at the lowest end of the spectrum. The actual mobility of this carrier cannot be resolved below 100 cm^2/Vs, as there is a minimum resolvable mobility limit $\mu_{min} = 1/B_{max}$ for the QMSA algorithm [241], and the Lakeshore program only accepts data up to 10 T. Thus, Figure 5.9 allowed the direct observation of the high mobility bulk carrier in sample A with mobility comparable to the best reported value in the literature [86]. This confirms the dominating effect of the degenerate layer in the conventional Hall effect measurement. Furthermore, it can be seen that the bulk carrier concentration is reduced 100 times upon annealing, with the maximum mobility increased from 150 cm^2/Vs to 225 cm^2/Vs. Thus, Figure 5.9 directly confirms the improvement of electrical quality with annealing.

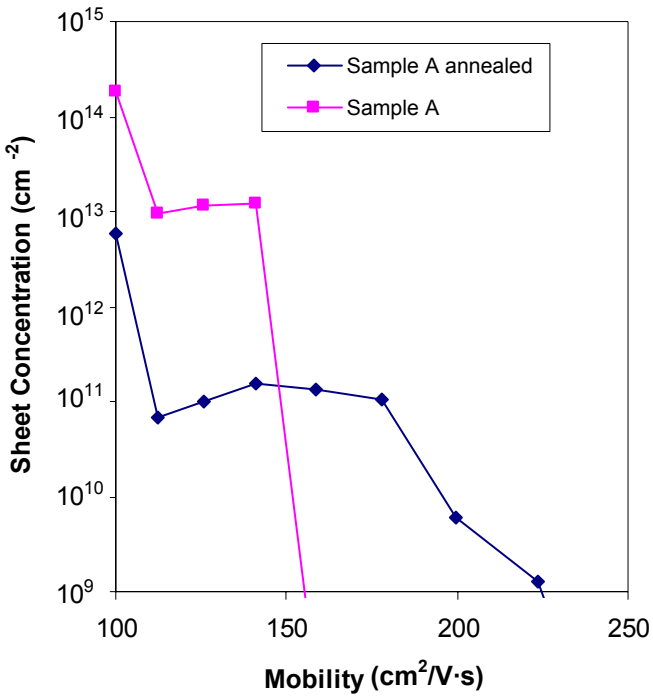

Figure 5.9 Electron mobility spectra for as grown and annealed sample A showing the existence of high mobility carriers.

Figure 5.10 compares the MS of the as-grown sample with an O-polar commercial substrate from Tokyo Denpa. It can be seen that the mobility from the MBE film is lower than the mobility in the bulk sample, with the bulk carrier in the Tokyo-Denpa sample ranging from ~140 cm^2/Vs to ~270 cm^2/Vs. The considerably larger spread observed for the bulk sample suggests a higher non-uniformity in the sample, which is expected due to the considerably higher thickness of the bulk sample (0.5 mm) compared to a ~1 μm film. Comparing the thickness of the two samples, it can also be seen that the total carrier density in the bulk ZnO sample is lower than that of the bulk carrier in the MBE grown film. This suggests that the bulk layer of the MBE film contains more n-type impurities, as well as structural defects and dislocations, which resulted in an increase in carrier concentration and reduction in carrier mobility.

To complement the MCF analysis performed in the previous section, the variable field Hall data for sample A, sample D and sample F were analysed using QMSA. Figure 5.11 shows the mobility spectra for these three samples. All three samples show mobility components above 100 cm^2/Vs, confirming the existence of

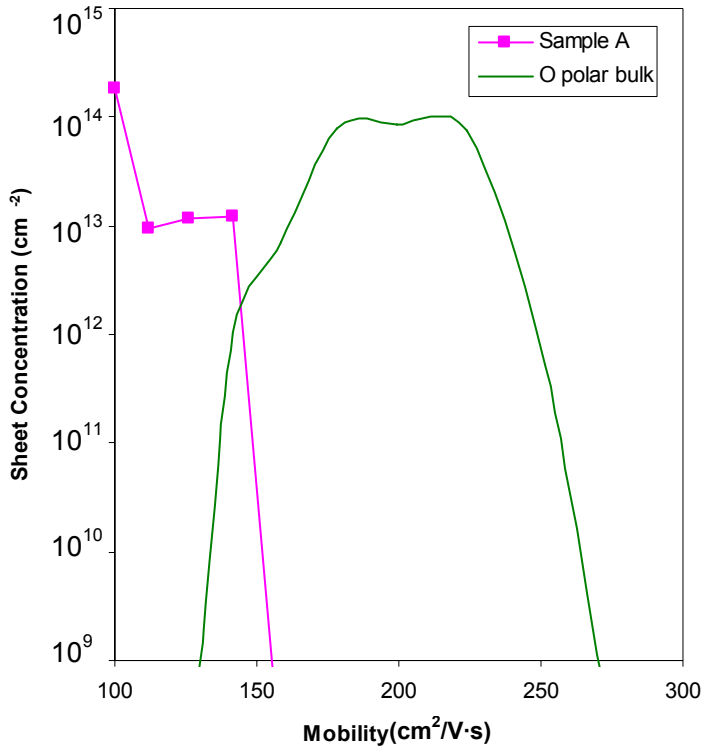

Figure 5.10 Mobility spectrum of sample A compared to the mobility spectrum of a Tokyo Denpa O-polar ZnO sample, showing the higher density of high mobility electron in commercial ZnO crystals.

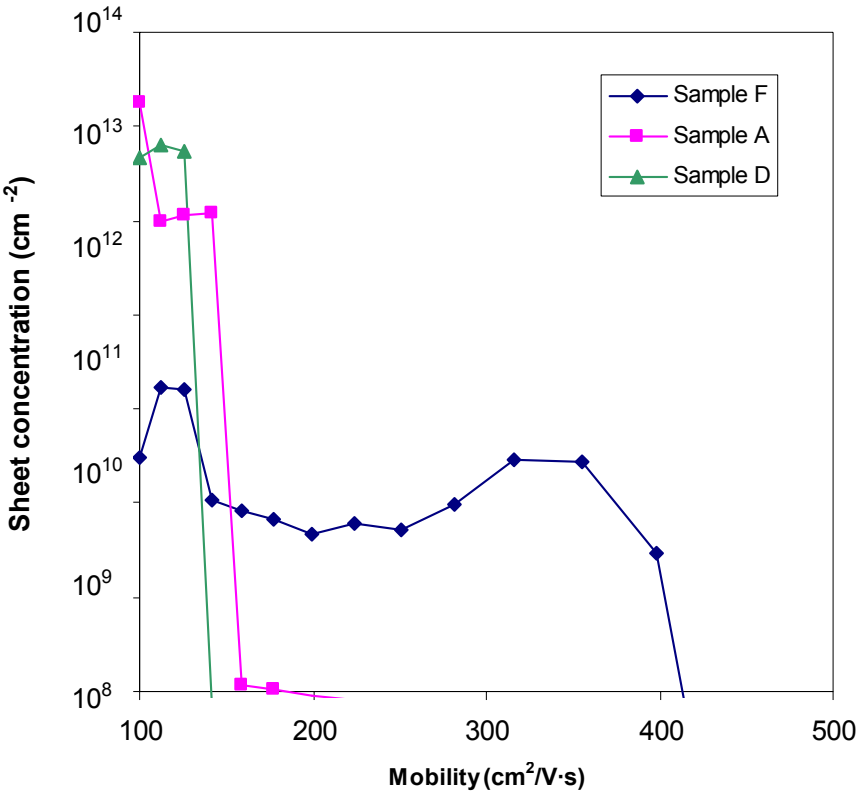

Figure 5.11 Mobility spectrum for samples A, D and F, each grown at the same RF power but using different aperture plate designs (sample F: 1 hole plate; sample D: 25 hole plate; sample A: 276 hole plate).

the high mobility bulk carrier in all samples. However, it can also be seen that both the low mobility carrier and high mobility carrier have varied mobility and concentration between samples. In particular, significantly lower carrier density for both the bulk and the interface layer can be seen for sample F (grown with the 1 hole plate), which is consistent with the low conductivity and carrier density observed using conventional Hall effect. The QMSA for sample F also shows a wide spread of mobility for the bulk carrier, with a maximum mobility above 400 cm^2/Vs. This value is very high for ZnO. Furthermore, from studies described in Chapter 3, it was found that even though the resistivity increased with the use of the 1 hole plate, other properties such as structural characteristics and PL suggested that the sample has a high density of dislocation and defects, which is inconsistent with the improved bulk layer mobility. This abnormally high mobility therefore most likely originates from the high signal-to-noise ratio in the data due to the low conductivity of the sample.

The other two samples, sample A (grown with 276 hole plate) and sample D (grown with 25 hole plate) showed a similar bulk behaviour, with a relatively high

carrier concentration and only a small band of bulk carrier with a maximum mobility below 150 cm^2/Vs. It can be seen that the MS agrees very well with the solution obtained from the MCF. In particular, the relatively low mobility of the bulk carrier in sample D is consistent with the unresolvable bulk carrier at 300 K observed from the MCF. One important thing to note is that reports of mobility ~140 cm^2/Vs were observed in MBE grown films using conventional Hall effect measurement. Comparing these reports it can be seen that while the bulk layer of the MBE samples grown in this work is comparable with the literature, the buffer layer quality is much lower resulting in the low mobility and high carrier density measured with conventional methods.

Figure 5.12 shows the variation of the bulk carrier mobility of sample D as a function of temperature. It can be seen that as expected, the carrier concentration of the bulk carrier decreases with temperature. In particular, the area below the MS decreases with temperature, suggesting a decrease in the total bulk carrier density. In contrast, while it is expected that the mobility would increase with decreasing temperature, the QMSA suggests that the mobility actually remained unchanged if not decreased. This is again the direct result of the reduced bulk carrier density.

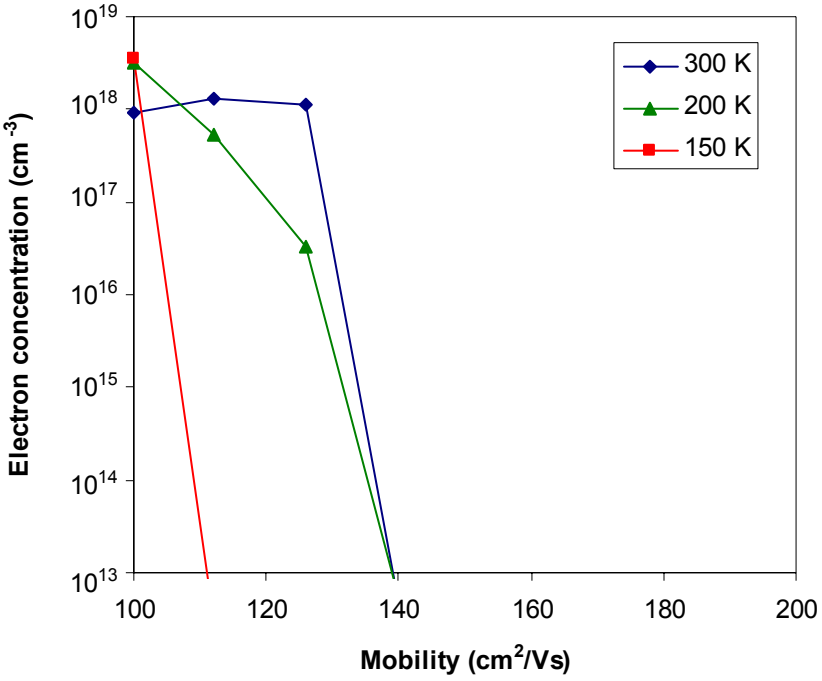

Figure 5.12 Mobility spectrum of sample D upon variation of temperature, showing the reduction of bulk electron density with temperature. The reduction of mobility observed suggests that the bulk mobility is quite low and the degenerate layer has a high dominance over the bulk layer.

In particular, as indicated from the conventional Hall effect measurements and MCF, the degenerate layer in this sample has a relatively high density and similar mobility to the bulk layer. Therefore, as the temperature decreased, the already scarce bulk carrier density decreased even further, which reduced the observable component from the bulk carrier to almost zero. As a result, the higher mobility carriers cannot be separated from the data, and the measured mobility decreased with temperature.

From these results, it can be seen that QMSA analysis can be applied readily to data from ZnO thin films, and provides a more accurate confirmation of results from the MCF analysis. However, there are also limitations to the technique. Apart from the existence of ghost peaks and artificial features that complicates the interpretation of the MS, the nature of the QMSA routine limits the mobility in which it can resolve. Therefore, unlike MCF, QMSA using 10 T data point cannot resolve the degenerate carriers with mobility below 100 cm^2/Vs. This is especially problematic for ZnO, as ZnO thin films in general have low mobility. There are other MS analysis algorithms such as maximum entropy mobility spectrum analysis (MEMSA), which relies on the maximum entropy fitting of the sum of the conductivities, that promises resolution down to 10 cm^2/Vs [247]. However, experimental simulation on the samples studied here showed that MEMSA suffers from even larger artefact issues, with frequent confusion between signs of the mobility due to the nature of the algorithm. Therefore, the QMSA routine remains to be the best MS technique for the analysis of ZnO thin films, but must be used in conjunction with MCF to provide a true quantitative analysis.

Apart from the need of high magnetic fields for resolving low mobilities, the variable field Hall effect in general also suffers from other issues such as anisotropy and polarity. For example, it has been observed that O-polar samples experience contact failures at a higher temperature than Zn-polar samples. It was also observed that Hall voltages of an m-plane sample suffer from anisotropic effects from the presence of in-plane polarisation fields. These limitations in general also apply to single field Hall effect measurements, but are especially manifested in variable field Hall effect due to the additional magnetic field variations.

In terms of practicality, high magnetic fields are hard to generate. Even at 12 T, the generation of the magnetic field requires large volumes of liquid helium that is expensive and hard to obtain. In addition, high magnetic fields can have adverse

effects on the measurements such as the failure of ohmic contacts or the occurrence of quantum oscillations [244]. Therefore, the variable field Hall effect technique is not viable as an everyday electrical characterisation technique for evaluation of reproducibility between samples. However, as seen with the ZnO thin films, the dominance of interface layer conduction clearly requires variable field Hall effect measurements for the electrical evaluation of the functional part of the sample. Hence, the variable field Hall effect technique would find usefulness in situations where conventional Hall effect measurements contradict other measurements implying the existence of multiple carriers, or in situations where there are very likely to be multiple carriers in the sample such as for a p-type doping attempt.

Chapter 6

RECOMBINATION DYNAMICS OF ZNO THIN FILMS

6.1 Optical Probing of Recombination Dynamics

In the previous chapter the use of the variable field Hall effect to characterise the electrical properties of ZnO was described. In particular, by using this alternative analysis instead of the conventional Hall effect technique, the carrier density and mobility of the majority carriers in the bulk of a given sample could be investigated, separated from the degenerate interface layer. While the knowledge of these two figures of merit allows quantitative comparison of the electrical performance between different samples, the usefulness of a sample for optoelectronic applications is dependent on the interaction between majority carriers and minority carriers. Therefore, quantitative measurement of the carrier recombination dynamics is also a valuable indicator of the electrical performance of a material. Carrier recombination in ZnO most typically leads to optical emission; by performing the appropriate optical measurements, the carrier recombination dynamics can be evaluated. Conventional (continuous-wave) PL measurements, although important, lack dynamic information of the recombination processes. Therefore, a variant of conventional PL, known as time resolved photoluminescence (TRPL), was used to observe the temporal evolution of the carrier recombination process in ZnO thin films.

In a typical PL experiment, above bandgap photons are used to create electron-hole pairs. In ZnO, these pairs typically form excitons or excitonic complexes, which can exist for a certain length of time before recombining and emitting a photon. In conventional PL, since a continuous photon source (or continuous-wave - CW) is used to excite the material, there are electrons and holes recombining continuously, resulting in a steady state PL intensity. However, in TRPL, the material is excited with a pulsed excitation source, i.e. a limited amount of photons. Therefore, after the

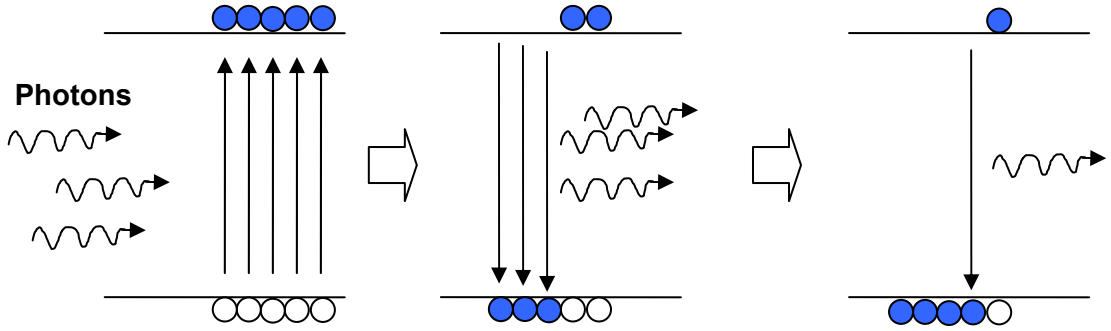

Figure 6.1 The sequential events in a short burst excitation during a TRPL measurement.

termination of the excitation pulse, no additional electron-hole pairs are created, and the PL intensity decreases with time as remaining electron-hole pairs recombine (Figure 6.1). Hence, TRPL allows the evaluation of the electron-hole pair recombination rate, a measure of the survival of carriers in the material and a direct measure of the sample quality. TRPL has been used for the characterisation of a wide variety of semiconductors including freestanding GaN [248] and GaN thin films [249]. It has also been used for bulk ZnO [9, 250, 251] and ZnO thin films [252, 253]. To investigate the recombination dynamics of the MBE grown ZnO films, TRPL was performed on a number of MBE grown ZnO samples, both as grown and annealed, at The University at Buffalo, State University of New York. The short burst excitation was provided by a pulsed 266 nm laser line generated by the frequency tripling of an 800 nm Ar laser. A Hamamasu streak camera was used to monitor and record the decay characteristics over the bandedge spectrum, giving a temporal resolution of < 2 ps and a spectral resolution of ~1 nm. For temperature dependent measurements, samples were cooled using a closed cycle cryogenic system to allow measurements at temperatures down to 14 K. From the streak camera image, the PL decay curve of the excitonic peak was extracted by using a 1 nm slice of the image at the wavelength of highest PL intensity. Note that since spectral resolution decreases with increasing temporal resolution, the decay observed would most likely be contributed by a number of excitonic states.

Figure 6.2 shows a typical PL decay curve observed from the MBE ZnO samples. It can be seen that the PL decay is fast compare to other common

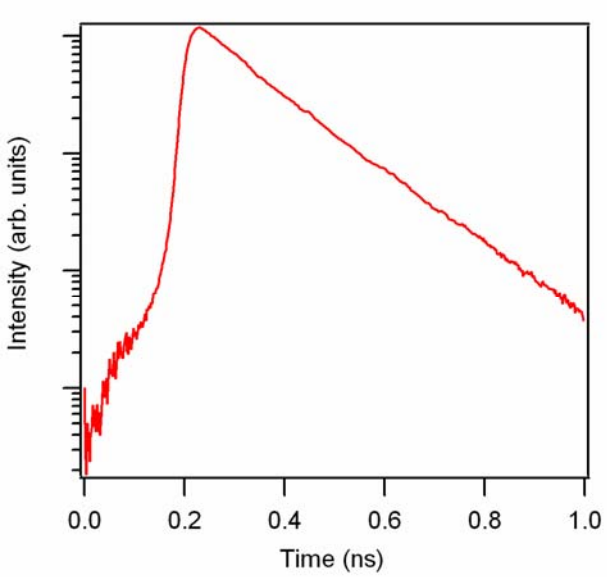

Figure 6.2 A typical PL decay signal observed for the bandedge emission of ~ 1μm thick ZnO thin film grown on sapphire with a LT-buffer layer, showing a single exponential decay.

semiconductors such as GaAs and SiGe [254, 255], with the PL intensity returning to almost the initial level within 1 ns. The decay curve can be adequately modelled by using a single exponential function,

$$I_t = I_0 \exp(-t/\tau) \qquad (6.1)$$

where the decay constant τ is known as the PL lifetime, which is proportional to the carrier lifetime of the sample. By modelling the PL decay curve with a single exponential function, it was found that at room temperature, a typical PL lifetime for these samples is ~70 ps. This is much smaller than the ~250 ps value reported for bulk materials [250], suggesting a much higher level of scattering in the MBE grown thin films. Note that not all PL decays from ZnO follows a single exponential model. In particular, Koida et al. [253] has observed a biexponential decay on PLD grown ZnO thin films, where the PL first follows a rapid decay with a short (~ps) decay constant followed by a slow decay with a long (~ns) decay constant. Some PL decay data from MBE grown thin films can also be modelled using a biexponential model. However, with such a model the two extracted lifetimes are almost the same, which suggests that the decay can be well approximated by a simpler single exponential model.

Figure 6.3 shows the PL lifetime as a function of temperature for a number of samples grown using the 25 hole plate with different RF power. It can be seen that in most cases, the lifetime is below 100 ps. The maximum PL lifetime observed for all samples was ~200 ps, which was measured at 14 K. Out of the four samples measured, the sample grown at 300 W (previously named sample D) has the longest PL lifetime with a lifetime of ~150 ps at room temperature. While the lifetime of samples grown at 400 W and 500 W increased only slightly and monotonically with temperature, similar to that reported for ZnO [252] and GaN [249] thin films, the lifetime of the other two samples showed a different trend. The PL lifetimes for these two samples initially decreased with increasing temperature until around 100 K, above which the lifetime started to increase again.

This curved trend has not been reported in any material previously, yet almost all of the ZnO thin films measured showed this parabolic trend. For example, Figure 6.4 shows the PL lifetime of two samples grown under identical conditions, one with a MgO buffer (sample M) and the other without (sample F). It can be seen that even though the crystal quality of sample M is much better (see Chapter 4), the PL lifetime

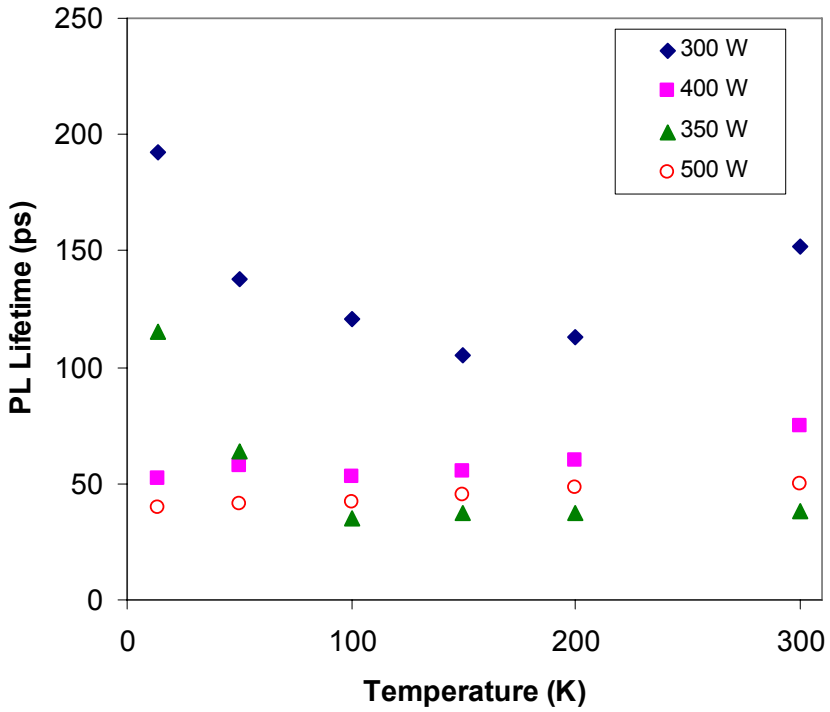

Figure 6.3 The temperature dependence of PL lifetime extracted using a single exponential model for four samples grown at different plasma conditions. Note that the sample grown at 300 W is sample D from previous chapters.

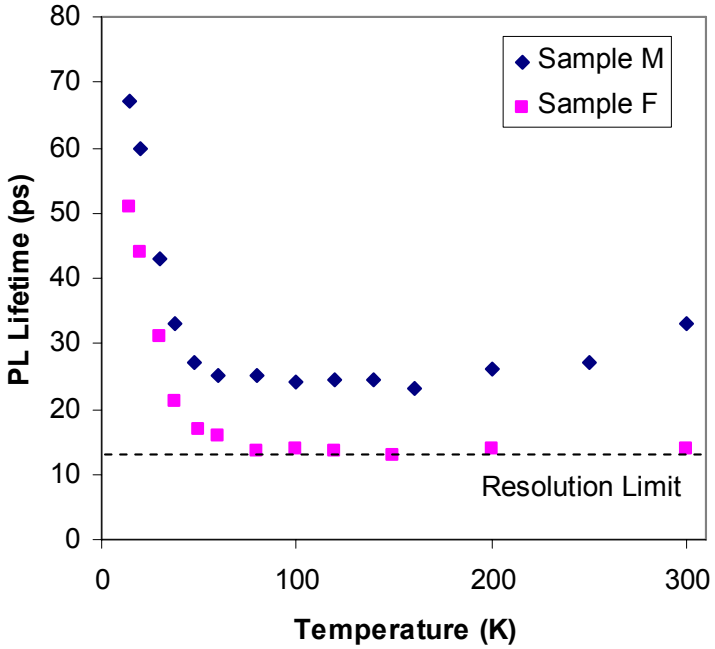

Figure 6.4 The PL lifetime extracted for sample M and sample F. Both samples were grown under the same conditions except sample M has a MgO buffer layer. The curved trend with temperature can be seen here as well.

of sample M is very short compared to the other samples measured, with a lifetime of ~35 ps at room temperature. The lifetime of sample F was measured to be even lower, towards the resolution limit of the streak camera. However, for both samples, it can be observed that the lifetime versus temperature trend still follows the curved trend previously described.

The temperature dependence of the PL lifetime represents the variation of the recombination mechanism with temperature. While Figure 6.1 gives a general picture of the light emission from carrier recombination in a material, it is a simplistic picture with the assumption that no states exist within the forbidden gap. In reality, structural defects, dislocations and impurities can cause local disruption of the crystal lattice, resulting in mid-gap states that electrons or holes can occupy. These states provide alternative pathways for the carriers to recombine. In particular, electrons can recombine through mid-gap states, releasing energy as photons for optically active states and phonons for optically inactive states (Figure 6.5). If the recombination involves the emission of a photon, the process is known as radiative recombination. Recombination processes that do not involve photon emission are known as non-radiative recombination.

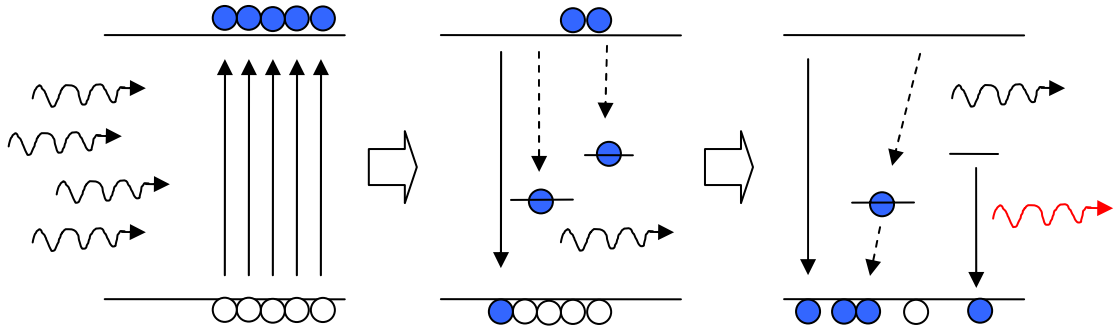

Figure 6.5 A possible sequence of events in a short burst excitation taking into account mid-gap states. The mid-gap states provides a pathway for non-radiative recombination (dashed lines) and sub-bandgap emission (red).

Since the excited carriers generated from an external excitation can recombine both radiatively and non-radiatively, the actual PL decay rate observed is the sum of the radiative recombination rate and non-radiative recombination rate of the excited carriers. Then, the PL lifetime is, by definition,

$$1/\tau_{pl} = 1/\tau_r + 1/\tau_{nr} \qquad (6.2)$$

where τ_r is the radiative lifetime and τ_{nr} is the non-radiative lifetime of the material.

The temperature dependence of the PL lifetime therefore illustrates the temperature dependence of the radiative and non-radiative recombination processes. The radiative lifetime τ_r and non-radiative lifetime τ_{nr} can be extracted from the PL lifetime by assuming the quantum efficiency of the PL is 100% at zero Kelvin [256]. Since PL emission originated from radiative recombination, the PL efficiency given by:

$$\eta_{PL}(T) = \frac{I(T)}{I(0)} \qquad (6.3)$$

gives a representation of the radiative efficiency (also known as the quantum efficiency) of the material. The internal quantum efficiency is related to the lifetimes by:

$$\eta(T) = \frac{R_{rad}}{R_{total}} = \frac{\Delta n / \tau_r}{\Delta n / \tau_{nr} + \Delta n / \tau_r} = \frac{\tau_{nr}}{\tau_{nr} + \tau_r} \tag{6.4}$$

where R_{rad} and R_{total} are the radiative recombination rate and total recombination rate, respectively, and Δn is the injected carrier density. Since $1/\tau_{pl}=1/\tau_r + 1/\tau_{nr}$, combining Equation 6.3 and Equation 6.4 gives

$$\tau_r = \tau_{PL} I(0) / I(T) \tag{6.5}$$

From Equation 6.5, it can be seen that the radiative and non-radiative lifetimes can be readily extracted from the PL lifetime, given that the PL intensity at 0 K and at temperature T are known. Since 0 K is impossible to achieve, it is in most cases approximated by the PL obtained from the lowest temperature achievable. Therefore, to study the variation of the radiative and non-radiative recombination dynamics, it is also necessary to obtain temperature dependent CW-PL data from the sample.

6.2 Radiative Lifetime and Modelling

This study focuses on two specific samples already described in previous chapters: sample A as-grown and sample A annealed at 750 °C. These two samples were chosen for TRPL measurements to complement the electrical measurements performed on these two samples as presented in the previous chapters. Figure 6.6 shows the PL lifetime of both samples. It can be seen that similar to the other samples measured, both the as grown and annealed samples showed a PL lifetime that decreased, then increased, with increasing temperature. For the as grown sample, the maximum lifetime is approximately 130 ps, with a room temperature lifetime of ~70 ps, double the lifetime observed for sample M, but slightly lower than the maximum of ~150 ps observed for the best sample measured. The annealed sample showed a similar lifetime for most temperatures except at the lowest temperatures where a maximum lifetime of 88 ps was measured.

Temperature dependent PL was performed on these two samples using the

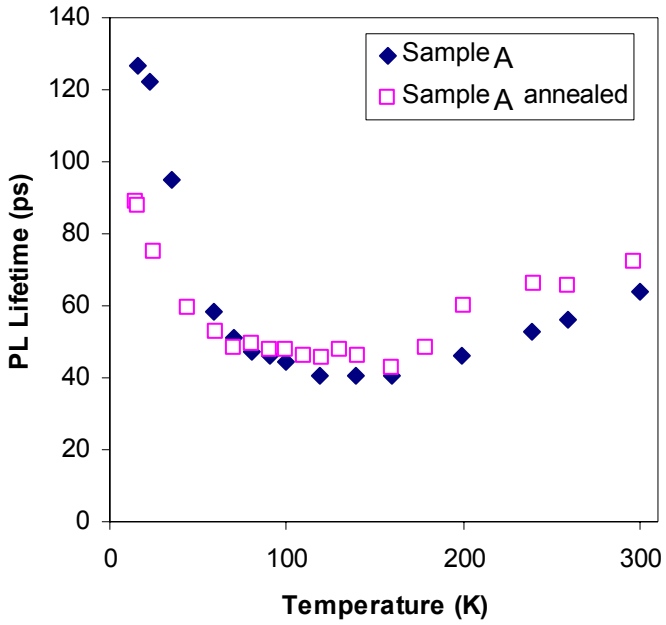

Figure 6.6 The variation of PL lifetime with temperature for sample A both as grown and annealed.

325 nm line of a CW He-Cd laser as the excitation source. A liquid helium cooled cold finger was used for sample cooling to allow measurements ranging from 4 K to room temperature. Figure 6.7 shows the bandedge PL of the two samples at selected temperatures. It can be seen that at 4 K the PL of these ZnO samples is dominated by donor bound exciton emission. Even though the emission is dominated by I_9 at 3.3594 eV, free exciton emission can also be seen, especially for the annealed sample. The observation of phonon replicas on both samples suggests that they have high crystalline quality. There is a slight red shift of the I_9 peak and the phonon replica features on the as grown sample, suggesting that the as grown sample was strained and annealing led to a more relaxed epilayer. For both samples, the near bandedge emission (NBE) can be attributed mainly to the following lines: I_9, I_4, I_1/I_0 and X_A [155]. However for the as grown sample, the I_9 dominance is much stronger and dominates the NBE even at room temperature. This is different from the annealed sample which has a stronger free exciton emission that starts to dominate above 100 K. The more defined excitonic complexes of the annealed sample confirm the improved optical quality of the sample upon annealing.

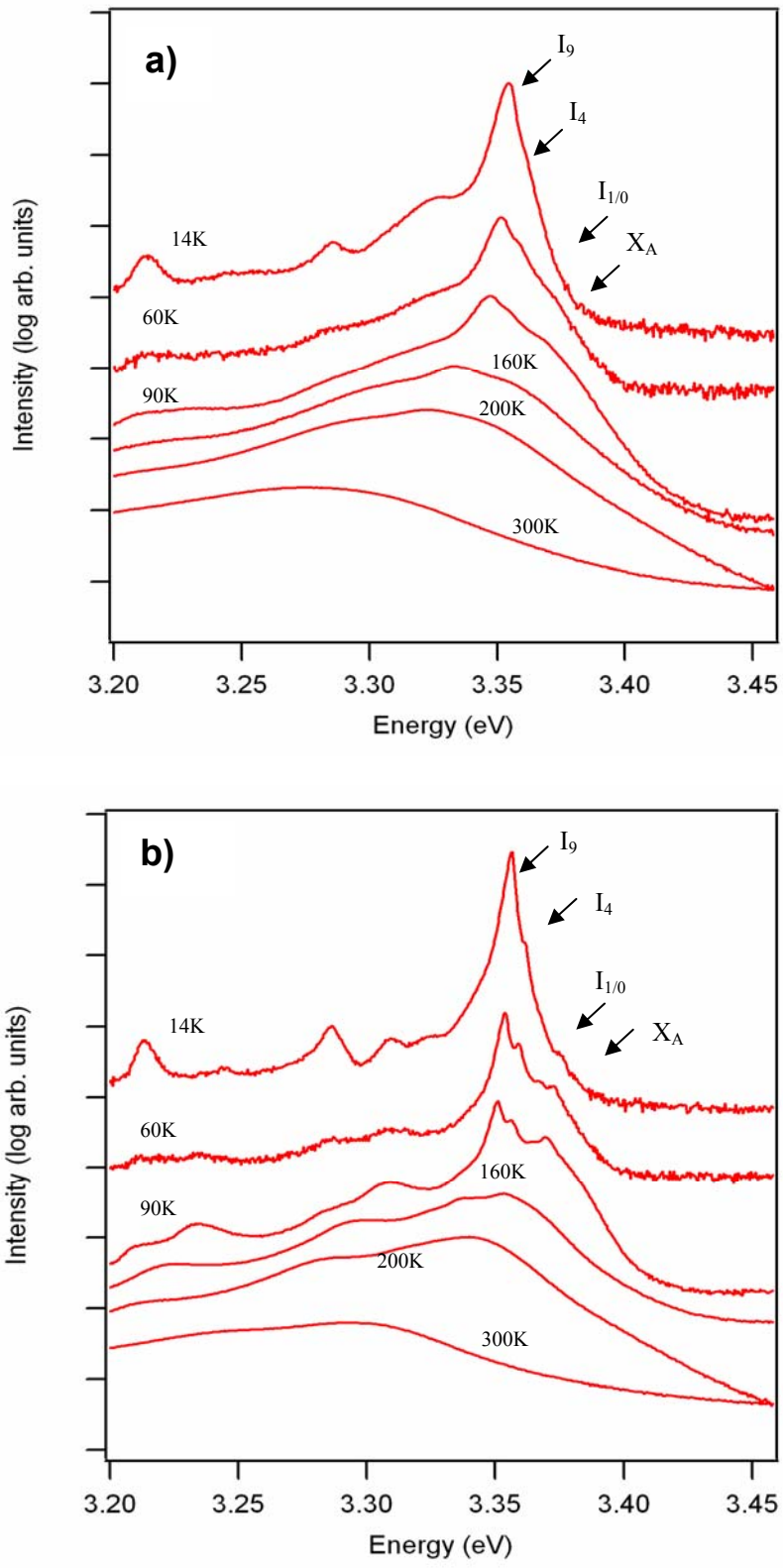

Figure 6.7 The temperature dependent PL of a) sample A as grown and b) sample A annealed (at 750 °C) showing the dominance of different excitonic features. Peak assignment is based on Meyers et al. [155]

To extract the radiative lifetime and non-radiative lifetime from the two samples, the integrated intensity of the NBE from 3.0 eV to 3.4 eV was taken as the radiative emission intensity for each temperature. Assuming the quantum efficiency at 4 K is approximately equal to unity, the radiative lifetime was calculated for both the as grown and annealed sample A according to Equation 6.5. Figure 6.8 shows the radiative lifetime of the as grown and annealed sample extracted from the PL lifetime. It can be seen that the radiative lifetime increased with temperature, and extended into the nanosecond range. Comparing this to the actual PL lifetime, it is evident that at the lowest temperatures the recombination process is dominated by radiative recombination, but as the temperature increases above 50 K, non-radiative processes become dominant.

Comparing the as grown and annealed sample, it can be seen that at low temperature, the annealed sample has a similar radiative lifetime to that of the as grown sample, while at higher temperatures the radiative lifetime of the annealed sample becomes substantially higher, with a maximum of 19 ns at room temperature compared to 6 ns for the as grown sample. Furthermore, there is a visible jump in the

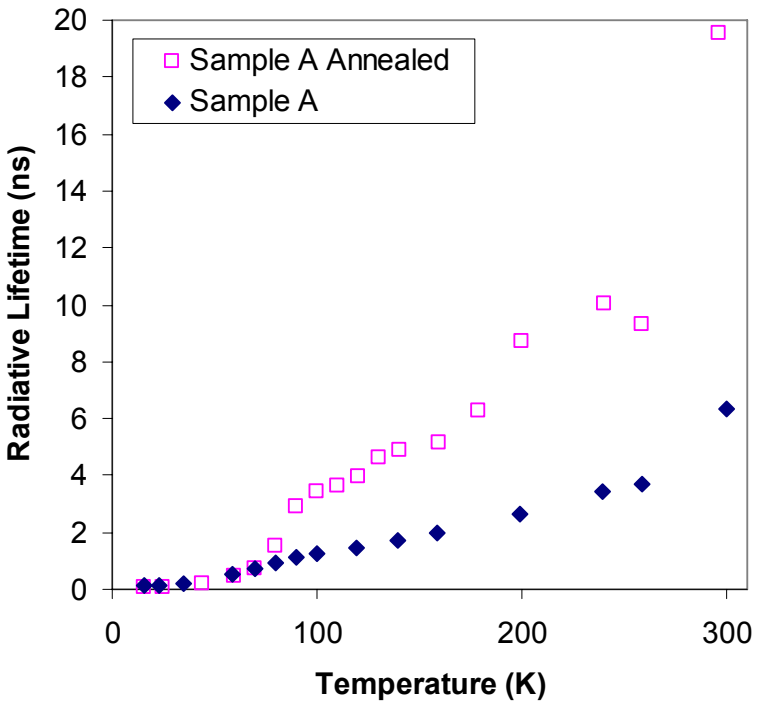

Figure 6.8 The variation of radiative lifetime with temperature as extracted from the PL lifetime and the temperature dependent PL for sample A as grown and sample A annealed.

temperature dependent trend of the annealed sample in the region around 80 K to 90 K, while the radiative lifetime of the as-grown sample followed essentially the same trend throughout the temperature range.

There are two methods that are in common usage for modelling radiative lifetime. The first method is derived from the first principal theory of carrier recombination. This modelling method, known as the spontaneous recombination rate model, has been used on a number of materials, including GaN and InN [248, 249, 256]. The spontaneous recombination rate model originated from the dependence of the spontaneous recombination rate of carriers R on temperature, given by [257]:

$$R = \frac{4Ne^2 E_g}{m^2 \hbar^2 c^3} \left(\frac{2\pi\hbar^2}{mkT} \right)^{3/2} \langle M \rangle np \qquad (6.6)$$

where N is the index of refraction, $\langle M \rangle$ is the optical matrix element related to the band structure and n and p are the electron and hole concentrations, respectively. Equation 6.6 is often simplified to $R = Bnp$, where B is known as the radiative recombination coefficient. The equation suggests that B has a $T^{3/2}$ dependence for non degenerate semiconductors. For an excited semiconductor, the net difference in the spontaneous emission rate is given by

$$R_{net} = B(n_0 + \Delta n)(p_0 + \Delta p) - Bn_0 p_0 \qquad (6.7)$$

where n_0 and p_0 are the electron and hole concentrations at thermal equilibrium, respectively (i.e. background concentration) and Δn and Δp are the photocarriers produced by the excitation. By assuming $\Delta n = \Delta p << n_0 + p_0$, one can rewrite Equation 6.7 as

$$R_{net} = B(n_0 + p_0)\Delta p \qquad (6.8)$$

Assuming that all of the excited carriers recombine radiatively, this net recombination rate would then be the decay rate of the excited carrier density N_e, i.e. $R_{net} = -dN_e/dt$. Solving for N_e gives $\Delta N_e(t) = \Delta N_{e0} \exp(-B(n_0 + p_0)t)$, giving a radiative lifetime:

$$\tau_{rad} = \frac{1}{B(n_0 + p_0)} \tag{6.9}$$

Equation 6.9 applies for non-degenerate semiconductors where the carrier dynamics are governed by electrons and holes. Modification of the same approach is necessary for materials such as ZnO where excitons are important. Im et al. has addressed this issue by assuming an equilibrium between excitons and free carriers upon excitation [248]. The total amount of excited carriers is given by $\Delta N_e = \Delta n + \Delta n_x$ where Δn is the number of excess free carriers, and Δn_x is the density of excitons produced. One can formulate a differential equation similar to the free carrier case by assuming separate radiative coefficients, B_f for free carriers and B_x for excitons:

$$\frac{d\Delta N_e}{dt} = -B_f(n_0 + \Delta n)\Delta p - B_x \Delta n_x \tag{6.10}$$

Note that the terms for thermal equilibrium (i.e. under no excitation) are omitted here as for n-type material, $p_0 \sim 0$ and therefore no excitons exist under thermal equilibrium. The equilibrium between exciton and free carrier population is related to the dissociation of the exciton by the mass-action law [248]:

$$\frac{(n_0 + \Delta n)\Delta p}{\Delta n_x} = CT^{3/2} exp(-E_x / kT) \tag{6.11}$$

where C is a constant related to the electron and hole mass, and E_x is the binding energy of the exciton. The right hand side of the equation is time independent and therefore can be regarded as an exciton dissociation constant D. Again by assuming $\Delta n = \Delta p << n_0 + p_0$, one can rearrange Equation 6.11 to get

$$n_0 \Delta n = D \Delta n_x \tag{6.12}$$

Solving for ΔN_e gives,

$$\Delta N_e = \Delta N_{e0}\, exp(-\frac{B_f D + B_x}{D+1} t) \tag{6.13}$$

yielding

$$\tau_{rad} = \frac{D+1}{B_f D + B_x} \qquad (6.14)$$

Equation 6.14 predicts that the radiative lifetime is dependent on the efficiency of the recombination of the free carrier and the free exciton, as well as the dissociation of the exciton into free carriers. If D << 1 and $B_f D << B_x$, then $\tau_{rad} \propto T^{3/2}$ as B_x is expected behave similarly to B_f [248]. The extent of deviation of the data from a $T^{3/2}$ trend is therefore an indication of the importance of free carrier recombination in the exciton - free carrier system.

Figure 6.9 shows a $T^{3/2}$ fit to the radiative lifetime of sample A, both as grown and annealed. For the as grown sample, a good fit was achieved, suggesting that the dissociation of excitons is limited in MBE grown ZnO thin films. This is consistent with the extremely high exciton binding energy of ZnO compared to other semiconductors, and explains the difference between the trend observed here and that observed by Im et al. for GaN [248]. Note that according to Equation 6.14, the radiative lifetime, and hence the exciton recombination rate, is independent of the

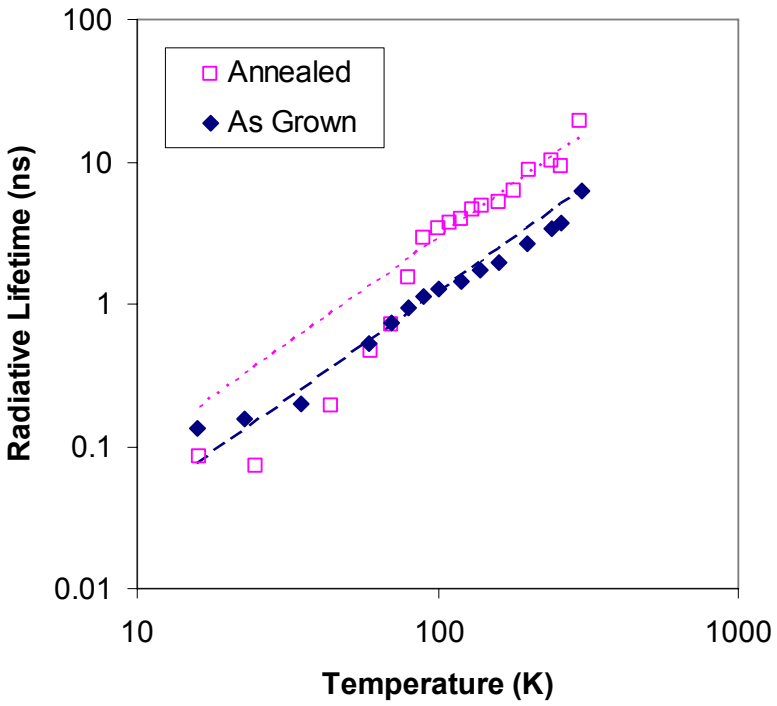

Figure 6.9 Radiative lifetime for as grown and annealed sample A as modelled using $T^{3/2}$ from the spontaneous recombination model (dashed lines), showing good agreement for both samples at high temperature. The deviation from $T^{3/2}$ at low temperature is possibly an artefact from the variation in peak dominance in that region.

background carrier concentration. This is expected as the exciton recombination is dependent on the exciton concentration, and the change in the background carrier concentration in the material would not affect the exciton concentration as the exciton formation is limited by the excess hole concentration. This is unlike free carrier recombination where the possibility of a hole generated by the excitation recombining with an electron is dependent on the total number of free electrons available.

Examining the annealed sample, it can be seen that it is not as closely fitted by the $T^{3/2}$ model. While the model fits the experimental data very well above 100 K, for data below 100 K, a change in slope can be seen. While a deviation from the $T^{3/2}$ behaviour can be due to an increase in the importance of exciton dissociation and free carrier recombination according to Equation 6.14, it is unlikely that the exciton dissociation would increase with reduced temperatures. A more plausible explanation would be related to the fact that the NBE is a combination of bound and free excitonic states and the observed lifetime is therefore affected by a number of different radiative coefficients. At very low temperatures, the NBE is overly dominated by the donor bound exciton peak I_9. In this region, the radiative lifetime is roughly proportional to $T^{3/2}$. In the region ~40 K to 90 K, this dominance shifts gradually from I_9 to the free exciton with a combination of other bound excitonic states dominating the emission in between, resulting in a different temperature dependence. Above 90 K, the free exciton becomes dominant, and the effective B_x becomes proportional to $T^{3/2}$ again. For the as grown sample, since I_9 dominates over the whole temperature range, the deviation from $T^{3/2}$ is minimal.

From this model, it can be seen that the longer radiative lifetime for the annealed sample compared to the as-grown sample at high temperatures is due to a decrease in the radiative coefficient B_x of the exciton system, which implies a decrease in radiative recombination efficiency. One can attribute this decrease in radiative efficiency to a difference in crystal quality. However, it is also possible that this decrease in radiative efficiency is in fact the difference in the recombination efficiency of free and bound excitons, as it was observed that free exciton emission dominates the high temperature NBE for the annealed sample but not the as grown sample. At low temperature, the two samples have similar radiative lifetime. This suggests that the radiative recombination at low temperature for the two samples originated from the same excitonic state with a similar radiative coefficient.

6.3 Nonradiative Lifetime Modelling

Comparing Figure 6.6 and Figure 6.8, it can be seen that although the radiative lifetime of both the as grown and annealed sample reaches the nanosecond range, the effective PL lifetime remains low at ~ 100 - 200 ps. This suggests that the carrier recombination process is dominated by non-radiative recombination, at least for these sample. Figure 6.10 shows the non-radiative lifetime of sample A as-grown and annealed, as calculated from Equation 6.2 using the radiative lifetimes presented in Figure 6.8. It can be clearly seen that the non-radiative lifetime is very long at temperatures below 30 K, with a measured value of 2.0 ns and 2.8 ns at 14 K for sample A as grown and annealed, respectively. This confirms the dominance of radiative recombination at low temperature. As the temperature was increased, the non-radiative lifetime decreased rapidly, dropping below 100 ps by 50 K. Therefore, above 50 K, non-radiative recombination dominates the carrier recombination

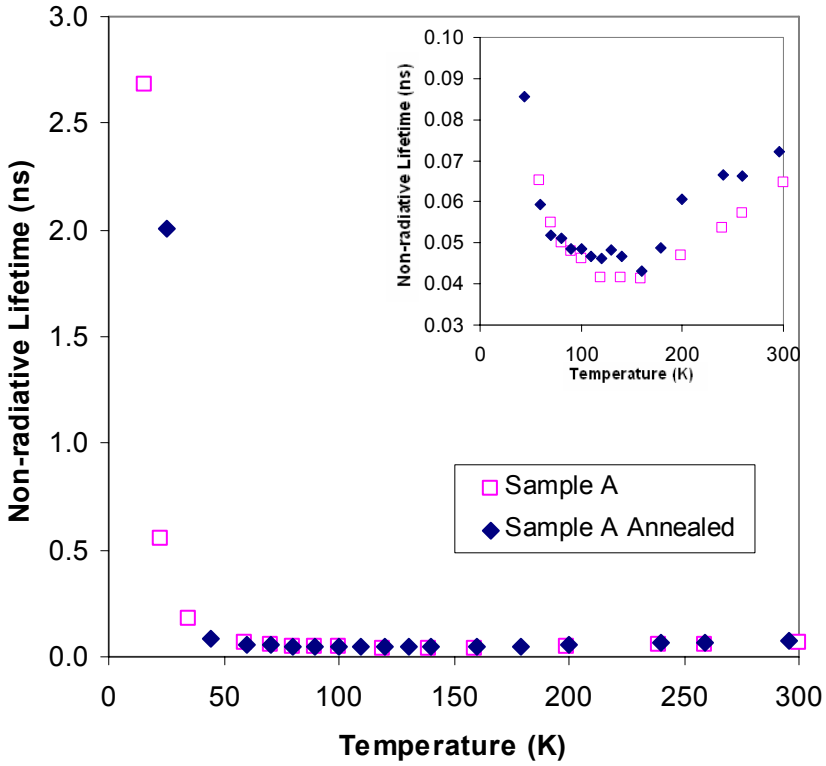

Figure 6.10 Non-radiative lifetime of Sample A as grown and annealed, as extracted from Equation 6.2 and Equation 6.5. The inset shows the non-radiative lifetime at high temperatures, which are much shorter than that measured for temperatures below 50 K.

process in ZnO thin films. This is confirmed by the very similar values between the non-radiative lifetime observed here and the effective lifetime measured for the two samples (c.f. Figure 6.6).

Carriers in a semiconductor can recombine non-radiatively via Auger recombination or Shockley-Read-Hall (SRH) recombination. Under low level excitation, SRH is the main mechanism governing non-radiative recombination in MBE grown ZnO thin films. SRH recombination is related to traps which are in turn originated from structural defects and impurities in the material. The SRH lifetime due to a single trap at mid-gap is given by [258]:

$$\tau_{trap} = \frac{(n_0 + n_1)\tau_{p0} + (p_0 + p_1)\tau_{n0}}{n_0 + p_0} \qquad (6.17)$$

where $\tau_{p0} = (V_p \sigma_p N_t)^{-1}$ and $\tau_{n0} = (V_n \sigma_n N_t)^{-1}$ are the capture lifetimes for electrons and holes for the trap. $V_{p,n}$, $\sigma_{p,n}$, and N_t are the thermal velocity of the carriers, capture cross-section for the carriers, and the trap density, respectively; p_0 and n_0 are the free carrier concentrations in the material, while n_1 and p_1 are the trapped carrier concentrations, given by $n_1 = N_c \exp(-E_t / k_B T)$ and $p_1 = N_c \exp((-E_g + E_t) / k_B T)$ where E_t is the trap level relative to the conduction band.

Equation 6.17 assumes that the excess carrier concentration is negligible. Since the samples considered here are n-type like most ZnO, and the intrinsic carrier concentration is negligible, $p_0 \approx 0$. Thus the equation can be simplified to:

$$\tau_{trap} = \frac{(n_0 + n_1)\tau_{p0} + p_1\tau_{n0}}{n_0} \qquad (6.18)$$

Note that this equation is applicable to one mid-gap trap and describes a lifetime originated from successive trapping of an electron and a hole or vice versa. If there is more then one trap present, then each trap has an associated lifetime dependent on the different capture cross-section and/or the trap energy. The overall SRH lifetime would therefore be:

$$\tau_{SRH} = \left(\frac{1}{\tau_{trap1}} + \frac{1}{\tau_{trap2}} + \frac{1}{\tau_{trap3}} + ...\right)^{-1} \qquad (6.19)$$

It is interesting to note that unlike radiative recombination, the Shockley-Read-Hall recombination is still valid for excitonic systems. That is because a trapped hole in an exciton would recombine with any electrons that become trapped in the same trap and vice versa, and hence the recombination rate is dependent on both the trap concentration and the background carrier concentration [258].

Figure 6.11 shows the non-radiative lifetime of the as grown and the annealed sample above 50 K, and the theoretical fit of τ_{nr} using 1 electron trap, 1 hole trap, and 1 electron and 1 hole trap, by using previous Hall measurements on these samples (as described in Chapter 5) and assuming a single donor model. In the modelling procedure, a number of values such as the capture cross-section for electron and holes, the trap concentrations and trap energy levels were adjusted within a reasonable range to obtain a best fit. While this is a crude method for obtaining the precise values of these parameters, it is nevertheless an effective way to observe the general trend under each proposed model.

It can be seen from Figure 6.11 that the increase of lifetime towards high temperatures can be explained either by a single electron trap model or a two trap model, while the single hole trap model can be ruled out. However, it can be seen that a two trap model provided a better fit to the data. Furthermore, the 1 electron trap model required an electron trap at ~0.04 eV, previously unreported, whereas the two trap model required a shallow electron trap at ~0.065 eV, which was previously reported in the literature [259]. The two trap model also suggests the existence of a previously unreported deep hole trap at ~0.1 eV. The corresponding trap concentration is approximately 5 - 7×10^{16} cm^{-3} for both electron and hole traps, with a slightly different capture cross-section value for each trap. The data for the annealed sample is very similar to that for the as grown sample, but noisier. It was observed from the data that the annealing does not change the non-radiative lifetime. Considering that the room temperature carrier concentration has been shown to decrease upon annealing as seen from Chapter 5, this suggests that the annealing process increases the trap concentration, and results in the same if not shorter non-radiative lifetime compared to the as grown sample.

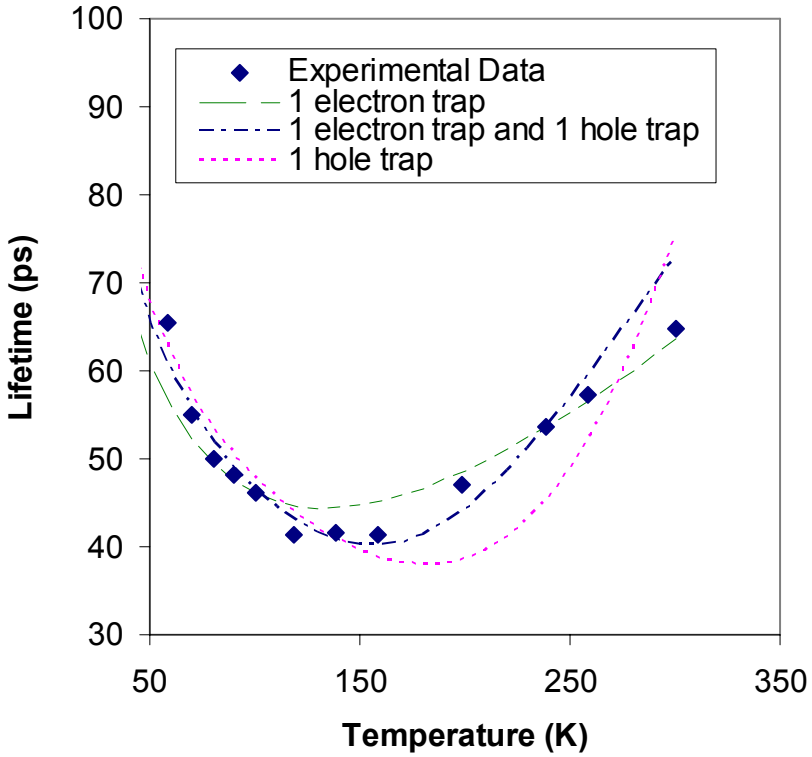

Figure 6.11 The fitting of the non-radiative lifetime of the as grown sample A using the SHR model with 1 electron trap, 1 hole trap, and 1 electron and 1 hole trap. It can be seen that the best fitting can be obtained using both an electron and a hole trap.

Note that the model suggests that an increased trap density would reduce the overall PL lifetime given that non-radiative recombination is dominant. Applying this to sample M (Figure 6.4) shows that sample M has a high density of traps compared to the other samples measured in this study. This is consistent with the low mobility and high PPC observed for the sample as described in Section 4.3. From this, it can be seen that the non-radiative lifetime can provide an alternative measure of the carrier mobilities in a sample. Below 50 K, the non-radiative lifetime increases in a super exponential manner with decreasing temperature, suggesting a freeze out of carriers. This increase cannot be adequately modelled by the SRH equations. One possible explanation is that at these low temperatures, the carrier concentration is so low that the injected carrier density is no longer negligible. Figure 6.12 shows the SRH fit for the as grown sample for the whole temperature range, showing the effect of the 1×10^{15} cm^{-3} injected carrier density, which corresponds to a ~1 mm excitation spot size. The extremely good fit gives evidence to the validity of this model, and suggests that the injected carriers become important below 50 K.

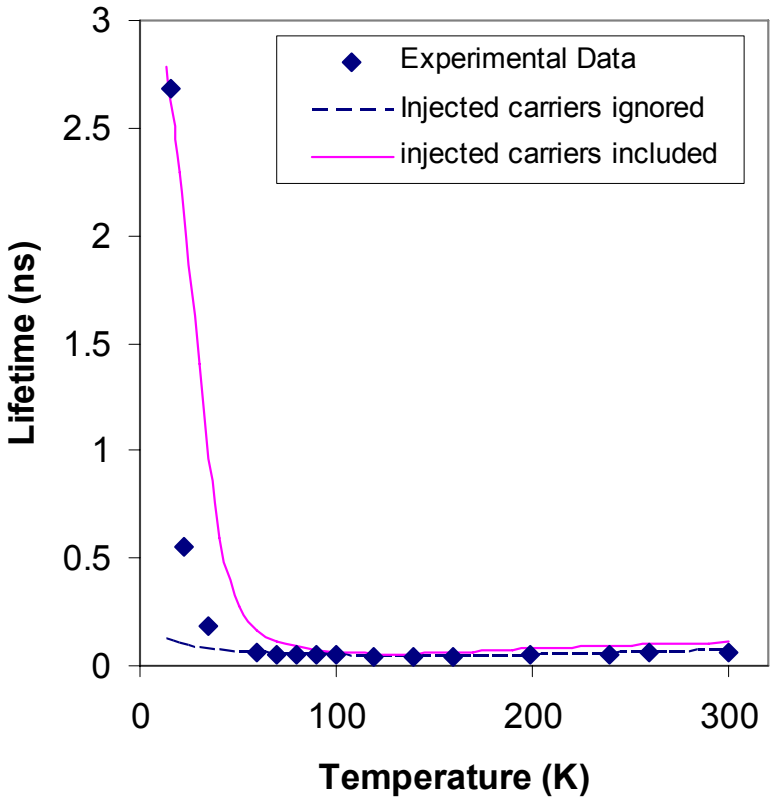

Figure 6.12 Fitting of the non-radiative lifetime of sample A as grown showing the importance of the injected carrier concentration at low temperature.

The analysis above explains the curvature observed in the temperature variation of the PL lifetime. However, from Figure 6.3 it was observed that not all samples showed a curved PL lifetime variation with temperature. In particular, two samples showed a monotonic increase in PL lifetime with temperature. It should also be noted that for both of these samples, the lifetime values are very low. As seen in the modelling above, the carrier freeze out with temperature is expected to result in an increase in the PL lifetime at the lowest temperatures, given that non-radiative recombination dominates the carrier recombination process. Therefore, the low lifetime observed at low temperatures for these two samples suggests that either the trap density is sufficiently high that trap filling through carrier freeze out does not reduce the non-radiative pathways available; or that radiative recombination is dominant for all temperatures.

Considering that the PL intensity decreases substantially with temperature, it is unlikely that the second case is true. In fact, analysis with temperature dependent PL shows that even though the PL lifetime of these samples follows a monotonic trend

with temperature, the radiative lifetime still obeys the $T^{3/2}$ trend, and the non-radiative lifetime still shows a curved trend with the injected carriers dominating at the lowest temperature. However, only a small variation in τ_{nr} was observed for these samples from 50 K to 300 K. This suggests that the carrier recombination of the sample is still governed by Equations 6.13 and 6.17. This means that the available trap density has minimal change with temperature. Note that Hall effect measurements have shown that these samples have a reduced carrier density compared to the other samples. Therefore, it is possible that the actual carrier density in the bulk of these samples is sufficiently low that a large density of empty traps still remains even upon carrier freeze out, providing sufficient pathways at all temperatures to sustain a temperature independent non-radiative recombination rate.

The results in this chapter show that by using TRPL, the behaviour of excited carriers in ZnO thin films can be studied more thoroughly. It was found that for ZnO thin films, radiative recombination due to spontaneous radiative recombination of excitons and non-radiative recombination through Shockley-Read-Hall processes are the dominant recombination processes upon excitation. Due to a high exciton binding energy the radiative recombination in ZnO is dominated by excitonic processes rather than free carrier recombination. Therefore, the radiative lifetime gives an indication of the excitonic dynamics of the ZnO material, and provides an indicator for the optical performance of the material for device purposes. The non-radiative recombination in contrast is affected by free carrier dynamics, and ultimately related not only to the carrier concentration, but also to the mobility. Therefore, non-radiative lifetime measurements can be used to supplement conventional electrical characterisation of ZnO thin films.

Chapter 7

CONCLUSIONS AND FUTURE OUTLOOK

In Chapter 1, it was pointed out that there is a number of issues associated with the development of ZnO optoelectronic devices, and the aim of this research has been to provide insights into solving some of these issues. Three main goals of this thesis were identified: to develop a greater understanding of the MBE ZnO growth processes, enabling the universal optimisation of the MBE system and processes for growing high quality ZnO thin films; to optimise the quality of the ZnO epilayers, especially through the reduction of carrier concentration; and to investigate the application of alternative characterisation techniques to overcome some of the limitations of conventional measurements for gaining further understanding of the material properties, in particular, transport and recombination processes. In this concluding chapter, some of the major results are revisited, and their implications on the three main goals of this thesis are discussed.

7.1 Summary of Results

7.1.1 Summary of the Study on Growth Efficiency

The growth efficiency of the ZnO thin films is mainly governed by the net chemisorption rate. This chemisorption rate is dependent on the reactant concentration and temperature. Under O-rich conditions, it was observed that the increase in Zn flux resulted in a direct linear increase in growth efficiency, suggesting that the chemisorption rate is directly proportional to the Zn flux provided. The effect of active oxygen on the chemisorption rate is complicated by the variation of plasma composition with applied RF power, flow and aperture plate design. In particular, it was found that both O^* and O_2^* participated in growth, with the involvement of O_2^* increasing with decreased sidewall interactions from the aperture plate orifices.

However, atomic oxygen remained the dominant growth species in all cases. It was also found that the growth rate is dependent more on the absolute density of the active oxygen species than the relative atomic content of the plasma, as indicated by the increased growth rate observed from the 25 hole. Ionic species do not appear to be involved directly with growth.

The effect of growth temperature on the growth efficiency is associated with its effect on the chemisorption barrier and the desorption rate. It was observed that the growth rate monotonically decreased with increasing growth temperature, suggesting that the chemisorption barrier for the ZnO reaction in a MBE growth process is sufficiently small that increasing the growth temperature simply leads to an increased Zn desorption rate. Therefore, given that enough Zn and oxygen are provided, the growth efficiency in general is not a major problem in the growth of ZnO thin films by MBE.

By comparing the Zn flux required for the saturation of growth rate under different flux ratios, it was observed that under Zn-rich and O-rich conditions, non-stoichiometric incorporation can occur. As a consequence, the dependence of growth rate on Zn flux close to the stoichiometric region becomes non-linear, making the determination of the exact stoichiometric point by growth rate saturation ambiguous. This observation places doubt on the conclusions associated with the flux ratio drawn by previous studies.

7.1.2 Summary on the Study on Growth Quality

The quality of the ZnO thin films grown in this work was mainly affected by the surface diffusion of adatoms during growth and the lattice strain originated from the lattice mismatch between ZnO and sapphire. The surface diffusion of adatoms can be controlled by altering the flux ratio and the growth temperature, whereas the lattice strain can be reduced by the employment of buffer layer systems.

Investigations on the flux ratio suggested that the surface adatom diffusion is at a maximum under Zn-rich conditions due to the increase of Zn adatom mobility with decreasing O adatom concentration. Zn-rich conditions therefore led to films with smoother surfaces and higher crystal quality. An extremely high Zn flux, however, was found to reduce the adatom mobility leading to rough surfaces. O-rich

conditions in contrast result in a limited diffusion growth regime where the Zn adatoms become immobile due to immediate stabilisation, resulting in statistical roughening. ZnO thin films grown under O-rich conditions therefore have irregular surfaces and poor crystal quality.

Investigations on the active oxygen species generated by the RF plasma source suggested that active oxygen affects the growth of ZnO thin films by controlling the flux ratio and providing different active species for growth. In particular, the increased atomic content with applied RF power was found to improve the surface roughness by decreasing the Zn adatom concentration on the surface, thereby moving the growth regime from an island formation regime to a pit formation regime. The increased importance of O_2^* with decreasing sidewall interaction from the aperture plate may have led to increased non-stoichiometric incorporation that resulted in high defect density and poorer crystal quality. There is also evidence to suggest that increasing the plasma ion content would decrease the near band-edge emission and reduce the conductivity of the films. The quality of the ZnO films is also affected by the growth temperature, which directly affects the adatom diffusion as the diffusion rate is directly proportional to the thermal energy provided. As a consequence, ZnO thin films grown at 400 °C are of a very poor quality that approaches polycrystallinity, whereas growing at 750 °C resulted in ZnO thin films with a smooth surface characterised by streaky RHEED patterns.

In contrast to the adatom diffusion, lattice strain is mainly affected by the interaction between the substrate lattice and the thin film crystal lattice. A large lattice mismatch exists between ZnO and c-plane sapphire, inducing a large mismatch strain. This mismatch strain affects the growth of ZnO by severely reducing the wetting of the substrate and by inducing distortions and defects in the ZnO crystal lattice. It was found that even with sufficient wetting, a 2-D ZnO epilayer can only be sustained up to 6 nm. Once the film exceeds this thickness, both the creation of dislocations and the roughening of the surface become dominant strain relief mechanisms which lead to the degradation of optical and electrical quality.

The employment of a homoepitaxial LT-ZnO buffer and heteroepitaxial MgO buffer layer on the sapphire substrate was found to limit the effects of these degradations to a certain extent. The employment of a LT-ZnO buffer was found to suppress dislocation propagation by dislocation pinning. The LT-buffer also improved the substrate wetting. These led to ZnO thin films with improved surface quality and

optical emission. However, the low temperature growth resulted in an interface layer that is electrically degenerate, leading to degradation in the apparent electrical quality of the film. LT-buffers also have limited effects in reducing the strain of the crystal lattice. In contrast, the employment of an ultra-thin MgO buffer layer (~ 1 nm) was found to significantly reduce the strain in the ZnO crystal lattice, leading to films with a narrower XRD rocking curve, stronger free exciton emission and considerably lower carrier density. By altering the thickness of the MgO buffer, the polarity of the films can also be controlled. However, it was found that these beneficial effects of a MgO buffer are strongly dependent on the coherence of the MgO layer, which is hard to maintain due to the ease of cubic phase formation even at a small thickness.

7.1.3 Transport and Recombination Measurements

The need for alternative methods of measuring the electrical properties of ZnO thin films became apparent when the degenerate layer originated from LT-ZnO buffer growth was observed to alter the Hall effect measurements. As a result, an increased carrier concentration and decreased mobility was observed, inconsistent with the improved crystal quality observed for the samples. To provide a true measure of the electrical quality of the films grown in this work, the variable magnetic field Hall effect was employed to study buffer layer and bulk conductivity in the ZnO thin films.

By applying the variable magnetic field Hall effect technique on selected films, it was found that two types of electrons are present in most ZnO films grown in this work. One of these is the degenerate electron population originated from the interface/buffer layer, while the other originated from the bulk of the high quality ZnO epilayer. The bulk electron has a mobility of ~120 - 150 cm^2/Vs in reasonably high quality as grown samples, comparable to the best MBE grown materials reported in the literature. Upon annealing at 750 °C the bulk electron mobility increased to ~120 - 225 cm^2/Vs, approaching the value reported for commercial ZnO substrates. The electron concentration was also reduced by almost two orders of magnitude as a result of annealing. Comparing these results to the values obtained from conventional (single magnetic field) Hall effect measurements, it is clear that at least when a low temperature buffer layer is employed, conventional electrical measurements do not

give a true representation of the quality of the HT-epilayer and instead are dominated by interfacial layers with a high density of defects.

In moving a semiconductor material towards device quality, particularly for optoelectronic applications, recombination is just as important as transport properties. TRPL was found to be useful in measuring the dynamic behaviour of the carriers in ZnO epilayers. It was found that for most samples, the PL decays in a single exponential style. A typical PL lifetime of ~ 70 ps was measured at room temperature, although some samples have a lifetime of up to ~ 150 ps at room temperature. This figure increases to a maximum of ~ 200 ps as the temperature is decreased to 14 K. These PL lifetime values are comparable to that observed previously in ZnO thin films, but is much shorter than the lifetime (~ 1 ns) reported in bulk ZnO material which exhibits a biexponential decay. Combining steady-state PL and TRPL the radiative lifetime and non-radiative lifetime of several samples were extracted and examined in detail. It was found that the radiative lifetime is independent of the residual carrier concentration of the ZnO thin films, and can reach up to ~ 10 ns at 300 K in as-grown samples. Annealing increases this value to ~ 19 ns. The radiative lifetime of both as grown and annealed sample showed a $T^{3/2}$ dependence with temperature, suggesting that both samples are of high quality with excitonic recombination dominating the radiation process. However, it was also found that the radiative lifetime only dominates recombination when the temperature is below 50 K. Above 50 K the non-radiative lifetime dominates, resulting in the low PL lifetime observed. The non-radiative recombination in the ZnO thin films studied can be modelled by SRH recombination model with a ~ 0.065 eV electron trap and ~ 0.1 eV hole trap. The non-radiative lifetime increases exponentially below 50 K due to carrier freeze out, which again confirms the non-degenerate nature of the HT-ZnO epilayer.

7.2 Implications of Findings

7.2.1 The Optimisation of a ZnO MBE System

It was seen throughout this work that the growth of ZnO thin films can be affected by many system dependent variables. These system related issues must be

taken into account when building an MBE system optimised for ZnO growth. For example, one of the most significant results from this study is the importance of plasma composition. It was found that an oxygen plasma for ZnO growth should optimally have high atomic density and low molecular density to improve the growth efficiency and film quality, as well as a controllable ionic density for better control of the residual carrier concentration. Therefore, the optimised growth system should have a plasma source that is designed to operate at low flow rate to increase the cracking efficiency, and high power for an increased atomic oxygen generation. The plasma aperture plate should have a large number of small holes such that the operating region is large enough for the plasma to operate in a range of conditions. This will allow the atomic oxygen content to be finely tuned by adjusting both the RF power and the flow rate. The plasma source should also ideally have an ion deflection plate with controllable voltage to finely control the amount of ions that reach the growing film surface.

Additionally, in order to avoid source oxidation, the Zn must be provided through a Zn effusion cell with a crucible covered with an aperture plate. This requires a dual-zone heating design in order to minimise aperture clogging. The plate must also be made as thin as possible to retain the Zn flux uniformity. The system should also have an oxidation resistant substrate heater that allows growth and annealing to at least 750 °C, the highest temperature at which high quality ZnO was obtained in this work. The substrate manipulator, heater feedthrough and thermocouple designs should be mechanically simple and robust, and physically isolated from each other, such that movements of different parts and oxide coating deposited during growth will not interfere with the temperature measurements. Above all, the system should have both an ion pump and a turbomolecular pump to maintain a low base pressure and enable safe evacuation of process gases during growth.

The system should also provide various in-situ monitoring that allow better control of the growth of buffer layer systems, an essential growth step for high quality ZnO films. For example, the installation of an oxidation resistant RHEED system will allow better control of the thickness and integrity of MgO buffer layers. It is also recommended that the system should be designed such that LRI can be used in every experiment to monitor the bulk ZnO growth. For example, a fixed laser and detector mount will allow more meaningful comparison between LRI data from different growth experiments; a high transmittance laser port normal to the substrate will

reduces noise in the data; and a heater at the laser port will be useful for preventing oxide coating which could interfere with the LRI experiments. It is also desirable to have an alternative, non-contact temperature measurement system, such as BandIT, to confirm and monitor the real time temperature variation.

7.2.2 The Optimisation of Film Properties

It was found in this work that for the growth of ZnO thin films by MBE, the optimisation of the growth quality is much more important than the optimisation of the growth efficiency, and has to be given more consideration as it is expected that the optimisation of growth efficiency would sacrifice the film quality. In particular, it is expected that the optimisation of the MBE growth of ZnO on sapphire will involve the maximisation of surface adatom diffusion during growth, minimising strain propagation, while maintaining a reasonable net deposition rate.

Results on the effect of flux ratio in this work showed that the surface adatom diffusion can be maximised by growing in a Zn-rich regime. Results also suggested that the optimised flux ratio is provided by a Zn-rich condition with high atomic oxygen flux to control the behaviour and concentration of Zn adatoms. It was observed that a high growth temperature can also improve the surface diffusion rate. However, due to problems encountered with the substrate temperature measurements, this work does not clearly give the optimal growth temperature for ZnO thin films. Therefore, the optimisation of the growth temperature is one of the most important factors to consider for growth optimisation in the near future.

The reduction of strain propagation can be achieved without using an alternative substrate by using different buffer layer systems. However, the effectiveness of these buffer layer systems depends heavily on the buffer layer quality. In particular, it was found that with unoptimised MgO buffer layer and/or LT-ZnO buffer layer, the resulting film can be dominated by undesirable structural and point defects. The optimisation of buffer layers is therefore another important step in growth optimisation.

The optimal thickness of a MgO buffer layer was found to be ~ 1 nm, or just below the critical thickness for the hexagonal to cubic transition of the MgO layer. It is also known that a low MgO deposition rate, which allows a higher diffusion rate, is

required for a coherent MgO interface. The effect of temperature and Mg/O ratio on the MgO buffer quality is not well understood. However, based on the results of ZnO from this work, some speculations on their effects can be made. For example, because of the relatively smaller lattice mismatch between MgO and sapphire, it is expected that a higher temperature may be used to increase the surface diffusion without encountering a wetting problem. A Mg-rich condition may also be more beneficial based on the effect of flux ratio on ZnO layers. Ultimately, the optimisation of these two variables will be essential for the optimisation of MgO buffer layer growth.

The optimisation of the LT-ZnO buffer will involve the optimisation of the thickness, growth temperature, as well as the Zn flux used. The optimal thickness is expected to be below 60 nm and above 6 nm, whereas the optimisation of the growth temperature will involve the determination of the maximum temperature that ZnO can be deposited directly on sapphire in a 2-D fashion. A different Zn flux than the HT-ZnO growth is likely to be needed for the buffer layer to maintain a Zn-rich condition without an over-concentration of Zn adatoms due to the low substrate temperature. The LT-ZnO buffer will also benefit from a low deposition rate.

While it is obvious that further optimisation is needed to obtain the perfect material, results from this study provides a starting point for researchers interested in the growth of high quality ZnO thin films. In particular, the following guidelines for the growth of ZnO on sapphire by MBE can be deduced from this study:

1. Deposit under Zn rich condition.
2. Deposit at high RF power.
3. Maximise atomic oxygen flux and minimise molecular oxygen flux.
4. Operate plasma with a controllable deflection plate to control ion density.
5. Deposit at high temperature - up to 750 °C.
6. Deposit with a ultra thin MgO buffer (up to 1 nm) follow by a low temperature ZnO buffer layer prior to high temperature deposition.

7.3 Recommended Future Work

This work has provided valuable insights into the major issues that are surrounding the development of ZnO epilayers and devices. From these insights new

research directions can be identified. In particular, the future of ZnO thin film researches, based on the observations in this thesis, is expected to be associated with two major areas: alternative substrate and buffer layer structures, and p-type doping and devices (both junction and non junction based).

It was observed in this work that even with employment of buffer layers, the strain and resulting dislocations can still lead to undesirable effects on the optical and electrical properties of the ZnO thin films. Therefore, the use of alternative substrates that are more lattice-matched to ZnO will play an important part in the future investigation of ZnO thin films. In particular, while exotic and hard to obtain substrates such as SCAM and $MgAlO_4$ have shown promising results, more common substrates such as a-plane sapphire and r-plane sapphire are being investigated as possible alternative substrates for ZnO epitaxial growth, due to the lower lattice mismatch and the absence of surface polarity. For example, initial investigations on the growth of ZnO on r-plane sapphire (as part of this work) showed clear terrace formations, with a dominance of free excitonic emission even at low temperature. It is expected that the achievable quality under optimised conditions will surpass that achievable by c-sapphire substrates. The use of homoepitaxy for ZnO growth has also become increasingly common despite the high cost of commercial ZnO substrates, as it is expected to eliminate many heteroepitaxy associated problems. Successful homoepitaxial growth of ZnO will open up new opportunities for different device applications in the near future.

Apart from reducing the lattice mismatch, it may also be desirable to further investigate other techniques or processes that can possibly offer better strain relaxation than the use of buffer layers. For example, twin formation may possibly be used as an alternative strain relief mechanism to dislocation formation. By promoting the formation of twin crystals using a substrate that exerts a tensile stress on the ZnO lattice, the dislocation density can possibly be reduced without sacrificing the electrical quality. The applications of other surface modifications such as epitaxial lateral overgrowth may also be a promising route to dislocation free ZnO thin films.

The doping of ZnO remains a critical issue, as researchers are still struggling to understand the formation of both donors and acceptors in ZnO material. For in-situ doping of ZnO by MBE, nitrogen is the most practical dopant because of its abundant availability and it can be easily activated. However, the incorporation of nitrogen into ZnO is problematic. In particular, preliminary investigations on nitrogen doping in

this work have shown that a nitrogen concentration $\sim 1 \times 10^{19}$ cm^{-3} can be incorporated at a growth temperature of 650 ºC by using an oxygen plasma mixture with 10% nitrogen. Since not all of the incorporated nitrogen will be activated, this concentration is relatively low. Moreover, it was observed that the concentration stayed virtually constant even with a ten times increase in nitrogen flow, suggesting that the incorporation is limited by the high growth temperature. A possible route to remedy this problem is to use a multiple step growth process where a smooth, undoped high temperature epilayer is grown on the buffer layer prior to the introduction of nitrogen at a low growth temperature to increase nitrogen incorporation while maintaining a reasonable crystal quality.

Apart from p-n junctions, optical and electronic devices can also be formed via other pathways. One of the more common ways to fabricate devices without a p-n junction is to use Schottky contacts, which are commonly used for UV-detectors, solar cells and related light absorption applications. While Schottky contact formation has traditionally been problematic on ZnO thin films, a number of preliminary diodes were successfully fabricated using AgO as the Schottky contact on films grown on a MgO buffer layer, resulting in Schottky barrier heights of almost 1 eV and an ideality factor of 1.2. Unfortunately because of the high resistivity of the films, only a low forward current has so far been obtained, giving a low rectification factor and a small voltage dependent capacitance, thus preventing practical use of these diodes. Nonetheless, further investigations towards the usage of AgO as Schottky diode on MBE ZnO thin films is worthwhile. In particular, the successful and repeatable fabrication of high quality Schottky contacts on ZnO thin films will enable the fabrication of ZnO field effect transistors.

Regardless of the specific devices ultimately realised from ZnO, it is clear in looking to many compound semiconductors already commercialised that the epitaxial growth of ZnO will play an important role. Throughout the course of the present work considerable progress has been made in the development of the growth processes and the understanding of the material. Therefore, while many challenges that still remain, the progress from this work suggests that the future of ZnO epitaxial optoelectronic devices is bright and hopeful.

References

[1] E. F. Schubert, J. K. Kim, H. Luo, and J. Q. Xi, "Solid-state lighting - a benevolent technology," *Reports on Progress in Physics*, vol. 69, pp. 3069-3099, 2006.

[2] D. H. W. Li, T. N. T. Lam, and S. L. Wong, "Lighting and energy performance for an office using high frequency dimming controls," *Energy Conversion and Management*, vol. 47, pp. 1133-1145, 2006.

[3] E. F. Schubert and J. K. Kim, "Solid-state light sources getting smart," *Science*, vol. 308, pp. 1274-1278, 2005.

[4] M. S. Shur and A. Zukauskas, "Solid-state lighting: Toward superior illumination," *Proceedings of the IEEE*, vol. 93, pp. 1691-1703, 2005.

[5] A. Bergh, G. Craford, A. Duggal, and R. Haitz, "The promise and challenge of solid-state lighting," *Physics Today*, vol. 54, pp. 42-47, 2001.

[6] J. Y. Tsao, "Solid-state lighting - Lamps, chips, and materials for tomorrow," *IEEE Circuits & Devices*, vol. 20, pp. 28-37, 2004.

[7] T. Whitaker and R. Steveson, "LED makers reveal performance records and high-power products," in *Compund Semiconductor*, vol. 10, pp18 - 23 December 2004

[8] Dioscorides, *De materia medica*, 1st Century.

[9] T. Koida, S. F. Chichibu, A. Uedono, A. Tsukazaki, M. Kawasaki, T. Sota, Y. Segawa, and H. Koinuma, "Correlation between the photoluminescence lifetime and defect density in bulk and epitaxial ZnO," *Applied Physics Letters*, vol. 82, pp. 532-534, 2003.

[10] J. Weissman and A. Nikischer, "Photographic guide to mineral species," Excalibur Mineral Corporation, New York, 2004.

[11] C. G. Maier and O. C. Ralston, "Reduction equilibria of zinc oxide and carbon monoxide," *Journal of the American Chemical Society*, vol. 48, pp. 364-374, 1926.

[12] J. J. Porter, "Zinc oxide in iron-ores, and the effect of zinc in the iron blast-furnace," *Transactions of the American Institute of Mining and Metallurgical Engineers*, vol. 38, pp. 448-454, 1907.

[13] W. M. Johnson, "Physical factors in the metallurgical reduction of zinc oxide," *Transactions of the American Institute of Mining and Metallurgical Engineers*, vol. 38, pp. 656-663, 1907.

[14] H. Adkins and W. A. Lazisr, "The reactions of the alcohols over zinc oxide catalysts," *Journal of the American Chemical Society*, vol. 48, pp. 1671-1677, 1926.

[15] W. A. Lazier and H. Adkins, "Dehydrogenation and dehydration of alcohols over a zinc oxide catalyst," *Journal of the American Chemical Society*, vol. 47, pp. 1719-1722, 1925.

[16] E. Baur and A. Perret, "On the action of light on dissolved silver salts in the presence of zinc oxide," *Helvetica Chimica Acta*, vol. 7, pp. 910-915, 1924.

[17] H. M. James and V. A. Johnson, "Electron distribution in ZnO crystals," *Physical Review*, vol. 56, pp. 119-119, 1939.

[18] M. L. Fuller, "A method of determining the axial ratio of a crystal from x-ray diffraction data the axial ratio and lattice constants of zinc oxide," *Science*, vol. 70, pp. 196-198, 1929.

[19] R. W. Millar, "The heat capacity at low temperatures of zinc oxide and of cadmium oxide," *Journal of the American Chemical Society*, vol. 50, pp. 2653-2656, 1928.

[20] P. H. Miller, "The electrical conductivity of zinc oxide," *Physical Review*, vol. 60, pp. 890-895, 1941.

[21] Y. Kubokawa and O. Toyama, "The Electrical Conductivity Change Caused by the Chemisorption of Hydrogen on ZnO, $ZnO.Cr_2O_3$ and $ZnO.MoO_3$," *Journal of Physical Chemistry*, vol. 60, pp. 833-836, 1956.

[22] J. T. C. Vankemenade and R. K. Eijnthoven, "Measurements on Single Barriers in ZnO Varistor Ceramics," *American Ceramic Society Bulletin*, vol. 56, pp. 324-324, 1977.

[23] A. R. Hutson, "Piezoelectricity and Conductivity in ZnO and CdS," *Physical Review Letters*, vol. 4, pp. 505-507, 1960.

[24] O. Yamazaki, T. Mitsuyu, and K. Wasa, "ZnO Thin-Film Saw Devices," *IEEE Transactions on Sonics and Ultrasonics*, vol. 27, pp. 369-379, 1980.

[25] H. Geistlinger, "Electron Theory of Thin-Film Gas Sensors," *Sensors and Actuators B-Chemical*, vol. 17, pp. 47-60, 1993.

[26] D. M. Bagnall, Y. F. Chen, Z. Zhu, T. Yao, S. Koyama, M. Y. Shen, and T. Goto, "Optically pumped lasing of ZnO at room temperature," *Applied Physics Letters*, vol. 70, pp. 2230-2232, 1997.

[27] D. C. Reynolds, D. C. Look, and B. Jogai, "Optically pumped ultraviolet lasing from ZnO," *Solid State Communications*, vol. 99, pp. 873-875, 1996.

[28] T. Fukumura, Y. Yamada, H. Toyosaki, T. Hasegawa, H. Koinuma, and M. Kawasaki, "Exploration of oxide-based diluted magnetic semiconductors toward transparent spintronics," *Applied Surface Science*, vol. 223, pp. 62-67, 2004.

[29] Q. H. Li, Y. X. Liang, Q. Wan, and T. H. Wang, "Oxygen sensing characteristics of individual ZnO nanowire transistors," *Applied Physics Letters*, vol. 85, pp. 6389-6391, 2004.

[30] E. Topoglidis, A. E. G. Cass, B. O'Regan, and J. R. Durrant, "Immobilisation and bioelectrochemistry of proteins on nanoporous TiO2 and ZnO films," *Journal of Electroanalytical Chemistry*, vol. 517, pp. 20-27, 2001.

[31] W. I. Park, J. S. Kim, G. C. Yi, and H. J. Lee, "ZnO nanorod logic circuits," *Advanced Materials*, vol. 17, pp. 1393-1396, 2005.

[32] U. Ozgur, Y. I. Alivov, C. Liu, A. Teke, M. A. Reshchikov, S. Dogan, V. Avrutin, S. J. Cho, and H. Morkoc, "A comprehensive review of ZnO materials and devices," *Journal of Applied Physics*, vol. 98, 041301, 2005.

[33] J. G. E. Gardeniers, Z. M. Rittersma, and G. J. Burger, "Preferred orientation and piezoelectricity in sputtered ZnO films," *Journal of Applied Physics*, vol. 83, pp. 7844-7854, 1998.

[34] M. W. Allen, P. Miller, R. J. Reeves, and S. M. Durbin, "Influence of spontaneous polarization on the electrical and optical properties of bulk, single crystal ZnO," *Applied Physics Letters*, vol. 90, 2007.

[35] M. E. Levinshtein, S. L. Rumyantsev, and M. Shur, *Properties of advanced semiconductor materials: GaN, AlN, InN, BN, SiC, SiGe*. New York: Wiley, 2001.

[36] M. C. Tamargo, *II-VI semiconductor materials and their applications*. New York: Taylor & Francis, 2002.

[37] D. C. Reynolds, D. C. Look, B. Jogai, C. W. Litton, G. Cantwell, and W. C. Harsch, "Valence-band ordering in ZnO," *Physical Review B*, vol. 60, pp. 2340-2344, 1999.

[38] M. Shiloh and J. Gutman, "Growth of ZnO Single Crystals by Chemical Vapour Transport," *Journal of Crystal Growth*, vol. 11, pp. 105-&, 1971.

[39] D. C. Reynolds, C. W. Litton, D. C. Look, J. E. Hoelscher, B. Claflin, T. C. Collins, J. Nause, and B. Nemeth, "High-quality, melt-grown ZnO single crystals," *Journal of Applied Physics*, vol. 95, pp. 4802-4805, 2004.

[40] E. Ohshima, H. Ogino, I. Niikura, K. Maeda, M. Sato, M. Ito, and T. Fukuda, "Growth of the 2-in-size bulk ZnO single crystals by the hydrothermal method," *Journal of Crystal Growth*, vol. 260, pp. 166-170, 2004.

[41] D. Schulz, S. Ganschow, D. Klimm, M. Neubert, M. Rossberg, M. Schmidbauer, and R. Fornari, "Bridgman-grown zinc oxide single crystals," *Journal of Crystal Growth*, vol. 296, pp. 27-30, 2006.

[42] B. T. Khuriyakub, G. S. Kino, and P. Galle, "Studies of Optimum Conditions for Growth of Rf-Sputtered ZnO Films," *Journal of Applied Physics*, vol. 46, pp. 3266-3272, 1975.

[43] Z. K. Tang, G. K. L. Wong, P. Yu, M. Kawasaki, A. Ohtomo, H. Koinuma, and Y. Segawa, "Room-temperature ultraviolet laser emission from self-assembled ZnO microcrystallite thin films," *Applied Physics Letters*, vol. 72, pp. 3270-3272, 1998.

[44] A. Tsukazaki, A. Ohtomo, and M. Kawasaki, "High-mobility electronic transport in ZnO thin films," *Applied Physics Letters*, vol. 88, 2006.

[45] E. M. Kaidashev, M. Lorenz, H. von Wenckstern, A. Rahm, H. C. Semmelhack, K. H. Han, G. Benndorf, C. Bundesmann, H. Hochmuth, and M. Grundmann, "High electron mobility of epitaxial ZnO thin films on c-plane sapphire grown by multistep pulsed-laser deposition," *Applied Physics Letters*, vol. 82, pp. 3901-3903, 2003.

[46] B. J. Jin, S. Im, and S. Y. Lee, "Violet and UV luminescence emitted from ZnO thin films grown on sapphire by pulsed laser deposition," *Thin Solid Films*, vol. 366, pp. 107-110, 2000.

[47] Y. Liu, C. R. Gorla, S. Liang, N. Emanetoglu, Y. Lu, H. Shen, and M. Wraback, "Ultraviolet detectors based on epitaxial ZnO films grown by MOCVD," *Journal of Electronic Materials*, vol. 29, pp. 69-74, 2000.

[48] J. D. Ye, S. L. Gu, S. M. Zhu, T. Chen, L. Q. Hu, F. Qin, R. Zhang, Y. Shi, and Y. D. Zheng, "The growth and annealing of single crystalline ZnO films by low-pressure MOCVD," *Journal of Crystal Growth*, vol. 243, pp. 151-156, 2002.

[49] B. P. Zhang, K. Wakatsuki, N. T. Binh, N. Usami, and Y. Segawa, "Effects of growth temperature on the characteristics of ZnO epitaxial films deposited by metalorganic chemical vapor deposition," *Thin Solid Films*, vol. 449, pp. 12-19, 2004.

[50] C. G. Van de Walle, "Hydrogen as a cause of doping in zinc oxide," *Physical Review Letters*, vol. 85, pp. 1012-1015, 2000.

[51] M. A. Herman and H. Sitter, *Molecular Beam Epitaxy: Fundermentals and Current Status*: Springer, 1996.

[52] S. Ino, "Some New Techniques in Reflection High-Energy Electron-Diffraction (Rheed) Application to Surface-Structure Studies," *Japanese Journal of Applied Physics*, vol. 16, pp. 891-908, 1977.

[53] P. E. H. Nielsen, "Investigation of Surface-Structure by Reflection High-Energy Electron-Diffraction (Rheed)," *Surface Science*, vol. 35, pp. 194-210, 1973.

[54] T. R. Albrecht and C. F. Quate, "Atomic Resolution Imaging of a Nonconductor by Atomic Force Microscopy," *Journal of Applied Physics*, vol. 62, pp. 2599-2602, 1987.

[55] H. J. Leamy, "Charge Collection Scanning Electron-Microscopy," *Journal of Applied Physics*, vol. 53, pp. R51-R80, 1982.

[56] D. L. Smith, "Thin-Film Deposition: Principles and Practices," McGraw-Hill, 1995, pp. 211 - 215.

[57] P. F. Fewster, "X-Ray-Diffraction from Low-Dimensional Structures," *Semiconductor Science and Technology*, vol. 8, pp. 1915-1934, 1993.

[58] M. A. G. Halliwell, M. H. Lyons, and M. J. Hill, "The Interpretation of X-Ray Rocking Curves from III-V Semiconductor-Device Structures," *Journal of Crystal Growth*, vol. 68, pp. 523-531, 1984.

[59] D. C. Look, G. C. Farlow, P. Reunchan, S. Limpijumnong, S. B. Zhang, and K. Nordlund, "Evidence for native-defect donors in n-type ZnO," *Physical Review Letters*, vol. 95, 2005.

[60] D. C. Look, H. L. Mosbacker, Y. M. Strzhemechny, and L. J. Brillson, "Effects of surface conduction on Hall-effect measurements in ZnO," *Superlattices and Microstructures*, vol. 38, pp. 406-412, 2005.

[61] S. B. Zhang, S. H. Wei, and A. Zunger, "Intrinsic n-type versus p-type doping asymmetry and the defect physics of ZnO," *Physical Review B*, vol. 6307, 2001.

[62] Z. Y. Xiao, Y. C. Liu, J. Y. Zhang, D. X. Zhao, Y. M. Lu, D. Z. Shen, and X. W. Fan, "Electrical and structural properties of p-type ZnO : N thin films prepared by plasma enhanced chemical vapour deposition," *Semiconductor Science and Technology*, vol. 20, pp. 796-800, 2005.

[63] X. H. Wang, B. Yao, Z. Z. Zhang, B. H. Li, Z. P. Wei, D. Z. Shen, Y. M. Lu, and X. W. Fan, "The mechanism of formation and properties of Li-doped p-type ZnO grown by a two-step heat treatment," *Semiconductor Science and Technology*, vol. 21, pp. 494-497, 2006.

[64] G. Xiong, J. Wilkinson, B. Mischuck, S. Tuzemen, K. B. Ucer, and R. T. Williams, "Control of p- and n-type conductivity in sputter deposition of undoped ZnO," *Applied Physics Letters*, vol. 80, pp. 1195-1197, 2002.

[65] A. Tsukazaki, A. Ohtomo, T. Onuma, M. Ohtani, T. Makino, M. Sumiya, K. Ohtani, S. F. Chichibu, S. Fuke, Y. Segawa, H. Ohno, H. Koinuma, and M. Kawasaki, "Repeated temperature modulation epitaxy for p-type doping and light-emitting diode based on ZnO," *Nature Materials*, vol. 4, pp. 42-46, 2005.

[66] J. L. Zhao, X. M. Li, A. Krtschil, A. Krost, W. D. Yu, Y. W. Zhang, Y. F. Gu, and X. D. Gao, "Study on anomalous high p-type conductivity in ZnO films on silicon substrate prepared by ultrasonic spray pyrolysis," *Applied Physics Letters*, vol. 90, 2007.

[67] A. Y. Cho and S. E. Stokowsk, "Molecular Beam Epitaxy and Optical Evaluation of A1xga1-Xas," *Solid State Communications*, vol. 9, pp. 565-&, 1971.

[68] A. Y. Cho, "How molecular beam epitaxy (MBE) began and its projection into the future," *Journal of Crystal Growth*, vol. 202, pp. 1-7, 1999.

[69] F. W. Smith, A. R. Calawa, C. L. Chen, M. J. Manfra, and L. J. Mahoney, "New Mbe Buffer Used to Eliminate Backgating in Gaas-Mesfets," *IEEE Electron Device Letters*, vol. 9, pp. 77-80, 1988.

[70] M. Zandian, J. M. Arias, R. Zucca, R. V. Gil, and S. H. Shin, "Hgcdte Double Heterostructure Injection-Laser Grown by Molecular-Beam Epitaxy," *Applied Physics Letters*, vol. 59, pp. 1022-1024, 1991.

[71] J. S. Harris, J. N. Eckstein, E. S. Hellmann, and D. G. Schlom, "Mbe Growth of High Critical-Temperature Superconductors," *Journal of Crystal Growth*, vol. 95, pp. 607-616, 1989.

[72] M. A. Haase, J. Qiu, J. M. Depuydt, and H. Cheng, "Blue-Green Laser-Diodes," *Applied Physics Letters*, vol. 59, pp. 1272-1274, 1991.

[73] J. Faist, F. Capasso, D. L. Sivco, C. Sirtori, A. L. Hutchinson, and A. Y. Cho, "Quantum Cascade Laser," *Science*, vol. 264, pp. 553-556, 1994.

[74] D. C. Tsui, H. L. Stormer, and A. C. Gossard, "Two-Dimensional Magnetotransport in the Extreme Quantum Limit," *Physical Review Letters*, vol. 48, pp. 1559-1562, 1982.

[75] M. A. L. Johnson, S. Fujita, W. H. Rowland, W. C. Hughes, J. W. Cook, and J. F. Schetzina, "MBE growth and properties of ZnO on sapphire and SiC substrates," *Journal of Electronic Materials*, vol. 25, pp. 855-862, 1996.

[76] K. Matsubara, P. Fons, A. Yamada, M. Watanabe, and S. Niki, "Epitaxial growth of ZnO thin films on $LiNbO_3$ substrates," *Thin Solid Films*, vol. 347, pp. 238-240, 1999.

[77] H. J. Ko, Y. F. Chen, Z. Zhu, T. Hanada, and T. Yao, "Effects of a low-temperature buffer layer on structural properties of ZnO epilayers grown on (111)CaF2 by two-step MBE," *Journal of Crystal Growth*, vol. 208, pp. 389-394, 2000.

[78] X. L. Du, M. Murakami, H. Iwaki, and A. Yoshikawa, "Complete elimination of multi-angle rotation domains in ZnO epilayers grown on (0001) sapphire substrate," *Physica Status Solidi a-Applied Research*, vol. 192, pp. 183-188, 2002.

[79] T. Ohgaki, T. Nakata, N. Ohashi, S. Wada, and T. Tsurumi, "Effect of buffer layers on electric property of ZnO thin films," in *Electroceramics in Japan Iv*, vol. 216, *Key Engineering Materials*, 2002, pp. 73-76.

[80] Y. F. Chen, H. J. Ko, S. K. Hong, T. Yao, and Y. Segawa, "Two-dimensional growth of ZnO films on sapphire(0001) with buffer layers," *Journal of Crystal Growth*, vol. 214, pp. 87-91, 2000.

[81] H. Kato, M. Sano, K. Miyamoto, and T. Yao, "Effect of O/Zn flux ratio on crystalline quality of ZnO films grown by plasma-assisted molecular beam epitaxy," *Japanese Journal of Applied Physics Part 1-Regular Papers Short Notes & Review Papers*, vol. 42, pp. 2241-2244, 2003.

[82] K. Sakurai, M. Kanehiro, K. Nakahara, T. Tanabe, S. Fujita, and S. Fujita, "Effects of oxygen plasma condition on MBE growth of ZnO," *Journal of Crystal Growth*, vol. 209, pp. 522-525, 2000.

[83] Y. S. Jung, O. Kononenko, J. S. Kim, and W. K. Choi, "Two-dimensional growth of ZnO epitaxial films on c-Al_2O_3(0001) substrates with optimized growth temperature and low-temperature buffer layer by plasma-assisted molecular beam epitaxy," *Journal of Crystal Growth*, vol. 274, pp. 418-424, 2005.

[84] K. Sakurai, M. Kanehiro, K. Nakahara, T. Tanabe, S. Fujita, and S. Fujita, "Effects of substrate offset angles on MBE growth of ZnO," *Journal of Crystal Growth*, vol. 214, pp. 92-94, 2000.

[85] K. Ogata, K. Sakurai, S. Fujita, S. Fujita, and K. Matsushige, "Effects of thermal annealing of ZnO layers grown by MBE," *Journal of Crystal Growth*, vol. 214, pp. 312-315, 2000.

[86] K. Miyamoto, M. Sano, H. Kato, and T. Yao, "High-electron-mobility ZnO epilayers grown by plasma-assisted molecular beam epitaxy," *Journal of Crystal Growth*, vol. 265, pp. 34-40, 2004.

[87] D. C. Look, D. C. Reynolds, J. R. Sizelove, R. L. Jones, C. W. Litton, G. Cantwell, and W. C. Harsch, "Electrical properties of bulk ZnO," *Solid State Communications*, vol. 105, pp. 399-401, 1998.

[88] C. Swartz and S. Durbin, Private Communication.

[89] K. Iwata, P. Fons, A. Yamada, K. Matsubara, and S. Niki, "Nitrogen-induced defects in ZnO : N grown on sapphire substrate by gas source MBE," *Journal of Crystal Growth*, vol. 209, pp. 526-531, 2000.

[90] D. C. Look, D. C. Reynolds, C. W. Litton, R. L. Jones, D. B. Eason, and G. Cantwell, "Characterization of homoepitaxial p-type ZnO grown by molecular beam epitaxy," *Applied Physics Letters*, vol. 81, pp. 1830-1832, 2002.

[91] F. X. Xiu, Z. Yang, L. J. Mandalapu, D. T. Zhao, J. L. Liu, and W. P. Beyermann, "High-mobility Sb-doped p-type ZnO by molecular-beam epitaxy," *Applied Physics Letters*, vol. 87, 2005.

[92] X. Wang, Y. M. Lu, D. Z. Shen, Z. Z. Zhang, B. H. Li, B. Yao, J. Y. Zhang, D. X. Zhao, X. W. Fan, and Z. K. Tang, "Electrical properties of N-doped ZnO grown on sapphire by P-MBE," *Semiconductor Science and Technology*, vol. 22, pp. 65-69, 2007.

[93] S. M. Durbin, J. Han, S. O, M. Kobayashi, D. R. Menke, R. L. Gunshor, Q. Fu, N. Pelekanos, A. V. Nurmikko, D. Li, J. Gonsalves, and N. Otsuka, "Zincblende MnTe - Epilayers and Quantum Well Structures," *Applied Physics Letters*, vol. 55, pp. 2087-2089, 1989.

[94] I. W. Kim, Y. B. Kwon, J. M. Yi, J. H. Je, G. Nouet, T. Wojtowicz, P. Ruterana, and J. Kioseoglou, "Twin formation in sputter-grown

$ZnO/Al_2O_3(0001)$ epitaxial film: A real time x-ray scattering study," *Journal of Vacuum Science & Technology A*, vol. 22, pp. 2159-2162, 2004.

[95] M. Knudsen, "The maximum rate of vaporisation of mercury," *Annalen Der Physik*, vol. 47, pp. 697-708, 1915.

[96] I. Langmuir, "The vapor pressure of metallic tungsten," *Physical Review*, vol. 2, pp. 329-342, 1913.

[97] M. Knudsen, "The molecular current of gases through openings and the effusion," *Annalen Der Physik*, vol. 29, pp. 999-1016, 1909.

[98] F. F. Coleman and A. Egerton, "A study of the vapour pressures of magnesium, thallium, and zinc, and he determination of their chemical constants," *Philosophical Transactions of the Royal Society of London Series a-Mathematical and Physical Sciences*, vol. 234, pp. 177-204, 1935.

[99] M. Fujita, Private Communication.

[100] P. Clausing, "The flow of extremely diluted gases through tubes of any length," *Annalen Der Physik*, vol. 12, pp. 961-989, 1932.

[101] K. Motzfeldt, "The Thermal Decomposition of Sodium Carbonate by the Effusion Method," *Journal of Physical Chemistry*, vol. 59, pp. 139-147, 1955.

[102] M. A. Herman, "Physical Problems Concerning Effusion Processes of Semiconductors in Molecular-Beam Epitaxy," *Vacuum*, vol. 32, pp. 555-565, 1982.

[103] C. S. Lu, "Mass Determination with Piezoelectric Quartz Crystal Resonators," *Journal of Vacuum Science & Technology*, vol. 12, pp. 578-583, 1975.

[104] V. M. Mecea, J. O. Carlsson, P. Heszler, and M. Bartan, "Development and Testing of a High-Temperature Quartz-Crystal Microbalance," *Vacuum*, vol. 46, pp. 691-694, 1995.

[105] A. Rahtu and M. Ritala, "Compensation of temperature effects in quartz crystal microbalance measurements," *Applied Physics Letters*, vol. 80, pp. 521-523, 2002.

[106] S. Grimshaw, "Increasing the Accuracy of Quartz Crystal Thin Film Thickness Sensors," Technical papers, Virginia Beach Sensors.

[107] M. N. Rocklein and S. M. George, "Temperature-induced apparent mass changes observed during quartz crystal microbalance measurements of atomic layer deposition," *Analytical Chemistry*, vol. 75, pp. 4975-4982, 2003.

[108] A. C. Westerheim, L. S. Yujahnes, and A. C. Anderson, "Off-Axis Magnetron Sputtering of Ybco Films - the Influence of Atomic Oxygen," *IEEE Transactions on Magnetics*, vol. 27, pp. 1001-1005, 1991.

[109] R. J. Spah, H. F. Hess, H. L. Stormer, A. E. White, and K. T. Short, "Parameters for Insitu Growth of High-Tc Superconducting Thin-Films Using an Oxygen Plasma Source," *Applied Physics Letters*, vol. 53, pp. 441-443, 1988.

[110] D. M. Lind, S. D. Berry, G. Chern, H. Mathias, and L. R. Testardi, "Growth and Structural Characterization of Fe_3O_4 and NiO Thin-Films and Superlattices Grown by Oxygen-Plasma-Assisted Molecular-Beam Epitaxy," *Physical Review B*, vol. 45, pp. 1838-1850, 1992.

[111] R. Kita, T. Hase, R. Itti, M. Sasaki, T. Morishita, and S. Tanaka, "Synthesis of Cuo Films Using Mass-Separated, Low-Energy O+ Ion-Beams," *Applied Physics Letters*, vol. 60, pp. 2684-2685, 1992.

[112] D. D. Berkley, B. R. Johnson, N. Anand, K. M. Beauchamp, L. E. Conroy, A. M. Goldman, J. Maps, K. Mauersberger, M. L. Mecartney, J. Morton, M. Tuominen, and Y. J. Zhang, "Insitu Formation of Superconducting Yba2cu3o7-X Thin-Films Using Pure Ozone Vapor Oxidation," *Applied Physics Letters*, vol. 53, pp. 1973-1975, 1988.

[113] T. Shimizu, H. Nonaka, and K. Arai, "Growth-Behavior of $YBa_2Cu_3O_7$-Delta and $NdBa_2Cu_3O_7$-Delta Thin-Films Observed by Electron-Diffraction," *Applied Physics Letters*, vol. 59, pp. 600-602, 1991.

[114] J. D.G. Schlom and J.S. Harris, "MBE Growth of High Tc Superconductors," in *Molecular Beam Epitaxy: Applications to Key Materials*, R. F. C. Farrow, Ed.: Noyes, Park Ridge, 1995, pp. 505-622.

[115] K. Sakurai, D. Iwata, S. Fujita, and S. Fujita, "Growth of ZnO by molecular beam epitaxy using NO_2 as oxygen source," *Japanese Journal of Applied Physics Part 1-Regular Papers Short Notes & Review Papers*, vol. 38, pp. 2606-2608, 1999.

[116] M. Fujita, N. Kawamoto, T. Tatsumi, K. Yamagishi, and Y. Horikoshi, "Molecular beam epitaxial growth of ZnO on Si substrate using ozone as an oxygen source," *Japanese Journal of Applied Physics Part 1-Regular Papers Short Notes & Review Papers*, vol. 42, pp. 67-70, 2003.

[117] A. Bakin, A. El-Shaer, A. C. Mofor, M. Kreye, A. Waag, F. Bertram, J. Christen, M. Heuken, and J. Stoimenos, "MBE growth of ZnO layers on sapphire employing hydrogen peroxide as an oxidant," *Journal of Crystal Growth*, vol. 287, pp. 7-11, 2006.

[118] B. L. VanMil, H. C. Guo, L. J. Holbert, K. Lee, T. H. Myers, T. Liu, and D. Korakakis, "High temperature limitations for GaN growth by RF-plasma assisted molecular beam epitaxy: Effects of active nitrogen species, surface polarity, hydrogen, and excess Ga-overpressure," *Journal of Vacuum Science & Technology B*, vol. 22, pp. 2149-2154, 2004.

[119] J. P. Locquet and E. Machler, "Characterization of a Radio-Frequency Plasma Source for Molecular-Beam Epitaxial-Growth of High-Tc Superconductor

Films," *Journal of Vacuum Science & Technology A-Vacuum Surfaces and Films*, vol. 10, pp. 3100-3103, 1992.

[120] A. J. Ptak, K. S. Ziemer, M. R. Millecchia, C. D. Stinespring, and T. H. Myers, "Influence of active nitrogen species on the nitridation rate of sapphire," *Mrs Internet Journal of Nitride Semiconductor Research*, vol. 4, pp. art. no.-G3.10, 1999.

[121] P. Okeeffe, C. Omorain, S. Den, Y. Hayashi, S. Komuro, and T. Morikawa, "Characterization and in-Situ Monitoring of a Novel Compact Electron-Cyclotron-Resonance Plasma Source," *Review of Scientific Instruments*, vol. 66, pp. 5252-5256, 1995.

[122] Y. Yoshida, Y. Okazaki, K. Ito, and S. I. Mizuguchi, "Production of an Atomic Oxygen Beam by a Nozzle-Beam-Type Microwave Radical Source," *Review of Scientific Instruments*, vol. 66, pp. 4166-4169, 1995.

[123] M. Sarfaty, M. Harper, and N. Hershkowitz, "A novel electro-optical probe to diagnose plasma uniformity," *Review of Scientific Instruments*, vol. 69, pp. 3176-3180, 1998.

[124] C. E. Moore and J. W. Gallagher, *Tables of spectra of hydrogen, carbon, nitrogen, and oxygen atoms and ions*. Boca Raton: CRC Press, 1993.

[125] W. F. Meggers, *Tables of spctral-line intensities*, 2nd ed. Washington D. C.: NBS, U. S. Dept. of Commerce, 1975.

[126] R. W. B. Pearse and A. G. Gaygon, *The identification of molecular spectra*. London: Chapman and Hall, 1976.

[127] D. C. Seo and T. H. Chung, "Observation of the transition of operating regions in a low-pressure inductively coupled oxygen plasma by Langmuir probe measurement and optical emission spectroscopy," *Journal of Physics D-Applied Physics*, vol. 34, pp. 2854-2861, 2001.

[128] J. T. Gudmundsson, A. M. Marakhtanov, K. K. Patel, V. P. Gopinath, and M. A. Lieberman, "On the plasma parameters of a planar inductive oxygen discharge," *Journal of Physics D-Applied Physics*, vol. 33, pp. 1323-1331, 2000.

[129] A. J. Ptak, M. R. Millecchia, T. H. Myers, K. S. Ziemer, and C. D. Stinespring, "The relation of active nitrogen species to high-temperature limitations for (000(1)over-bar) GaN growth by radio-frequency-plasma-assisted molecular beam epitaxy," *Applied Physics Letters*, vol. 74, pp. 3836-3838, 1999.

[130] P. A. Anderson, R. J. Reeves, and S. M. Durbin, "RF plasma sources for III-nitrides growth: influence of operating conditions and device geometry on active species production and InN film properties," *Physica Status Solidi a-Applications and Materials Science*, vol. 203, pp. 106-111, 2006.

[131] P. H. Dawson, "The Quadrupole - System-Design and Residual-Gas Analyzer Performance," *Journal of Vacuum Science & Technology a-Vacuum Surfaces and Films*, vol. 4, pp. 1709-1714, 1986.

[132] B. V. Shanabrook, J. R. Waterman, J. L. Davis, and R. J. Wagner, "Large Temperature-Changes Induced by Molecular-Beam Epitaxial-Growth on Radiatively Heated Substrates," *Applied Physics Letters*, vol. 61, pp. 2338-2340, 1992.

[133] J. M. Depuydt, H. Cheng, J. E. Potts, T. L. Smith, and S. K. Mohapatra, "Growth of Undoped Znse on (100) Gaas by Molecular-Beam Epitaxy - an Investigation of the Effects of Growth Temperature and Beam Pressure Ratio," *Journal of Applied Physics*, vol. 62, pp. 4756-4762, 1987.

[134] J. M. Myoung, O. Gluschenkov, K. Kim, and S. Kim, "Growth kinetics of GaN and effects of flux ratio on the properties of GaN films grown by plasma-assisted molecular beam epitaxy," *Journal of Vacuum Science & Technology A*, vol. 17, pp. 3019-3028, 1999.

[135] H. J. Ko, T. Yao, Y. F. Chen, and S. K. Hong, "Investigation of ZnO epilayers grown under various Zn/O ratios by plasma-assisted molecular-beam epitaxy," *Journal of Applied Physics*, vol. 92, pp. 4354-4360, 2002.

[136] T. E. Murphy, D. Y. Chen, and J. D. Phillips, "Growth and electronic properties of ZnO epilayers by plasma-assisted molecular beam epitaxy," *Journal of Electronic Materials*, vol. 34, pp. 699-703, 2005.

[137] J. W. Dong, A. Osinsky, B. Hertog, A. M. Dabiran, P. P. Chow, Y. W. Heo, D. P. Norton, and S. J. Pearton, "Development of MgZnO-ZnO-AlGaN heterostructures for ultraviolet light emitting applications," *Journal of Electronic Materials*, vol. 34, pp. 416-423, 2005.

[138] F. Vigue, P. Vennegues, S. Vezian, M. Laugt, and J. P. Faurie, "Defect characterization in ZnO layers grown by plasma-enhanced molecular-beam epitaxy on (0001) sapphire substrates," *Applied Physics Letters*, vol. 79, pp. 194-196, 2001.

[139] R. Held, D. E. Crawford, A. M. Johnston, A. M. Dabiran, and P. I. Cohen, "In situ control of GaN growth by molecular beam epitaxy," *Journal of Electronic Materials*, vol. 26, pp. 272-280, 1997.

[140] B. Heying, R. Averbeck, L. F. Chen, E. Haus, H. Riechert, and J. S. Speck, "Control of GaN surface morphologies using plasma-assisted molecular beam epitaxy," *Journal of Applied Physics*, vol. 88, pp. 1855-1860, 2000.

[141] E. J. Tarsa, B. Heying, X. H. Wu, P. Fini, S. P. DenBaars, and J. S. Speck, "Homoepitaxial growth of GaN under Ga-stable and N-stable conditions by plasma-assisted molecular beam epitaxy," *Journal of Applied Physics*, vol. 82, pp. 5472-5479, 1997.

[142] K. Hirano, M. Fujita, M. Sasajima, T. Kosaka, and Y. Horikoshi, "ZnO epitaxial films grown by flux-modulated RF-MBE," *Journal of Crystal Growth*, vol. 301, pp. 370-372, 2007.

[143] Y. Tazoh and S. Miyazawa, "Extremely Smooth Yba2cu3oy Thin-Films Grown Using the Reactive Coevaporation Technique in Radical Oxygen at an Ultralow Growth-Rate," *Applied Physics Letters*, vol. 62, pp. 408-410, 1993.

[144] D. Litvinov, T. O'Donnell, and R. Clarke, "In situ thin-film texture determination," *Journal of Applied Physics*, vol. 85, pp. 2151-2156, 1999.

[145] Y. F. Chen, H. J. Ko, S. K. Hong, T. Yao, and Y. Segawa, "Morphology evolution of ZnO(000-1) surface during plasma-assisted molecular-beam epitaxy," *Applied Physics Letters*, vol. 80, pp. 1358-1360, 2002.

[146] T. E. Murphy, S. Walavalkar, and J. D. Phillips, "Epitaxial growth and surface modeling of ZnO on c-plane Al_2O_3," *Applied Physics Letters*, vol. 85, pp. 6338-6340, 2004.

[147] J. Tersoff and F. K. Legoues, "Competing Relaxation Mechanisms in Strained Layers," *Physical Review Letters*, vol. 72, pp. 3570-3573, 1994.

[148] M. T. Lung, C. H. Lam, and L. M. Sander, "Island, pit, and groove formation in strained heteroepitaxy," *Physical Review Letters*, vol. 95, 2005.

[149] M. Bouville, J. M. Millunchick, and M. L. Falk, "Pit nucleation in the presence of three-dimensional islands during heteroepitaxial growth," *Physical Review B*, vol. 70, 2004.

[150] A. Riposan, G. K. M. Martin, M. Bouville, M. L. Falk, and J. M. Millunchick, "The effect of island density on pit nucleation in In0.27Ga0.73As/GaAs films," *Surface Science*, vol. 525, pp. 222-228, 2003.

[151] P. I. Tamborenea and S. Dassarma, "Surface-Diffusion-Driven Kinetic Growth on One-Dimensional Substrates," *Physical Review E*, vol. 48, pp. 2575-2594, 1993.

[152] F. X. Xiu, Z. Yang, L. J. Mandalapu, D. T. Zhao, and J. L. Liu, "Photoluminescence study of Sb-doped p-type ZnO films by molecular-beam epitaxy," *Applied Physics Letters*, vol. 87, 2005.

[153] J. Saan and P. Miller, Private Communication.

[154] D. C. Reynolds, D. C. Look, and B. Jogai, "Fine structure on the green band in ZnO," *Journal of Applied Physics*, vol. 89, pp. 6189-6191, 2001.

[155] B. K. Meyer, H. Alves, D. M. Hofmann, W. Kriegseis, D. Forster, F. Bertram, J. Christen, A. Hoffmann, M. Strassburg, M. Dworzak, U. Haboeck, and A. V. Rodina, "Bound exciton and donor-acceptor pair recombinations in ZnO," *Physica Status Solidi B-Basic Research*, vol. 241, pp. 231-260, 2004.

[156] K. J. Jin and S. J. Xu, "Fano resonance in the luminescence spectra of donor bound excitons in polar semiconductors," *Applied Physics Letters*, vol. 90, 2007.

[157] P. J. Hansen, Y. E. Strausser, A. N. Erickson, E. J. Tarsa, P. Kozodoy, E. G. Brazel, J. P. Ibbetson, U. Mishra, V. Narayanamurti, S. P. DenBaars, and J. S. Speck, "Scanning capacitance microscopy imaging of threading dislocations in GaN films grown on (0001) sapphire by metalorganic chemical vapor deposition," *Applied Physics Letters*, vol. 72, pp. 2247-2249, 1998.

[158] T. Michely, M. Kalff, G. Comsa, M. Strobel, and K. H. Heinig, "Coarsening mechanisms in surface morphological evolution," *Journal of Physics-Condensed Matter*, vol. 14, pp. 4177-4185, 2002.

[159] J. G. Lu, Y. Z. Zhang, Z. Z. Ye, Y. J. Zeng, H. P. He, L. P. Zhu, J. Y. Huang, L. Wang, J. Yuan, B. H. Zhao, and X. H. Li, "Control of p- and n-type conductivities in Li-doped ZnO thin films," *Applied Physics Letters*, vol. 89, 2006.

[160] A. I. Titov, P. A. Karaseov, and S. O. Kucheyev, "Furthering the understanding of ion-irradiation-induced electrical isolation in wide band-gap semiconductors," *Nuclear Instruments & Methods in Physics Research Section B-Beam Interactions with Materials and Atoms*, vol. 243, pp. 79-82, 2006.

[161] R. Dingle, "Luminescent Transitions Associated with Divalent Copper Impurities and Green Emission from Semiconducting Zinc Oxide," *Physical Review Letters*, vol. 23, pp. 579-&, 1969.

[162] K. Vanheusden, C. H. Seager, W. L. Warren, D. R. Tallant, and J. A. Voigt, "Correlation between photoluminescence and oxygen vacancies in ZnO phosphors," *Applied Physics Letters*, vol. 68, pp. 403-405, 1996.

[163] A. Y. L. Sim, G. K. L. Goh, S. Tripathy, D. Andeen, and F. F. Lange, "Photoluminescence of hydrothermally epitaxied ZnO films," *Electrochimica Acta*, vol. 52, pp. 2933-2937, 2007.

[164] S. F. Chichibu, T. Yoshida, T. Onuma, and H. Nakanishi, "Helicon-wave-excited-plasma sputtering epitaxy of ZnO on sapphire (0001) substrates," *Journal of Applied Physics*, vol. 91, pp. 874-877, 2002.

[165] S. F. Chichibu, T. Onuma, M. Kubota, A. Uedono, T. Sota, A. Tsukazaki, A. Ohtomo, and M. Kawasaki, "Improvements in quantum efficiency of excitonic emissions in ZnO epilayers by the elimination of point defects," *Journal of Applied Physics*, vol. 99, 2006.

[166] S. K. Hong, H. J. Ko, Y. Chen, T. Hanada, and T. Yao, "ZnO/GaN heterointerfaces and ZnO films grown by plasma-assisted molecular beam epitaxy on (0001) GaN/Al_2O_3," *Journal of Vacuum Science & Technology B*, vol. 18, pp. 2313-2321, 2000.

[167] C. Roland and G. H. Gilmer, "Growth of Germanium Films on Si(001) Substrates," *Physical Review B*, vol. 47, pp. 16286-16298, 1993.

[168] Y. F. Chen, D. M. Bagnall, Z. Q. Zhu, T. Sekiuchi, K. T. Park, K. Hiraga, T. Yao, S. Koyama, M. Y. Shen, and T. Goto, "Growth of ZnO single crystal thin films on c-plane (0 0 0 1) sapphire by plasma enhanced molecular beam epitaxy," *Journal of Crystal Growth*, vol. 181, pp. 165-169, 1997.

[169] H. Amano, N. Sawaki, I. Akasaki, and Y. Toyoda, "Metalorganic Vapor-Phase Epitaxial-Growth of a High-Quality Gan Film Using an Ain Buffer Layer," *Applied Physics Letters*, vol. 48, pp. 353-355, 1986.

[170] P. Waltereit, O. Brandt, A. Trampert, M. Ramsteiner, M. Reiche, M. Qi, and K. H. Ploog, "Influence of AlN nucleation layers on growth mode and strain relief of GaN grown on 6H-SiC(0001)," *Applied Physics Letters*, vol. 74, pp. 3660-3662, 1999.

[171] W. Xie, D. C. Grillo, R. L. Gunshor, M. Kobayashi, G. C. Hua, N. Otsuka, H. Jeon, J. Ding, and A. V. Nurmikko, "Blue Green Pn Junction Electroluminescence from ZnSe-Based Multiple Quantum-Well Structures," *Applied Physics Letters*, vol. 60, pp. 463-465, 1992.

[172] D. K. Fork and G. B. Anderson, "Epitaxial Mgo on Gaas(111) as a Buffer Layer for Z-Cut Epitaxial Lithium-Niobate," *Applied Physics Letters*, vol. 63, pp. 1029-1031, 1993.

[173] A. Nahhas, H. K. Kim, and J. Blachere, "Epitaxial growth of ZnO films on Si substrates using an epitaxial GaN buffer," *Applied Physics Letters*, vol. 78, pp. 1511-1513, 2001.

[174] Y. F. Chen, H. J. Ko, S. K. Hong, and T. Yao, "Layer-by-layer growth of ZnO epilayer on Al_2O_3(0001) by using a MgO buffer layer," *Applied Physics Letters*, vol. 76, pp. 559-561, 2000.

[175] D. C. Look, "Electrical transport properties of III-nitrides," *Materials Science and Engineering B-Solid State Materials for Advanced Technology*, vol. 50, pp. 50-56, 1997.

[176] H. Tampo, A. Yamada, P. Fons, H. Shibata, K. Matsubara, K. Iwata, S. Niki, K. Nakahara, and H. Takasu, "Degenerate layers in epitaxial ZnO films grown on sapphire substrates," *Applied Physics Letters*, vol. 84, pp. 4412-4414, 2004.

[177] D. E. Jesson, S. J. Pennycook, J. M. Baribeau, and D. C. Houghton, "Direct Imaging of Surface Cusp Evolution During Strained-Layer Epitaxy and Implications for Strain Relaxation," *Physical Review Letters*, vol. 71, pp. 1744-1747, 1993.

[178] S. C. Jain, M. Willander, J. Narayan, and R. Van Overstraeten, "III-nitrides: Growth, characterization, and properties," *Journal of Applied Physics*, vol. 87, pp. 965-1006, 2000.

[179] J. Narayan and B. C. Larson, "Domain epitaxy: A unified paradigm for thin film growth," *Journal of Applied Physics*, vol. 93, pp. 278-285, 2003.

[180] G. H. Lee, B. C. Shin, and I. S. Kim, "Critical thickness of BaTiO3 film on SrTiO3 (001) evaluated by reflection high-energy electron diffraction," *Materials Letters*, vol. 50, pp. 134-137, 2001.

[181] A. M. Ceschin and J. Massies, "Strain Induced 2d-3d Growth Mode Transition in Molecular-Beam Epitaxy of $In_xGa_{1-x}As$ on GaAs (001)," *Journal of Crystal Growth*, vol. 114, pp. 693-699, 1991.

[182] Y. S. Jung, Y. S. No, J. S. Kim, and W. K. Choi, "The effect of ZnO homo-buffer layer on ZnO thin films grown on c-Al_2O_3(0001) by plasma assisted molecular beam epitaxy," *Journal of Crystal Growth*, vol. 267, pp. 85-91, 2004.

[183] H. J. Osten and J. Klatt, "In-Situ Monitoring of Strain Relaxation During Antimony-Mediated Growth of Ge and $Ge_{1-y}C_y$ Layers on Si(001) Using Reflection High-Energy Electron-Diffraction," *Applied Physics Letters*, vol. 65, pp. 630-632, 1994.

[184] M. W. Cho, A. Setiawan, H. J. Ko, S. K. Hong, and T. Yao, "ZnO epitaxial layers grown on APO c-sapphire substrate with MgO buiter by plasma-assisted molecular beam epitaxy (P-MBE)," *Semiconductor Science and Technology*, vol. 20, pp. S13-S21, 2005.

[185] A. El-Shaer, A. C. Mofor, A. Bakin, M. Kreye, and A. Waag, "High-quality ZnO layers grown by MBE on sapphire," *Superlattices and Microstructures*, vol. 38, pp. 265-271, 2005.

[186] X. H. Wu, D. Kapolnek, E. J. Tarsa, B. Heying, S. Keller, B. P. Keller, U. K. Mishra, S. P. DenBaars, and J. S. Speck, "Nucleation layer evolution in metal-organic chemical vapor deposition grown GaN," *Applied Physics Letters*, vol. 68, pp. 1371-1373, 1996.

[187] A. Shigemori, J. Shike, K. Takahasi, K. Ishida, and R. Kimura, "Cubic GaN Film Growth Using AlN/GaN Ordered Alloy by RF Plasma-Assisted Molecular Beam Epitaxy," *Physica Status Solidi C*, vol. 0, pp. 170 -174, 2002.

[188] T. Minegishi, J. Yoo, H. Suzuki, Z. Vashaei, K. Inaba, K. Shim, and T. Yao, "Selective growth of Zn- and O-polar ZnO layers by plasma-assisted molecular beam epitaxy," *Journal of Vacuum Science & Technology B*, vol. 23, pp. 1286-1290, 2005.

[189] D. W. Pashley, J. H. Neave, and B. A. Joyce, "A model for the appearance of chevrons on RHEED patterns from InAs quantum dots," *Surface Science*, vol. 476, pp. 35-42, 2001.

[190] D. J. Dyson, *X-Ray and Electron Diffraction Studies in Materials Science*: Maney Publishing, 2004.

[191] R. W. Vook, "X-ray Diffraction," in *Epitaxial Growth*, vol. 1, *Material Science Series*, J. W. Matthews, Ed. New York: Academic Press, 1975.

[192] A. Boulle, C. Legrand, R. Guinebretiere, J. P. Mercurio, and A. Dauger, "X-Ray diffraction line broadening by stacking faults in $SrBi_2Nb_2O_9/SrTiO_3$ epitaxial thin films," *Thin Solid Films*, vol. 391, pp. 42-46, 2001.

[193] J. I. Langford, A. Boultif, J. P. Auffredic, and D. Louer, "The Use of Pattern Decomposition to Study the Combined X-Ray-Diffraction Effects of Crystallite Size and Stacking-Faults in Ex-Oxalate Zinc-Oxide," *Journal of Applied Crystallography*, vol. 26, pp. 22-33, 1993.

[194] D. B. Williams and C. B. Carter, *Transmission electron microscopy: a textbook for material science*. New York: Plenum Press, 1996.

[195] J. L. Rouviere, M. Arlery, B. Daudin, G. Feuillet, and O. Briot, "Transmission electron microscopy structural characterisation of GaN layers grown on (0001) sapphire," *Materials Science and Engineering B-Solid State Materials for Advanced Technology*, vol. 50, pp. 61-71, 1997.

[196] J. S. Speck, M. A. Brewer, G. Beltz, A. E. Romanov, and W. Pompe, "Scaling laws for the reduction of threading dislocation densities in homogeneous buffer layers," *Journal of Applied Physics*, vol. 80, pp. 3808-3816, 1996.

[197] O. Contreras, F. A. Ponce, J. Christen, A. Dadgar, and A. Krost, "Dislocation annihilation by silicon delta-doping in GaN epitaxy on Si," *Applied Physics Letters*, vol. 81, pp. 4712-4714, 2002.

[198] P. Sheldon, K. M. Jones, M. M. Aljassim, and B. G. Yacobi, "Dislocation Density Reduction through Annihilation in Lattice-Mismatched Semiconductors Grown by Molecular-Beam Epitaxy," *Journal of Applied Physics*, vol. 63, pp. 5609-5611, 1988.

[199] M. Tachikawa and M. Yamaguchi, "Film Thickness Dependence of Dislocation Density Reduction in GaAs-on-Si Substrates," *Applied Physics Letters*, vol. 56, pp. 484-486, 1990.

[200] R. L. Cummerow and A. R. Cherry, "Dislocation Pinning in N-Type Germanium," *Physical Review Letters*, vol. 3, pp. 367-368, 1959.

[201] R. Hull and J. C. Bean, "Misfit Dislocations in Lattice-Mismatched Epitaxial-Films," *Critical Reviews in Solid State and Materials Sciences*, vol. 17, pp. 507-546, 1992.

[202] H. Kato, K. Miyamoto, M. Sano, and T. Yao, "Polarity control of ZnO on sapphire by varying the MgO buffer layer thickness," *Applied Physics Letters*, vol. 84, pp. 4562-4564, 2004.

[203] S. K. Hong, H. J. Ko, Y. F. Chen, and T. Yao, "Control of ZnO film polarity," *Journal of Vacuum Science & Technology B*, vol. 20, pp. 1656-1663, 2002.

[204] M. W. Allen, M. M. Alkaisi, and S. M. Durbin, "Metal Schottky diodes on Zn-polar and O-polar bulk ZnO," *Applied Physics Letters*, vol. 89, 2006.

[205] Y. Wang, X. L. Du, Z. X. Mei, Z. Q. Zeng, M. J. Ying, H. T. Yuan, J. F. Jia, Q. K. Xue, and Z. Zhang, "Cubic nitridation layers on sapphire substrate and their role in polarity selection of ZnO films," *Applied Physics Letters*, vol. 87, 2005.

[206] Z. X. Mei, Y. Wang, X. L. Du, M. J. Ying, Z. Q. Zeng, H. Zheng, J. F. Jia, Q. K. Xue, and Z. Zhang, "Controlled growth of O-polar ZnO epitaxial film by oxygen radical preconditioning of sapphire substrate," *Journal of Applied Physics*, vol. 96, pp. 7108-7111, 2004.

[207] Y. Wang, X. L. Du, Z. X. Mei, Z. Q. Zeng, Q. Y. Xu, Q. K. Xue, and Z. Zhang, "Defect characteristics of ZnO film grown on (0001) sapphire with an ultrathin gallium wetting layer," *Journal of Crystal Growth*, vol. 273, pp. 100-105, 2004.

[208] H. Tampo, P. Fons, A. Yamada, K. K. Kim, H. Shibata, K. Matsubara, S. Niki, H. Yoshikawa, and H. Kanie, "Determination of crystallographic polarity of ZnO layers," *Applied Physics Letters*, vol. 87, 2005.

[209] T. Yamaguchi, T. Araki, Y. Saito, K. Kano, H. Kanazawa, Y. Nanishi, N. Teraguchi, and A. Suzuki, "Effect of sapphire substrate nitridation on determining rotation domain in GaN growth," *Journal of Crystal Growth*, vol. 237, pp. 993-997, 2002.

[210] A. Yoshikawa, X. Q. Wang, Y. Tomita, O. H. Roh, H. Iwaki, and T. Ishitani, "Rotation-domains suppression and polarity control of ZnO epilayers grown on skillfully treated c-Al_2O_3 surfaces," *Physica Status Solidi B-Basic Research*, vol. 241, pp. 620-623, 2004.

[211] Y. Z. Liu, M. J. Ying, X. L. Du, J. F. Jia, Q. K. Xue, X. D. Han, and Z. Zhang, "The 30 degrees rotation domains in wurtzite ZnO films," *Journal of Crystal Growth*, vol. 290, pp. 631-636, 2006.

[212] H. Akinaga, K. Ando, T. Abe, and S. Yoshida, "Control of the Crystal Orientation of Zincblende MnTe Epitaxial-Films Grown on GaAs," *Journal of Applied Physics*, vol. 74, pp. 746-748, 1993.

[213] Z. L. Wang and A. J. Shapiro, "Studies of Laalo3(100) Surfaces Using Rheed and Rem .1. Twins, Steps and Dislocations," *Surface Science*, vol. 328, pp. 141-158, 1995.

[214] J. W. Christian and S. Mahajan, "Deformation Twinning," *Progress in Materials Science*, vol. 39, pp. 1-157, 1995.

[215] T. W. Clyne, *Lecture Notes for Materials and Minerals Science Course E: Mechanical Behaviour of Solids*, University of Cambridge, 2007.

[216] L. L. Liu, Y. S. Zhang, and T. Y. Zhang, "Strain relaxation in heteroepitaxial films by misfit twinning. I. Critical thickness," *Journal of Applied Physics*, vol. 101, 2007.

[217] N. Sridhar, J. M. Rickman, and D. J. Srolovitz, "Twinning in thin films .1. Elastic analysis," *Acta Materialia*, vol. 44, pp. 4085-4096, 1996.

[218] Y. F. Yan, M. M. Al-Jassim, M. F. Chisholm, L. A. Boatner, S. J. Pennycook, and M. Oxley, "[1(1)over-bar00]/(1102) twin boundaries in wurtzite ZnO and group-III-nitrides," *Physical Review B*, vol. 71, 2005.

[219] S. O. Kucheyev, J. E. Bradby, J. S. Williams, C. Jagadish, and M. V. Swain, "Mechanical deformation of single-crystal ZnO," *Applied Physics Letters*, vol. 80, pp. 956-958, 2002.

[220] M. W. Allen, Private Communications.

[221] L. T. Romano, J. E. Northrup, A. J. Ptak, and T. H. Myers, "Faceted inversion domain boundary in GaN films doped with Mg," *Applied Physics Letters*, vol. 77, pp. 2479-2481, 2000.

[222] J. L. Weyher, P. D. Brown, J. L. Rouviere, T. Wosinski, A. R. A. Zauner, and I. Grzegory, "Recent advances in defect-selective etching of GaN," *Journal of Crystal Growth*, vol. 210, pp. 151-156, 2000.

[223] K. Shiojima, "Atomic force microscopy and transmission electron microscopy observations of KOH-etched GaN surfaces," *Journal of Vacuum Science & Technology B*, vol. 18, pp. 37-40, 2000.

[224] S. K. Hong, B. J. Kim, H. S. Park, Y. Park, S. Y. Yoon, and Y. I. Kim, "Evaluation of nanopipes in MOCVD grown (0001) GaN/Al_2O_3 by wet chemical etching," *Journal of Crystal Growth*, vol. 191, pp. 275-278, 1998.

[225] H. Morkoc, "Comprehensive characterization of hydride VPE grown GaN layers and templates," *Materials Science & Engineering R-Reports*, vol. 33, pp. 135-207, 2001.

[226] S. B. Samavedam, W. J. Taylor, J. M. Grant, J. A. Smith, P. J. Tobin, A. Dip, A. M. Phillips, and R. Liu, "Relaxation of strained Si layers grown on SiGe buffers," *Journal of Vacuum Science & Technology B*, vol. 17, pp. 1424-1429, 1999.

[227] K. Iwata, P. Fons, K. Matsubara, A. Yamada, S. Niki, and K. Nakahara, "Methods of manufacturing semiconductor device having ZnO based oxide semiconductor layer." United States, 2002.

[228] H. J. Gao and W. D. Nix, "Surface roughening of heteroepitaxial thin films," *Annual Review of Materials Science*, vol. 29, pp. 173-209, 1999.

[229] M. Zinkeallmang, L. C. Feldman, and S. Nakahara, "Role of Ostwald Ripening in Islanding Processes," *Applied Physics Letters*, vol. 51, pp. 975-977, 1987.

[230] S. H. Lim, S. Song, T. S. Park, E. Yoon, and J. H. Lee, "Si adatom diffusion on Si (100) surface in selective epitaxial growth of Si," *Journal of Vacuum Science & Technology B*, vol. 21, pp. 2388-2392, 2003.

[231] B. Van Zeghbroeck, "Principles of Semiconductor Devices," University of Colorado, http://ece-www.colorado.edu/~bart/book/, 2004.

[232] W. S. Baer, "Faraday Rotation in ZnO - Determination of Electron Effective Mass," *Physical Review*, vol. 154, pp. 785-&, 1967.

[233] M. Lundstrom, *Fundamentals of Carrier Transport*, Second ed: Cambridge University Press, 2000.

[234] Y. S. Jung, O. V. Kononenko, and W. K. Choi, "Electron transport in high quality undoped ZnO film grown by plasma-assisted molecular beam epitaxy," *Solid State Communications*, vol. 137, pp. 474-477, 2006.

[235] T. Makino, Y. Segawa, A. Tsukazaki, A. Ohtomo, and M. Kawasaki, "Electron transport in ZnO thin films," *Applied Physics Letters*, vol. 87, 2005.

[236] E. H. Hall, "On a New Action of Magnet on Electric Currents," *American Journal of Mathematics*, vol. 2, pp. 287 - 291 1879.

[237] D. C. Look and R. J. Molnar, "Degenerate layer at GaN/sapphire interface: Influence on hall-effect measurements," *Applied Physics Letters*, vol. 70, pp. 3377-3379, 1997.

[238] I. Mahboob, T. D. Veal, C. F. McConville, H. Lu, and W. J. Schaff, "Intrinsic electron accumulation at clean InN surfaces," *Physical Review Letters*, vol. 92, 2004.

[239] D. C. Look, "Bulk and Contact Electrical-Properties by the Magneto-Transmission-Line Method - Application to Gaas," *Solid-State Electronics*, vol. 30, pp. 615-618, 1987.

[240] C. H. Swartz, R. P. Tompkins, T. H. Myers, D. C. Look, and J. R. Sizelove, "Characterization of multiple carriers in GaN using variable magnetic-field Hall measurements," *Journal of Electronic Materials*, vol. 33, pp. 412-417, 2004.

[241] J. Antoszewski, L. Faraone, I. Vurgaftman, J. R. Meyer, and C. A. Hoffman, "Application of quantitative mobility-spectrum analysis to multilayer HgCdTe structures," *Journal of Electronic Materials*, vol. 33, pp. 673-683, 2004.

[242] P. A. Anderson, C. H. Swartz, D. Carder, R. J. Reeves, S. M. Durbin, S. Chandril, and T. H. Myers, "Buried p-type layers in Mg-doped InN," *Applied Physics Letters*, vol. 89, 2006.

[243] D. C. Look, "Progress in ZnO materials and devices," *Journal of Electronic Materials*, vol. 35, pp. 1299-1305, 2006.

[244] W. A. Beck and J. R. Anderson, "Determination of Electrical Transport-Properties Using a Novel Magnetic Field-Dependent Hall Technique," *Journal of Applied Physics*, vol. 62, pp. 541-544, 1987.

[245] J. R. Meyer, C. A. Hoffman, F. J. Bartoli, D. A. Arnold, S. Sivananthan, and J. P. Faurie, "Methods for Magnetotransport Characterization of Ir Detector Materials," *Semiconductor Science and Technology*, vol. 8, pp. 805-823, 1993.

[246] I. Vurgaftman, J. R. Meyer, C. A. Hoffman, D. Redfern, J. Antoszewski, L. Faraone, and J. R. Lindemuth, "Improved quantitative mobility spectrum analysis for Hall characterization," *Journal of Applied Physics*, vol. 84, pp. 4966-4973, 1998.

[247] J. Rothman, J. Meilhan, G. Perrais, J. P. Belle, and O. Gravrand, "Maximum entropy mobility spectrum analysis of HgCdTe heterostructures," *Journal of Electronic Materials*, vol. 35, pp. 1174-1184, 2006.

[248] J. S. Im, A. Moritz, F. Steuber, V. Harle, F. Scholz, and A. Hangleiter, "Radiative carrier lifetime, momentum matrix element, and hole effective mass in GaN," *Applied Physics Letters*, vol. 70, pp. 631-633, 1997.

[249] G. Pozina, J. P. Bergman, B. Monemar, B. Heying, and J. S. Speck, "Radiative and nonradiative exciton lifetimes in GaN grown by molecular beam epitaxy," *Physica Status Solidi B-Basic Research*, vol. 228, pp. 485-488, 2001.

[250] D. C. Reynolds, D. C. Look, B. Jogai, J. E. Hoelscher, R. E. Sherriff, M. T. Harris, and M. J. Callahan, "Time-resolved photoluminescence lifetime measurements of the Gamma(5) and Gamma(6) free excitons in ZnO," *Journal of Applied Physics*, vol. 88, pp. 2152-2153, 2000.

[251] A. Teke, U. Ozgur, S. Dogan, X. Gu, H. Morkoc, B. Nemeth, J. Nause, and H. O. Everitt, "Excitonic fine structure and recombination dynamics in single-crystalline ZnO," *Physical Review B*, vol. 70, 2004.

[252] F. Y. Jen, Y. C. Lu, C. Y. Chen, H. C. Wang, C. C. Yang, B. P. Zhang, and Y. Segawa, "Temperature-dependent exciton dynamics in a ZnO thin film," *Applied Physics Letters*, vol. 87, 2005.

[253] T. Koida, S. F. Chichibu, A. Uedono, T. Sota, A. Tsukazaki, and M. Kawasaki, "Radiative and nonradiative excitonic transitions in nonpolar (11-20) and polar (000-1) and (0001) ZnO epilayers," *Applied Physics Letters*, vol. 84, pp. 1079-1081, 2004.

[254] D. J. Wolford, G. D. Gilliland, T. F. Kuech, L. M. Smith, J. Martinsen, J. A. Bradley, C. F. Tsang, R. Venkatasubramanian, S. K. Ghandi, and H. P. Hjalmarson, "Intrinsic Recombination and Interface Characterization in Surface-Free Gaas Structures," *Journal of Vacuum Science & Technology B*, vol. 9, pp. 2369-2376, 1991.

[255] N. L. Rowell, J. P. Noel, D. C. Houghton, A. Wang, L. C. Lenchyshyn, M. L. W. Thewalt, and D. D. Perovic, "Exciton Luminescence in Si1-Xgex/Si Heterostructures Grown by Molecular-Beam Epitaxy," *Journal of Applied Physics*, vol. 74, pp. 2790-2805, 1993.

[256] F. Chen, A. N. Cartwright, H. Lu, and W. J. Schaff, "Temperature dependence of carrier lifetimes in InN," *Physica Status Solidi a-Applications and Materials Science*, vol. 202, pp. 768-772, 2005.

[257] G. Lasher and F. Stern, "Spontaneous + Stimulated Recombination Radiation in Semiconductors," *Physical Review a-General Physics*, vol. 133, pp. A553-&, 1964.

[258] V. C. Lopes, A. J. Syllaios, and M. C. Chen, "Minority-Carrier Lifetime in Mercury Cadmium Telluride," *Semiconductor Science and Technology*, vol. 8, pp. 824-841, 1993.

[259] D. C. Oh, T. Suzuki, J. J. Kim, H. Makino, T. Hanada, M. W. Cho, and T. Yao, "Electron-trap centers in ZnO layers grown by molecular-beam epitaxy," *Applied Physics Letters*, vol. 86, 2005.

[260] B. Martini, "Enthalpy of Sublimation Using Knudsen Method," University of California Santa Cruz, 2003.

Appendix A

Simulation of Zn flux distributions

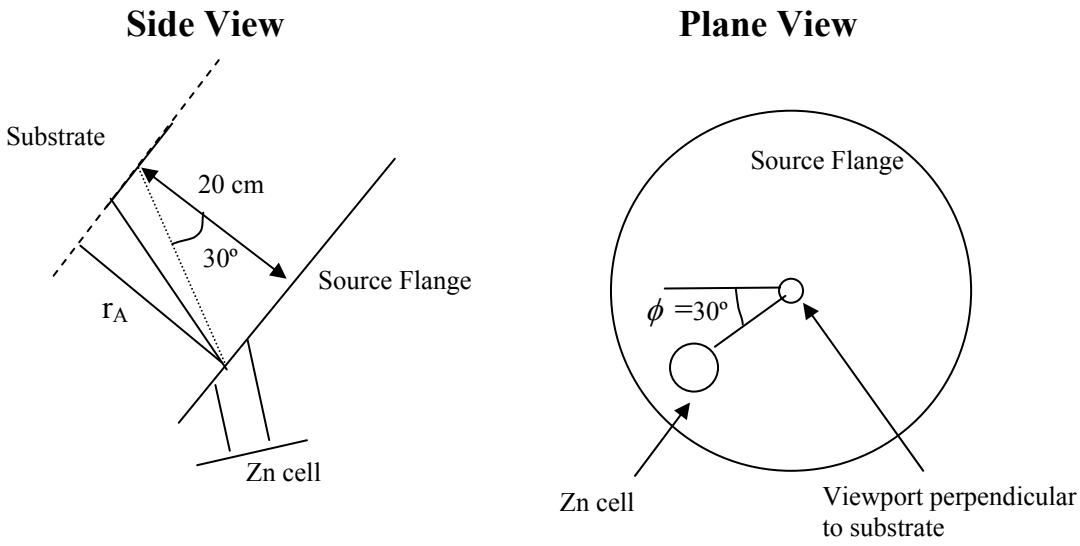

Figure A. 1 The geometry of the Perkin-Elmer 430 system showing the relative position of the Zn cell and the substrate.

Figure A.1 shows the geometric relationship between the Zn cell and the substrate in the Perkin-Elmer 430 system. Assuming the axis perpendicular to the substrate is the z-axis and the plane parallel to the substrate as the x-y plane. One can simplify the situation by saying that the Zn cell is perpendicular to the point (x = 5, y = 5), i.e. that the cell is 5 cm away from the flange centre (This has been measured and confirmed). Then, the actual flux can be calculated relative to the point (5,5), using the cosine law for off axis cell (Equation 2.9) by taking ϕ = 30°, r_A = 20 cm and r_B calculated geometrically using r_A and the x-y position of the point in interest (i.e. r_B is the distance between the point (x,y,0) and (5,5,20). It can be calculated that r_B for point (0,0,0) (i.e. centre of the substrate) is 23.7 cm.

For the Clausing model, the extra parameter used is the correction factors W_A, W_B and C_0. The Clausing transmission factor is given by the empirical formula [260]:

$$W = \frac{0.98441 + 0.00466 \times (L0/2D0)}{1 + 0.46034 \times (L0/2D0)}$$

By using L0 = 0.5 and D0 = 0.1 for the orifice, and L0 = 14 and D0 = 2.75 for the cell, the Clausing factors were found to be 0.463 and 0.459.

The correction factor C is given by:

$$C = 1 - \frac{2}{\pi}(1-\alpha)(\arcsin p + p\sqrt{1-p^2}) + \frac{4}{3\pi p}(1-2\alpha)\left[1-(\sqrt{1-p^2})^3\right]$$

where

$$p = \frac{L0}{D0}\tan\theta$$

and

$$\alpha = \frac{\sqrt{L0^2 + D0^2} - L0}{D0 + D0^2/\sqrt{L0^2 + D0^2}}$$

where θ is the same angle as that used in Equation 2.8, which is the angle between r_A and r_B.

Appendix B

Identification of Films

At University of Canterbury, the ZnO thin films grown using the Perkin-Elmer 430 MBE system are catalogued using a standard code with the form A - B / C - D, where A is the overall film number, B signifies the material, C represents the substrate material, and D is the film number in the growth series. For example, 232 - ZO/Sa-18 is the 232nd film grown by the Canterbury MBE group, and it is the 18th ZnO thin film on sapphire that was grown by the group.

The following table shows the catalogue code for a selection of samples studied in this thesis:

Table A-1 Catalogue code for selected films discussed in this thesis.

Chapter/Figure	Identifier in the thesis	Catalogue code
Figure 3.3	a	276-ZO/Sa-34
Figure 3.3	b	280-ZO/Sa-35
Figure 3.3	c	410-ZO/Sa-56
Figure 3.3	d	433-ZO/Sa-64
Figure 3.3	e	460-ZO/MO-Sa-02
Figure 3.3	f	471-ZO/Sa-73
Figure 3.3	g	472-ZO/Sa-74
Figure 3.3	h	458-ZO/MO-Sa-01
Figure 3.3	i	303-ZO/Sa-41
Figure 3.3	j	445-ZO/Sa-65
Figure 3.3	k	310-ZO/Sa-42
Figure 3.3	l	347-ZO/Sa-51
Chapter 3.2	Zn-rich	568-ZO/Sa-83
Chapter 3.2	Stoichiometric	567-ZO/Sa-82
Chapter 3.2	O-rich	570-ZO/Sa-84
Chapter 3.3	150 W, 276 hole	301-ZO/Sa-40

Chapter 3.3	200 W, 276 hole	312-ZO/Sa-44
Chapter 3.3	250 W, 276 hole	305-ZO/Sa-42
Chapter 3.3	300 W, 276 hole	300-ZO/Sa-39
Chapter 3.3	400 W, 276 hole	303-ZO/Sa-41
Chapter 3.3	300 W, 25 hole	346-ZO/Sa-50
Chapter 3.3	400 W, 25 hole	347-ZO/Sa-51
Chapter 3.3	500 W, 25 hole	352-ZO/Sa-56
Chapter 3.3	400 W, 1 hole	445-ZO/Sa-65
Chapter 3.3	500 W, 1 hole	447-ZO/Sa-66
Chapter 3.4	400 °C	470-ZO/Sa-72
Chapter 3.4	550 °C	208-ZO/Sa-13
Chapter 3.4	650 °C	303-ZO/Sa-41
Chapter 3.4	750 °C	310-ZO/Sa-43
Chapter 4.2	With LT-buffer	232-ZO/Sa-18
Chapter 4.2	Without LT-buffer	234-ZO/Sa-19
Chapter 4.2 onwards	Sample A	303-ZO/Sa-41
Chapter 4.2 onwards	Sample B	300-ZO/Sa-39
Chapter 4.2 onwards	Sample C	305-ZO/Sa-42
Chapter 4.3	MgO on sapphire	370-MgO/Sa-01
Chapter 4.3	0.5 nm MgO	376-MgO/Sa-02
Chapter 4.3	1 nm MgO	381-MgO/Sa-04
Chapter 4.3	2 nm MgO	377-MgO/Sa-03
Chapter 4.3	3 nm MgO	382-MgO/Sa-05
Chapter 4.3 onwards	Sample M	458-ZO/MO-Sa-01
Chapter 4.3 onwards	Sample E	347-ZO/Sa-51
Chapter 4.3 onwards	Sample F	445-ZO/Sa-65
Figure 4.29	1 nm MgO buffer film	500-ZO/MO-Sa-03
Figure 4.29	3 nm MgO buffer film	500-ZO/MO-Sa-04
Chapter 4.4.5	Porous ZnO on GaN	210-ZO/GN-01
Chapter 5 onwards	Sample D	346-ZO/Sa-50
Figure 6.3	300 W	346-ZO/Sa-50
Figure 6.3	350 W	349-ZO/Sa-53

Figure 6.3	400 W	347-ZO/Sa-51
Figure 6.3	500 W	352-ZO/Sa-56